UNIVERSITY OF CALIFORNIA

Los Angeles

Realistic Modeling of the Catalytic Heterogeneous Interface

A dissertation submitted in partial satisfaction of the

requirements for the degree Doctor of Philosophy

in Chemistry

by

Mai-Anh Ha

2017

ABSTRACT OF THE DISSERTATION

Realistic Modeling of the

Catalytic Heterogeneous Interface

by

Mai-Anh Ha

Doctor of Philosophy in Chemistry

University of California, Los Angeles, 2017

Professor Anastassia N. Alexandrova, Chair

At the catalytic interface, catalysts are represented by an ensemble of cluster isomers or surfaces, each of which may contribute to the system's stability, activity, selectivity, and resistance to sintering or poisons by reaction byproducts. I use *ab-initio* methods in conjunction with statistical-mechanical arguments to predict physico-chemical properties and guide development of premiering catalysts. Specifically, I utilize the work-horse of computation, density functional theory (DFT) calculations, to characterize systems of interest. Statistical-mechanical arguments such as Boltzmann-populations allow us to understand the role of relevant cluster isomers, surfaces, and reagents within the high temperature regime of real catalysis. My theoretical work applies this ensemble perspective of heterogeneous catalysis to diverse systems, from supported subnano-clusters to surfaces such as defective anatase for photocatalysis and Pt-Ni for fuel cells.

Supported metal clusters often display non-monotonic behavior in which a cluster of a specific *n* size may be especially active. My theoretical work at UCLA explores the high activity and tunability of supported clusters by investigating the system as an ensemble. Three of my four first author papers represent fundamental, surface science work into tuning supported clusters. In particular, the well-known Pt-Pd resistance to sintering i.e. agglomeration of the clusters to bulk inertness was explained successfully through this ensemble consideration. 1:1 ratios of Pt:Pd featured more accessible isomers than their pure and mixed counterparts, resulting in an entropic contribution to chemical stability. In collaboration with experiment, we identified the highly active Pt_7 for ethylene dehydrogenation, each negatively charged cluster able to adsorb and activate a maximum of 3 ethylenes. Pt_7's high activity over that of a similar cluster size, Pt_8, resulted from Pt_7's fluxionality, the ensemble is able to access isomer geometries with more exposed Pt sites. Selective de(hydrogenation) forms the basis for fossil fuel refinery through cracking of hydrocarbons[3] and, due to its endothermic nature, can act as a self-cooling mechanism for jet engines. It also represents a tractable process for testing the tunability of cluster size and dopant effects. Successive de(hydrogenation) often results in deactivation as catalyst sites are blocked by carbon (coking). We therefore tempered that high activity and predilection towards coke formation by doping Pt_7 with the electropositive boron, which sustained activity during successive reaction cycles by adsorbing and activating ~1 ethylene.

The ensemble perspective may also be extended to surfaces by accounting for non-equivalent defect sites, the local minima of reaction reagents and their subsequent products, or the distribution of facets present at the interface. The anatase surface remains ubiquitous in the field of catalysis for its unique photoactivity and reactivity, specifically, for CO_2 reduction and water-splitting. CO_2 reduction is an intermediate step towards the formation of organic products such as methanol and water-splitting for hydrogen evolution remains key to renewable energy. Both theory and experiment have cited surface defects such as oxygen vacancies to be a major

contributing factor in anatase's catalytic activity. I examined 9 non-equivalent oxygen vacancy sites under varying levels of theory and characterized a new surface oxygen vacancy minimum, whose electrons localized at unique Ti sites as compared to previous studies. This has important ramifications on the catalysis of reaction intermediates due to their interaction with surface oxygen vacancies. For example, the co-adsorption of CO_2 and H_2O at an oxygen vacancy results in spontaneous splitting of water (global minimum) and the formation of other organic species such as formic acid (local minima). Tilocca, et. al. estimated the barrier to be circa 0.1 eV and this barrier is eliminated in the presence of CO_2 and an oxygen vacancy. In addition to a comprehensive study of defective anatase, I also characterized the interface of Pt-Ni nanowires in depth by considering varying lattice constants, facets, and Pt-skins on a sub-alloy of Pt-Ni. The Pt-Ni nanowires expressed high catalytic activity and durability for the oxygen reduction reaction (ORR). ORR remains the limiting factor in fuel cells due to cost (requiring high Pt-loadings) and kinetics (occurring at a rate of six orders of magnitude slower than the hydrogen oxidation reaction). By considering the interface in such complexity, I converged upon the same facet distribution and lattice constant as experiment's high performer of (100) ~ (111) > (110) at a compressed lattice constant of ~ 3.7 Å. This trend in stability observed by theory explained in part the durability of this high performer.

Thus, the system-specific investigations for catalysis presented in this dissertation show that I have successfully applied *ab-initio* methods in conjunction with statistical-mechanical arguments to understand the role of heterogeneity (e.g., cluster isomers, defect sites, facets) in determining catalytic properties. Our *in silico* predictions of stability and activity have complemented and informed or even prompted the development of novel catalysts from supported clusters to extended surfaces.

The dissertation of Mai-Anh Ha is approved.

Kendall N. Houk

Yu Huang

Anastassia N. Alexandrova, Committee Chair

University of California, Los Angeles

2017

To my dear husband, family, friends, and all the women who have inspired me to greater heights than I thought possible

TABLE OF CONTENTS

LIST OF FIGURES

5. CHAPTER 5 *Diborane Interactions with Pt_7/alumina: Preparation of Size-Controlled Boronated Pt Model Catalysts with Improved Coking Resistance*

LIST OF TABLES

6. CHAPTER 6 *Photocatalysis with Defective Anatase*

7. *Exceptional Oxygen Reduction Reaction Activity and Durability of Platinum-Nickel Nanowires Through Synthesis and Post-Treatment Optimization*

ACKNOWLEDGEMENTS

I want to first thank my Mount Holyoke professors for sending me down this rabbit hole of science, Professor Maria Gomez and Professor Himali Jayathilake. You are both an inspiration: Professor Jayathilake for prompting my interest in chemistry while teaching general chemistry to (at the time) this little first year and Professor Gomez for engaging me with her final exams in Physical Chemistry (to derive and recreate results from published papers!) and encouraging me to do summer research in proton conduction related to fuel cells. In fact, during that summer doing research and attending conferences, I was able to meet my now husband. So, I owe Professor Gomez a double thank-you, for introducing me to computational chemistry and encouraging me to apply to graduate school as well as for bringing me to conferences where I made new friends and met the man who would one day become my husband, Shaun Alia. On that note, thank you darling for your staunch support throughout the ups and downs of graduate school. Our conversations, whether in the sciences, the humanities, or the miscellaneous subjects of life, have always emboldened me to be better (with a little laughter in the process).

Here at UCLA, I would like to begin by thanking my PI, Professor Anastassia Alexandrova, for mentoring me these four and a half years into the scientific researcher I am today. It's thrilling to look back on my graduate school visit to UCLA to where I am now. When I heard you speak about Jin Zhang's work on Pd clusters, I thought, how lucky it would be if I got to work on such interesting projects… and the rest is history. Thank you for giving me the chance to work on interesting project after interesting project, you've sparked my scientific imagination and supported me along all the meandering roads of research. I would also like to thank my committee members, Professor Ken Houk for your encouragement that I should come to UCLA for graduate school and continued enthusiasm for my work here at UCLA and Professor Yu Huang for your patience as an experimentalist in engaging with my computational work.

And, of course, I must thank my lab mates for their illuminating conversation and our frequent tea/coffee and snack breaks. I am forever grateful to the post-doctoral researchers Jonny Dadras for mentoring me through my first project on Pt-Pd, your encouragement, support, and endless patience to my questions will always be remembered; Tony Smith for being the voice of reason, in every situation, and your acts of charity, whether they were snide, but amusing remarks on life and academia or a much-needed cookie donation to the always-starving graduate student; Sean Nedd for cracking dad jokes and sprinkling our conversations with puns (cuing groans from all of us); Elisa Jimenez-Izal for being my dear, dear friend, your cheers and cheering conversations were the highlights of my day and I will always miss this precious time when you and I would talk and talk and talk.

It's been my delight to have wonderful lab-mates to share my graduate school days: Crystal Valdez for reminding me that there is life outside research, your wedding was a beautiful, colorful celebration of that (you and Manasa are such wonderful dancing fiends!); Michael Nechay for being the best baking buddy a food lover could hope for, our creations still live on in my dreams (and my computer hard drive); Nathan Gallup and Anjan Nandula for starting out with me during these tumultuous years, Nathan for being loquacious when we most needed a break from staring at the computer and Anjan for sprinkling our desks with chocolate (always a welcome treat), I wish you both the absolute best as our paths diverge; Addis Fuhr for tickling my funny bone with his observations of Los Alamos, UCLA, California, and all the people therein; Derek Urwin for being so cool and smart, balancing being a firefighter, father, and graduate student all at once; Huanchen Zhai, my summer undergraduate protégé, who's now a graduate student of our lab, for being a pleasure to mentor (not that you ever really needed a mentor, even when you were an undergrad) and a pleasure as a colleague; PJ Robinson, our undergraduate soon to be a graduate student on his own scientific path, for always being ready to gossip science and the gamut of topics (and being a fellow sous chef to Mike's delicious creations); and all our new members for being willing to go on a little food jaunt through LA or

chat about the miscellaneous et cetera of life (Daniel Hatfield, Olivia Irving, David Reilley, Jack Fuller, Borna Zandkarimi, Amy Lai, Jiyuan Liu).

Last, but not least, I have been blessed to work with wonderful experimentalists across the nation: Professor Scott Anderson and graduate students Eric Baxter and Ashley Cass at University of Utah; Professor Stephen Cronin and graduate student Jing Qiu at the University of Southern California; Electrochemical Engineering and Materials Chemistry Group Manager Bryan Pivovar and Staff Scientist Shaun Alia at the National Renewable Energy Laboratory. Thank you for the always refreshing dialogue between experiment and theory, which has amounted to a considerable number of co-authored publications.

This dissertation is a collection of previous publications listed below:

Chapter 1 is adapted with permission from publication “Oxygen Vacancies of Anatase 101: Extreme Sensitivity to the Density Functional Theory Method.” **Ha, M.-A**.; Alexandrova, A. N. *J. Chem. Theor. Comput.,* **2016**, *12,* pp. 2889-2895. Copyright (2017) American Chemical Society. This work was supported by the Air Force Office of Scientific Research (No. BRI 10029173-S3) and NSF CAREER AWARD (No. CHE1351968).

Chapter 2 is adapted with permission from publication “Rutile Deposited Pt-Pd Clusters: A Hypothesis Regarding the Stability at 50/50 Ratio.” **Ha, M.-A.**; Dadras, J.; Alexandrova, A.N. *ACS Catalysis*, **2014**, *4*, pp. 3570-3580. Copyright (2017) American Chemical Society. This work was supported by the Air Force Office of Scientific Research (No. BRI 10029173-S3). A.N.A. also thanks the Alfred P. Sloan Foundation Fellowship.

Chapter 3 is a modified version of the publication “Ethylene Dehydrogenation on $Pt_{4,7,8}$ Clusters on Al_2O_3: Strong Cluster Size Dependence Linked to Preferred Catalyst Morphologies.” Baxter, E. T.*; **Ha, M.-A**.*; Cass, A. C.; Alexandrova, A. N.; Anderson, S. L. *ACS Catalysis*, **2017**, *7*, pp. 3322-3335. Baxter, E. T. and **Ha, M.-A**. contributed equally to this work. This work was supported by the Air Force Office of Scientific Research under a Basic Research Initiative

grant (AFOSR FA9550-16-1-0141) to A.N.A. and S.L.A. M.-A.H. was also funded by the UCLA Graduate Division Dissertation Year Fellowship.

Chapter 4 is adapted with permission from publication “Boron Switch for Selectivity of Catalytic Dehydrogenation on Size-Selected Pt clusters on Al_2O_3.” **Ha, M.-A.**; Baxter, E. T.; Cass, A. C.; Anderson, S. L. ; Alexandrova, A. N. *J. Am. Chem. Soc.*, **2017**, *139*, pp. 11568–11575. Copyright (2017) American Chemical Society. This work was supported by the Air Force Office of Scientific Research under a Basic Research Initiative grant (AFOSR FA9550-16-1-0141) to A.N.A. and S.L.A. M.-A.H. was also funded by the UCLA Graduate Division Dissertation Year Fellowship.

Chapter 5 is a modified version of the submitted manuscript “Diborane Interactions with Pt_7/alumina: Preparation of Size-Controlled Borated Pt Model Catalysts with Improved Coking Resistance.” Baxter, E. T.; Ha, M.-A.; Cass, A. C.; Zhai, H.; Alexandrova, A. N.; Anderson, S. L. *J. Am. Chem. Soc.*, **2017**, *139*, pp. 11568–11575. This work was supported by the Air Force Office of Scientific Research under a Basic Research Initiative grant (AFOSR FA9550-16-1-0141) to A.N.A. and S.L.A. M.-A.H. was also funded by the UCLA Graduate Division Dissertation Year Fellowship.

Chapter 6 is adapted with permission from publications:

“Artificial Photosynthesis on TiO2-Passivated InP Nanopillars.” Qiu, J.; Zeng, G.; **Ha, M.-A.;** Ge, M.; Lin, Y.; Hettick, M.; Alexandrova, A. N.; Javery, A.; Cronin, S. B.*. *Nano Lett.*, **2015**, *15*, pp. 6177-6181. Copyright (2017) American Chemical Society.

“A microscopic study of atomic layer deposition of TiO2 on GaAs and its photocatalytic applications.” Qiu, J.; Zeng, G.; **Ha, M.-A.;** Hou, B.; Mechlenburg, M.; Shi, H.; Alexandrova, A. N.; Cronin, S. B. *Chem. Mater.*, **2015,** *27*, pp. 7977-7981. Copyright (2017) American Chemical Society.

"Joint Experimental and Theoretical Study on Photocatalysis involving Co-adsorption of H_2O and CO_2 on Reduced Anatase." Qiu, J.; **Ha, M.-A**.; Alexandrova, A. N.; Cronin, S. B. *Manuscript in preparation.*

This work was supported by the Air Force Office of Scientific Research under the eBasic Research Initiative grants (AFOSR FA9550-12-1-0481 and AFOSR FA9550-16-1-0141) to A.N.A. M.-A.H. was also funded by the UCLA Graduate Division Dissertation Year Fellowship.

Chapter 7 is a modified version of the publication "Exceptional Oxygen Reduction Reaction Activity and Durability of Platinum-Nickel Nanowires Through Synthesis and Post-Treatment Optimization." Alia, S. M.; Ngo, C.; Shulda, S.; **Ha, M.-A**.; Dameron, A.; Weker, J. N.; Neyerlin, K. C.; Kocha, S. S.; Pylypenko, S.; Pivovar, B. S. *ACS Omega*, **2017**, *2*, pp. 1408-1418. Financial support for DFT calculations was provided by the U.S. Department of Energy (DOE) Office of Science Graduate Student Research (SCGSR) award for project, "Modeling of High-Performing Pt-Based ORR Catalysts to Facilitate Future Design and Development of New Materials."

VITA

2009-2013	Bachelor of Arts in Chemistry and English, *magna cum laude* Mount Holyoke College, 50 College St., South Hadley, MA 01075
2010-2012	Student Manager of Abbey Dining Hall, Mount Holyoke College
2010	Grader for General Chemistry
2011-2013	Department of Chemistry Liaison
2011-2013	Department of English Liaison
2011-2013	Webmaster of Sceptical Chymist, student resources website
2012	Howard Hughes Medical Institute Summer Research Fellow (mentor of first-year Erin A. Pierce), HHMI #52006307
2013	Physical Chemistry Teaching Assistant
2013	Chemistry Department Book Award
2013-2017	Graduate Student Teaching Assistant or Researcher, University of California, Los Angeles
2015-2017	American Chemistry Society (ACS) Scholars Mentor
2016	U.S. Department of Energy (DOE) Office of Science Graduate Student Research (SCGSR) award
2016	Ernest F. Hare, Jr. Memorial Scholarship
2017	UCLA Graduate Division Dissertation Year Fellowship
2017	UCLA Research Showcase Fellowship Award
2017	UCLA's Nominee for the Schmidt Science Fellows program

PUBLICATIONS

Baxter, E. T.; **Ha, M.-A**.; Cass, A. C.; Zhai, H.; Alexandrova, A. N.; Anderson, S. L. "Diborane Interactions with Pt_7/alumina: Preparation of Size-Controlled Boronated Pt Model Catalysts with Improved Coking Resistance." **Submitted**.

Ha, M.-A.; Baxter, E. T.; Cass, A. C.; Anderson, S. L. ; Alexandrova, A. N. "Boron Switch for Selectivity of Catalytic Dehydrogenation on Size-Selected Pt clusters on Al_2O_3." *J. Am. Chem. Soc.*, **2017**, *139*, pp. 11568–11575.

Baxter, E. T.*; **Ha, M.-A**.*; Cass, A. C.; Alexandrova, A. N.; Anderson, S. L. "Ethylene Dehydrogenation on $Pt_{4,7,8}$ Clusters on Al_2O_3: Strong Cluster Size Dependence Linked to Preferred Catalyst Morphologies." *ACS Catalysis*, **2017**, *7*, pp. 3322-3335. ***Authors contributed equally**

Alia, S. M.; Ngo, C.; Shulda, S.; **Ha, M.-A**.; Dameron, A.; Weker, J. N.; Neyerlin, K. C.; Kocha, S. S.; Pylypenko, S.; Pivovar, B. S. "Exceptional Oxygen Reduction Reaction Activity and Durability of Platinum-Nickel Nanowires Through Synthesis and Post-Treatment Optimization." *ACS Omega*, **2017**, *2*, pp. 1408-1418.

Ha, M.-A.; Alexandrova, A. N. "Oxygen Vacancies of Anatase 101: Extreme Sensitivity to the Density Functional Theory Method." *J. Chem. Theor. Comput.,* **2016**, *12,* pp. 2889-2895.

Qiu, J.; Zeng, G.; **Ha, M.-A.;** Hou, B.; Mechlenburg, M.; Shi, H.; Alexandrova, A. N.; Cronin, S. "A microscopic study of atomic layer deposition of TiO2 on GaAs and its photocatalytic applications." B. *Chem. Mater*., **2015,** *27*, pp. 7977-7981.

Qiu, J.; Zeng, G.; **Ha, M.-A.;** Ge, M.; Lin, Y.; Hettick, M.; Alexandrova, A. N.; Javery, A.; Cronin, S. B. "Artificial Photosynthesis on TiO2-Passivated InP Nanopillars." *Nano Lett.*, **2015**, *15*, pp. 6177-6181.

Zhai, H; **Ha, M.-A.;** Alexandrova, A. N. "AFFCK: Adaptive Force Field-Assisted ab initio Coalescence Kick Method for Global Minimum Search," *J. Chem. Theor. Comput*., **2015***, 11*, pp. 2385-2393.

Ha, M.-A.; Dadras, J.; Alexandrova, A.N. "Rutile Deposited Pt-Pd Clusters: A Hypothesis Regarding the Stability at 50/50 Ratio." *ACS Catalysis*, **2014**, *4*, pp. 3570-3580.

PRESENTATIONS

Ha, M.-A.; Baxter, E. T.; Dadras, J.; Jimenez-Izal, E.; Anderson, S. L. ; Alexandrova, A. N. "Borated Pt Subnanoclusters on Metal Oxides: Coke Prevention via Minimizing Dehydrogenation of Alkenes and C-Sticking." 253rd National Meeting of the American Chemical Society (ACS), San Francisco, CA 2017. Oral Presentation.

Ha, M.-A.; Baxter, E. T.; Dadras, J.; Jimenez-Izal, E.; Anderson, S. L. ; Alexandrova, A. N. "Borated Pt Subnanoclusters on Metal Oxides: Coke Prevention via Minimizing Dehydrogenation of Alkenes and C-Sticking." UCLA Research Showcase, 253rd National Meeting of the American Chemical Society (ACS), San Francisco, CA 2017. Poster Presentation.

Ha, M.-A.; Baxter, E. T.; Dadras, J.; Jimenez-Izal, E.; Anderson, S. L. ; Alexandrova, A. N. "Borated Pt Subnanoclusters on Metal Oxides: Coke Prevention via Minimizing Dehydrogenation of Alkenes and C-Sticking." 2nd Annual Southern California Theoretical Chemistry Symposium (SoCal TheoChem 2.0), University of California, Irvine, CA 2017. Poster Presentation.

CHAPTER 1

Oxygen Vacancies of Anatase (101): Extreme Sensitivity to the Density Functional Theory Method

1.1. INTRODUCTION

The anatase surface remains ubiquitous in the field of catalysis for its unique photoactivity[1-3], tunable through the use of dopants[4,5], or size and structural selection[6-8], and reactivity, such as water-splitting[9,10] and the decomposition of organic pollutants[11,12]. Both theory and experiment have cited surface defects such as oxygen vacancies to be a major contributing factor in anatase's catalytic activity. Although recent theoretical studies have concentrated on the more reactive 001 facet[13], a return to the more thermodynamically stable 101 facet[14] reveals interesting subtleties regarding the presence of surface and subsurface oxygen vacancies.

Previous studies neglected spin polarization and used semilocal functional Perdew-Burke-Ernzerhof (PBE)[15] in collaboration with scanning tunneling microscopy (STM) studies[16,17]to establish the formation of subsurface oxygen vacancies to be favored over that of surface vacancies. However, a recent STM study found that surface oxygen vacancies formed in the presence of a high positive sample bias or an electric field.[18] In experimental conditions such as an electrochemical cell, the presence of a potential bias and electric field would guarantee the formation of surface oxygen vacancies. Anatase remains a complex system to understand, both experimentally and computationally. This study will strive to elucidate a complete computational description of oxygen vacancies in anatase (101) under varying parameters available to Density Functional Theory (DFT).

While the use of a semilocal functional may correct in some part the tendency in DFT calculations to over-delocalize electrons, it still falls short in reflecting the moderate to extreme localization present in semiconductors and insulators.[19] Strongly correlated systems that feature localized *d* or *f* orbitals require a hybrid functional or a DFT+*U* (LDA+U or GGA+*U*) approach to reflect the properties of this system in agreement with experiments. This becomes especially important in nonstoichiometric systems such as those containing oxygen vacancies. When a neutral oxygen vacancy is present, the additional two electrons from this defect may localize on nearby Ti atoms, reducing Ti^{4+} to Ti^{3+}.[20,21] Moreover, spin-restricted and generalized gradient

approximation (GGA) calculations neglect the magnetic properties of oxygen-deficient TiO_2.[22] Previous theoretical studies using a hybrid functional or a DFT+*U* approach recovered the antiferromagnetism of reduced anatase[23], the band gap >3 eV typical of TiO_2 (PBE underestimates at 1.77 eV)[24], and gap states ~1 eV below the conduction band found in experiment[22,25]. These studies have primarily focused on characterizing the effects of an oxygen vacancy in bulk anatase.

Although the DFT+*U* formalism describes well the oxygen vacancy in the rutile phase of TiO_2, both in the bulk and on the surface, the results for anatase remain ambiguous. Bulk anatase featured quasi-degenerate simple and split geometries, i.e. the two electrons from a neutral oxygen vacancy either localized on a single Ti atom together or individually localized on neighboring Ti atoms.[20] Allen, et. al.'s occupation matrix control, which investigated specific occupation of *d*- and *f*-orbitals, found the same localization as DFT+*U* and identified the stability of integer occupation of d_{-2}, d_{-1}, d_1 orbitals.[21] Moreover, the incorporation of nonlocal effects such as dispersion forces using Grimme's method[26] (the DFT+D formalism) correctly predicted the thermodynamic stability of the phases of TiO_2 (rutile > brookite > anatase)[27].

Clarification of the presence of surface and subsurface oxygen vacancies with additional computational parameters such as those mentioned above has not been pursued. This study proposes a comprehensive three-fold approach in accounting for the presence of surface and sub-surface oxygen vacancies (V_O). These parameters include spin polarization, localization of the two electrons due to the V_O through the Hubbard *U* value, and consideration of long-range interactions such as London dispersion and van der Waal forces. These parameters will be investigated individually and in combination in order to explore the method dependence of the formation of oxygen vacancies in anatase. Results will be compared to the experiment. Finazzi, et. al. had explored the dependence of *U* in bulk anatase, specifying a *U* range of 3-4 eV to best reflect experimental data, and that range will be pursued here for surface anatase[22].

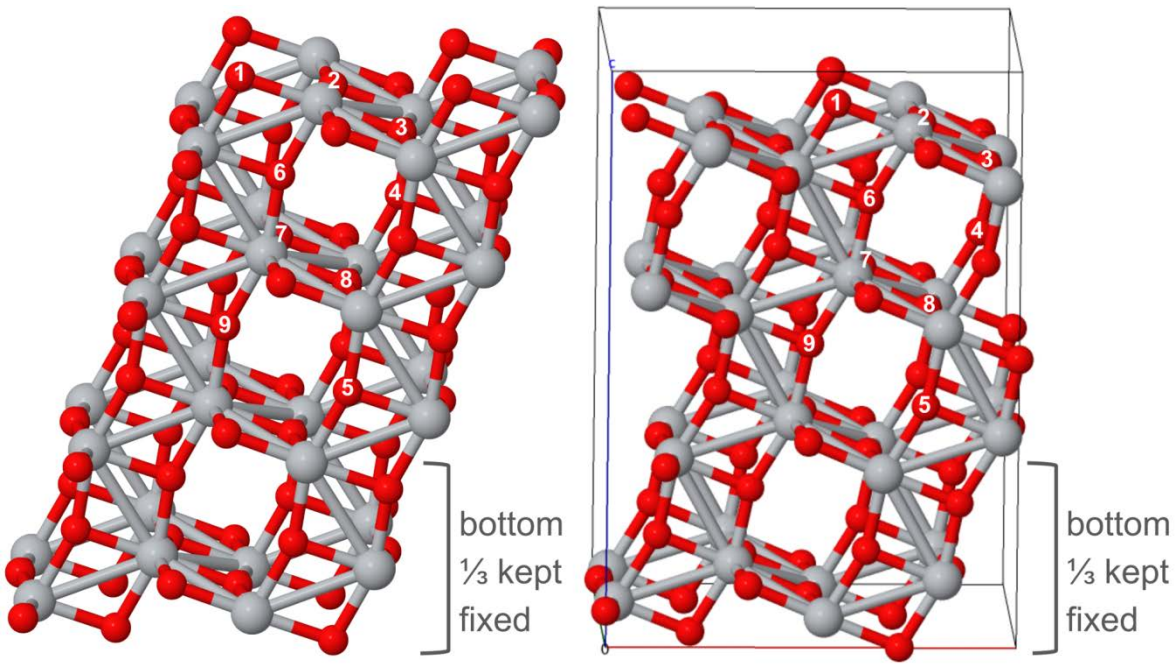

Figure 1.1. The 32 TiO_2 unit cell with oxygen vacancy (V_O) labeled. (L) A monoclinic cell is displayed for ease of viewing the nonequivalent sites for oxygen vacancy formation. (R) For calculations and post-processing, the lattice vectors were modified to represent an orthorhombic cell (a = 9.869 Å, b = 7.569 Å, c > 25 Å, α = β = γ = 90°).

1.2. COMPUTATIONAL METHODOLOGIES

All plane wave density functional theory (PW-DFT) calculations were performed with the QUANTUM ESPRESSO package.[28-31]Spin-restricted and unrestricted calculations were performed employing the PBE[15] functional and using the most recently available ultrasoft pseudopotentials[32] with scalar relativistic corrections. The PBE functional was used in all cases. For brevity, DFT+PBE+D is referred to as DFT+D and DFT+PBE+*U*, DFT+*U*. All calculations were spin unrestricted except for the system labeled “Spin Restricted” in **Table 1.1** and **Table 1.2** in order to recover the presence of localized electrons forming Ti^{3+} states. The gap states caused by these Ti^{3+} states will be further discussed in the following section. Large kinetic energy cutoffs of 32 (320) Ry were applied to the wave functions (charge density). For comparison, calculations utilizing the screened hybrid functional by Heyd, Scuseria, and Ernzerhof (HSE) were also pursued.[33,34] The implementation of HSE required use of norm-

conserving pseudopotentials with the PBE potential and kinetic energy cutoffs of 32 (128) Ry with respect to the wave functions (charge density).[35] The HSE functional with 25% Hartree-Fock (HF) exchange and a screening parameter of ω = 0.200 $bohr^{-1}$ was able to reproduce anatase's band gap (see **Table 1.1**).[36] Janotti, et. al.'s values of 20% HF exchange and ω = 0.106 $bohr^{-1}$ (~0.200 $Å^{-1}$) were also tested. For their study, these parameters yielded accurate band gaps and lattice constants for the rutile phase of TiO_2, but for our anatase slab these same parameters resulted in large band gaps of >3.60 eV and are not further reported here. All calculations were done at the gamma point with a convergence threshold of 10^{-6} Ry implemented during SCF cycles.

The anatase slab was modeled with lattice constants of *a* = 3.7845 Å, *c* = 9.5143 Å from experimental crystallographic data.[37] The appropriate cuts were made to construct the most stable and dominant facet (>94%) of the anatase crystal, the 101 surface, as a cell of 16 TiO_2 units.[14] This cell was first relaxed in the bulk under a Monkhorst-Pack grid of 4x4x4 centered at Γ and then doubled along the *z* for a total of 96 atoms. In surface calculations, the bottom ⅓ was fixed to reflect the bulk and ~ 12 Å vacuum gap was added to minimize spurious effects between periodic cells. In order to facilitate calculations and post-processing, lattice vectors describing an orthorhombic cell were used. Post-processing of calculations was done with QUANTUM ESPRESSO to generate charge density files and projected density of states (PDOS) plots. Visualization of charge density difference was generated through VESTA.[38] The Bader charge algorithm for PW-DFT was used to analyze shifts in electron density following the formation of an oxygen vacancy.[39]

It must be noted that for ease of comparison, the surfaces utilized in this study were grown from a bulk unit cell modeled from experimental crystallographic data. Other sample cases were examined under a denser k-point mesh (DFT+D+(U=3.6) with 3 x 3 x 1) or with an optimized lattice constant (DFT+D+(U=3.0)). Both of these cases resulted in some changes to the energy, but did not change resulting trends in the lowest three to four minima of oxygen

vacancies as listed in **Tables 1.1** and **1.1.** These conditions resulted in a minimum whose geometry was midway between the initial and final geometries described in **Figure 1.2**. This is unsurprising given the sensitivity of oxygen vacancy sites to computational parameters (as evidenced below in **Figures 1.2** and **1.3** and the following section of **1.3. RESULTS AND DISCUSSION**).

1.3. RESULTS AND DISCUSSION

The formation energies of oxygen vacancies were calculated using the equation below:

$$E_{form}(V_O) = E_{tot}\,(\text{def}) - E_{tot}\,(\text{no def}) + \tfrac{1}{2}\,\mu(O_2)$$

where E_{tot} (def) represents the total energy of defective anatase, E_{tot} (no def) of stoichiometric anatase, and the $\mu(O_2)$ as the total energy of an O_2 molecule. The reference energies of stoichiometric anatase and oxygen were calculated under the same conditions as the defective anatase. **Figure 1.1** illustrates the cell and possible oxygen vacancy sites, $V_{O1\text{-}O9}$, and **Table 1.1** lists the lowest formation energies. The trend in formation energies at other sites as compared to the minimum is presented in **Table 1.2**. Cheng, et. al. had previously investigated sites $V_{O1\text{-}O6}$ under DFT+PBE, and V_{O1} and V_{O4} under DFT+*U*.[16,40] Slight differences in formation energies are a result of our more rigorous kinetic energy cut-off and cell size. Although Cheng, et. al. found V_{O5} to be particularly stable at larger cell sizes of 216 atoms, we did not find this to occur in our cell. The formation energy of V_{O5} remained >0.5 eV from the minimum.

Due to the interest in anatase for photocalysis and solar cell use, the band gaps (E_g) of stoichiometric and reduced anatase were extracted from PDOS plots (**Table 1.1** for energies, **Figure 1.5** for plots). PDOS plots will be discussed in conjunction with surface oxygen vacancy formation. Typically, DFT underestimates the band gaps of materials with DFT+*U* providing some correction to increase the band gap and hybrid functions or GW many-body perturbations providing the best correction to directly reproduce experiment.[22,24,41] As band gap is a bulk property, the band gaps calculated for surfaces will not necessarily be reflective of the bulk. He,

et. al. observed that the anatase surface is particularly sensitive to experimental conditions, displaying color changes from orange-clear to darker blue so band gaps extracted from surface calculations might still be of considerable interest.[17] Our values of the band gap at the surface are not unusual for DFT with E_g ~1.7 eV and DFT+*U* with E_g ~2.1. HSE reflected the most accurate band gap with E_g ~3.2 eV for both stoichiometric and defective anatase. In our calculations, DFT+D resulted in a slight decrease in the band gap, but the effect was negligible in conjunction with +*U*. The presence of an oxygen vacancy produces a slight compression of the band gap under DFT+PBE and DFT+D and slight expansion under DFT+*U* and DFT+D+*U* levels of theory.

Table 1.1. Lowest Formation Energy (E_{Form}) and Band Gaps (E_g) in eV of Oxygen Vacancy under Varying Computational Parameters

System	V_o	Vacancy Site	Settings	E_{Form} (eV)	$E_{g,stoich}$ (eV)	$E_{g,def}$ (eV)
I	9	subsurface (see **Figure 1.3**)	Spin Restricted	3.88	1.72	1.67
II	9	subsurface (see **Figure 1.3**)	Spin Polarized	3.88	1.71	1.62, 1.71
III	1	Surface	DFT+D	4.19	1.72	1.58
IV	1	Surface	DFT+(U=3.0)	4.12	2.02	2.10
V	1	Surface	DFT+(U=3.6)	3.82	2.10	2.15
VI	1	Surface	DFT+(U=4.0)	3.61	2.15	2.22
VII	1	Surface	DFT+D+(U=3.6)	3.93	2.10	2.15
VIII	1	Surface	HSE ($HF_{0.25}$, $PBE_{0.75}$)	2.91	3.21	3.20
Experiment					3.2[42,43], 3.4[44]	

Note: Band gaps (E_g) were calculated from density of states plots of both stoichiometric (stoic) and defective (def) anatase with the lowest oxygen vacancy formation energy. There are two values for spin polarized calculations on the defective surface due to the splitting at the conduction band. The total DOS plots revealed a shift in energy apart of the spin up and spin down components at the conduction band resulting in two different band gaps. Systems II-VIII are spin unrestricted.

Table 1.2. Sorted Formation Energy, ΔE_F, in eV with Respect to Minimum of Oxygen Vacancy under Varying Computational Parameters

I		**II**		**III**		**IV**		**V**		**VI**		**VII**		**VIII**	
Spin Restricted (DFT+PBE)		**Spin Polarized (DFT+PBE)**		**DFT+D**		**DFT+ (U=3.0)**		**DFT+ (U=3.6)**		**DFT+ (U=4.0)**		**DFT+D+ (U=3.6)**		**HSE ($HF_{0.25}$, $PBE_{0.75}$)**	
V_o	ΔE_F (eV)	**V_o**	ΔE_F (eV)	**V_o**	ΔE_F (eV)	**V_o**	ΔE_F (eV)	**V_o**	ΔE_F (eV)	**V_o**	ΔE_F (eV)	**V_o**	ΔE_F (eV)	**V_o**	ΔE_F (eV)
9	0.00	9	0.00	1	0.00	1	0.00	1	0.00	1	0.00	1	0.00	1	0.00
4	0.05	4	0.05	9	0.00	6	0.35	6	0.31	9	0.78	6	0.32	4	0.39
6	0.22	6	0.22	6	0.01	4	0.49	4	0.73	5	0.78	4	0.83	6	0.50
1	0.23	1	0.23	4	0.02	5	0.68	3	0.92	8	0.81	3	0.93	5	0.83
5	0.85	5	0.70	5	0.58	9	0.70	5	0.92	6	0.82	5	0.98	7	0.89
8	0.93	8	0.90	8	0.74	8	0.80	9	0.93	7	0.84	9	0.98	9	0.89
7	1.05	7	0.98	7	0.81	7	0.82	8	0.99	4	0.89	8	1.02	8	0.90
3	1.30	3	1.23	3	1.01	3	0.86	7	1.02	3	1.01	7	1.04	3	1.21
2	1.83	2	1.70	2	1.49	2	1.32	2	1.38	2	1.10	2	1.40	2	1.22

Note: In all systems except for **System I**. **Spin Restricted (DFT+PBE)**, calculations were spin polarized and often exhibited gap states of localized Ti^{3+} in PDOS plots.

In our systematic investigation of oxygen vacancy formation in anatase, we found a significant dependence on computational parameters in influencing not only the geometry and energy of surface and subsurface sites V_{O1} and V_{O4}, but also a number of other sites. Notably, further analysis of V_{O6} and V_{O9} yielded other unique, DFT method dependent minima (see **Figures 1.2** and **1.4** on V_{O6}**, Figure 1.3** on V_{O9}**)**. Cheng, et. al. noted that subsurface site V_{O6} is unstable, resulting in the surface O_{2c} filling the site (in **Figure 1.2**, surface O_{2c} colored green to clarity). Our investigations show that this takes place in all calculations except for DFT+(*U*=4.0) and HSE, whether we remain at the DFT+PBE level or continue in complexity towards the DFT+D, DFT+(*U*=3.0, 3.6), and DFT+D+(*U*=3.6) formalism.

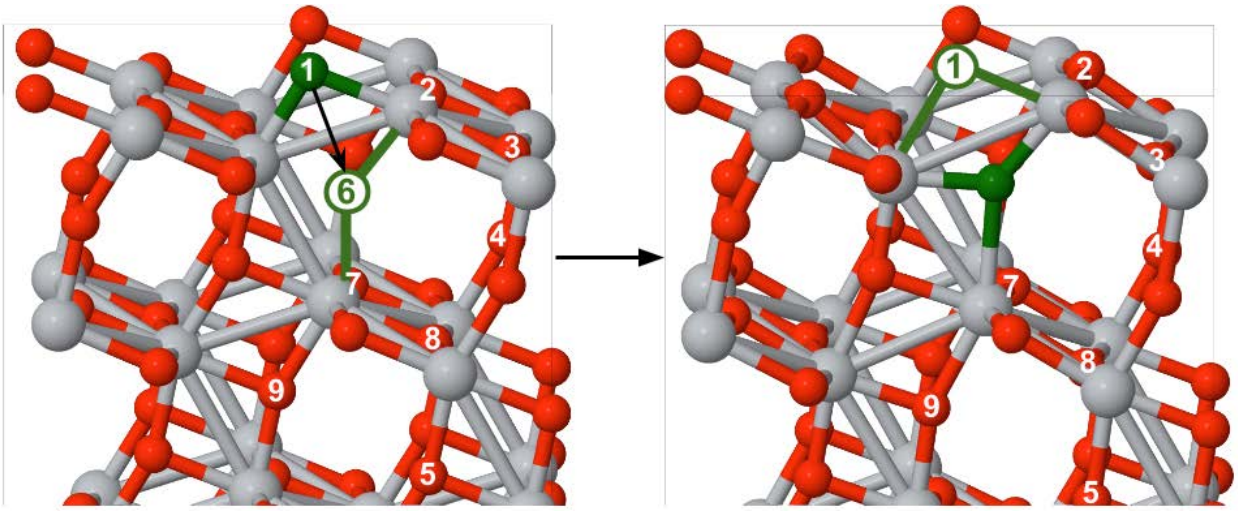

Figure 1.2. Under the DFT+D, DFT+(*U*=3.0, 3.6), and DFT+D+(*U*=3.6) formalism, the surface oxygen O_{2c} (colored green) will migrate to fill the vacancy site V_{O6} during geometric relaxation. This results in a surface oxygen vacancy, whose electronic structure is identical to the one formed through vacancy site V_{O1} under DFT+D, but remains unique as compared to V_{O1} under the DFT+*U* and DFT+D+*U* (see **Figure 1.4**).

In comparison to V_{O6}, the formation of V_{O9} remains unstable only at DFT+PBE and DFT+D levels of theory and minimizes to form a distorted V_{O4} (see **Figure 1.3**). This phenomenon at sites V_{O6} and V_{O9} reinforce the need for acknowledgment and understanding of the theoretical parameters in use to characterize oxygen vacancies in anatase. At DFT+PBE and DFT+D levels of theory, V_{O1} and V_{O6} (see **Figure 1.2** for formation of the surface oxygen vacancy), V_{O4} and V_{O9} (see **Figure 1.3** for formation of the subsurface oxygen vacancy) are nearly interchangeable, resulting in the same minimum. At DFT+(*U*=4.0) and HSE, all V_O sites remain stable. Moreover, the formation energies of these sites reflect the symmetry of their coordination to other atoms. The energies become increasingly degenerate for vacancies formed deeper in the cell; V_{O7} and V_{O8} are nearly degenerate while sites V_{O5} and V_{O9} are degenerate.

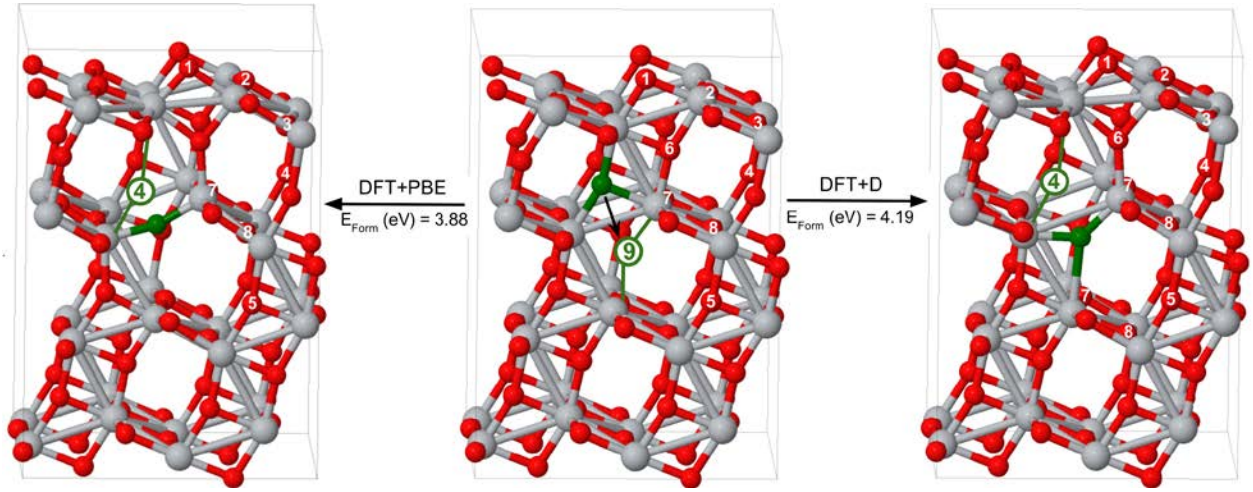

Figure 1.3. The creation of an oxygen vacancy V_{O9} (green, labeled) is unstable in DFT+PBE and DFT+D calculations, resulting in the oxygen above (green) attempting to fill the site (indicated by a black arrow). The resulting geometry is that of a distorted subsurface oxygen vacancy with the site symmetry of V_{O4} (green, labeled). These are the global minima of DFT+PBE and DFT+D calculations.

Under the DFT+*U* formalism, the surface oxygen vacancy that results from minimization of V_{O6} differs from surface oxygen vacancy V_{O1}. Plots of the charge density difference with respect to the stoichiometric cell reveal subtle shifts in the electron density at the subsurface oxygen vacancy cite (see **Figure 1.4**). Bader charge analysis pinpoints the shift. Integration of the density along the zero flux surface results in occupation of ~0.3-0.4e on neighboring titanium atoms. The localization of electrons on two Ti atoms differs between the resulting surface oxygen vacancy from V_{O4} and V_{O1}. At V_{O1}, a localization of ~0.3-0.4e occurs on both surface Ti atoms connected to V_{O1} while the localization is split between the surface Ti and subsurface Ti atom bridged by V_{O6}. A shift of ~0.3-0.4e is significant with respect to the original charge of +2.2e on Ti atoms, reflective of the mixed ionic-covalent nature of the Ti-O bonds in semiconductor titania characteristic of easily reducible oxides.[45] The subsurface oxygen vacancy V_{O6} is stable only at the DFT+(*U*=4.0) and HSE levels of theory, but atoms are significantly distorted around the site, resulting in a higher formation energy. Surprisingly, the shift in electronic occupation between the DFT+(*U*=4.0) and HSE is different. In DFT+(*U*=4.0), the occupation resembles that of a surface oxygen vacancy, localizing at the Ti atoms below

V_{O1}, whereas with HSE the occupation remains at the neighboring Ti atoms, 0.45 e at the surface Ti and 0.46 e at the subsurface Ti.

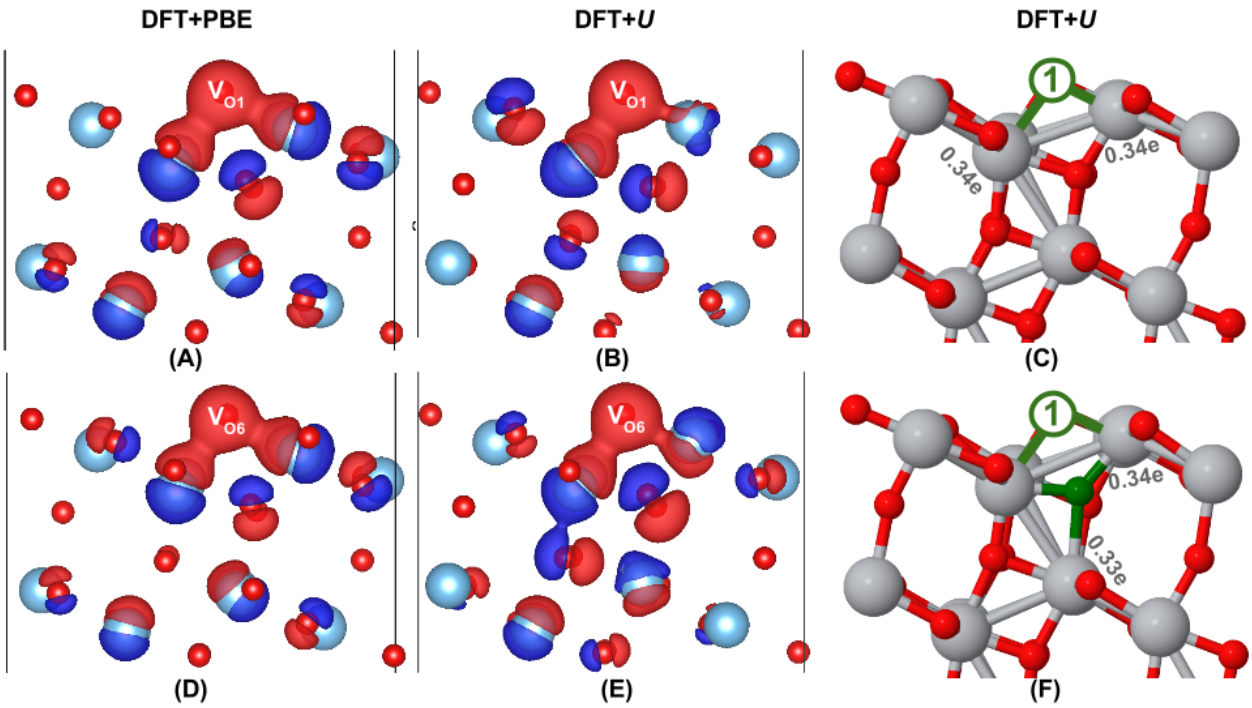

Figure 1.4. Isosurfaces of defective anatase depicting charge density difference with respect to the stoichiometric cell. The considered defects are the surface oxygen vacancy resulting from V_{O1} (top) and surface oxygen vacancy resulting from V_{O6} (bottom, see **Figure 1.2** for labels). Red represents a negative charge density difference and blue, a positive difference, with respect to the stoichiometric cell. Surface oxygen vacancy formed from minimization of site V_{O1} or site V_{O6} indicated on image. (A), (D) In the DFT+PBE and DFT+D formalism, the charge density differences remain negligible between the surface oxygen vacancy formed by minimization of V_{O1} and V_{O6}. (B), (E) In the DFT+*U* and DFT+D+*U* formalism, the surface oxygen vacancy formed by V_{O6} results in more extreme shifts in the electron density of atoms surrounding the site. (C), (F) Under the DFT+(*U*=3.6), Bader charges at neighboring Ti atoms for a surface oxygen vacancy formed from site V_{O1} (C, electronic occupations at surface Ti) and from site V_{O6} (F, electronic occupations at surface and subsurface Ti).

The two surface oxygen vacancies are further examined through PDOS plots (**Figure 1.5**), which show band gap states comparable to experiment, displaying Ti^{3+} states ~1 eV below the conduction band.[46,47] Moreover, the PDOS of *d*-orbitals of neighboring Ti atoms corroborates features observed in charge density difference plots and Bader charge analysis. The characterization of the formation of a surface oxygen vacancy from site 1 and site 6 by PDOS reinforces their unique identity. An oxygen vacancy formed at V_{O1} presents close,

overlapping peaks in the band gap states related to the neighboring surface Ti atoms. Smearing occurs due to the similarity between the neighboring surface Ti atoms, both featuring 4 Ti-O bonds. In contrast, a surface oxygen vacancy resulting from V_{O6} presents distinct split peaks ~0.5 eV from each other as a resulting of the differing coordination of the Ti atoms: surface Ti coordinates to 4 O atoms and sub-surface Ti to 6 O atoms. In other words, this electron experiences an electrostatic penalty by localizing in the bulk as opposed to the surface resulting in the ΔE_{form} ~ 0.3 eV.

The geometries of these surface oxygen vacancies may be comparable, but their electronic occupations are not and may influence future studies on the catalysis and binding of small molecules.[48,49] Furthermore, in a recent STM study, the formation of surface oxygen vacancies was observed to be a result of subsurface oxygen vacancy clusters migrating to the surface.[18] Setvin, et. al. suggested that the presence of a positive potential bias or electric field from the STM tip led to the injection of “hot” electrons into the surface that aided in the migration of subsurface vacancies to the surface. These migrations resulted in pair and triangular formations of surface oxygen vacancies, which may have been stabilized and precipitated by these unequal occupations on neighboring Ti atoms.

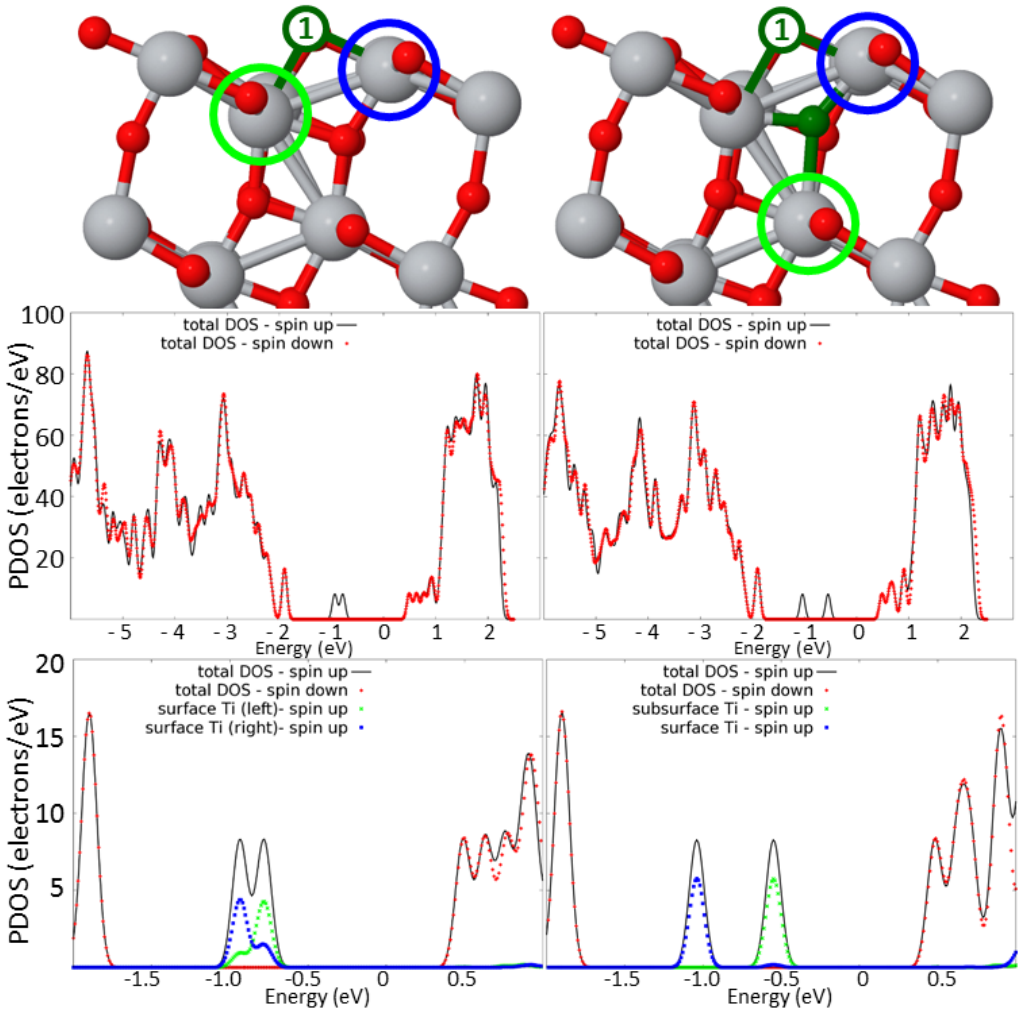

Figure 1.5. (L) Density of states (DOS) plots depicting localization of electrons in the band gap on surface Ti atoms with the formation of a surface oxygen vacancy at V_{O1}. (R) DOS plots of electrons localized on the surface and subsurface Ti atoms with the formation of a surface oxygen vacancy from V_{O6} (for visualization of this process, see **Figure 1.2**). The top graph displays total DOS with respect to spin and the bottom graph illustrates features of the partial DOS of Ti's *d*-orbitals. Energies are shifted with respect to the Fermi energy set at zero. These plots are from DFT+D+(*U*=3.6) calculations.

1.4. CONCLUSIONS

In this theoretical study on oxygen vacancies, we have shown the influence of computational parameters on the energy, geometry, and electronic occupation of these vacancies. While there have been many studies conducted for bulk anatase or surface anatase with an oxygen vacancy at V_{O1} or V_{O4}, none have attempted a comprehensive outlook on all

nonequivalent sites and their subsequent optimization beyond DFT+PBE. Under the DFT+*U* formalism, analysis of these nonequivalent sites resulted in the discovery of two distinct surface oxygen vacancies related to their component reduced Ti^{3+} states. This may affect future studies regarding catalysis of small molecules on surface anatase or aggregation of clusters of oxygen vacancies. This study is meant to inform and guide future modeling of defective anatase (101) to be aware of the dependence of results on computational parameters on oxygen vacancies.

Since the formation of surface versus subsurface oxygen vacancies in anatase (101) seems to be condition dependent in experiment as well as in theory, the choice of DFT method lies in what material properties are currently being investigated. DFT studies comparing to experiments under ultra-high vacuum might neglect dispersion and Hubbard *U* corrections to preferentially treat sub-surface oxygen vacancies while those considering catalysis in the presence of a potential gradient (as in photocatalysis related to electrochemical cells) may well include dispersion and Hubbard *U* corrections or hybrid levels of theory to consider surface oxygen vacancies. Moreover, consideration of gap states in experimental DOS absolutely requires spin unrestricted, Hubbard *U* or hybrid levels of theory.

1.5. REFERENCES

1 Henderson, M. A. A surface science perspective on photocatalysis. *Surface Science Reports* 2011*, 66*, 185-297.

2 Fujishima, A.; Zhang, X.; Tryk, D. A. TiO*2* photocatalysis and related surface phenomena. *Surface Science Reports* 2008*, 63*, 515-582.

3 Linsebigler, A. L.; Lu, G.; Yates Jr, J. T. Photocatalysis on TiO2 surfaces: principles, mechanisms, and selected results. *Chem. Rev.* 1995*, 95*, 735-758.

4 Batzill, M.; Morales, E. H.; Diebold, U. Influence of nitrogen doping on the defect formation and surface properties of TiO_2 rutile and anatase. *Phys. Rev. Lett.* 2006*, 96*, 026103.

5 Pham, H. H.; Wang, L. Electronic structures and current conductivities of B, C, N and F defects in amorphous titanium dioxide. *Physical Chemistry Chemical Physics* 2015*, 17*, 11908-11913.

6 Luttrell, T.; Halpegamage, S.; Tao, J.; Kramer, A.; Sutter, E.; Batzill, M. Why is anatase a better photocatalyst than rutile?-Model studies on epitaxial TiO_2 films. *Scientific reports* 2014*, 4*.

7 Close, T.; Tulsyan, G.; Diaz, C. A.; Weinstein, S. J.; Richter, C. Reversible oxygen scavenging at room temperature using electrochemically reduced titanium oxide nanotubes. *Nature nanotechnology* 2015*, 10*, 418-422.

8 Yang, H. G.; Sun, C. H.; Qiao, S. Z.; Zou, J.; Liu, G.; Smith, S. C.; Cheng, H. M.; Lu, G. Q. Anatase TiO2 single crystals with a large percentage of reactive facets. *Nature* 2008*, 453*, 638-641.

9 Tilocca, A.; Selloni, A. Reaction pathway and free energy barrier for defect-induced water dissociation on the (101) surface of TiO_2-anatase. *J. Chem. Phys.* 2003*, 119*, 7445-7450.

10 Tilocca, A.; Selloni, A. Structure and reactivity of water layers on defect-free and defective anatase TiO_2 (101) surfaces. *The Journal of Physical Chemistry B* 2004*, 108*, 4743-4751.

11 Zhao, W.; Ma, W.; Chen, C.; Zhao, J.; Shuai, Z. Efficient degradation of toxic organic pollutants with $Ni_2O_3/TiO_{2-x}B_x$ under visible irradiation. *J. Am. Chem. Soc.* 2004*, 126*, 4782-4783.

12 Wang, C.; Groenzin, H.; Shultz, M. J. Comparative study of acetic acid, methanol, and water adsorbed on anatase TiO_2 probed by sum frequency generation spectroscopy. *J. Am. Chem. Soc.* 2005*, 127*, 9736-9744.

13 Selloni, A. Crystal growth: anatase shows its reactive side. *Nature materials* 2008*, 7*, 613-615.

14 Lazzeri, M.; Vittadini, A.; Selloni, A. Structure and energetics of stoichiometric TiO_2 anatase surfaces. *Physical Review B* 2001*, 63*, 155409.

15 Perdew, J. P.; Burke, K.; Ernzerhof, M. Generalized gradient approximation made simple. *Phys. Rev. Lett.* 1996*, 77*, 3865.

16 Cheng, H.; Selloni, A. Surface and subsurface oxygen vacancies in anatase TiO_2 and differences with rutile. *Physical Review B* 2009*, 79*, 092101.

17 He, Y.; Dulub, O.; Cheng, H.; Selloni, A.; Diebold, U. Evidence for the predominance of subsurface defects on reduced anatase TiO_2 (101). *Phys. Rev. Lett.* 2009*, 102*, 106105.

18 Setvin, M.; Schmid, M.; Diebold, U. Aggregation and electronically induced migration of oxygen vacancies in TiO_2 anatase. *Physical Review B* 2015*, 91*, 195403.

19 Himmetoglu, B.; Floris, A.; Gironcoli, S.; Cococcioni, M. Hubbard-corrected DFT energy functionals: The LDA U description of correlated systems. *International Journal of Quantum Chemistry* 2014*, 114*, 14-49.

20 Morgan, B. J.; Watson, G. W. Intrinsic n-type defect formation in TiO_2: a comparison of rutile and anatase from GGA U calculations. *The Journal of Physical Chemistry C* 2010*, 114*, 2321-2328.

21 Allen, J. P.; Watson, G. W. Occupation matrix control of d-and f-electron localisations using DFT U. *Physical Chemistry Chemical Physics* 2014*, 16*, 21016-21031.

22 Finazzi, E.; Di Valentin, C.; Pacchioni, G.; Selloni, A. Excess electron states in reduced bulk anatase TiO_2: comparison of standard GGA, GGA+U, and hybrid DFT calculations. *J. Chem. Phys.* 2008*, 129*, 154113.

23 Yang, K.; Dai, Y.; Huang, B.; Feng, Y. P. Density-functional characterization of antiferromagnetism in oxygen-deficient anatase and rutile TiO_2. *Physical Review B* 2010*, 81*, 033202.

24 Janotti, A.; Varley, J.; Rinke, P.; Umezawa, N.; Kresse, G.; Van de Walle, C. Hybrid functional studies of the oxygen vacancy in TiO_2. *Physical Review B* 2010*, 81*, 085212.

25 Sanjines, R.; Tang, H.; Berger, H.; Gozzo, F.; Margaritondo, G.; Levy, F. Electronic structure of anatase TiO_2 oxide. *J. Appl. Phys.* 1994*, 75*, 2945-2951.

26 Grimme, S.; Antony, J.; Ehrlich, S.; Krieg, H. A consistent and accurate ab initio parametrization of density functional dispersion correction (DFT-D) for the 94 elements H-Pu. *J. Chem. Phys.* 2010*, 132*, 154104.

27 Conesa, J. C. The relevance of dispersion interactions for the stability of oxide phases. *The Journal of Physical Chemistry C* 2010*, 114*, 22718-22726.

28 Giannozzi, P.; Baroni, S.; Bonini, N.; Calandra, M.; Car, R.; Cavazzoni, C.; Ceresoli, D.; Chiarotti, G. L.; Cococcioni, M.; Dabo, I. QUANTUM ESPRESSO: a modular and open-source software project for quantum simulations of materials. *Journal of Physics: Condensed Matter* 2009*, 21*, 395502.

29 Kohn, W.; Sham, L. J. Self-consistent equations including exchange and correlation effects. *Physical Review* 1965*, 140*, A1133.

30 Lee, C.; Yang, W.; Parr, R. G. Development of the Colle-Salvetti correlation-energy formula into a functional of the electron density. *Physical review B* 1988*, 37*, 785.

31 Burke, K.; Werschnik, J.; Gross, E. Time-dependent density functional theory: Past, present, and future. *J. Chem. Phys.* 2005*, 123*, 062206.

32 Vanderbilt, D. Soft self-consistent pseudopotentials in a generalized eigenvalue formalism. *Physical Review B* 1990*, 41*, 7892.

33 Heyd, J.; Scuseria, G. E.; Ernzerhof, M. Hybrid functionals based on a screened Coulomb potential. *J. Chem. Phys.* 2003*, 118*, 8207-8215.

34 Heyd, J.; Scuseria, G. E.; Ernzerhof, M. Erratum:“Hybrid functionals based on a screened Coulomb potential”[J. Chem. Phys. 118, 8207 (2003)]. *J. Chem. Phys.* 2006*, 124*, 219906.

35 Troullier, N.; Martins, J. L. Efficient pseudopotentials for plane-wave calculations. *Physical review B* 1991*, 43*, 1993.

36 Krukau, A. V.; Vydrov, O. A.; Izmaylov, A. F.; Scuseria, G. E. Influence of the exchange screening parameter on the performance of screened hybrid functionals. *J. Chem. Phys.* 2006*, 125*, 224106.

37 Howard, C.; Sabine, T.; Dickson, F. Structural and thermal parameters for rutile and anatase. *Acta Crystallographica Section B: Structural Science* 1991*, 47*, 462-468.

38 Momma, K.; Izumi, F. VESTA 3 for three-dimensional visualization of crystal, volumetric and morphology data. *Journal of Applied Crystallography* 2011*, 44*, 1272-1276.

39 Tang, W.; Sanville, E.; Henkelman, G. A grid-based Bader analysis algorithm without lattice bias. *Journal of Physics: Condensed Matter* 2009*, 21*, 084204.

40 Cheng, H.; Selloni, A. Energetics and diffusion of intrinsic surface and subsurface defects on anatase TiO_2 (101). *J. Chem. Phys.* 2009*, 131*, 054703.

41 Patrick, C. E.; Giustino, F. GW quasiparticle bandgaps of anatase TiO_2 starting from DFT U. *Journal of Physics: Condensed Matter* 2012*, 24*, 202201.

42 Tang, H.; Berger, H.; Schmid, P.; Levy, F.; Burri, G. Photoluminescence in TiO_2 anatase single crystals. *Solid State Commun.* 1993*, 87*, 847-850.

43 Tang, H.; Berger, H.; Schmid, P. E.; Lévy, F. Optical properties of anatase (TiO_2). *Solid State Commun.* 1994*, 92*, 267-271.

44 Tang, H.; Levy, F.; Berger, H.; Schmid, P. Urbach tail of anatase TiO_2. *Physical Review B* 1995*, 52*, 7771.

45 *Defects at Oxide Surfaces;* Springer: 2015, Eds.: Jupille, J.; Thornton, G., ISBN 978-3-319-14367-5.

46 Jackmana, M. J.; Deák, P.; Syres, K. L.; Adell, J.; Thiagarajan, B.; Levy, A.; Thomas, A. G. Observation of vacancy-related polaron states at the surface of anatase and rutile TiO_2 by high-resolution photoelectron spectroscopy. *arXiv preprint arXiv:1406.3385* 2014.

47 Sanjines, R.; Tang, H.; Berger, H.; Gozzo, F.; Margaritondo, G.; Levy, F. Electronic structure of anatase TiO_2 oxide. *J. Appl. Phys.* 1994*, 75*, 2945-2951.

48 Qiu, J.; Zeng, G.; Ha, M.; Hou, B.; Mecklenburg, M.; Shi, H.; Alexandrova, A. N.; Cronin, S. B. A Microscopic Study of Atomic Layer Deposition of TiO_2 on GaAs and its Photocatalytic Application. *Chemistry of Materials* 2015, *27*, 7977-7981.

49 Qiu, J.; Zeng, G.; Ha, M.; Ge, M.; Lin, Y.; Hettick, M.; Hou, B.; Alexandrova, A. N.; Javey, A.; Cronin, S. B. Artificial Photosynthesis on TiO_2-Passivated InP Nanopillars. *Nano letters* 2015, *15*, 6177-6181.

CHAPTER 2

Rutile-Deposited Pt-Pd Clusters: A Hypothesis Regarding the Stability at 50/50 Ratio

2.1. INTRODUCTION

Supported Pt nano-clusters have shown great catalytic activity and selectivity for alkane dehydrogenation and cracking.[1-4] Recently, it has been shown that Pt and Pd on zeolite (ZSM-5) greatly increased these catalytic properties beyond that of ZSM-5 alone. [5, 6] Additional dehydrogenation to alkynes can occur as well as methane formation from cracking, both of these can result in coke deposition. For dehydrogenation catalyzed by deposited clusters, two mechanisms for catalysis deactivation are the prime suspects: coke deposition and cluster sintering. Coke fouling reduces catalytic activity of the clusters, therefore, a primary approach to reduce coking involves alloying Pt with main group metals, as well as some transition metals.[7-12] Gutierrez et. al. have demonstrated that deactivation of Pt-Pd clusters resulting from deposited coke can be reduced by controlling the acidity of the support.[13] Sintering of metal nanoparticles is a result of the particles minimizing their surface energy; hence populations of small sized particles decrease with a corresponding increase of large sized particle populations. Graham et. al. have shown that mixed Pt-Pd clusters, supported on alumina, have improved stability over those of just pure Pt.[14] However, Johns et. al. showed conflicting results of the sintering rate of Pt-Pd nano-particles.[15] It is noted that the latter study observed no core-shell structure of nano-particles under conditions relevant for industrial applications, in contrast with results of, e.g., Anderson et. al. on smaller sized (approximately 2 nm) bi-metallic nano-particles. [16] A proper understanding of the catalytic properties of these Pt-Pd bi-metallic clusters as well as their structure, stability, and mobility requires deeper knowledge of this system at the nano and sub-nano scales.

For sub-nano-clusters, the role of the surface goes beyond that of a stage on which the action of catalysis is played. The rutile TiO_2(110) is a popular model support of the transition metal-oxide interface, providing controllable surface conditions (e.g. adsorption sites) to study various catalytic reaction pathways.[17-19] Previously, one of the authors (Alexandrova) has shown that pure Pd clusters deposited on TiO_2 will readily sinter, by the Ostwald ripening mechanism,[20]

greatly decreasing the catalytic activity of the clusters by reducing the number of edge or step-sites. Ostwald ripening, as opposed to particle coalescence, is indeed the mechanism expected to be operational for Pt, Pd, and mixed Pt-Pd clusters on titania.[21]

In the present work, the process of sintering of mixed Pt-Pd clusters on titania via Ostwald ripening is tackled. To this end, our newly-extended *ab initio* Metropolis Monte Carlo method and *ab initio* and PW-DFT are employed. Sintering at various initial conditions and several experimentally-relevant temperatures is modeled and our results agree with the experimental observations that claim the Pt-Pd clusters containing Pt and Pd in equal proportions are the most stable against sintering. Finally, the long-standing question of why these clusters exhibit special stability is addressed by an extensive chemical bonding analyses of the thermally-relevant isomers of the studied systems; statistical mechanical arguments are also provided. A detailed and physically well-motivated hypothesis is presented to explain the puzzling and appealing stability of 1:1 mixtures of surface-supported Pt-Pd clusters.

2.2. COMPUTATIONAL METHODOLOGIES

2.2.1. Electronic Structure Methods

As was previously done,[20] all PW-DFT calculations were performed with the Quantum Espresso package using the most recently available ultra-soft pseudopotentials with scalar relativistic corrections [22-25] and spin-unrestricted calculations were done employing the PBE functional.[26] Large kinetic energy cutoffs of 435.2 eV and 4.352 keV were applied to the wavefunctions and charge density, respectively. A 1x1x1 Monkhorst-Pack k-point grid was used for all calculations and shifts away from the gamma-point were applied in *x* and *y* in order to maintain good accuracy. The titania slab was modeled as a 4x2 unit cell with four-trilayers along *z* with a lattice constant of a = 4.67 Å and c = 3.02 Å. A vacuum gap of about 13 Å between the top and bottom surface atoms of repeating images ensures errors in the energies are on the order of a few meV. The bottom two trilayers of titania were held fixed and—as encouraged by Kowalski et. al.[27, 28] to prevent spurious surface states and other effects—dangling bonds of Ti

and O atoms were saturated with pseudo-hydrogens having charges of 4/3 e and 2/3 e, respectively.

For the clusters in the gas-phase, a variety of DFT and ab initio methods were employed to check the performance of PW-DFT for the studied systems. Geometries and relative energies of isomers were refined using the TPSS(h)[29] (hybrid) functional with the aug-cc-pVTZ-pp basis set.[30-31] Additionally, CASSCF(m,n)[32-37]/LANL2DZ[38-41] results were used to check the nature of the wavefunctions and the applicability of single-determinant methods. It was found that results across theoretical methods are in good agreement (presented in the Supporting Information), and also that the single-reference approximation is valid with the Hartree-Fock contribution to the CASSCF expansion being greater than 0.9 for all systems. All *ab initio* gas phase calculations were done using *Gaussian*09.[42]

For the chemical bonding analysis, the Bader charge localization scheme for PW-DFT systems was used.[43-45] For gaseous clusters, NBO[46] at the TPSSh /aug-cc-pVTZ-pp level of theory was used. NPA charges were found to be in close agreement with Bader, for the clusters in the gas phase, and therefore Bader charges were used for our arguments to be consistent with the methods used for surface-supported clusters. Molecular orbitals (MOs) were plotted using the post-processing package provided with Quantum Espresso at the Γ-point. Results presented in the main text are based on PW-DFT.

2.2.2. Monte Carlo Algorithm for Sintering

In order to assess the evolution of cluster sizes and compositions at different temperatures and to illustrate how certain very small sizes are not stable enough to withstand elevated temperatures relevant to experiment, a Monte Carlo scheme was employed. The algorithm, first published in 2011,[20] was based on the original proposal of Metropolis et. al.[47] and extended by Hastings.[48] Briefly, it is a Markov Chain Monte Carlo scheme sampling the canonical ensemble that seeks the configuration-space global minimum of monomers interacting with the support and forming clusters, via pre-computed potential energy surfaces

(PESs), i.e. it models sintering by the Ostwald ripening mechanism. A monomer will, upon "collision," sinter to any multimer with unit probability. An atom is allowed to dissociate from a cluster forming a monomer and reduced cluster providing the Metropolis condition is satisfied:

$$\mathbb{P} = \min(1, \exp(-\beta E_s))$$

where β is thermodynamic beta ($1/k_B T$, k_B is Boltzmann's constant and T is the temperature) and E_s is the sintering energy further discussed below.

In the present implementation, the original procedure is extended in several ways. First of all, it can handle bi-metallic clusters, i.e. two separate PESs for the Pt and Pd monomers are used in simulations. The grid for the monomers' movement is made finer than in the original implementation, to better explore the PES. The, so-called, sintering energy (E_s)[20] is generalized to taking the energy difference ($\Delta E = E_f - E_i$) for the reaction

$$[\mathrm{Pt-Pd}]_j + [\mathrm{Pt-Pd}]_k \rightarrow [\mathrm{Pt-Pd}]_{j-1} + [\mathrm{Pt-Pd}]_{k+1},$$

where j and k are sums of the numbers of Pt and Pd atoms in a given cluster. Hence,

$$\Delta E = E\left[[\text{Pt-Pd}]_{j-1}\right] + E\left[[\text{Pt-Pd}]_{k+1}\right] - E\left[[\text{Pt-Pd}]_{j}\right] - E\left[[\text{Pt-Pd}]_{k}\right].$$

The energies here are given by the Boltzmann weighted average of the few most energetically favorable structures found by an extensive search (using PW-DFT) for the global and local minima of the given cluster type (Pt_mPd_n) on titania—this is further explained in the following section. It is noted that the above equation reduces to the same expression for E_s of [20] in the limiting case where there is only a single element and when the final configuration includes a monomer. The above also generalizes the 2nd-order energy difference ($\Delta_2 E$), a measure of cluster's relative stability (defined in e.g. Wei et. al.),[49] as it appears as a special case where the initial configuration is two of the same cluster type. The algorithm uses the energies of the monomers, dimers, trimers, and tetramers, while the sintering energies for going to higher multimers was assumed to be equal that of going from the monomer plus trimer to the tetramers containing Pt and Pd in the appropriate proportion. This approach was used in the

past[20] and additionally justified recently in a joint theoretical and experimental paper by Addou et. al.[50] The searches for global and local minima were done *ad nauseam* by sampling over the geometries of the clusters and the potential binding sites on the support.

Only the stoichiometric TiO_2(100) surface was considered, since it was known that d-electron-rich atoms with electronic configuration of d^9 or d^{10}, such as Pt and Pd, preferentially bind to stoichiometric oxides.[20, 51, 52] O vacancies are electron-rich defects and even though there exists a minimum near the vacancy for Pd, approaching it requires surmounting a large barrier, and vacancies can help cluster dissociation.[20] It is noted that to correctly ensure an atom breaking away from a cluster and given that this model will tend to favor 2D irregular-shaped (i.e. filamentary) cluster growth, a cluster-size dependent step-size is enforced that represents a closed-form analytic expression of the average of the sizes of clusters that would form when optimally packing in circles,[53] squares,[54] and linear chains (see SI).

Evaporation of monomers is allowed for by applying a Metropolis-like algorithm to the Boltzmann-factor containing the adsorption energy of the monomer at the given location (E_{ads}) scaled by some factor. Pt and Pd are quite insensitive to evaporation at the studied temperatures, to zeroth-order the scaling factor was treated as a free parameter (γ) that was adjusted between the ranges of 0.5—2.0 for several test cases. Hence, the criteria to accept an "evaporation move" is given by the following probability distribution:

$$\mathbb{P} = \min\left(1, \exp\beta\left(E_{ads} - \gamma\right)\right)$$

Monomer redeposition on the support is also allowed and coverage dependence is implicitly included in the model as monomers can only redeposit in an unoccupied region of the support.

$$\mathbb{P} = \min\left(1, \exp\beta\left(E_{ads} + \gamma\right)\right)$$

Evaporation was negligible for both species under the considered parameters; this is due to the fact that the binding energy for a monomer to the support is on the order of ~ 1 eV

(shown in section 3) corresponding to a temperature of ~ 10^4 K. When the evaporation rate is not negligible, like in the case of Zn,[55,56] a more physically motivated model is required; this is the subject of a forthcoming publication. It is noted that the effect of direct atom evaporation from a supported cluster is ignored as the energy cost for such an event is several eV.

The effect of temperature in the MC is addressed in two ways: first of all, it impacts the Boltzmann-weighted populations of each cluster and thus determines the average energies used in the simulations that determine whether an atom changes its configurational state. Secondly, the Metropolis criterion for accepting new structures in the simulations is explicitly temperature dependent. Deficiencies of the model include: the lack of O_2 and H_2O in the simulations, which are present in small quantities even under vacuum, leading some Pd to be taken up by PdO clusters (the present results shift toward Pd-rich phases when compared to data from O-rich environments); as well as not permitting surface modification or reconstruction. While the effective relative well-depths of the PES change, depending on temperature, their relative locations do not. Other effects, such as vibrational excitations with rising temperature and potential electronic excitations are not included in the Monte Carlo. However, these limitations of the model did not prevent the method from reproducing the cluster-size distributions resembling those found in experiment.[20, 50]

2.3. RESULTS AND DISCUSSION

The relevant clusters that define the parameters of the sintering MC will be discussed briefly. Only the tetramers will be highlighted, smaller clusters are presented in **SI Figures 8.1.1** and **8.1.2** in the Supporting Information. In **Figure 2.1**, the global and low-energy local minima for Pt_mPd_n (m,n = 0,..,4 and $m + n = 4$) clusters in the gas phase and on TiO_2(110) are shown. The calculated formation energies of the most stable gas phase clusters are listed in **Table 2.1** and the calculated adsorption energies and sintering energy penalties of the global minima of supported clusters at varying ratios of Pd and Pt are listed in **Tables 2.2**. A comprehensive table of the local minima with relative cluster-support adsorption energies, Boltzmann probabilities,

and relative entropies may be found in **Table 2.3**. All results were obtained with PW-DFT, as described in the Methods section. Again, for the gas-phase clusters, calculations using a variety of correlated electronic structure methods, with different basis sets, were carried out using *Gaussian*09. It was found that the relative energies and geometries of clusters are consistent across theoretical methods, justifying the use of the PW-DFT methodology. Discussion of coordination to rutile oxygen utilizes the following notation: bridging surface oxygen atoms are denoted O_b and in plane surface oxygen atoms are denoted O_s. See **Figure 2.2** for visualization.

2.3.1. Clusters in the Gas Phase

In the gas phase, tetramers adopt tetrahedral structures with square planar and rhomboidal isomers being noncompetitive at the temperatures of interest. Total formation energies (E_f) were calculated by

$$E_f = E_{cluster} - N_{Pd}\, E[Pd_1] - N_{Pt}\, E[Pt_1]$$

where $E_{cluster}$ is the total DFT energy of the cluster, $E[Pd_1(Pt_1)]$ is the DFT energy of a Pd(Pt) atom, and $N_{Pd(Pt)}$ is the number of Pd(Pt) atoms composing the cluster. The Boltzmann probability (for a given Pt:Pd ratio) for *i*-th configuration (P_i) was found by taking the Boltzmann distribution of each minimum (e^{-E_i/k_BT}) divided by the sum of the distributions of all relevant low energy minima :

$$P_i = \frac{e^{-E_i/k_BT}}{\Sigma\, e^{-E_i/k_BT}}.$$

Here E_i is the *i*-th configuration energy of a cluster (i.e. $E_{cluster}$ as defined above), k_B is the Boltzmann constant and T is the temperature.

In **Table 2.1** and **Figure 2.1**, only the relevant local minima are shown, and although other local minima were found, their relative probability fractions were negligible—i.e. below the level of a part in 10^3. It is noted that all global minima for the tetramers had a tetrahedral geometry, but this is often not the case for the supported clusters, discussed below. At 1,000 K,

a 0.44 eV difference between the tetrahedral and planar structures of $PdPt_3$ translates to 99.41% of the cluster adopting the tetrahedral geometry in the gas phase. Differences in formation energies greater than 0.44 eV would only serve to underline the dominance of tetrahedra in the gas phase (see **Table 2.1** and **Figure 2.1**).

Table 2.1. DFT Formation Energies (E_f) of the Gas-Phase Structures

No. Pd	No. Pt	E_f Tetrahedral (eV)	$P_{700\,K}$	$P_{1000\,K}$	E_f Planar (eV)	$P_{700\,K}$	$P_{1000\,K}$
0	4	-11.89	97.49%	92.84%	-11.67	2.51%	7.16%
1	3	-9.68	99.93%	99.41%	-9.24	0.07%	0.59%
2	2	-8.81	100.00%	99.91%	-8.17[A]	<0.01%	0.06%
					-8.10[B]	<0.01%	0.03%
3	1	-7.84	100.00%	99.99%	-7.07	<0.01%	0.01%
4	0	-6.65	100.00%	99.99%	-5.85	<0.01%	0.01%

A. Pd-Pd-Pt-Pt planar structure, which is bilaterally symmetric through the plane bisecting the edge of the square planar structure.
B. Pd-Pt-Pd-Pt planar structure, which is bilaterally symmetric through the plane bisecting the diagonal of the square planar structure.

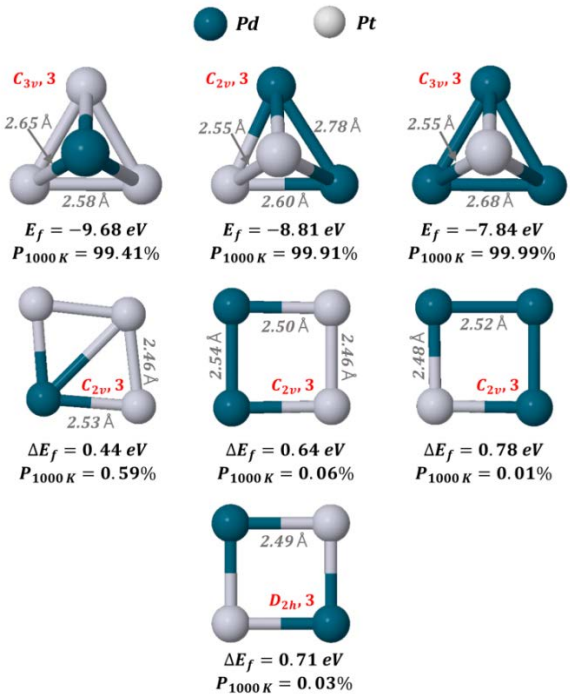

Figure 2.1. The most stable structures of the mixed clusters in the gas phase with their formation energies (E_f) or relative energies (ΔE_f) and Boltzmann-weighted relative populations at catalytically relevant temperature of 1,000 K. Point group symmetry and spin multiplicities are shown in red. Point group symmetry was assigned by inspection; multiplicities and energies were calculated from Quantum Espresso.

2.3.2. Clusters Deposited on TiO_2(110)

In **Tables 2.2** and **2.3**, the adsorption energies (E_{ads}) for a given cluster are given by

$$E_{ads}[\mathrm{Pt}_m\mathrm{Pd}_n] = E[\mathrm{Surf} + \mathrm{Pt}_m\mathrm{Pd}_n] - E[\mathrm{Surf}] - E_{gas,min}[\mathrm{Pt}_m\mathrm{Pd}_n],$$

where, E [Surf + Pt_mPd_n] is the total DFT energy of the supported cluster system, E[Surf] is the total energy of the bare support, and $E_{gas,min}$[Pt_mPd_n] is the global minimum of the gas-phase cluster. **Table 2.3** lists the adsorption energies of the global minima of adsorbed clusters at varying ratios of Pt:Pd, as well as the sintering energy penalty, i.e. the energy cost of an atom of a given element to break away from a tetramer, forming a trimer and a monomer on the support:

$$E_s[\mathrm{Pt_mPd_n} - \mathrm{Pt}] = E[\mathrm{Surf} + \mathrm{Pt_{m-1}Pd_n}] + E[\mathrm{Surf} + \mathrm{Pt_1}] - E[\mathrm{Surf} + \mathrm{Pt_mPd_n}] - E[\mathrm{Surf}],$$

if a Pt atom is "de-sintering," or

$$E_s[\mathrm{Pt_mPd_n} - \mathrm{Pd}] = E[\mathrm{Surf} + \mathrm{Pt_mPd_{n-1}}] + E[\mathrm{Surf} + \mathrm{Pd_1}] - E[\mathrm{Surf} + \mathrm{Pt_mPd_n}] - E[\mathrm{Surf}],$$

if a Pd atom is dissociating. It is emphasized that for the data in **Table 2.2**, all DFT energies used are of global minima, but this was not the case for the Metropolis MC where Boltzmann weighted averages of the energies were employed.

Table 2.3 presents the relative adsorption energies (ΔE_{ads}) of local minima (E_{ads}[Pt_mPd_n]) with respect to the global minimum, as well as Boltzmann probabilities (P_I)and Gibb's entropies (S_G). The P_I are calculated in an analogous manner to the probabilities calculated for gas phase configurations, i.e.

$$P_I = \frac{e^{-E_I/k_BT}}{\Sigma\, e^{-E_I/k_BT}}$$

For the I-th adsorbed cluster, E_I is the total energy of the adsorbed cluster on the support E[Surf+Pt_mPd_n] and the partition function ($\Sigma\, e^{-E_I/k_BT}$) is the sum of the discrete configurational states listed in **Table 2.3**. The lowest minima are displayed in **Figure 2.2** and all other local minima may be found in SI. A statistical definition of entropy utilizing the Boltzmann probabilities

of these discrete states was applied to obtain the entropy (S_G) of the various cluster types given by:

$$S_G = k_B \sum_I P_I \ln(P_I)$$

where the P_I are the Boltzmann weights and k_B is the Boltzmann constant. In this way, the entropic contribution to the free energy of the system may be found. The fundamental thermodynamic relation of the Helmholtz free energy ($F = U - TS$) allows for the entropic energy contributions (TS_G) of the system, at the different ratios of Pt:Pd, to be accounted. It is noted that these entropic and probabilistic measures are defined in a canonical ensemble, wherein the partition function is defined by the sum of Boltzmann distributions of discretized states at varying ratios of Pt and Pd. The use of calculated or theoretical probabilities to define a discretized partition function in the canonical or microcanonical ensemble in order to derive free energies and entropies may be found in a number of other related works.[57-60] Again, Boltzmann probabilities were also used as weights in sintering simulations at the desired temperatures in calculating energy penalties for a monomer to dissociate from a cluster.

In general, cluster atoms tend to coordinate with surface oxygen atoms, and so, all dimer and trimers adsorb parallel and in plane to the support. Pure and mixed tetramers in the gas phase primarily adopt a tetrahedral geometry, but adsorbed clusters' geometry may differ remarkably from their original state, ranging from a two-dimensional square-planar or rhomboidal arrangement to a slightly compressed tetrahedron. The geometric evolution from gas to adsorbed cluster is the result of two chemical bonding trends competing with each other: maximization of binding to the surface oxygen atoms versus maximization of the intra-cluster bonding. These two effects drive the adsorbed clusters to flatten and become planar to the support (Isomer **I** of Pt_3Pd, Pd_4 and Pt_4, Isomers **II** and **IV** of Pd_2Pt_2 and **III** and **IV** of Pd_3Pt) or remain 3D and compact (Isomers **II** and **III** of $PdPt_3$, **II** of Pd_4 and Pt_4, Isomers **I** of Pd_2Pt_2 and Pd_3Pt). See **Table 2.3** for details. Flattening of Pd_4 upon deposition on TiO_2(110) was noticed

before and explained by matching the positions of surface-O atoms for Pd-O bonding and developing σ-aromatic character of chemical bonding within the cluster.[52]

Table 2.2 Calculated Adsorption Energies (E_{ads}) and Sintering Energy Penalties (E_s) of Global Minima of Adsorbed Clusters

No. Pd	No. Pt	Geometry	E_{ads} (eV)	E_s–Pt (eV)	E_s–Pd (eV)
0	4	Square Planar	-4.08	2.20	-
1	3	Square Planar	-3.67	2.13	1.67
2	2	Tetrahedron	-3.34	2.23	1.67
3	1	Tetrahedron	-2.88	2.17	1.53
4	0	Square planar	-2.64	-	1.47

Table 2.3 Relative Adsorption Energies (ΔE_{ads}) and Boltzmann Probabilities (P) of Local Minima, and Entropic Energies (TS) at Catalytically Relevant Temperatures: 700, 1000 K

No. Pd	No. Pt	Isomer	Geometry	ΔE_{ads} (eV)	P, 700 K	P, 1000 K	TS, 700 K (eV)	TS, 1000 K (eV)
0	4	I	Square Planar	0.00	94.70%	88.25%	0.013	0.031
		II	Tetrahedron	0.17	5.30%	11.73%		
		III	Diamond	0.55	0.001%	0.021%		
1	3	I	Square Planar	0.00	86.46%	74.84%	0.030	0.064
		II	Tetrahedron	0.14	7.02%	12.91%		
		III	Tetrahedron	0.19	6.52%	12.25%		
2	2	I	Tetrahedron	0.00	68.61%	55.89%	0.055	0.102
		II	Square Planar	0.07	20.62%	24.09%		
		III	Tetrahedron	0.15	5.28%	9.28%		
		IV	Square Planar	0.16	4.95%	8.88%		
		V	Tetrahedron	0.29	0.54%	1.87%		
3	1	I	Tetrahedron	0.00	56.93%	54.55%	0.042	0.063
		II	Tetrahedron	0.02	42.99%	44.82%		
		III	Rhombus	0.41	0.07%	0.48%		
		IV	Diamond	0.51	0.01%	0.15%		
4	0	I	Square Planar	0.00	70.40%	64.71%	0.037	0.056
		II	Tetrahedron	0.05	29.60%	35.29%		

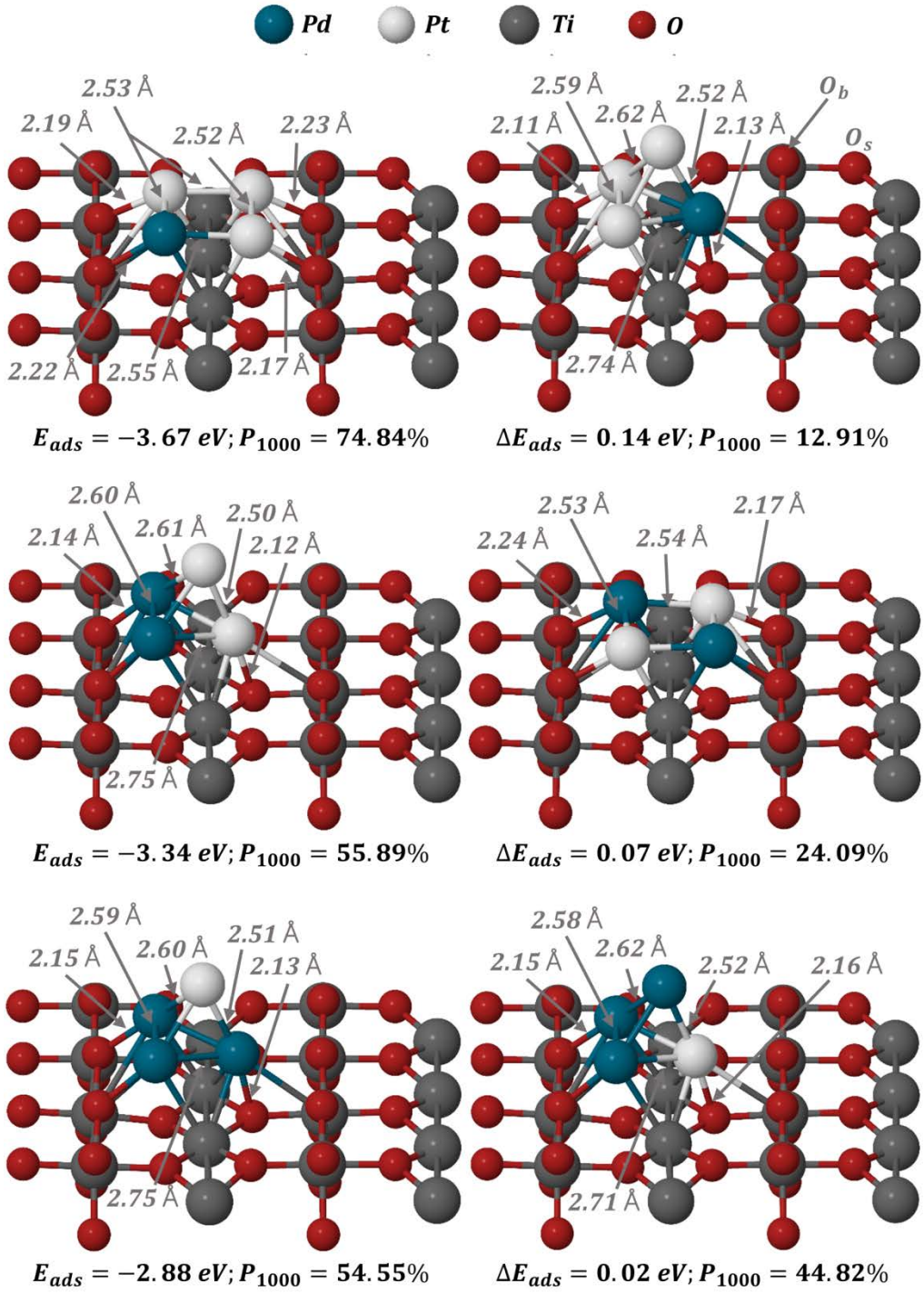

Figure 2.2. The global minimum and second lowest minimum of the mixed clusters once supported on rutile are displayed with their Boltzmann-weighted relative populations at 1000 K. In simulations of cluster sintering on the support, the experimentally relevant temperature range for clusters used in catalysis is from 700 to 1,000 K. In this range, several low-energy isomers for supported clusters become relevant and thermally accessible. Only the adsorbed cluster and topmost layer of stoichiometric TiO_2 are visualized. Other local minima are visualized in SI.

This above analysis leads to a thermodynamic argument that suggests that a 1:1 mixture of Pt-Pd clusters is entropically favored as a result of the high number of thermally-accessible isomers relative to those accessible to other clusters. Although the corresponding entropies reveal a fairly minute energetic contribution of 0.055 eV and 0.102 eV for 700 and 1000 K, respectively, such contributions can become more pronounced with increasing cluster size—i.e. such entropic contributions to the free energy may increase with the system size.

2.3.3. Simulations of Cluster Sintering on the Support at Various Temperatures and Relative Concentrations

Sintering simulation were carried out at 300 K, 700 K, and 1,000 K, starting with the monomers strewn randomly on the support at 0.16 ML coverage, with Pd:Pt ratios of 1:3, 1:1, and 3:1. Again, evaporation and redeposition of the monomers was allowed. However, no significant loss of the population was observed, consistent with the fairly deep and stabilizing minima on the PESs of the monomers moving on the support and visualized in **Figure 2.3** (j, k). Results of these sintering simulations are shown in **Figure 2.3** (a—i). An explanation of what is presented is the following: A given initial configuration (C_i) after a given number of Metropolis cycles (M) will have a "final" configurational state (C_f), wherein a certain fraction of the atoms (F) will be members of a particular cluster type (Pt_mPd_n). Given that C_i is a stochastic variable, several different states can exist. If these were all allowed to evolve for, perhaps, billions of steps then all such configurations would end up with all atoms joined into one large cluster. By sampling over all pseudo-random configurations and averaging these atom-fractions for a particular Pt_mPd_n over all C_f, an expectation value for the fraction of atoms belonging to a given m and n type cluster is acquired ($<F_{mn}>$) and an estimation of the stability of certain cluster types can be gained by looking at the distributions in **Figure 2.3**. For example, if the distributions were relatively flat, spread everywhere within the range of the given number of atoms in the simulation cell, this could indicate a very sensitive dependence on the initial configuration and/or that a great deal more cycles (M) are required. If the distribution was

completely shifted to the larger clusters (limited again by the number of atoms in the simulation space), then this would be an indication that the smaller clusters are easily “eaten” by larger ones, thus, sintering is not suppressed. Tight distributions near the origin imply that the system is relatively resistant to sintering.

Assessments of the stability of certain cluster types can be gained by looking at the distributions in **Figure 2.3**. The data represent the average cluster size and composition distributions of 1,000 independent random initial configurations at a given temperature and Pt:Pd molar fraction after each has been run for more than 10,000,000 MC steps. Again, the plots do not represent true final-state distributions, since the final state of a system subject to Ostwald ripening will always result in a single large island of all the deposited atoms on the support. More interesting are the trends in cluster size evolution as the temperature increases and the Pt content varies.

The distributions that are tightest, with peaks near the origin, are those at 300 K with initial Pt concentrations of 50% or greater, **Figure 2.3** (d,g). At Pt:Pd ratios of 1:3, there is evidence showing that some of the initial configurations evolved to relatively large clusters within the given number of Metropolis cycles. This implies that conditions of 50% or greater initial Pt concentrations lead to good cluster stability as the monomers do not all rapidly evolve into a single large island (from classical transition state theory, it is predicted here that tetramers form within a fraction of a second). **Figure 2.3** (a—c) show that high concentrations of Pd generally leads to relatively poor stability for small sub-nano-clusters at all temperatures. It is noted that at 300 K a clear peak for small Pd_n clusters is present; one of these clusters is Pd_4. This cluster was previously explored and found to exhibit a good matching with the underlying surface oxygen atoms and stabilizing σ-aromatic character of chemical bonding within the cluster.[52] However, at temperatures relevant to the industrial use of Pt-Pd clusters in catalysis (i.e. 700 to 1,000 K), the systems “boil” out of this minimum and move away from the Y-axis (labeled by the Number of Pd) toward the diagonal of the XY plane, corresponding to 1:1

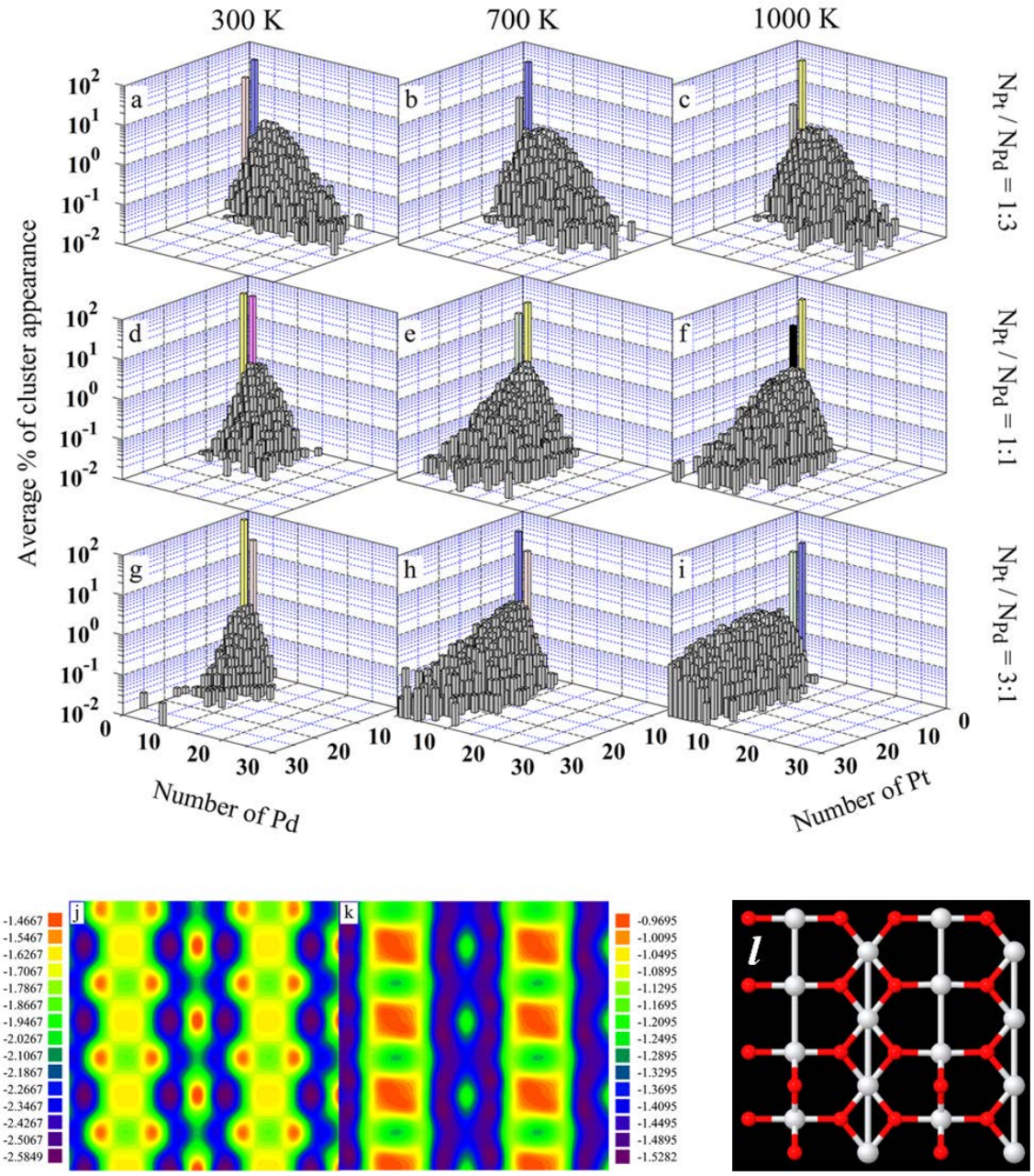

Figure 2.3. Results of sintering simulations at 300 K (a,d,g), 700 K (b,e,h), 1,000 K (c,f,i) and compositions of the initial mixtures of the monomers for Pt:Pd ratio of 1:3 (a,b,c), Pt:Pd ratio of 1:1 (d,e,f), Pt:Pd ratio of 3:1 (g,h,i). Parts (j) and (k) show the PES for the Pt and Pd monomers, respectively; scales show the adsorption energy in eV; the locations of the underlying surface atoms are illustrated in (l).

mixtures— **Figure 2.3** (b, c). Also at higher temperatures, it is shown that having 50% or less Pt improves the stability of small clusters as can be seen in **Figure 2.3** (c, f, i), where 1:3 and 1:1 distributions are tighter than 3:1. There is a hint that perhaps at very high temperatures an ideal

initial Pt concentration may be somewhere around 35—40%. To determine this would require a more detailed study using DFT and/or MD to model clusters composed of several tens of atoms or more; this is beyond the scope of the present work.

From **Figure 2.3**, it is argued that there is a general preference for roughly equimolar clusters as the tightest distributions and most clearly defined peaks close to the origin are those belonging to such, with heavier populations of the clusters with one dominant component also being obvious when the starting monomer distribution is unequal. However, there are indications that the 1:1 ratio leads to more sintering resistant clusters for reasons noted above. This result is also intuitive based on the higher sintering energy penalties of the 1:1 tetramers (**Table 2.2**). Thus, the experimental observation that equimolar Pt-Pd clusters are more stable against sintering on the support than clusters of vastly different compositions is generally reproduced.

2.3.4. Explanations for the Preference for a 1:1 Phase

It has been an outstanding interest as to why Pt-Pd clusters prefer to form a 50/50 phase on oxide supports. Such a phase is confirmed by the sintering simulations at experimentally-relevant temperatures. It is natural to suspect that there must be something unique about the geometric and electronic structures of these clusters. Several forms of chemical bonding analyses were performed to address this question. In general, as will be shown, there exists a competition between maximized binding to the surface O atoms (favoring flat structures) and the intra-cluster bonding, i.e. delocalized overlap (favoring more compact 3D structures).

2.3.4.1. Explanations for the Preference for a 1:1 Phase

The projected density of states (PDOS) of Pd-O/Pt-O coordination and Pd-Pt coordination was extracted in order to compare density of states overlap of cluster-support against that of intra-cluster bonding. In PDOS analysis, the intensity and broadness of the peaks of the PDOS represent the distribution of electrons within atomic orbitals.[61] Favorable orbital

mixing between two atoms arises when there is optimal overlap between their respective PDOS.[62]

In **Figures 2.4** and **2.5**, only the energy ranges for integration of valence electrons were visualized: **Figure 2.4** is focused on cluster-support interactions and **Figure 2.5** on intra-cluster bonding. Only *d* projections are visualized as integration of *s* and *p* PDOS yielded small fractional contributions (*s*-electrons are also addressed separately in the following section). Optimal *p-d* mixing occurs between cluster-O in the range of -6 to -2 eV, while intense *d-d* mixing occurs between cluster atoms in the range of -2 eV up to the Fermi energy, which is set at 0 for ease of visualization. The distribution between these two ranges reveals the unique bonding environment for one structure over the other.

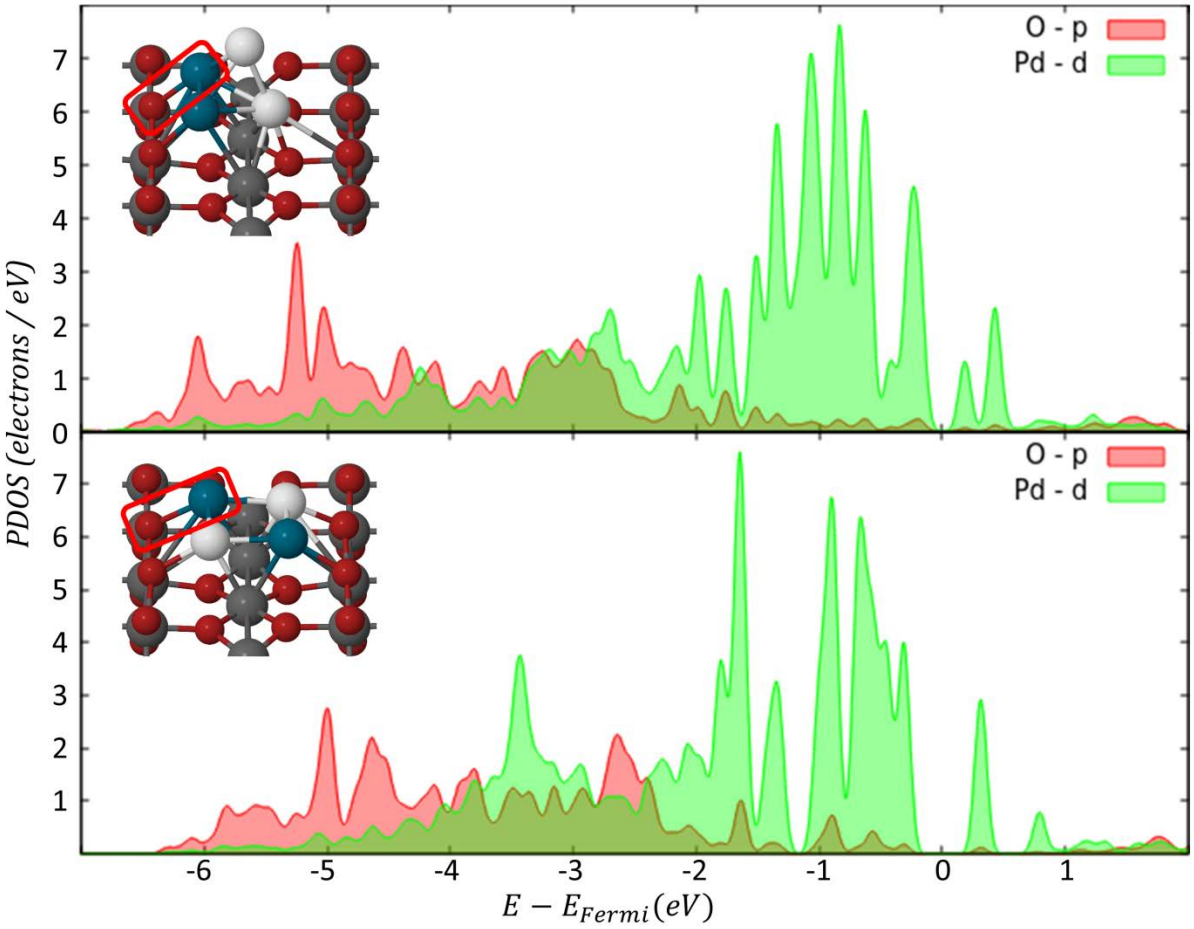

Figure 2.4. Projected Density of States of Pd coordinated to O_b. (Top) The global minimum of Pd_2Pt_2, a tetrahedron. (Bottom) The second lowest minimum of Pd_2Pt_2, square planar.

Integration of the PDOS in *s, p,* and *d* distributions reveals Pt's approximately equal distribution of 5 electrons for cluster-support interaction and 5 electrons for the high intensity peaks of *d-d* mixing in intra-cluster bonding; Pd's differs slightly with 4 and 6, respectively. A similar trend takes place in planar Pt_3Pd and explains in part the predominance of 2D over 3D as Pt favors covalent Pt-O bonds. Due to the symmetric electronic environment of planar Pd_2Pt_2, Pd-Pd and Pt-Pt *s, p,* and *d* distributions overlap completely and Pt-Pd overlap nearly perfectly.

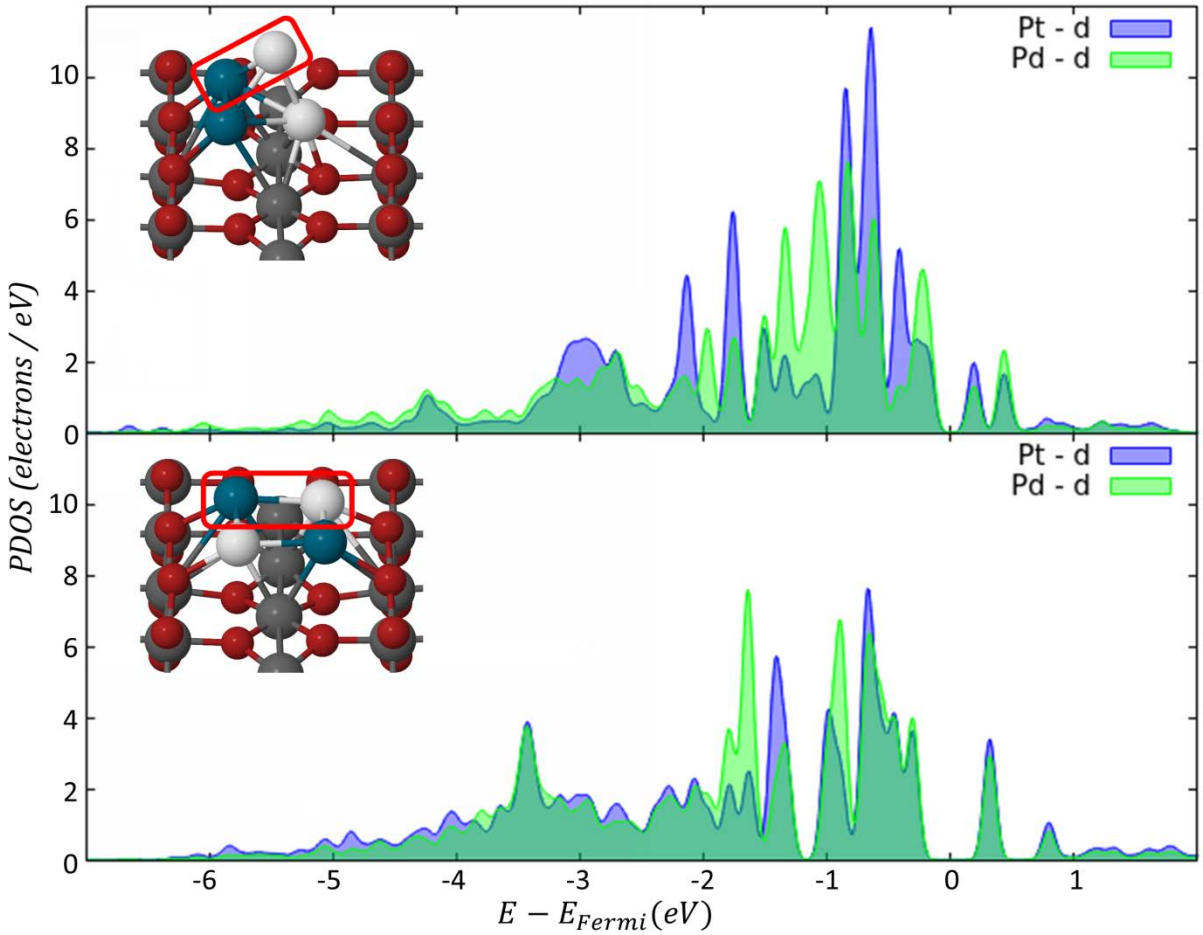

Figure 2.5. Projected Density of States of Pd coordinated to Pt. (Top) Pd-Pt_{apex} of the global minimum of Pd_2Pt_2, a tetrahedron. (Bottom) Pd-Pt (symmetric to the other half of the structure) of the second lowest minimum of Pd_2Pt_2, square planar.

In contrast, the 50/50 global minimum, a tetrahedron, exhibits a more uneven distribution although a similar *p-d* mixing trend may be observed in **Figure 2.4**. The tetrahedron's triangular

base features 2 Pd-O_b coordination and 1 Pt-O_s coordination (O_b, O_s are labeled in **Figure 2.2**). The two basal Pd and the apical Pt illustrate a preference for *d-d* mixing, Pd conserving 6 electrons for high intensity *d-d* mixing and 4 electrons for Pd-O_b coordination and Pt reserving 6 electrons within the high intensity range and 4 electrons in the delocalized ranges of -6 to -2 eV. The basal Pt preferentially delocalizes 7 electrons in the lower energy range of -2 eV and below for optimal Pt-O_s coordination and compensation for Pd *d-d* mixing where the apical Pt distribution falls; only 3 electrons fall in the maximum *d-d* peak range of -2 eV to the Fermi energy. This trend repeats in Pd_3Pt tetrahedra and contributes to the predominance of 3D over 2D as Pd favors *d-d* mixing over Pd-O_b coordination.

In general, in binding to surface oxygen atoms, 2D clusters are favored. They lay flat and wet the support, maximizing the number of interactions with surface O atoms, and exhibit a significant degree of covalency in these bonds. The 3D structures also coordinate with surface O atoms but these interactions are compromised due to poor geometric matching with the interface. In terms of binding to the support, pure and mixed clusters show some difference due to the relative electronegativities of Pt, Pd, and O, where the degree of charge transfer to the support and the resultant ionic component are mildly affected—discussed further in **subsection 2.3.4.3.** Intra-cluster bonding is analyzed next, from a Molecular Orbital (MO) picture.

2.3.4.2. Intracluster and Cluster-Support Bonding

Intra-cluster bonding is also similar between all considered tetramers, as the basic bonding principle is the same for the 2D and 3D structures. The Pd and Pt atoms in isolation have the electronic configuration of [RG]$d^{10}s^0$ and [RG]d^9s^1, respectively, which renders them rather inert. When four atoms come together to form a cluster, the four sets of valence *d*- and *s*-AOs form a total of twenty-four MOs being populated by forty electrons. Population of the MOs originates from the valence *s*-AOs as required for the clusters to be bound. In the case of pure Pd clusters, the MOs formed by *d*- and *s*-AOs completely separate. By inspection, it is found that only one MO originating from *s*-AOs is populated for the square-planar global minimum; it is

delocalized and completely symmetric; it is a σ-MO. Starting from the Pd_4 cluster being populated by two electrons, this σ-MO makes the cluster obeys the (4*n*+2) Hückel's rule with *n*=0 for aromatic species, hence, Pd_4 is σ-aromatic.[51, 63-65] Aromaticity can be 2D (as in the planar) or 3D (as in the tetrahedral, see SI for gas-phase results). The two-electron hole left in the *d*-set in Pd_4 also contributes to the net-bonding effect.[51] Aromaticity is a stabilizing and symmetrizing effect in chemistry[66] and stability is the current topic under investigation. The electron count holds up in all the gas-phase and when the cluster is deposited on TiO_2(100).

The σ-MOs formed by *s*-AOs are easily distinguishable in planar adsorbed clusters (**Figure 2.6**). In 3D adsorbed clusters, the σ-bonding overlap is stronger as the corresponding MO goes deeper in the valence set, mixes with the MOs formed by *d*-AOs, and becomes indistinguishable. In 2D species, σ-states are energy-separated from d-states and can be easily found by inspection, but the 3D species require an alternative mode of analysis such as projected DOS to recognize the same bonding pattern. The previous section examined in detail the delocalized chemical bonding present in tetrahedral clusters and determined Pd's preference towards *d*-*d* mixing and Pt's preference towards *p*-*d* mixing with coordinating O. An analogous shift in electron density may be found in the extracted σ-MOs of the planar clusters.

Thus, overall, the chemical bonding in all studied clusters is delocalized, and can be qualified as σ-aromatic. It is also important to note that the delocalized overlap is optimal when the cluster is most compact, i.e. 3D and not 2D. Therefore, the intra-cluster bonding overlap is more pronounced in tetrahedral clusters rather than planar clusters. This contributes to the dominance of tetrahedral over planar gas phase clusters (see SI). Hence, for clusters on the support, binding to surface oxygen favors planar structures and intra-cluster bonding favors tetrahedral structures, as a result the two forms are very close in energy. In STEM images of larger nano-particles,[15] 3D species prevail; ultimately, intra-cluster bonding dominates.

Importantly, the difference in the electron constitution of Pt-Pd clusters of all compositions is small; metal-substitution has very little effect on the nature and the population of

valence MOs in these systems. Given that the bonding is very similar, it cannot be the major culprit for the special stability of the 1:1 clusters.

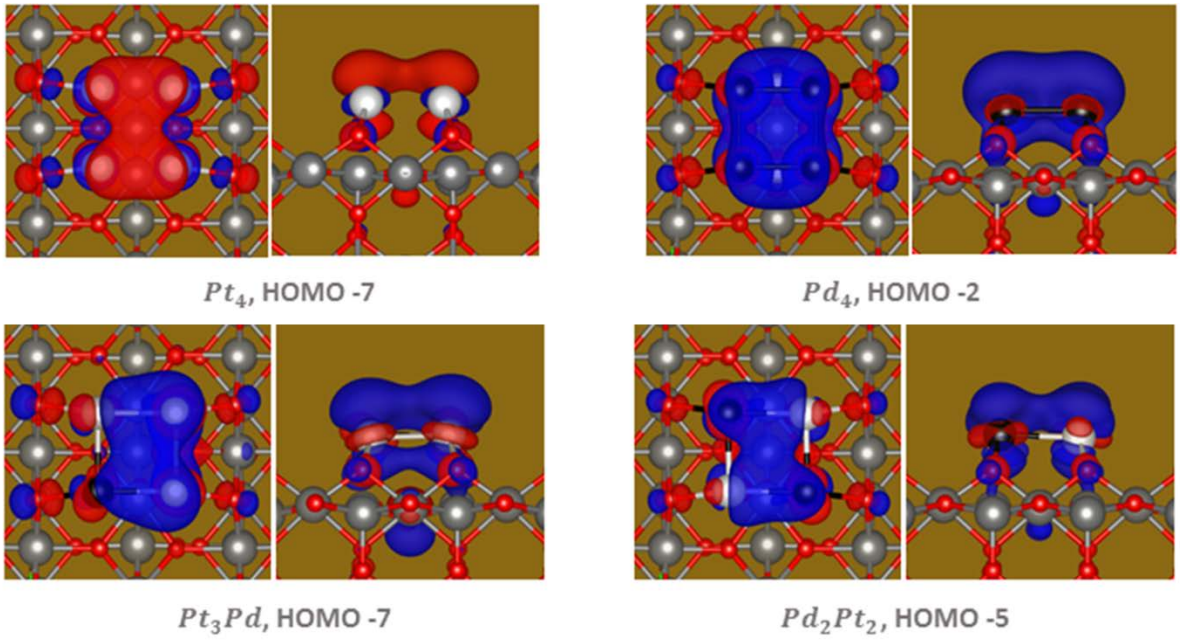

Figure 2.6. σ-MOs formed by *s*-AOs of pure (top) and mixed (bottom) planar clusters. MOs are not separable from the d-states. For clarity, Pt is white, Pd is black, Ti is dark gray, and O is red.

2.3.4.3. Charging and Electrostatics

The small difference between electonegativities of Pt and Pd (respectively 2.28 and 2.20) leads to the Pt atoms becoming slightly negatively charged; all Pd atoms becoming slightly positive. Due to charge-separation, there is an additional electrostatic contribution to the binding in mixed clusters. It was hypothesized that the Coulomb potential, V_C = ($\Sigma q_i q_j / r_{ij}$), between these partial charges would lead to an additional stabilization, favoring the 1:1 mixtures. **Table 2.4** shows the value of the Coulomb potential of the given cluster in gas-phase and the Boltzmann-weighted average Coulomb potential (using weights from **Table 2.1**). It was found that when compared to the gas-phase clusters—wherein all clusters are neutral—the adsorbed clusters undergo a modest charge transfer from the cluster to the support, as a result of the more electronegative O atoms. **Table 2.5** summarizes the electrostatic results for the global and local minima of adsorbed clusters. Charges of planar structures range from 0.32 to

0.44 e and the tetrahedra range from 0.21 to 0.34 e (see **Table 2.5**). The net charge on the cluster indicates that during adsorption charge transfer has taken place from the cluster to the TiO_2(110) surface.

Table 2.4. Coulomb Potential (V_C) of Gas Phase Clusters [A, B]

No. Pd	No. Pt	V_C Tetrahedral (eV)[1]	V_C Planar (eV)	$\Sigma P_i V_{Ci}$ 1000 K (eV)
0	4	-0.01	-0.12	-0.02
1	3	-0.10	-0.23	-0.10
2	2	-0.15	-0.08 [C]	-0.15
			-0.25 [D]	
3	1	-0.11	-0.14	-0.11
4	0	-0.01	-0.05	-0.01

A. Partial charges were summed for all gas-phase structures to confirm the neutrality of the cluster.
B. In gas phase clusters, the global minimum is always tetrahedral.
C. Pd-Pd-Pt-Pt planar structure, which is bilaterally symmetric through the plane bisecting the edge of the square planar structure.
D. Pd-Pt-Pd-Pt planar structure, which is bilaterally symmetric through the plane bisecting the diagonal of the square planar structure.

Table 2.5. Charges (Q) and Coulomb Potentials (V_{Ci}) of Local Minima and Weighted Average Coulomb Potential for Accessible Isomers ($\Sigma P_i V_{Ci}$)

No. Pd	No. Pt	Isomer	Geometry	Q (e)	V_{Ci} (eV)	$\Sigma P_i V_{Ci}$ 700 K (eV)	$\Sigma P_i V_{Ci}$ 1000 K (eV)
0	4	I	Square Planar	0.28	-0.13	0.08	0.06
		II	Tetrahedron	0.20	0.09		
		III	Diamond	0.22	-1.16		
1	3	I	Square Planar	0.32	0.15	0.12	0.09
		II	Tetrahedron	0.25	-0.21		
		III	Tetrahedron	0.21	0.07		
2	2	I	Tetrahedron	0.28	-0.41	-0.25	-0.20
		II	Square Planar	0.36	0.16		
		III	Tetrahedron	0.29	-0.27		
		IV	Square Planar	0.36	0.21		
		V	Tetrahedron	0.27	0.04		
3	1	I	Tetrahedron	0.32	-0.30	-0.22	-0.21
		II	Tetrahedron	0.29	-0.11		
		III	Rhombus	0.38	-0.09		
		IV	Diamond	0.43	-0.88		
4	0	I	Square Planar	0.44	0.33	0.26	0.25
		II	Tetrahedron	0.34	0.35		

All gas phase clusters are electrostatically stabilized, as is shown in **Table 2.4**. Overall, the planar structure has greater electrostatic stability with the Coulomb potential of the lowest energy planar isomer being roughly double that of the lowest energy tetrahedral structure and, for the case of the pure tetramer, an order of magnitude greater (there is a small charge separation even in monometallic clusters). Pure Pd and Pt clusters exhibit the weakest electrostatic stabilization and 1:1 ratios the strongest for all gas-phase structures. A reversal in the trend of electrostatic stabilization occurs between 2D and 3D structures going from the gas phase to adsorption.

For adsorbed clusters, charge separation decreases in the 2D and increases in the 3D. This results in the electrostatically destabilization of planar structures in favor of 1:1 Pd-O or Pt-O coordination, whose net repulsion (0.15 to 0.36 eV) amongst mixed clusters is compensated by consistently higher partial positive charges as compared to tetrahedra. Mixed 3D structures are electrostatically stabilized due to the increase in charge separation between Pt and Pd with a net intra-cluster attraction on the order of a few tenths of an eV — e.g. from **Table 2.5**: Pd_3Pt-Isomer I and II, Pd_2Pt_2-Isomer I, and $PdPt_3$-Isomer II. In such clusters, where the global minimum is a tetrahedron, the apex is always Pt, whose negative partial charge almost doubles when compared with the gas phase cluster. Thus, an electrostatic sandwiching effect occurs with the tetrahedron's positive base interleaved between the negative apex and the electronegative surface oxygens. This explains the dominance of Pd_3Pt tetrahedra over their planar counterpart since the tetrahedra can maximize this electrostatic binding with an electropositive Pd_3 base (Isomer I) or Pd_2Pt base (Isomer II).

Just as 50/50 ratios of Pd and Pt in the gas phase demonstrated the greatest electrostatic stability, 50/50 ratios of Pd and Pt adsorbed to the surface attain the optimal balance between surface-cluster coordination and intra-cluster attraction. The global minimum of Pd_2Pt_2, a tetrahedron, has the greatest electrostatic stability at -0.41 eV and one of the highest induced charges amongst 3D structures (0.28 e). The next local minimum, a planar

structure, acquires the greatest charge amongst mixed clusters at 0.36 e, but also one of the highest intra-cluster Coulomb repulsions of 0.16 eV, second only to pure Pd_4 and comparable to Pt_3Pd. By Boltzmann-averaging the Coulomb potentials an estimate can be gained for the net electrostatic interaction within a particular tetramer type. When this is done only the 1:1 and 1:3 Pt to Pd structures, possess an overall Coulombic stabilization. However, the 1:3 Pt to Pd structures exhibit distorted planar structures of a rhombus and diamond, which display minimal coordination to the surface (see SI) in contrast to their high positive partial charges (0.38 and 0.44 e) and calculated electrostatic stabilization (-0.09 and -0.88 eV). The nonappearance of Pd-rich phases in experiments could be due to such phases becoming oxygenated before sintering to large nanoparticles, coupled with the fact that Pd more readily dissociates from Pd-rich clusters relative to other fragmentation processes (see **Table 2.2**).

To estimate the contribution of the Coulomb interaction as a function of cluster growth solid-state calculations were carried out on several unit-cells of various composition of Pt and Pd. **Table 2.6** summarizes the results for several mixed lattices, showing the Strukturbericht label, the cohesive energy (E_{coh}), the optimized lattice constant (a_{lat}), and the percent of the Ewald contribution to the total DFT energy — it is noted that all Ewald contributions are attractive. Calculations are in reasonable agreement with other theoretical results.[67]

Table 2.6. Cohesive Energy (E_{coh}), Lattice Constant (a_{lat}), and Percent of Ewald to DFT energy for Several Unit Cells of Various Compositions of Pt and Pd

Strukturbericht Pt:Pd	**E_{coh} (eV/atom)**	**a_{lat} (Å)**	**V_{Ewald}/V_{DFT} (%)**
$L1_2$ 3:1	-5.60	3.97	66.42
$L1_0$ 1:1	-5.01	3.98 3.90	68.39
B2 1:1	-4.99	3.13	73.34
B1 1:1	-4.26	5.28	67.96
$L1_2$ 1:3	-4.40	3.94	75.78

The Pt dominant unit cell is the most stable from the magnitude of E_{coh}, two structures of the 1:1 lattices follow behind and are very close in energy (a *fcc*-like $L1_0$ structure and a CsCl-like B2 structure), differing by 0.02 eV. The 1:1 mixtures have a slightly larger Ewald contribution than the 3:1(Pt:Pd) lattice, but smaller than that of the 1:3 lattice, which itself is overall the most weakly bound. The results suggest that electrostatic stabilization does play an important role as the clusters sinter to larger nanoparticles and acquire more bulk-like properties.

2.4. CONCLUSIONS

An in depth theoretical study of sintering of mixed Pt-Pd clusters on TiO_2(110) was presented. Our in-house *ab initio* Monte Carlo algorithm simulates the process of Ostwald ripening, including cluster dissociation and formation through the exchange of monomers, and monomer evaporation from the support and coverage-dependent redeposition. The evolution of cluster size- and composition-distributions at experimentally relevant temperatures was modeled. In agreement with earlier observations, the 1:1 clusters are relatively favored at relevant temperatures. Further structural and chemical bonding analyses revealed no obvious reason for favoring the equally mixed clusters. One subtle difference that was shown to lead to a unique stability was electrostatic stabilization within the cluster. Charge redistribution, from Pd to Pt, results in an intra-cluster Coulomb interaction. This interaction was shown to be the most favorable for clusters containing Pt and Pd in equal proportions. In addition, the 50/50 mixtures were shown to have considerably more thermally relevant isomers at higher temperatures than clusters of any other compositions. As a result, there is a configurational entropic stabilization, which is smaller than the electrostatic effect. Both the entropic and Coulombic stabilization can be enhanced as the clusters grow larger. Thus, a well-motivated hypothesis was presented to explain why at catalytically relevant temperatures, small Pt-Pd nanoparticles of roughly 1:1 concentration are the most resistant to sintering.

This study sites two subtle but apparently critical effects leading to stabilization of deposited clusters against sintering: entropic and electrostatic. It is likely that such effects may govern the stability of other bi- and poly-metallic deposited clusters.

2.5. REFERENCES

1 Bhasin M.; McCain, J.; Vora, B.; Imai, T.; Pujado, P. *Appl. Catal. A-Gen.*, **2001**, *221*, 397-419.

2 Galvita, V.; Siddiqi, G.; Sun, P.; Bell, A. *J. Catal.*, **2010**, *271*, 209-219.

3 Burch, R.; Garla, L. *J. Catal.*, **1981**, *71*, 360-372.

4 Weckhuysen, B.; Schoonheydt, R. *Catal. Today*, **1999**, *51*, 223-232.

5 Kim, J.; Park, S.; Chun, B.-H.; Jeong, B.; Han, J.; Kim, S. *Catal. Today*, **2012**, *185*, 47-53.

6 Zhao, H.-L.; Meng, F.-X.; Guo, W.; Zou, J.-J.; Zhang, X.-W. *J. Fuel Chem. Technol*, **2008**, *36*, 462-467.

7 Bariås, O.; Holmen, A.; Blekkan, E. *J. Catal.*, **1996**, *158*, 1-12.

8 Jablonski, E.; Castro, A.; Scelza, O.; de Miguel, S. *Appl. Catal. A-Gen.*, **1999**, *183*, 189-198.

9 Sun, P.; Siddiqi, G.; Vining, W.; Chi, M.; Bell, A. *J. Catal.*, **2011**, *282*, 165-174.

10 Siddiqi, G.; Sun, P.; Galvita, V.; Bell, A. *J. Catal.*, **2010**, *274*, 200-206.

11 Ren, H.; Humbert, M.; Menning, C.; Chen, J.; Shu, Y.; Singh, U.; Cheng, W. *Appl. Catal. A-Gen.*, **2010**, *375*, 303-309.

12 Jovanovic, M.; Putanov, P. *Appl. Catal. A-Gen.*, **1997**, *159*, 1-7.

13 Gutiérrez, A.; Arandes, J.; Castaño, P.; Aguayo, A.; Bilbao, J. *Energy Fuels*, **2011**, *25*, 3389–3399.

14 Graham, G.; Jen, H.-W.; Ezekoye, O.; Kudla, R.; Chun, W.; Pan, X.; McCabe, R. *Catal. Lett.*, **2007**, *116*, 1-8.

15 Johns, T.; Gaudet, J.; Peterson, E.; Miller, J.; Stach, E.; Kim, C.; Balogh, M.; Datye, A. *ChemCatChem*, **2013**, *5*, 2636-2645.

16 Anderson, R.; Zhang, L.; Loussaert, J.; Frenkel, A.; Henkelman, G.; Crooks, R. *ACS Nano*, **2013**, *7*, 9345-9353.

17 Henrich, V.; Cox, P. *The Surface Science of Metal Oxides*. Cambridge University Press, Cambridge, England, **1996**.

18 Henry, C. *Surf. Sci. Rep.*, **1998**, *31*, 231-325.

19 Diebold, U. *Surf. Sci. Rep.*, **2003**, *48*, 53-229.

20 Zhang, J.; Alexandrova, A. *J. Chem. Phys.*, **2011**, *135*, 174702.

21 Hansen, T.; DeLaRiva, A.; Challa, S.; Datye, A. *Acc. Chem. Res.*, **2013**, *46*, 1720-1730.

22 Giannozzi, P.; Baroni, S.; Bonini, N.; Calandra, M.; Car, R.; Cavazzoni, C.; Ceresoli, D.; Chiarotti, G.; Cococcioni, M.; Dabo, I.; Dal A.; de S.; Fabris, S.; Fratesi, G.; Gebauer, R.; Gerstmann, U.; Gougoussis, C.; Kokalj, A.; Lazzeri, M.; Martin-Samos, L.; Marzari, N.; Mauri, F.; Mazzarello, R.; Paolini, S.; Pasquarello, A.; Paulatto, L.; Sbraccia, C.; Scandolo, S.; Sclauzero, G.; Seitsonen, A.; Smogunov, A.; Umari P.; Wentzcovitch, R. *J. Phys.: Condens. Mat.*, **2009**, *21*, 395502.

23 Kohn, W.; Sham, L. *Phys. Rev*., **1965**, *140*, A1133-A1138.

24 Lee, C.; Yang, W.; Parr, R. *Phys. Rev. B*, **1988**, *37*, 785-789.

25 Burke, K.; Werschnik J.; Gross, E., *J. Chem. Phys.*, **2005**, 123, 062206.

26 Perdew, J.; Burke K.; Ernzerhof, M., *Phys. Rev. Lett*., **1996**, 77, 3865-3868.

27 Kowalski, P.; Meyer, B.; Marx, D., *Phys. Rev. B*, **2009**, 79, 115410.

28 Kowalski, P.; Camellone, M.; Nair, N.; Meyer, B.; Marx, D., *Phys. Rev. Lett.*, **2010**, *105*, 146405.

29 Tao, J.; Perdew, J.; Staroverov, V.; Scuseria, G., *Phys. Rev. Lett.*, **2003**, *91*, 146401.

30 Peterson, K.; Puzzarini, C., *Theor. Chem. Acc*, **2005**, *114*, 283-296.

31 Figgen, D.; Rauhut, G.; Dolg, M.; Stoll, H., *Chem. Phys.*, **2005**, *311*, 227-244.

32 Hegarty, D.; Robb, M., *Mol. Phys.*, **1979**, *38*, 1795-1812.

33 Eade, R.; Robb, M., *Chem. Phys. Lett.*, **1981**, *83*, 362-368.

34 Schlegel, H.; Robb, M., *Chem. Phys. Lett*, **1982**, *93*, 43-46.

35 Bernardi, F.; Bottoni, A.; Mcdouall, J.; Robb, M.; Schlegel, H., *Faraday Symp. Chem. Soc.*, **1984**, *19*, 137-147.

36 Frisch, M.; Ragazos, I.; Robb, M.; Schlegel, H., *Chem. Phys. Lett*, **1992**, *189*, 524-528.

37 Yamamoto, N.; Vreven, T.; Robb, M.; Frisch, M.; Schlegel, H., *Chem. Phy. Lett.*, **1996**, *250*, 373-378.

38 Dunning, T.; Hay, P., *Modern Theoretical Chemistry*, Ed. H. F. Schaefer III, Vol. 3, Plenum, New York, **1977**, 1-28.

39 Hay, P.; Wadt, W., *J. Chem. Phys.*, **1985**, *82*, 270-283.

40 Wadt, W.; Hay, P., *J. Chem. Phys.*, **1985**, *82*, 284-298.

41 Hay, P.; Wadt, W., *J. Chem. Phys.*, **1985**, *82*, 299-310.

42 Gaussian 09, Revision D.01, Frisch, M.; Trucks, G.; Schlegel, H.; Scuseria, G.; Robb, M.; Cheeseman, J.; Scalmani, G.; Barone, V.; Mennucci, B.; Petersson, G.; Nakatsuji, H.; Caricato, M.; Li, X.; Hratchian, H.; Izmaylov, A.; Bloino, J.; Zheng, G.; Sonnenberg, J.; Hada, M.; Ehara, M.; Toyota, K.; Fukuda, R.; Hasegawa, J.; Ishida, M.; Nakajima, T.; Honda, Y.; Kitao, O.; Nakai, H.; Vreven, T.; Montgomery,Jr., J.; Peralta, J.; Ogliaro, F.; Bearpark, M.; Heyd, J.; Brothers, E.; Kudin, K.; Staroverov, V.; Kobayashi, R.; Norm, J.; Raghavachari, K.; Rendell, A.; Burant, J.; Iyengar, S.; Tomasi, J.; Cossi, M.; Rega, N.; Millam, J.; Klene, M.; Knox, J.; Cross, J.; Bakken, V.; Adamo, C.; Jaramillo, J.; Gomperts, R.; Stratmann, R.; Yazyev, O.; Austin, A.; Cammi, R.; Pomelli, C.; Ochterski, J.; Martin, R.; Morokuma, K.; Zakrzewski, V.; Voth, G.; Salvador, P.; Dannenberg, J.; Dapprich, S.; Daniels, A.; Farkas, Ö.; Foresman, J.; Ortiz, J.; Cioslowski, J.; Fox, D., Gaussian, Inc., Wallingford CT, **2009**.

43 Tang, W.; Sanville, E.; Henkelman, G., *J. Phys.: Condens. Matter*, **2009**, *21*, 084204.

44 Sanville, E.; Kenny, S.; Smith, R.; Henkelman, G., *J. Comb. Chem.*, **2007**, *28*, 899-908.

45 Henkelman, G.; Arnaldsson, A.; Jonsson, H., *Comp. Mater. Sci.*, **2006**, *36*, 354-360.

46 NBO Version 3.1, Glendening, E.; Reed, A.; Carpenter, J.; Weinhold., F.

47 Metropolis, N.; Rosenbluth, A.; Rosenbluth, M.; Teller, A.; Teller, E., *J. Chem. Phys.*, **1953**, 21, 1087–1092.

48 Hastings, W., *Biometrika*, **1970**, 57, 97-109.

49 Wei, S.; Zeng, Z.; You, J.; Yan, X.; Gong, X., *J. Chem. Phys.*, **2000**, *113*, 11127-11133.

50 Addou, R.; Senftle, T.; O'Connor, N.; Janik, M.; van Duin, A.; Batzill, M., *ACS Nano*, **2014**, *8*, 6321-6333.

51 Zhang, J.; Alexandrova, A., *J. Phys. Chem. Lett.*, **2012**, *3*, 751-754.

52 Zhang, J.; Alexandrova, A., *J. Phys. Chem. Lett.*, **2013**, *4*, 2250-2255.

53 Kravitz, S. *Math. Mag.*, **1967**, *40*, 65-71.

54 Peikert, R.; Würtz, D.; Monagan, M.; de Groot, C., *System Modelling and Optimization, Proceedings of the Fifteenth IFIP Conference*, *Zürich, September 2-6, 1991*, Ed. P. Kall, Springer-Verlag, **1992,** 45-54.

55 Dart, F. *Phys. Rev.*, **1950**, *78*, 761-764.

56 Shen, L.; Dadras, J.; Alexandrova, A., *Phys. Chem. Chem. Phys.*, **2014**, DOI: 10.1039/C4CP01877J.

57 Wales, D.; Bogdan, T., *J. Phys. Chem. B*, **2006**, 110, 20765.

58 Meng, G.; Arkus, M.; Brenner, M.; Manoharan, V., *Science*, **2010**, *327*, 560-563.

59 Oates, W.; Zhang, F.; Chen, S-L.; Chang, Y., *Phys. Rev. B*, **1999**, 59, 11221.

60 An, G. *J. Stat. Phys.*, **1988**, 52, 727-734.

61 Hoffman, R. *Rev. Mod. Phys.*, **1988**, 60, 601-628.

62 Carrasco, J.; Michaelides, A.; Scheffler, M., *J. Chem. Phys.*, **2009**, *130*, 184707.

63 Li, Z.; Moran, D.; Fan, K.; Schleyer, P., *J. Phys. Chem. A*, **2005**, *109*, 3711– 3716.

64 Alexandrova, A.; Boldyrev, A., *J. Phys. Chem. A*, **2003**, *107*, 554– 560.

65 Boldyrev, A.; Wang, L., *Chem. Rev.*, **2005**, *105*, 3716-3757.

66 Minkin, V.; Glukhovtsev, M.; Simkin, B., *Aromaticity and Antiaromaticity: Electronic and Structural Aspects*, John Wiley & Sons, Inc., New York, **1994**, 313.

67 Duan, Z.; Wang, G., *J. Phys.: Condens. Mat.*, **2011**, 23, 475301.

CHAPTER 3

Ethylene Dehydrogenation on $Pt_{4,7,8}$ Clusters on Al_2O_3: Strong Cluster Size Dependence Linked to Preferred Catalyst Morphologies

3.1. INTRODUCTION

The subnano clusters are known to have special catalytic reactivity.[1-4] For example, a specific range of cluster size often results in preferential reaction pathways or significantly altered reactivity, because in the subnano regime clusters are affected by size-dependent electronic and geometric structure. One issue complicating this situation is that there may be multiple, thermally accessible cluster structures with significantly different electronic and binding site properties. Here we use a combination of experimental probes of cluster structure and binding site distributions together with density functional theory (DFT) exploring the range of thermally accessible structures in order to study the effects of size-dependent cluster structure on ethylene binding and dehydrogenation.

Platinum's ability to (de)hydrogenate hydrocarbons is well-documented, and it is of interest to see if small clusters of Pt can be good dehydrogenation catalysts with useful selectivity that might enable more economical use of precious metals in catalysis. An important part of the problem is the stability of small clusters with respect to both sintering or agglomeration and deactivation by carbon deposition ("coking").[5-8]

This work focuses on catalytic dehydrogenation on Pt_4, Pt_7, and Pt_8 clusters supported on alumina. Significant differences have been found experimentally between Pt_7 and Pt_8, here and elsewhere, and much of our effort is focused on understanding why. Pt_4 was included as an example of a smaller cluster. In this size range, strong size effects on activity have been noted. Vajda *et al.* observed Pt_{8-10}'s activity of 40-100 times for oxidative dehydrogenation of propane;[2] Roberts *et al.* observed strongly size-dependent activity for CO oxidation, which was correlated to changes in both the valence electronic structure and the number of CO binding sites on top of the clusters.[9]

There is evidence suggesting that such effects may be, at least partly, related to a structural transition occurring around Pt_7 and Pt_8. Low energy ion scattering (ISS) for Pt_n/alumina/Re(0001) showed an abrupt ~15% drop in the Pt ISS signal going from Pt_7 to Pt_8,

indicating a transition to morphologies where fewer Pt atoms are in the ISS-accessible top layer of the clusters.[9] As discussed below, we verified that the effect also occurs for the Pt_n/alumina/Ta(110) system studied here. Indeed the drop between Pt_7 and Pt_8 is actually somewhat larger (~24%) for alumina/Ta(110). The inference of a drop in the fraction of Pt in the surface layer at Pt_8 is consistent with an STM study of Pt_n/TiO_2 by Watanabe *et al.,*[10-11] who observed a transition from single- to multi-layer clusters between Pt_7 and Pt_8. Such transitions change the number and type of adsorbate binding sites exposed on the clusters, however, it is important to recognize that adsorbate binding can drive cluster isomerization, i.e., it is necessary to characterize both adsorbate-free and adsorbate-covered structures. As shown below, Pt_7 is able to adsorb more ethylene than Pt_4 or Pt_8, on either a *per* Pt atom or *per* cluster basis, consistent with additional Pt atoms exposed in the surface layer. DFT allows this effect, and the earlier ISS observations, to be explained.

3.2. RESULTS AND DISCUSSION

We begin by discussing DFT results for adsorbate-free Pt_7 and Pt_8 on α-alumina, as summarized in **Figure 3.1** and **SI Table S8.2.4**. The charges on the Pt atoms in each structure are indicated and discussed below.

3.2.1. Cluster Catalyst Structures

Small Pt clusters have many structural isomers with similar energies[12] and both Pt_7/alumina and Pt_8/alumina are found to have 5 to 7 isomers of very different geometries, predicted to be populated in the 450-700 K temperature range where dehydrogenation is observed. At the elevated temperatures relevant to catalysis and in the limit of no kinetic trapping, strong structural fluxionality and the presence of several isomers are expected.[13] Because catalytic properties may be dominated by any one or few of the isomers, it is important to consider all thermally-relevant structures.[14] We will generally describe the structures as being either “single-layer”, where all Pt atoms are exposed in the surface layer or “prismatic,” where one or more atoms are buried under the cluster surface. The lowest energy isomers of Pt_7 and

Pt_8 on alumina are shown in **Figure 3.1**, together with their Bader charges and Boltzmann populations at 700K. Pt_7 is found to have both single layer and prismatic structures in the thermally-accessible set, with prismatic geometries (global minimum and 4th isomer) comprising 66.7% of the Boltzmann population at 700 K and with the balance being single-layer geometries (second, third, and fifth isomers). In contrast, all of the accessible isomers of Pt_8 are prismatic.

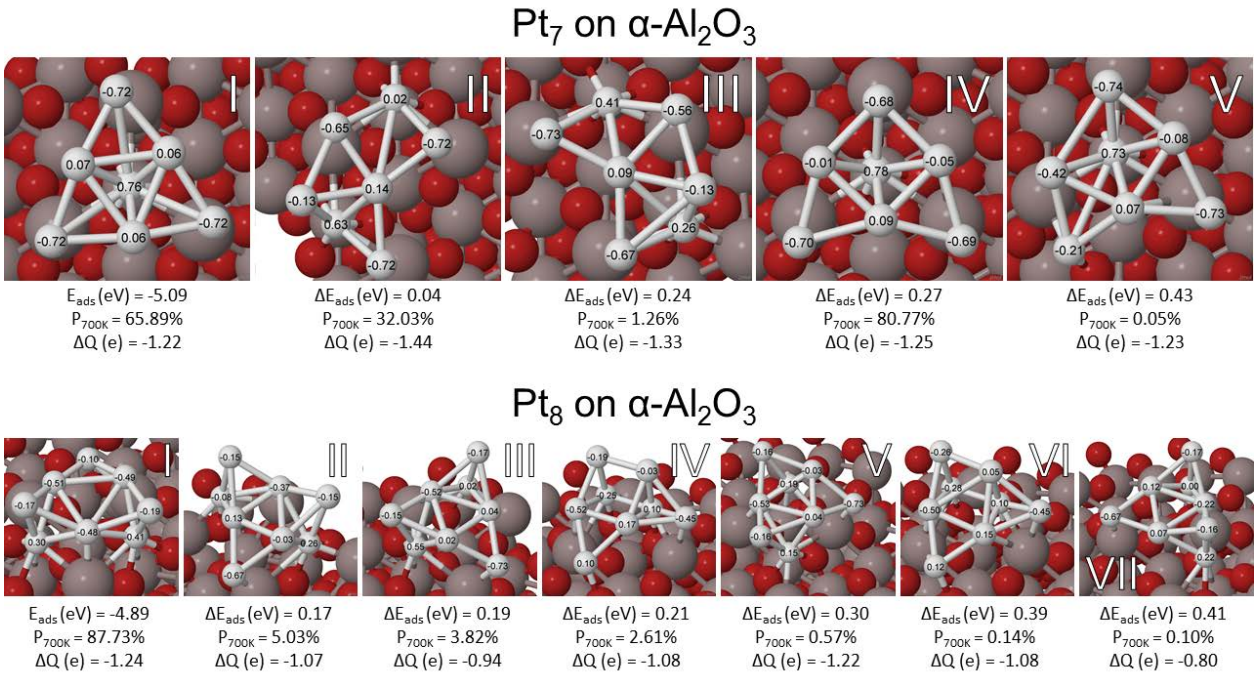

Figure 3.1. The lowest-energy minima of adsorbed Pt_7 and Pt_8, with adsorption energies (E_{ads}), Boltzmann population at catalytic temperature of 700 K (P_{700K}), and charge transfer from the support to the cluster (ΔQ).

The calculated structures provide an explanation for the ISS observation that the fraction of Pt in surface layer drops between Pt_7 and Pt_8.[9] ISS was done at 130 K, thus if the isomer distribution is equilibrated, only the lowest energy structures of each cluster would have significant populations. For Pt_7 this structure is prismatic, but exposes six of its seven atoms (i.e. ~86%) in the ISS-accessible surface layer. The lowest energy isomer of Pt_8 exposes only six of its eight atoms (75%) in the surface layer, thus we would predict a ~12.5% drop in ISS intensity between Pt_7 and Pt_8. It is not unlikely, however, that there are barriers to isomerization, such that some higher energy structures remain as the sample is cooled. To the extent that this

kinetic trapping occurs, it would tend to give an even larger intensity drop between Pt_7 and Pt_8, because Pt_7 has several single layer isomers where 100% of the Pt would be detectable, whereas all the Pt_8 isomers are prismatic.

At higher temperatures, relevant to the TPD/R experiments, the diversity of geometries of Pt_7 offers a richer set of binding sites for ethylene, as opposed to the more uniform structures populated for Pt_8, and this should be reflected in the chemical activity.

3.2.2. Size-Dependent Catalytic Activity

The chemical properties of the clusters, as probed by ethylene temperature-programmed desorption/reaction (TPD/R), are summarized in **Figure 3.2** for two consecutive TPD/R experiments on samples containing Pt_4, Pt_7, and Pt_8. For each experiment, the samples were dosed with 5 L of C_2D_4 at 150 K, then cooled to ~130 K prior to each TPD/R heat ramp (3 K/sec). The figure shows results for the two species, C_2D_4 and D_2, observed to have significant desorption signal. Desorption is reported in terms of C_2D_4 or D_2 molecules desorbing *per* Pt atom *per* second, taking advantage of the fact that we know the Pt loading quite precisely (1.5 x $10^{14}/cm^2$). The D_2 signals have been corrected for the contribution from mass spectrometer cracking of desorbing C_2D_4, and the uncorrected data are reported in **Figure S8.2.1**. To avoid interference from high background signals at masses 2 and 28, most experiments were done with C_2D_4. Experiments with C_2H_4 were also done to look for acetylene desorption, however, none was observed. In addition, no signal for ethane was observed, indicating that hydrogenation is negligible under these conditions.

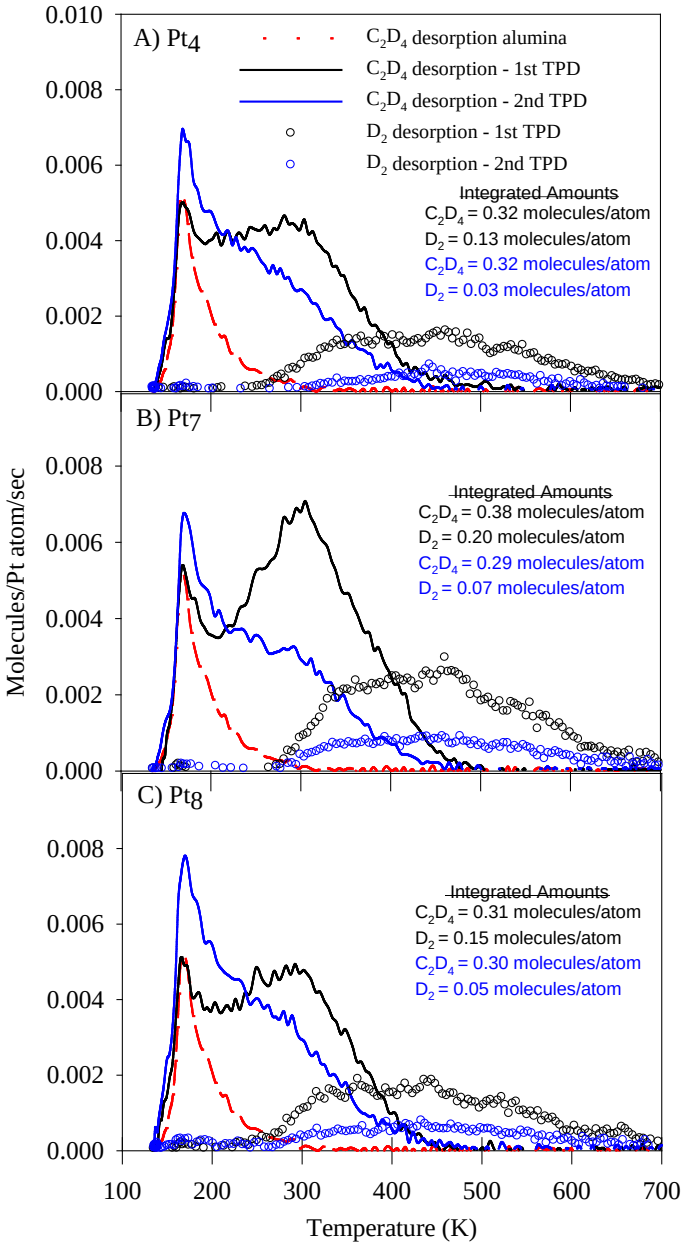

Figure 3.2. Intact C_2D_4 (solid) and D_2 (circles) desorbing from Pt_n/alumina/Ta(110) (n=4,7,8) sample during two consecutive TPD measurements. Intact C_2D_4 (red dashed line) desorbing from a cluster free alumina/Ta(110) sample. All samples were exposed to 5 L of C_2D_4 at 150 K before starting the TPD measurement

C_2D_4 desorption from the cluster-free alumina/Ta(110) support is shown for comparison to the Pt_n/alumina results. Only the result of the first TPD/R run is shown, because the second run was identical. To allow direct comparison, the data for cluster-free alumina have been scaled as if these samples also contained the same amount of Pt as the Pt_n/alumina samples.

For the cluster-free alumina film, C_2D_4 began to desorb at the TPD starting temperature, with desorption peaking at ~165 K, and rapidly declining at higher temperatures. After correcting for the contribution from C_2D_4 cracking in the mass spectrometer, the D_2 signal is zero, i.e., all ethylene adsorbed on the alumina film desorbs intact. The integrated number of C_2D_4 molecules desorbing from alumina is ~$7x10^{12}/cm^2$, i.e., on the order of 0.01 ML. The low intensity indicates that ethylene does not bind stably to most sites on the alumina film at 150 K, but that there are a few stable binding sites, presumably corresponding to defects in the alumina surface. Even these defect sites bind C_2D_4 weakly, such that it desorbs intact well below room temperature.

For the cluster-containing samples, ethylene desorption also begins as the heat ramp is started, with a sharp peak near ~165 K for all three cluster sizes. There is weak D_2^+ signal at low temperatures (**Figure S8.2.1**), but this is entirely due to dissociative ionization of desorbing C_2D_4. Both the temperature dependence and intensity of the 165 K peak match those for cluster-free alumina, indicating that this low temperature feature is simply due to C_2D_4 desorbing from defect sites on the alumina film. The fact that this low temperature component is not significantly affected by deposition of 0.1 ML equivalent of Pt_n suggests that the clusters do not diffuse to and occupy these defect sites, at least in the < 300K range where Pt_n deposition, C_2D_4 exposure, and desorption of thus low temperature feature occur.

For Pt_n-containing samples, there is also a broad C_2D_4 desorption component extending between ~200 and 420 K, which clearly results from ethylene bound to the Pt clusters. The peak temperature of this component is ~280 K for Pt_4 and Pt_8, and ~300 K for Pt_7, and the intensity is also significantly higher for the Pt_7-containing sample. Below ~250 K (Pt_4, Pt_8) or ~275 K (Pt_7), only intact C_2D_4 desorption is observed, but at higher temperatures, D_2 desorbs in a broad component extending to 650 K. In each case, the onset of D_2 desorption is just below the peak C_2D_4 desorption temperature, as would be expected if dehydrogenation to generate D_2 is in competition with C_2D_4 desorption.

The figure also lists the integrated amounts of C_2D_4 and D_2 observed to desorb from each sample, given in terms of number of molecules desorbing *per* Pt atom. Desorption/cm^2 can be obtained simply by multiplying by the Pt coverage (1.5 x 10^{14} Pt atoms/cm^2). These numbers include desorption from both alumina and Pt_n sites, and to compare the Pt_n-only desorption, it is necessary to subtract the alumina contribution, equivalent to ~0.08 C_2D_4/Pt atom. Thus, in the first TPD/R experiment the corrected desorption is 0.24 C_2D_4 and 0.13 D_2 molecules *per* Pt atom for Pt_4, compared to 0.30 C_2D_4 and 0.20 D_2 for Pt_7, and 0.23 C_2D_4 and 0.15 D_2 for Pt_8.

No additional D_2 desorption was observed in select experiments where the temperature was ramped to 900 K, thus it is reasonable to assume that dehydrogenation is complete by 650 K. In that case, the total number of initially adsorbed C_2D_4 molecules *per* Pt_n cluster can be estimated as the sum of the C_2D_4 desorption plus half the D_2 desorption. This amounts to ~0.3 C_2D_4/Pt atom for both Pt_4 and Pt_8, compared to 0.4 C_2D_4/Pt atom for Pt_7. The numbers of C_2D_4 molecules initially adsorbed *per* cluster are ~1.1, ~2.7 and ~2.4, respectively, for Pt_4, Pt_7, and Pt_8. Thus, Pt_7 provides significantly more binding sites than the other two cluster sizes on either a *per* atom or *per* cluster basis.

Study of small supported clusters is complicated by substrate-mediated adsorption, in which molecules initially landing on the alumina support, where they bind too weakly to be stable, diffuse and bind stably to the Pt_n. For our experiments with 0.1 ML equivalent Pt coverage, the effect is to substantially amplify the effective adsorbate exposure to the clusters, as will be demonstrated for C_2D_4 below. During the ~20 minutes elapsing between the start of cluster deposition and the first TPD/R hear ramp, the clusters, on average, are exposed to ~0.04 L of background CO, corresponding to ~0.01 CO impacting *per* surface atom. During the first TPD/R run, CO desorption amounting to ~0.5 CO molecules/cluster is observed, independent of cluster size. CO binds strongly to Pt_n (see below), and likely competes with C_2D_4 for Pt binding sites. Therefore, we expect that the integrated C_2D_4 numbers are somewhat lower than they would be if no CO were present.

As discussed above, a larger fraction of the Pt atoms is exposed in the surface layer of Pt_7/alumina, compared to Pt_8/alumina, consistent with the observation that more C_2D_4 adsorbs on Pt_7 than on Pt_8. Clearly, however, understanding the TPD/R experiments requires consideration of how the Pt_n isomer distribution is affected by ethylene adsorption, also of the factors that control branching between ethylene desorption and dehydrogenation.

Before discussing DFT results for ethylene-Pt_n interactions, we consider the question of whether the temperature dependence observed for D_2 desorption is controlled by the energetics of C_2D_4 decomposition, or simply reflects the activation energy for desorption of D_2. This point was tested by studying D_2 TPD, and **Figure S8.2.2** compares the D_2 desorption from separate samples of Pt_8/alumina/Ta(110) after 5 L exposure to either D_2 or C_2D_4 at 150 K. It can be seen that for the D_2 exposure, desorption starts at ~160 K, compared to ~220 K for the C_2D_4 exposure, and is 90 % complete by ~400 K, at which point only about half the D_2 from C_2D_4 has desorbed. In this temperature range, D_2 desorption from Pt almost certainly involves recombination of absorbed D atoms, thus the higher temperatures required to drive D_2 desorption after C_2D_4 exposure suggest that the limiting factor is the activation energy for some step(s) in the C_2D_4 decomposition process, rather than the D_2 recombinative desorption energetics.

The desorption spectra were simulated to extract activation energies as described in the SI, which reports the best-fit energy distributions in **Figure S8.2.3**. Simulation was based on assuming first order kinetics for the limiting step, as might be expected for intact C_2D_4 desorption. Based on this assumption, the desorption energy for C_2D_4 bound on the alumina film is in the ~0.5 eV range, while for C_2D_4 at Pt cluster sites, the desorption energy would range from ~0.6 to 1.4 eV. For D_2 production, under the assumption of a first order limiting step, the activation energy would be in the 0.7 – 2.3 eV range. A combination of DFT and coverage-dependent TPD/R studies was used to probe C_2D_4 adsorption and desorption, resulting in a more complex picture of the process.

Because theory on supported cluster systems is computationally demanding due to the large number of isomers and adsorption geometries involved, we focus our DFT work on ethylene adsorption and activation for dehydrogenation as the key processes influencing the kinetics for ethylene and hydrogen desorption. In addition, we chose the Pt_7/alumina system for the most in-depth work, both experimentally and theoretically. Since the TPD results indicate that roughly three C_2D_4 molecules adsorb initially per Pt_7, we consider theoretically adsorption of one, two, and three ethylene molecules on the most important Pt_7 isomers, and also the factors that influence desorption vs. dehydrogenation.

The literature for ethylene binding and hydrogenation/dehydrogenation on various Pt surfaces provides an important insight aiding interpretation of the DFT results. Ethylene adsorption and decomposition has been extensively studied on various platinum surfaces using techniques such as TPD, reflection/absorption infrared spectroscopy (RAIRS), and high-resolution electron energy loss spectroscopy (HREELS). At temperatures below 100 K, adsorbed ethylene forms di-σ bonds on close-packed Pt(111)[15-16] and Pt(100)[17] surfaces, and π-bonds on the stepped sites of Pt(210) and (1×1)Pt(110).[18] On the close-packed surfaces, some of the di-σ bound ethylene desorbs intact at temperatures around 285 K, however, TPD of C_2D_4 and C_2H_4 co-adsorbed on Pt(111) also yielded C_2D_3H and C_2H_3D, indicating that recombinative desorption of dissociatively chemisorbed ethylene also contributes to the ethylene desorption signal.[19] At temperatures just above the ethylene desorption peak, H_2 desorption begins, indicating the onset of dehydrogenation. The first dehydrogenation step results in formation of ethylidyne ($\equiv CCH_3$), which has been shown to adsorb in threefold hollow sites by HREELS[20] and tensor LEED.[21] Most studies consider ethylidene to be a spectator species.[22-24] At higher temperatures, the ethylidyne undergoes further decomposition, giving rise to additional H_2 desorption, going to completion by ~ 700 K. For the stepped surface of Pt(210), some of the π-bound ethylene desorbs at ~ 250 K, then the remaining π-bound ethylene dehydrogenates at ~300 K, resulting in desorption of H_2 and formation of adsorbed ethylylidyne

(≡CCH_2−, both C atoms bound to the surface), which undergoes further decomposition giving rise to additional H_2 desorption, going to completion by ~700 K. In contrast, upon heating the (1×1)Pt(110) surface to ~160 K, some of the π-bound ethylene is converted to di-σ bound ethylene. Between 270 and 330 K, the adsorbed ethylene reacts to form carbon atoms and ethylidyne on the surface accompanied by desorption of methane and H_2. The remaining ethylidyne undergoes complete dehydrogenation by 450 K. Studies on alumina-supported Pt nanoparticles showed that at temperatures below 180 K, ethylene adsorbs in three distinct forms: π-bound ethylene, di-σ bound ethylene, and the ethylidyne species.[25] By room temperature, all of the π-bound ethylene desorbs intact, while at higher temperatures the remaining di-σ bound ethylene is converted to ethylidyne.

From the perspective of interpreting the DFT results, the key insight from these studies is a correlation between the adsorbed configuration of ethylene and its subsequent reactivity.[22, 24, 26-29] This correlation, which applies to both Pt surfaces and Pt clusters, is that π-bonded, sp^2 configurations tend to result in hydrogenated products, while di-σ bonded, sp^3 configurations result in dehydrogenated products. For our system, where no hydrogen is added and hydrogenation is not observed, we interpret this correlation as suggesting that the precursor to dehydrogenation is di-σ bonded ethylene, while π-bonded ethylene should tend to desorb intact. Our bonding analysis of ethylene adsorbed to Pt_7 corresponds well to near-edge x-ray-absorption fine-structure (NEXAFS) studies on Pt(111) with di-σ bound ethylene reflecting a bond-length of ~1.5 Å and π-bound ~1.4 Å.[29] Moreover, bond angles of ≈ 120° and ≈ 97-115° reflect sp^2 and sp^3 hybridization present in adsorbed ethylene, respectively. We, therefore, will use the geometries calculated for adsorbed ethylene as indicators of the propensity to dehydrogenate.

Figure 3.3 shows the DFT results for ethylene binding to both the single layer and prismatic Pt_7 isomers that were shown in **Figure 3.1**. The most stable structures (i) are shown at the top, and additional local minima are shown below, with energetics and thermal populations

summarized in **Table 3.1**. Recall that for adsorbate-free Pt_7/alumina, the global minimum is prismatic, however, because the binding energy for the first ethylene molecule is ~0.5 eV higher for the single-layer isomer, this becomes the global minimum for ethylene$_1$/Pt_7, and a variety of low energy ethylene$_1$/Pt_7 geometries based on the single layer isomer are shown in the left column. With one ethylene molecule adsorbed, the prismatic isomers shown in the second column are, therefore, local minima, stabilized by barriers associated with the considerable rearrangement required to convert to the single layer global minimum.

Bader charge analysis shows that ethylene adsorption is associated with electron transfer from Pt_n to the carbon atoms of ethylene, suggesting that the charges on the adsorbate-free Pt_n/alumina isomers should be related to their affinities for ethylene. The charges on each atom given in **Figure 3.1** show that on average, Pt_7 has greater electron transfer from the support, compared to Pt_8. Pt_7 isomers take up 1.22-1.44 e^-, compared to 0.80-1.24 e^- for Pt_8. In addition, the single-layer Pt_7 isomers have higher charge than the prismatic isomers and less uniform charge distributions, with some Pt atoms carrying the majority of the negative charge. Pt_8, which has only prismatic isomers, has more uniform and lower charge distributions.

In principle, the extent of Pt_n charging can be probed by XPS, and Pt 4d spectra for Pt_7/alumina and Pt_8/alumina are shown in **SI Figure S8.2.4**. The stronger Pt 4f peaks were unusable because of Al 2p background. Although the 4d signal is noisy for 0.1 ML Pt coverage, it appears that the 4d binding energy (BE) for Pt_7 is shifted ~0.4 eV to higher energy compared to the Pt_8 BE. We have previously reported XPS BEs for Pt_n on glassy carbon[30] and indium tin oxide,[31] and Isomura *et al.*[10] reported BEs for Pt_n/TiO_2(110). In all cases the Pt_7 BE is higher than that for Pt_8 – opposite to what might be expected if Pt_7 is more negatively charged than Pt_8. Note, however, that XPS BEs for small clusters are strongly affected by size-dependent final state effects,[1, 32-34] and size-dependent rehybridization of metal orbitals has recently been identified as another factor in BEs for supported Pd_n.[35-36]. As a result, interpreting the BE shift in terms of the initial state charge is not possible.

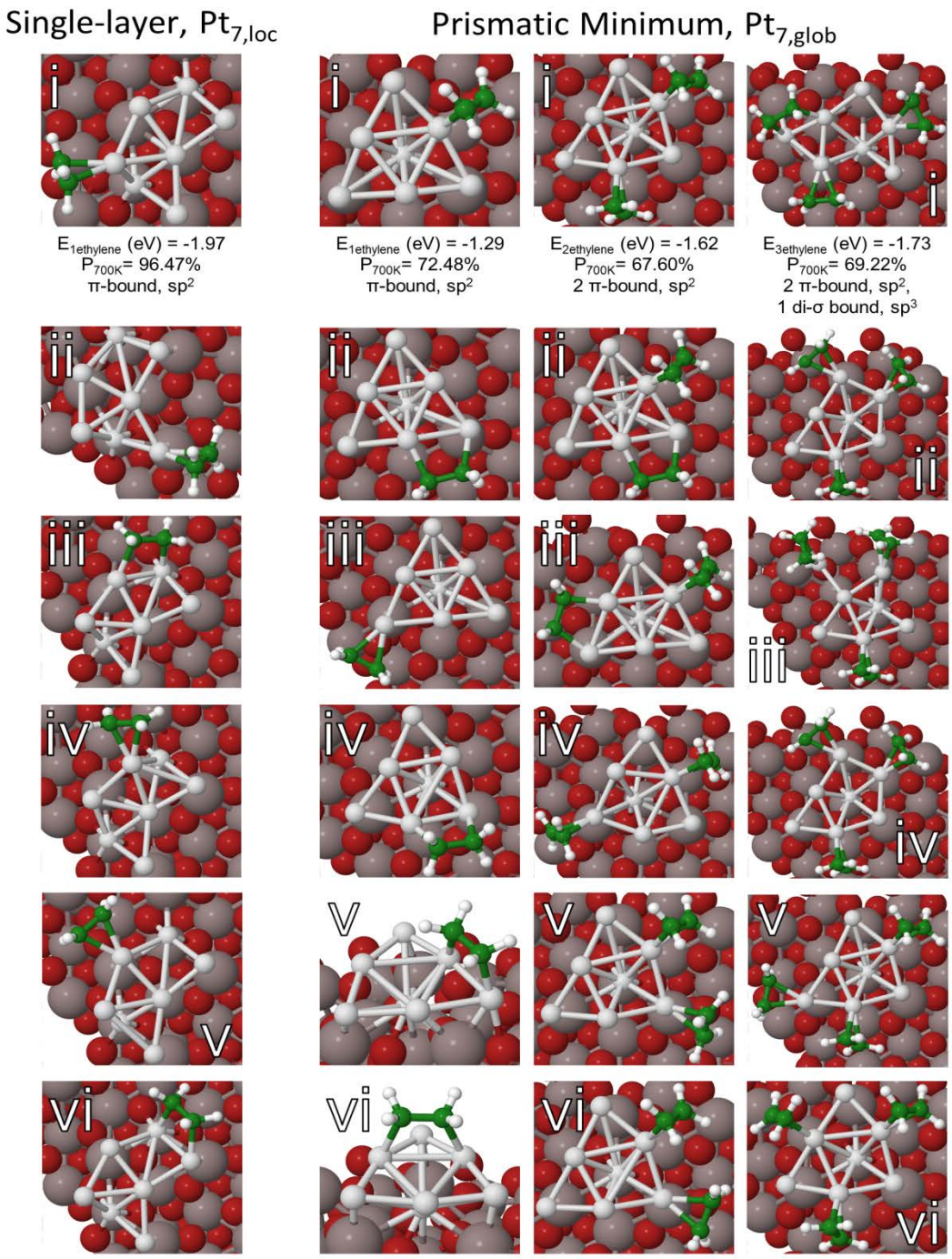

Figure 3.3. Structures of ethylene binding to Pt_7. Left column: Binding of a single ethylene molecule to different sites on single-layer Pt_7. Columns 2 – 4: Binding of 1, 2, or 3 ethylene molecules in different sites on the global minimum prismatic isomer of Pt_7. Energetics and bonding analysis are summarized in **SI Table S8.2.5** and adsorption geometries and thermal distributions are summarized in **Table 3.2**. For additional local minim at each coverage (n=2, 3), refer to the SI.

Upon ethylene binding, the calculated charge on the Pt binding site increases by ≈ +0.2 to +0.7 e, reflecting electron transfer from Pt to ethylene. Therefore it is not unreasonable to expect that the more negatively charged cluster isomers and binding sites should tend to have higher ethylene binding energies. For example, the single-layer local minimum is 0.22 e^- more negatively charged than the prismatic global minimum, and its ethylene adsorption energy is stronger by 0.68 eV. Therefore, both the larger average alumina-to-Pt_n electron transfer for Pt_7, and the existence of low-lying single-layer local minima that have the highest alumina-to-Pt_n electron transfer, is consistent with the observation (**Figure 3.2**) that Pt_7 binds ethylene more strongly than Pt_8. The fact that Pt_7 also binds more ethylene in saturation is also consistent with the larger fraction of Pt in the cluster surface layer. At low coverage, the prismatic global minimum Pt_7 structure shows more di-σ ethylene binding (configurations ii, iv-vi, **Figure 3.3**, **SI Table S8.2.5**) than the single-layer local minimum (only configuration iii). The di-σ bound ethylene often carries more negative total charge ($\Delta Q_{ethylene}$) as compared to its π-bound counterpart at all studied coverages (**Table 3.1** and **SI Tables S8.2.5-7**).

Since at the ethylene exposure temperature (150 K) the prismatic isomer of Pt_7 should dominate, and because of the great computational expense, coverage-dependent ethylene binding was studied only for starting geometries based on this isomer. All possible adsorption sites (atomic, bridging, and hollow) were evaluated for this global minimum Pt_7 isomer, and the six lowest energy geometries were used in further analysis. The lowest energy minimum for one ethylene adsorbed on prismatic Pt_7 was used as the starting geometry for adding the second ethylene, and the resulting two-ethylene minima were taken as starting geometries for adding the third. This is an approximation, since the lowest energy geometry is not necessarily the precursor for higher coverage structures. Thus, there is some uncertainty as to whether the thermal populations in our coverage study include all important structures, however, the results provide at least qualitative insights.

With one or two ethylene molecules adsorbed, the prismatic Pt_7 starting geometry is retained in the optimized structures, but for three adsorbed ethylene molecules, optimization from many of the prismatic starting geometries led to single layer isomers, dominating the thermally accessible ensemble (>78% Boltzmann populations at 450 and 700 K). As noted, even for the first adsorbed ethylene, the single layer structure is lower in energy than the prismatic isomer, but the prismatic isomer is stabilized by a barrier of unknown height. The same is likely true for two ethylene molecules, but clearly the isomerization barrier vanishes when the third ethylene binds. Therefore, one inference from DFT is that adsorption of ethylene will tend to drive transition toward single layer isomers and that such structures are therefore likely to be more important in the experiments than would be suggested by consideration of only adsorbate-free Pt_n geometries. Additionally, we observe that as ethylene coverage increases and cluster geometries flatten, the populations of di-σ ethylene binding geometries, which are precursors to dehydrogenation, also increase from 7.35% to 84.26% at 450 K, i.e. at the peak of D_2 desorption (**Table 3.1**).

Table 3.1. Boltzmann Populations of Adsorbed Ethylene of n = 1..3 Coverage in the di-σ, sp^3 Configuration (Precursor to Dehydrogenation)

Ethylene Coverage	n = 1	n = 2	n = 3
$E_{n\ ethylene,glob}$ (eV)	-1.29	-1.62	-1.73
$\Delta Q_{ethylene,glob}$ (e)	0.00	-0.02	-0.30
$\Sigma P_{450K,sp3}$	7.35%	17.51%	84.26%
$\Sigma P_{700K,sp3}$	14.93%	29.42%	69.22%

A coverage-dependent TPD/R experiment was performed on Pt_7/Al_2O_3 to gain further insight into the energetics and dynamics of ethylene desorption, and the competition between desorption and dehydrogenation. **Figure 3.4** compares C_2D_4 and D_2 desorption from separately prepared Pt_7/alumina samples exposed to 5, 0.1, and ~0.01 L of C_2D_4 at 150 K, otherwise following the same procedure as in **Figure 3.2**. For comparison, C_2D_4 desorption from the cluster-free alumina film is also shown for 5 and 0.1 L C_2D_4 exposures. The figure also gives the

numbers of C_2D_4 and D_2 molecules desorbing *per* Pt atom, calculated by subtracting the desorption from cluster-free alumina, and then integrating.

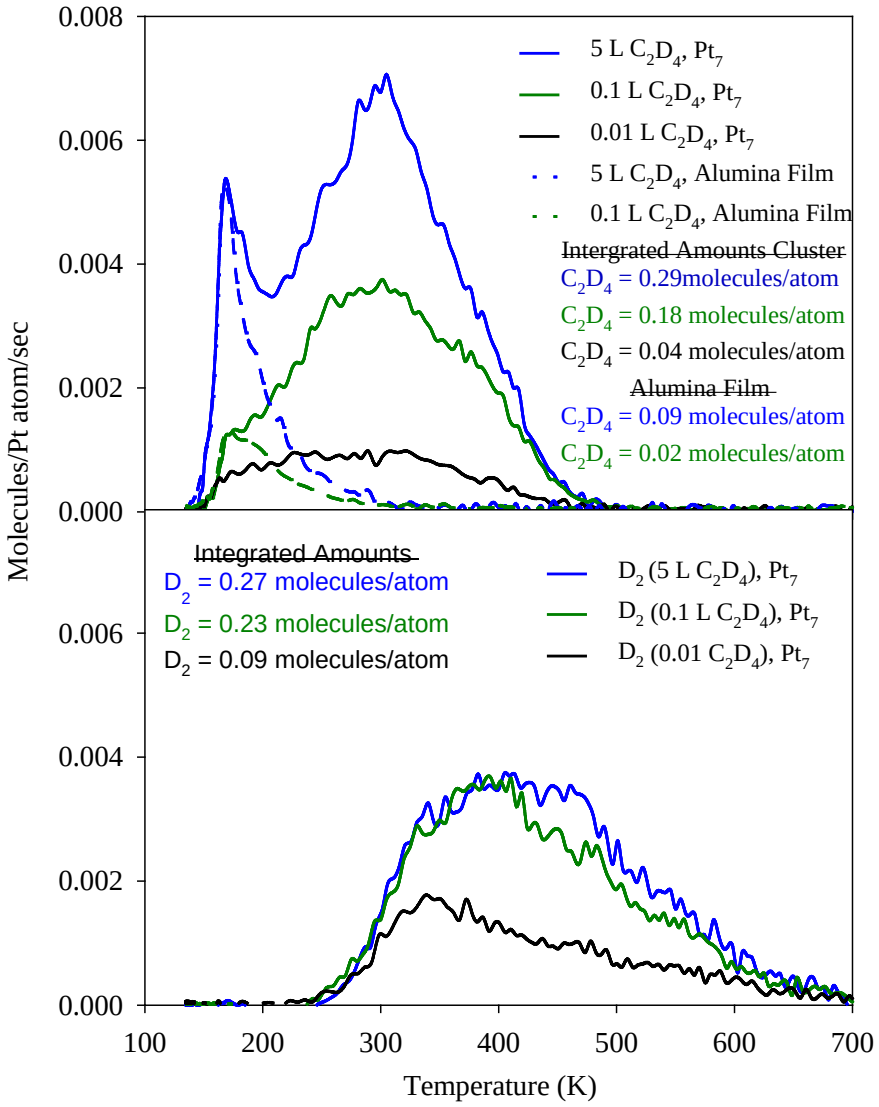

Figure 3.4. Intact C_2D_4 (top) and D_2 (bottom) desorbing from separately prepared Pt_7/alumina samples during the 1st TPD run, after exposing the samples to different amounts of C_2D_4 at 150 K.

For the Pt_7/alumina samples, C_2D_4 desorption clearly is mostly from sites on alumina at the lowest temperatures and from Pt-associated sites at temperatures above ~200 K. The Pt-associated desorption feature is quite broad, which normally would be taken as evidence for a wide distribution of desorption energies, as suggested by the fits to the TPD/R results discussed

above. In that scenario, we would expect desorption to shift to higher temperatures for decreasing coverage, because in sub-saturation coverages, adsorbates should tend to diffuse to, and desorb from the most stable sites available. Furthermore, if C_2D_4 in the strongest di-σ binding sites has the highest probability of decomposing, rather than desorbing intact, we might expect that the branching to D_2 should increase with decreasing coverage, as is observed, from ~32% in the 5 L exposure, to ~52% for the 0.01 L exposure.

The coverage-dependence of the desorption temperatures do not fit this simple scenario, however. The C_2D_4 desorption spectrum is weakly coverage dependent, and if anything, there is less desorption at the highest temperatures for the lowest coverage. Furthermore, while the upper and lower temperature limits for D_2 desorption are independent of initial coverage, the peak of D_2 production shifts to substantially lower temperatures for lower initial C_2D_4 coverage. Given the DFT results showing that the relative stability of different Pt_7 isomers is dependent on C_2D_4 coverage, and that the isomer distribution evolves with temperature, we believe that the measured desorption temperature distributions reflect complex dynamics involving changes in cluster structure as part of the C_2D_4 desorption and decomposition mechanism.

Figure 3.4 also illustrates the importance of substrate-mediated adsorption for highly dispersed clusters. 5 L exposure corresponds to 1.8 x 10^{15} C_2D_4 collisions/cm^2, or ~1.2 collisions/surface atom. If adsorption at Pt sites occurred only in C_2D_4 collisions on Pt_7, reducing the C_2D_4 exposure substantially should substantially reduce the C_2D_4 coverage on Pt_7. Assuming that adsorbed C_2D_4 either desorbs intact or generates two D_2 molecules, and subtracting the contribution alumina sites, the initial C_2D_4 coverage on Pt_7 in the 5 L dose is ~2.7 *per* Pt_7 cluster. For 50 times lower dose, the coverage is ~2.1 C_2D_4/Pt_7, and for 500 times lower exposure, the initial coverage is still ~0.6 molecules/Pt_7.

3.2.3. Routes of Deactivation

From the perspective of the catalytic properties of small Pt_n/alumina, it is important to

understand now the clusters are modified by heating, adsorption, desorption, and dehydrogenation of ethylene. The DFT results suggest that isomerization is likely during the TPD/R cycle, and the second TPD/R runs on each sample (**Figure 3.2**) indicate that irreversible changes also occur. The amount of C_2D_4 desorbing at high temperatures decreased in the second run, with an offsetting increase in desorption at low temperatures. The total amount of C_2D_4 desorbing in the second run was ~0.3 molecules *per* Pt atom for all three samples, which is essentially identical to the amount observed in the first runs for Pt_4 and Pt_8. For Pt_7, however, ~0.3 C_2D_4/Pt atom represents a ~25% drop compared to the first run. As shown above, C_2D_4 adsorbed on the alumina support all desorbs intact at low temperatures, and the results in the first and second TPD/R runs are identical for cluster-free alumina. For Pt_n/alumina it is reasonable to assume that the alumina contribution to the C_2D_4 signal is also identical in the first and second runs, thus implying that C_2D_4 desorption from Pt sites shifted to lower temperatures in the second TPD/R run, i.e., the ethylene-Pt desorption energies substantially decreased. The temperature dependence for D_2 desorption did not differ dramatically between the first and second TPD/R runs, however, the integrated amount of D_2 dropped by ~60-70%. This behavior is what would be expected if the activation energy for C_2D_4 dehydrogenation is unchanged in the second run, so that more of the C_2D_4, which is bound more weakly in the second run, desorbs at temperatures below the onset for decomposition.

In the second TPD/R run, the dependence on deposited cluster size is much weaker than in the first, where Pt_7 stands out. This change could indicate that thermal or adsorbate-induced ripening or sintering generate a size distribution that no longer depends on the deposited size, however, there are other possibilities. DFT suggests that the larger amount, stronger binding, and greater propensity toward dehydrogenation of C_2D_4 on Pt_7, compared to Pt_8 (based on its structural and electronic characteristics), is related to the existence of a larger number of strong di-σ binding sites on Pt_7. If carbon left on the surface by D_2 desorption in the first TPD/R run tends to poison the strong di-σ binding sites, this would reduce both the average

C_2D_4 binding energy in the second TPD/R run, and the amount of D_2 produced, in line with observations. The fact that more D_2 is produced *per* Pt atom in the first TPD/R run for Pt_7 than either Pt_4 or Pt_8, implies additional carbon poisoning for Pt_7 in the second run, tending to bring its binding/reactivity properties more in line with those of Pt_4 and Pt_8.

Several experiments were done to provide additional insight into how TPD/R changes the clusters. CO binds strongly to Pt and weakly to alumina, providing an alternative probe of the effect of different experimental manipulations on the availability of Pt binding sites. **Figure 3.5** compares CO TPD for a set of Pt_7/alumina/Ta(110) samples that were each first exposed to a particular manipulation, and then probed by CO TPD (10 L ^{13}CO exposure at 150 K, heating at 3 K/sec to 700 K). Little CO desorbs from the alumina support, but for as-deposited Pt_7/alumina, strong bimodal CO desorption is observed, with a low temperature component peaking at ~165 K and a broader "high temperature" component peaking at ~520 K. Simply heating Pt_7/alumina to 700K in vacuum results in a ~40% decrease in high temperature CO desorption, and an increase in low temperature desorption. We previously studied CO TPD from Pt_n/alumina/Re(0001) ($2 \leq n \leq 18$),[9] with similar results to the Pt_7/alumina/Ta(110) TPD shown here. We found that the high temperature CO desorption intensity during the first TPD on Pt_n/alumina/Re(0001) increased substantially with increasing cluster size. Therefore, we can conclude that the decrease in high temperature CO desorption following 700 K heating in **Figure 3.5** cannot be explained by thermal sintering or ripening alone. We are not claiming that sintering/ripening are unimportant, but there must be other changes as well. For example, 700 K annealing may cause changes in the as-deposited isomer distribution.

After a single C_2D_4 TPD/R run, there is a 55% decrease in the high temperature CO desorption, and the decrease is ~75% for CO TPD following six C_2D_4 TPD/R runs. Both heating and C_2D_4 TPD/R result in an increase in low temperature CO desorption, but overall, the total amount of CO desorbing decreased by ~25% after 700 K heating, and ~40% and 50%, respectively, for one and six ethylene TPD/R runs. The larger effect of C_2D_4 TPD/R, compared

to 700 K heating, is attributed to carbon left on the surface by D_2 desorption, blocking the Pt binding sites associated with high temperature CO desorption.

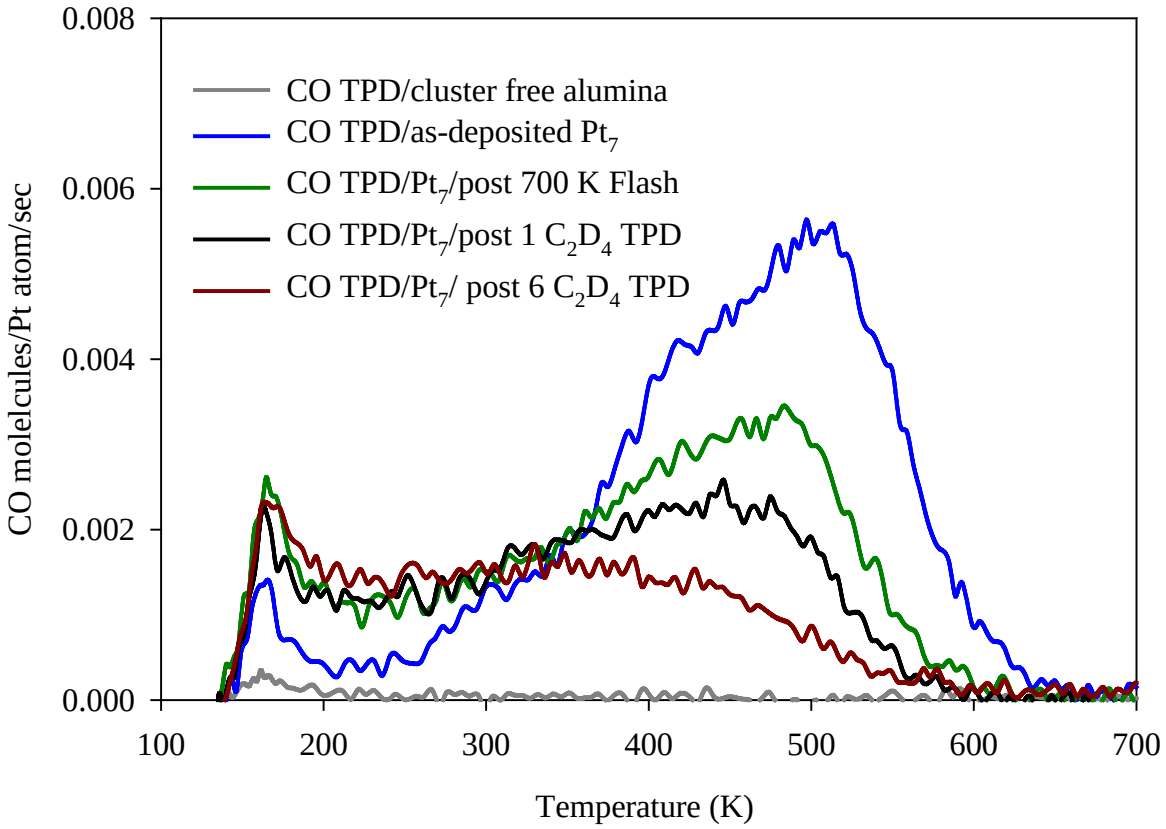

Figure 3.5. CO desorption from a Pt_7/alumina compared with CO desorption from separately prepared Pt_7/alumina samples after a 700 flash, a single C_2D_4 TPD, and 6 consecutive TPD's. All samples were exposed to 10 L of CO at 150 K.

To provide additional insight into how ethylene binds to Pt_n/alumina, and the effects of heating and carbon deposition, we did two types of He^+ ion scattering (ISS) experiments. **Figure 3.6** compares raw ISS data for Pt_7/alumina after a variety of experimental operations. The peaks primarily result from scattering of He^+ from single Pt, O, and Al atoms in the top layer of the sample. He^+ signal from multiple or sub-surface scattering events is strongly attenuated, contributing mostly to the weak background at $E/E_0 \leq 0.6$.[37-38] Small Pt clusters, where most or all of the Pt atoms are in the surface layer, should give large Pt ISS signals, and also cause

some attenuation of ISS signals from the alumina support, although the attenuation should be small because the Pt_n coverage is low. Isomerization or agglomeration of clusters to form multi-layer structures reduces the fraction of Pt in the surface layer, which should appear as a drop in Pt ISS signal. Similarly, adsorbates binding on top of the clusters attenuate the Pt ISS signal, while adsorbates binding on the alumina or around the cluster periphery have little effect on Pt signal, but may attenuate signal from alumina.

In the top frame of **Figure 3.6**, ISS data are compared for the cluster-free alumina film, as-deposited Pt_7/alumina, and Pt_7/alumina that was heated to 700 K in UHV. Note the presence of a small peak at $E/E_0 \approx 0.9$ for cluster-free alumina, attributed to a ~1% concentration of Ta in the surface layer, from diffusion during high temperature alumina growth on the Ta(110) substrate.[39-40] For samples with Pt_n deposited, this Ta signal is presumably still present, underlying the much stronger Pt peak. Because the Ta intensity is so small, we have not attempted to subtract it.

When as-deposited Pt_7/alumina is heated to 700 K, there is a small increase in Pt ISS intensity. As discussed above, TPD shows that the as-deposited clusters are decorated with ~0.5 adventitious CO molecules *per* cluster, and **SI Figure S8.2.6** implies that these CO molecules bind such that they attenuate ISS signal from the Pt clusters. Using the extrapolation procedure illustrated in **SI Figure S8.2.5** and detailed previously,[9, 41-42] we estimate the attenuation to be ~30%, and the star in **Figure 3.6** indicates the estimated value for adsorbate-free Pt_7/alumina. CO desorbs by 700 K (**Figure 3.5**), which should restore the Pt ISS intensity, thus the fact that only a small signal increase occurs, implies that heating also drives morphology changes that offset the expected increase. From the size of the offset, we can rule out formation of large three-dimensional particles, but thermal isomerization from single layer to prismatic isomers or modest ripening of the cluster size distribution are possible.

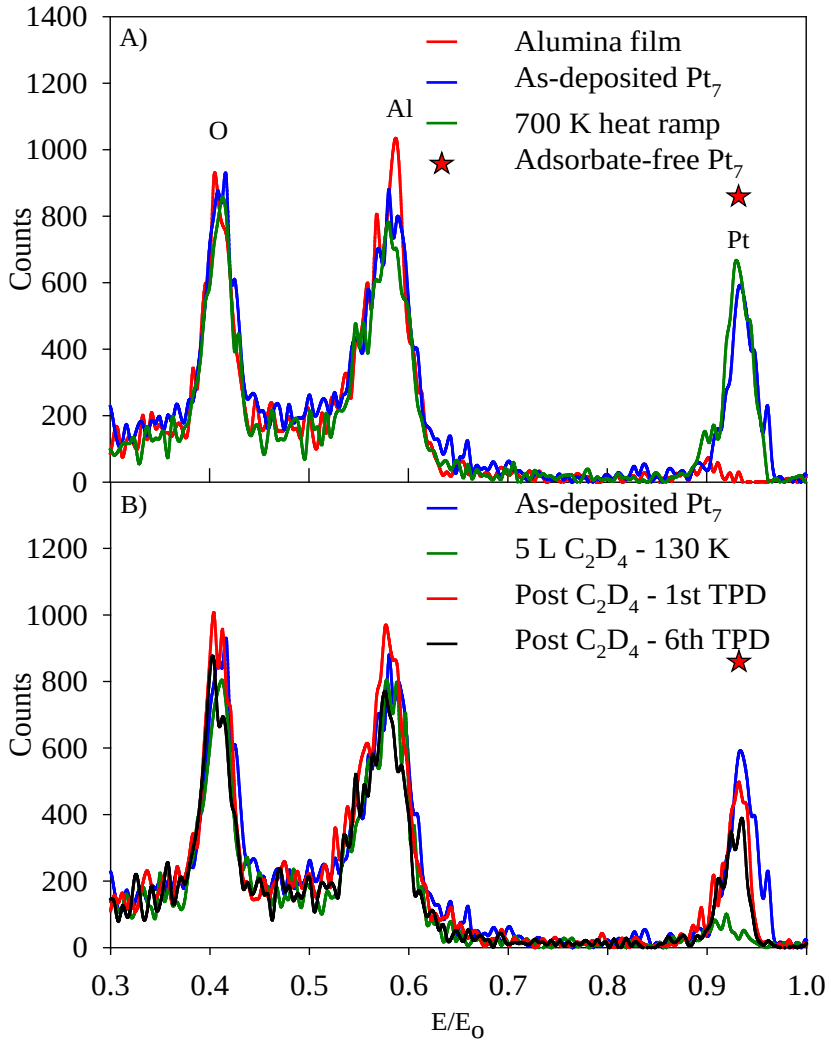

Figure 3.6. Raw ISS spectra for Pt_7/alumina samples (a) after a 700 K flash and measured as-deposited. Extrapolated as-deposited is represented by the star. (b) Raw ISS spectra Pt_7/alumina sample after the sample was exposed to 5 L of C_2D_4 at a 150 K and cooled to 130K, after one C_2D_4 TPD, and after six consecutive C_2D_4 TPDs.

The lower frame of **Figure 3.6** compares the effects of C_2D_4 exposure and TPD/R. One sample was exposed to 5 L of C_2D_4 at 150 K and then probed by ISS while cold, resulting in Pt ISS attenuation by ~90 %, compared to the adsorbate-free limit, demonstrating that C_2D_4 adsorbs in geometries that strongly attenuate He^+ signal from Pt. The Al and O ISS signals are attenuated by much smaller amounts, consistent with the TPD data indicating that little C_2D_4 adsorbs on alumina at this temperature. ISS data are also shown for a Pt_7/alumina sample after

a single C_2D_4 TPD/R run under the conditions of **Figure 3.2**, and for another sample run through 6 consecutive TPD/R runs prior to ISS analysis. After one TPD/R run, the Al and O intensities recover to the pre-exposure values, but the Pt ISS intensity remains ~15 % below the as-deposited value or ~45% below the adsorbate-free limit. This post TPD/R value is ~25% smaller than that measured after 700 K heating, and this additional attenuation is not surprising given that we know that carbon is left on the surface by D_2 desorption (~1.4 C atoms/Pt_7). **SI Figure S8.2.7** give the integrated D_2 desorption signal during 6 sequential C_2D_4 TPD/R runs, allowing us to estimate that a total of ~3.4 C atoms are left behind *per* initially deposited Pt_7. If this carbon remains on top of Pt, it would cause at least a substantial fraction of the ~65 % Pt ISS attenuation observed after 6 TPD/R runs, but the attenuation may also reflects sintering or other changes in the Pt morphology. We also probed the residual carbon by XPS. No C 1s signal was detected after one or two TPD/R runs, but as shown in **SI Figure S8.2.8**, after six runs, C 1s signal was observed, albeit too weak for accurate quantitation.

Temperature-dependent ISS (TD-ISS) provides more detailed information about the nature of the adsorbate binding on Pt_7. TD-ISS is essentially a C_2D_4 thermal desorption experiment, in which a Pt_7/alumina sample was dosed with 5 L of C_2D_4 at 150 K, then characterized by ISS. The sample temperature was then increased in 50 K steps, with ISS measurements at each step. **Figure 3.7** plots the Pt ISS intensities, normalized to the sum of Al and O intensities, as a function of temperature (open circles). The top axis gives the cumulative He^+ exposure to the sample at the time the Pt ISS peak was being measured at each temperature. For comparison, the C_2D_4 and D_2 desorption data from **Figure 3.2** are superimposed, and a horizontal solid line indicates the expected intensity for adsorbate-free Pt_7, estimated as shown in **SI Figure S8.2.6**. Comparing the first point, at 150 K, to the value for adsorbate-free Pt_7/alumina, we see that 5L C_2D_4 exposure at 150 K resulted in attenuation by ~93% - essentially the same attenuation seen in the raw ISS data in **Figure 3.6**. From TPD we know that this initial exposure leads to adsorption of ~2.7 C_2D_4 molecules associated with the

clusters, with some additional C_2D_4 bound on the alumina. The expectation is that as the sample is heated and C_2D_4 desorbs or decomposes, the Pt ISS signal should recover.

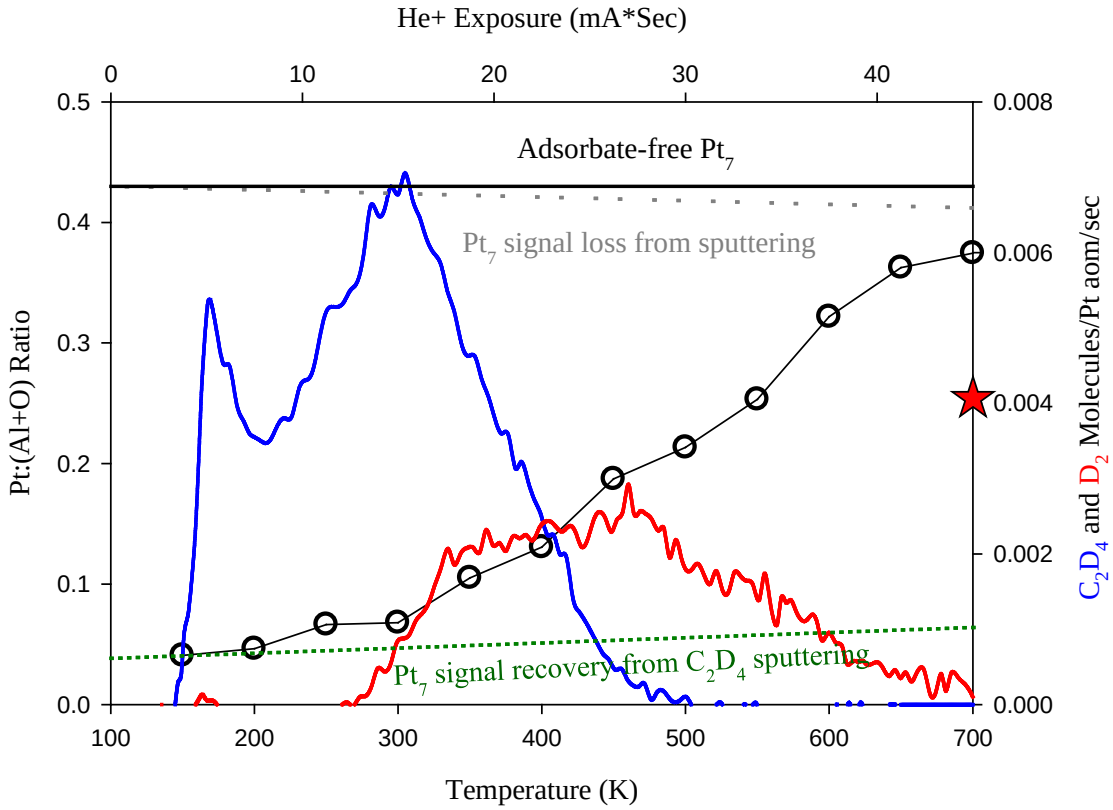

Figure 3.7. Pt/(Al+O) ISS intensity ratios for Pt_7/alumina after exposure to 5 L of C_2D_4 at 150 K, and during a sequence where the sample was heated to the indicated temperatures (black circles). The as-deposited Pt intensity and calibrated rates of Pt recovery from C_2D_4 sputtering, and for loss of Pt signal due to sputtering are represented by dashed lines. The Pt/(Al+O) intensity ratio (red star) measured after completion of a single ethylene TPD cycle.

To interpret the results quantitatively, it is necessary to understand how He^+ sputtering of Pt and C_2D_4 affects the Pt ISS signal. The extrapolation experiment (**SI Figure S8.2.5**) also gives the decay rate of Pt ISS signal as a function of He^+ exposure, and this is plotted in **Figure 3.6** as a grey dashed line labeled "Pt signal loss from sputtering". For C_2D_4-covered Pt_7/alumina, He^+ sputter removal of C_2D_4 will tend to increase the Pt signal, and this rate was measured in an experiment were a sample was dosed with 5 L of C_2D_4 at 150 K, then repeatedly probed by ISS

while held at 150 K (green dotted line labeled “Pt signal recovery by sputtering”). The Pt ISS intensity just after a single TPD/R cycle (**Figure 3.7**) is indicated on the right axis by a red star.

As shown by the superimposed TPD/R data, by 200 K the lowest temperature C_2D_4 component has desorbed, but there is no recovery of Pt ISS signal, beyond that expected from C_2D_4 sputtering. By 400 K, most of the C_2D_4 desorption and ~30% of D_2 desorption should have occurred, i.e., 85% of the initial C_2D_4 should have either desorbed or decomposed, but the Pt signal only recovered to ~30% of the adsorbate-free value. By 550 K ~95% of the total amount of C_2D_4 and D_2 desorption should have occurred, but the Pt ISS signal was still ~ 35% below that expected for adsorbate-free Pt_7/alumina. Note that the intensity at this point is essentially identical to that observed immediately after a TPD/R experiment (red star). The Pt ISS intensity continued to increase, then leveled off above ~600 K, at a value well above that seen after a TPD/R run (red star) but ~10% below the value that would be expected based on the “Pt signal loss from sputtering” trend line.

We interpret the results as follows. The TPD component below 200 K is associated with C_2D_4 bound on alumina (**Figure 3.2**), thus its desorption is not expected to have any effect on the Pt ISS signal, as observed. By 300 K, ~50% of the initial C_2D_4 has desorbed, including a significant fraction of the Pt-associated C_2D_4, but there is only modest recovery of Pt signal, indicating the weakly bound C_2D_4 is in sites where it does not strongly attenuate Pt ISS signal. Only as the more strongly bound C_2D_4 desorbs or decomposes at higher temperatures, does the Pt signal recovery accelerate, indicating that this strongest C_2D_4 binding component is in sites that are efficient at attenuating ISS from Pt_7. TPD/R shows that it is this strongly bound C_2D_4 that is most likely to decompose, generating D_2. Given our 45° angle of incidence and detection along the surface normal, we expect that these sites should be generally on top of the clusters. The fact that Pt ISS recovery only reaches 90% of the adsorbate-free limit is not surprising, because we know that carbon is left on the surface by D_2 desorption. Indeed, the substantially lower Pt ISS signal measured after a TPD/R run (red star), suggests that without

the effect of He^+ sputtering throughout the TD-ISS run, even more decomposition products are left on the cluster surface.

During an earlier study of CO interactions with Pt_n/alumina/Re(0001), we measured, but didn't publish, a TD-ISS study of CO binding for Pt_4/alumina/Re(0001), and this data is shown in **SI Figure S8.2.6** for comparison. The aspect that is relevant to the C_2D_4 results here is that the experiment shows that for CO, the strongest binding sites are also those which cause the largest Pt ISS attenuation, i.e., sites on top of the Pt clusters. A similar conclusion was reached in TD-ISS studies of CO on Pd_n/TiO_2[41] and Pd_n/alumina.

Finally, DFT was also used to examine carbon atom binding to Pt_7 and Pt_8 to determine the most stable binding geometries, and also to see if the propensity for coking has a role in the observed efficiency of dehydrogenation on these clusters. Shaikhutdinov, *et al.* noted that in alumina-supported Pd catalysts, carbon deposits began to form at circa 550 K from di-σ bound ethylene.[24] As a first approach to understanding coking, we analyzed C-sticking energetics for isomers of deposited Pt clusters whose Boltzmann populations sum to >99% at 700 K. By summing the C-sticking energies for the Boltzmann-weighed populations' for Pt_7 and Pt_8 (i.e., $\Sigma P\ E_C$**),** we obtain an estimate of the coking susceptibility of the isomer ensemble for each cluster size. Higher affinity to C should also correlate with a lower barrier to the dehydrogenation vs. desorption.

Pure Pt clusters succumb to coking at higher temperatures due to the increasing population of isomers with very little resistance to carbon deposits (**Figure 3.8**). For Pt_7, $\Sigma P\ E_C$ decreases with increasing temperature from -7.30 eV at 450 K to -7.38 eV at 700 K. For Pt_8, $\Sigma P\ E_C$ remains high at > -8.0 eV (see **Table 3.2** for details). This suggests that Pt_8 should undergo coking more readily. The electrophilic C pulls electrons from the Pt clusters, resulting in a ΔQ_C of -0.40 to -0.56 eV (**SI Figures S8.2.14-15**). C preferentially adsorbs on a hollow site with 3-4 Pt-C bonds and prefers the more electron-rich isomers of Pt_7 (**Figure 3.1**, Isomers II-IV) and Pt_8 (**Figure 3.1**, Isomers I-IV). We note that catalyst deactivation is a complicated process that may

involve the build-up of the C-rich deposits, cluster ripening, and more dramatic restructuring, and it is not fully captured by theory. Experimentally, it is clear that Pt_7 deactivates more strongly after the first TPD run.

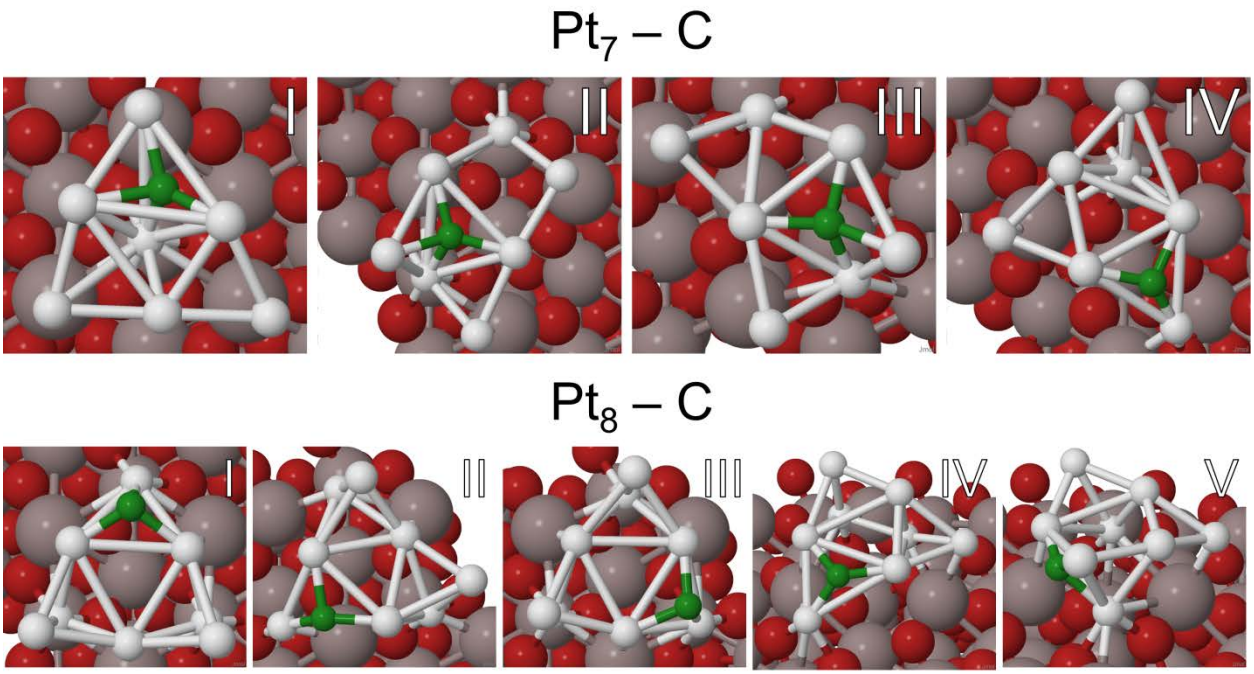

Figure 3.8. First Order Approximation of Coking on Pt_7, Pt_8: lowest-energy structures for a single C atom adsorbed on these clusters.

Table 3.2. Adsorbed isomers with C

Cluster	Isomer	E_C (eV)	$\Sigma P_{450K} E_C$ (eV)	$\Sigma P_{700K} E_C$ (eV)
Pt_7-C	I	-7.05	-7.30	-7.38
	II	-8.03		
	III	-7.70		
	IV	-7.61		
Pt_8-C	I	-8.17	-8.16	-8.12
	II	-7.60		
	III	-8.36		
	IV	-7.90		
	V	-7.27		

3.3. CONCLUSIONS

We reported on ethylene dehydrogenation on size-selected, alumina-deposited sub-nano Pt clusters, accessed via combination of experiment and theory. Remarkably, deposited Pt_7 is found to be significantly more active than deposited Pt_8 and Pt_4, which in turn have

comparable activities. Pt_7 also deactivates more easily through a number of potential ways including coking and ripening. Throughout this study, we have found that understanding many aspects of the experimental results requires consideration of the accessible ensemble of cluster isomers and how this evolves with C_2D_4 coverage and temperature. For example, the higher C_2D_4 binding affinity and dehydrogenation branching for Pt_7, as compared to Pt_8, can be recovered only if multiple cluster minima are considered. Furthermore, the importance of single-layer geometries becomes obvious only after realistic coverage is included, because C_2D_4 binding drives a transition to single layer isomers where binding is stronger and more likely to result in dehydrogenation. In addition, pronounced differential affinity for C binding is seen only in the ensemble. These results call for a change in paradigm when sub-nano cluster catalysts are characterized computationally, tracking isomer distributions, with and without the adsorbate(s) of interest.

3.4. METHODOLOGY

3.4.1. Experimental Section

The experiments were performed using a cluster deposition/surface analysis instrument described previously,[41, 43] which allows *in situ* sample preparation and characterization. Briefly, the instrument consists of a laser vaporization cluster ion source that feeds into a mass-selecting ion deposition beamline that terminates in an ultrahigh vacuum (UHV) chamber (base pressure ~ 1.5×10^{-10} Torr). The main UHV chamber is equipped for sample cleaning and annealing, and houses a differentially pumped mass spectrometer for temperature programmed desorption/reaction studies (TPD/TPR), and hardware for sample characterization by x-ray photoelectron spectroscopy (XPS) and low energy ion scattering spectroscopy (ISS).

The model catalysts supports were prepared alumina films grown on a 7×7 mm Ta(110) single crystal (Princeton Scientific Corporation), which was spot welded to tantalum heating wires, which were attached to a liquid-nitrogen cooled cryostat mounted at the end of a manipulator. The sample could be cooled to ~120 K and resistively heated to ~ 1200 K. A

filament mounted directly behind the sample allowed heating by electron bombardment to temperatures greater than 2100 K. Sample temperature was monitored by a type C thermocouple spot welded to the back side of the crystal. Because type C thermocouples have low output at temperatures below 300 K, the temperature scale was calibrated by temporarily attaching an additional type K thermocouple, with the result that the two thermocouples agreed to within 3 K over the 120 – 1000 K range where type K can be used.

Alumina thin films were grown using procedures adapted from work of the Goodman[44-46] and Madey[47-48] groups. Aluminum was evaporated from a crucible mounted normal to the Ta(110) surface in 5×10^{-6} Torr $^{16}O_2$ background pressure, while holding the sample temperature at 970 K. Film thicknesses were determined for each sample from the Al 2s and Ta 4d XPS intensities, and for these studies the growth rate was maintained at ~ 2 Å/min. As discussed by Chen and Goodman, thin (~1.5 nm) alumina films grown on Ta(110) show slightly distorted hexagonal symmetry attributed to either the (0001) or (111) face of α-alumina.[49] We studied the effects of alumina thickness on the core and valence electronic properties of alumina grown on both Ta(110)[39] and Re(0001),[40] and on the CO oxidation activity of Pd_n clusters supported on alumina/Ta and alumina/Re. Because we found that properties became thickness-independent only above ~3 nm, we have used 3 – 6 nm thick films in the present study. Note that all experiments were carried out on freshly prepared samples, to avoid issues of sample contamination or damage.

Model catalyst preparation began by cooling the cryostat and sample holder until the surface temperature reached 130 K, then flashing it to ~2100 K for 5 min to remove any contaminants (including the previous alumina film) and annealing the crystal. XPS and ISS of the surface after this heat treatment showed no contamination, with the exception of sub-monolayer amounts of surface oxygen. The sample was then lowered into a small UHV-compatible antechamber, where it was isolated from the main chamber by a triple differentially

pumped seal to the cryostat. The antechamber was then flooded with 5 x 10^{-6} Torr of O_2, and the alumina film was grown.

Following XPS characterization of the alumina film, the sample was flashed from ~120 to 800 K to desorb any adventitious adsorbates that might have adsorbed during XPS. In order to minimize exposure of the deposited clusters to background gases, deposition of mass-selected Pt_n (n=4,7,8) clusters was done as the sample cooled back to 120 K, beginning when the sample reached 300 K. During deposition, the sample was positioned directly behind a 2 mm in diameter exposure mask, which defined the size of the cluster spot on surface. The Pt_n coverage was monitored via the neutralization current of the soft landed (~ 1eV/atom) clusters on the support, and deposition was terminated for all samples such that they all had identical Pt loading of 1.5 ×10^{14} atoms/cm^2 (~0.1 ML), differing only in the size of clusters deposited. Deposition took 5 to 15 minutes.

For TPD/R measurements, a differentially pumped mass spectrometer (UTI 100 C with Extrel electronics) was used, viewing the main chamber through the ~2.5 mm diameter aperture in the tip of a skimmer cone. The skimmer cone is surrounded by four 6 mm diameter dosing tubes that point at the sample position, and can be connected to either continuous or pulsed valves. For dosing, the sample was positioned with the cluster spot centered on the skimmer aperture, with a 2 mm separation to allow line of site from the dosing tubes to the cluster area. Calibration experiments show that the gas exposure to the cluster spot is ten times greater than the exposure to the chamber walls. For ethylene TPD/R experiments the samples were exposed to 5 L of C_2D_4 at 150 K sample temperature, chosen to minimize adsorption on the alumina support. The sample was then moved to 0.5 mm distance from the skimmer aperture, cooled to 135 K, then ramped to 700 K at 3 K/sec, while monitoring masses of interest desorbing from the surface. To examine the effects of heating and adsorbate exposure on the clusters, the TPD/R experiment (with fresh ethylene exposure) was repeated multiple times on each sample. Select experiments were done under identical conditions, but with C_2D_4 exposures of 0.1 L and 0.01 L.

Because CO binds strongly to Pt_n, but not to alumina, we also did ^{13}CO TPD experiments to investigate the effects of heating and ethylene decomposition on the availability of Pt binding sites. These experiments were carried out by exposing samples to 10 L of $^{13}C^{16}O$ at 150 K, and then ramping the temperature from 135 K to 700 K at 3 K/sec, while monitoring desorption of ^{13}CO and other masses of interest. Because of substrate-mediated adsorption,[38] highly dispersed Pt clusters are also efficient at collecting adventitious CO, present in the chamber background at ~5 x 10^{-11} Torr. After correcting the mass 28 TPD signal for C_2D_4 cracking in the ion source, the amount of CO adsorbed onto the clusters was found to be ~0.5 CO molecules *per* cluster for Pt_4, Pt_7 and Pt_8, i.e., approximately half of the clusters have one CO molecule adsorbed, desorbing above 500 K. This adventitious signal is independent of whether the sample was dosed with C_2D_4, i.e., C_2D_4 is not able to displace CO from the clusters. The amount of adventitious CO desorbing from a Pt-free alumina film sample is negligible.

To convert the ion signals measured during TPD/R to absolute numbers of molecules desorbing from the surface, we calibrated the mass spectrometer sensitivity in several ways.[9, 50] Several times during the course of the experiments, we checked the calibration of C_2D_4 and other gasses of interest by filling the main UHV chamber with those gases to a measured pressure (correcting for ionization gauge sensitivity), while measuring the resulting ion signals. This results in a well-known flux of molecules effusing through the 2.5 mm diameter skimmer cone aperture into the mass spectrometer ion source (creating a known number density), allowing us to calculate the calibration factor for each gas. To check for possible changes in electron multiplier gain, this calibration was done daily for argon gas. The accuracy of this calibration approach was checked against calibrations based on desorption of saturated CO layers of known coverage from Pd(111) or Ni(110).[41] We estimate that the calibration should be accurate to ± 30%, mostly because of uncertainties in the angular distributions for desorption from clusters and the ionization efficiency vs. angle.

Low energy ion scattering spectroscopy (ISS) was used to observe the effects of cluster size, adsorbate binding, and TPD/R on the fraction of Pt atoms in the surface layer. ISS was done by loosely focusing a beam of 1 keV He^+ onto the sample at 45° angle of incidence, with an energy of 1 keV, onto the sample and measuring the energy of He^+ scattered along the surface normal. Peaks in the resulting energy spectrum are due to scattering of He^+ from single atoms in the sample surface layer, identifying the masses of those atoms. Multiple scattering or subsurface scattering events contribute to a broad background, which is weak due to low ion survival probability in such trajectories.[37] Because ISS is not a non-destructive technique, it was either done on separately prepared samples, or on samples at the end of experimental sequences.

3.4.2. Computational

Because the alumina film used in the experiments is structurally similar to α-alumina(0001),[49] all calculations were done for this surface, and the calculations focused on Pt_7 and Pt_8, because these showed interesting differences in the experiments. Plane wave density functional theory (PW-DFT) calculations of both gas-phase and adsorbed Pt_7 and Pt_8 were performed using Vienna Ab initio Simulation Package (VASP)[51-54] with projector augmented wave potentials [55] and the PBE[56] functional. Bulk calculations were performed with a 8 × 8 × 3 Monkhorst–Pack k-point grid with large kinetic energy cutoffs of 520.0 eV and a stringent SCF (geometric) convergence criteria of 10^{-6} (10^{-5}) eV, resulting in an optimized lattice constant of *a* = 4.807 Å and *c* = 13.126 Å for α-Al_2O_3 (0001), a slight increase as compared to experiment.[57-58] This over-estimation is typical of GGA functionals and corresponds to <0.1 Å increase in lattice constants. The α-alumina slab was modeled as a 3 x 3 unit cell with a vacuum gap of 15 Å and the bottom half of the slab kept fixed. For calculations presented in this paper, large kinetic energy cutoffs of 400.0 eV and convergence criteria of 10^{-5} (10^{-6}) eV for geometric (electronic) relaxations were employed. Only the most thermodynamically stable, Al-terminated surface was explored with an inward relaxation of 89.7% of the surface Al, O layers. Reproducing

experimental results of -51% to -63% relaxation would require hydroxylation of the surface and introduce even more permutations of adsorbed cluster configurations.[59-60] Thus, this is beyond the scope of the current study.

Adsorbed structures were formed from the deposition of the lowest 5-6 gas phase structures under PBE levels of theory *per manum* with a thorough sampling of cluster faces to possible binding sites. Gas phase structures of Pt_8 were found with the Adaptive Force Field Coalescence Kick (AFFCK)[61], an adaptive global minimum and local minima search based on the Coalescence Kick (CK)[62]. For Pt_7, structures from a study by Tian, et. al. were further optimized under VASP/PBE levels of theory, resulting in a new structure (Isomer II in **SI Figure S8.2.9**, **SI Tables S8.2.1-2**).[63] A CK search also uncovered a new configuration, Isomer III (see **SI Figure S8.2.9, Table S8.2.2**). Note that the order of clusters composed of 7 or more atoms will often be DFT method dependent.[61] This is further discussed in detail in the SI utilizing the TURBOMOLE V6.6 program with def2-TZVP basis and both pure (hybrid) versions of the functionals, PBE (PBE0) and TPSS (TPSSh), respectively.

The relevant equations regarding formation (E_{form}), adsorption (E_{ads}), and reagent (E_{reag}) energies may be found in the SI and follow the conventions presented in previous studies.[64-65] The SI also includes the relevant equations utilized for statistical and bonding analysis such as the Boltzmann probability for *i*-th configuration (P_i) and the Gibbs' entropy (S_G). The Gibbs' entropy (S_G) allows us to estimate at a specific temperature T the entropic contribution (TS_G) to the Helmholtz free energy ($F = U - TS_G$). In order to evaluate the ensemble effects of local minima at Pt_n, the summation of the Boltzmann-weighted adsorption energies ($\Sigma P_T E_{ads} = \sum_i P_{i,T} E_{i,ads}$) and carbon-sticking energies at a temperature T were calculated ($\Sigma P_T E_C = \sum_i P_{i,T} E_{i,C}$). For the coverage study of ethylene, the calculated adsorption of ethylene took on the forms:

$$E_{1\ ethylene} = E_{1\ ethylene+Pt7ads} - E_{1\ ethylene,gas} - E_{Pt7ads}$$

$$E_{2\ ethylene} = E_{2\ ethylene+glob,Pt7ads} - E_{1\ ethylene+glob,Pt7ads} - E_{1\ ethylene,gas}$$

$$E_{3\ ethylene} = E_{3\ ethylene+glob,Pt7ads} - E_{2\ ethylene+glob,Pt7ads} - E_{1\ ethylene,gas}.$$

Details of computational methods, isomers of gas phase and deposited clusters, clusters with 1-3 adsorbed ethylene molecules, and C with charges, populations, energies, and other properties are given in the **SI Figures S8.2.9-15**, **Tables S8.2.1-7**.

3.5. REFERENCES

1 Kaden, W. E.; Wu, T.; Kunkel, W. A.; Anderson, S. L., Electronic Structure Controls Reactivity of Size-Selected Pd Clusters Adsorbed on Tio_2 Surfaces. *Science* **2009**, *326*, 826-9.

2 Vajda, S.; Pellin, M. J.; Greeley, J. P.; Marshall, C. L.; Curtiss, L. A.; Ballentine, G. A.; Elam, J. W.; Catillon-Mucherie, S.; Redfern, P. C.; Mehmood, F.; Zapol, P., Subnanometre Platinum Clusters as Highly Active and Selective Catalysts for the Oxidative Dehydrogenation of Propane. *Nat. Mater.* **2009**, *8*, 213-216.

3 Lee, S.; Molina Luis, M.; Lopez Maria, J.; Alonso Julio, A.; Hammer, B.; Lee, B.; Seifert, S.; Winans Randall, E.; Elam Jeffrey, W.; Pellin Michael, J.; Vajda, S., Selective Propene Epoxidation on Immobilized Au(6-10) Clusters: The Effect of Hydrogen and Water on Activity and Selectivity. *Angew Chem Int Ed Engl* **2009**, *48*, 1467-71.

4 Kwon, G.; Ferguson, G. A.; Heard, C. J.; Tyo, E. C.; Yin, C.; DeBartolo, J.; Seifert, S.; Winans, R. E.; Kropf, A. J.; Greeley, J.; Johnston, R. L.; Curtiss, L. A.; Pellin, M. J.; Vajda, S., Size-Dependent Subnanometer Pd Cluster (Pd_4, Pd_6 and Pd_{17}) Water Oxidation Electrocatalysis. *ACS Nano* **2013**, *7*, 5808-5817.

5 Campbell, C. T.; Campbell, J.; Dalton, P.; Henn, F.; Rodriguez, J.; Seimanides, S., Probing Ensemble Effects in Surface Reactions. 1. Site-Size Requirements for the Dehydrogenation of Cyclic Hydrocarbons on Platinum (111) Revealed by Bismuth Site Blocking. . *J. Phys. Chem.* **1989**, *93*, 806-814.

6 Pettiette-Hall, C. L.; Land, D. P.; McIver Jr, R. T.; Hemminger, J. C., Identification of Multiple Steps in the Dehydrogenation of Cyclic C6 Hydrocarbons to Benzene on Platinum (111). . *J. Am. Chem. Soc.* **1991**, *113*, 2755-2756.

7 Hansen, T. W.; DeLaRiva, A. T.; Challa, S. R.; Datye, A. K., Sintering of Catalytic Nanoparticles: Particle Migration or Ostwald Ripening? *Acc. Chem. Res.* **2013**, *46*, 1720-1730.

8 Brizuela, G.; Hoffmann, R., C_5h_5 on a Pt (111) Surface: Electronic Structure and Bonding. . *J. Phys. Chem. A* **1998**, *102*, 9618-9624.

9 Roberts, F. S.; Kane, M. D.; Baxter, E. T.; Anderson, S. L., Oxygen Activation and Co Oxidation over Size-Selected Ptn/Alumina/Re(0001) Model Catalysts: Correlations with Valence Electronic Structure, Physical Structure, and Binding Sites. *Phys. Chem. Chem. Phys.* **2014**, *16*, 26443 – 26457.

10 Isomura, N.; Wu, X.; Hirata, H.; Watanabe, Y., Cluster Size Dependence of Pt Core-Level Shifts for Mass-Selected Pt Clusters on Tio2(110) Surfaces. *J. Vac. Sci. Technol., A* **2010**, *28*, 1141-1144.

11 Watanabe, Y.; Wu, X.; Hirata, H.; Isomura, N., Size-Dependent Catalytic Activity and Geometries of Size-Selected Pt Clusters on Tio2(110) Surfaces. *Catal. Sci. Technol.* **2011**, *1*, 1490-1495.

12 Zhai, H.; Alexandrova, A. N., Ensemble-Average Representation of Pt Clusters in Conditions of Catalysis Accessed through Gpu Accelerated Deep Neural Network Fitting Global Optimization. *J. Chem. Theor. Comput.* **2016**, *12*, 6213–6226.

13 Zhai, H.; Alexandrova, A. N., Fluxionality of Catalytic Clusters: When It Matters and How to Address It. *ACS Catal* **2017**, *7*, DOI: 10.1021/acscatal.6b03243.

14 Gao, M.; Lyalin, A.; Takagi, M.; Maeda, S.; Taketsugu, T., Reactivity of Gold Clusters in the Regime of Structural Fluxionality. *J. Phys. Chem. C* **2015**, *119*, 11120-11130.

15 Steininger, H.; Ibach, H.; Lehwald, S., Surface Reactions of Ethylene and Oxygen on Pt(111). *Surface Science* **1982**, *117*, 685-698.

16 Ibach, H.; Lehwald, S., Identification of Surface Radicals by Vibration Spectroscopy: Reactions of C2h2, C2h4, and H2 on Pt (111). *Journal of Vacuum Science & Technology* **1978**, *15*, 407-415.

17 Hatzikos, G.; Masel, R., Structure Sensitivity of Ethylene Adsorption on Pt (100): Evidence for Vinylidene Formation on (1× 1) Pt (100). *Surface science* **1987**, *185*, 479-494.

18 Yagasaki, E.; Backman, A. L.; Masel, R. I., The Adsorption and Decomposition of Ethylene on Pt(210), (1 · 1)Pt(110) and (2 · 1)Pt(110). *Vacuum* **1990**, *41*, 57-59.

19 Janssens, T. V. W.; Zaera, F., The Role of Hydrogen-Deuterium Exchange Reactions in the Conversion of Ethylene to Ethylidyne on Pt(111). *Surface Science* **1995**, *344*, 77-84.

20 Kesmodel, L.; Dubois, L.; Somorjai, G., Dynamical Leed Study of C 2 H 2 and C 2 H 4 Chemisorption on Pt (111): Evidence for the Ethylidyne Group. *Chemical Physics Letters* **1978**, *56*, 267-271.

21 Starke, U.; Barbieri, A.; Materer, N.; Van Hove, M.; Somorjai, G., Ethylidyne on Pt (111): Determination of Adsorption Site, Substrate Relaxation and Coverage by Automated Tensor Leed. *Surface science* **1993**, *286*, 1-14.

22 Neurock, M.; van Santen, R. A., A First Principles Analysis of Ch Bond Formation in Ethylene Hydrogenation. *The Journal of Physical Chemistry B* **2000**, *104*, 11127-11145.

23 Anderson, A. B.; Choe, S., Ethylene Hydrogenation Mechanism on the Platinum (111) Surface: Theoretical Determination. *The Journal of Physical Chemistry* **1989**, *93*, 6145-6149.

24 Shaikhutdinov, S. K.; Frank, M.; Bäumer, M.; Jackson, S. D.; Oldman, R. J.; Hemminger, J. C.; Freund, H.-J., Effect of Carbon Deposits on Reactivity of Supported Pd Model Catalysts. *Catalysis letters* **2002**, *80*, 115-122.

25 Mohsin, S. B.; Trenary, M.; Robota, H. J., Infrared Identification of the Low-Temperature Forms of Ethylene Adsorbed on Platinum/Alumina. *The Journal of Physical Chemistry* **1988**, *92*, 5229-5233.

26 Perry, D. A.; Hemminger, J. C., Σ-Bond Metathesis on a Surface: Dehydrogenation of Cyclohexane on Hydrogen-Saturated Pt (111). *Journal of the American Chemical Society* **2000**, *122*, 8079-8080.

27 Carlsson, A.; Madix, R., The Dynamics of Ethylene Adsorption on Pt (111) into Di-Σ and Π-Bonded States. *The Journal of Chemical Physics* **2001**, *115*, 8074-8082.

28 Paz-Borbón, L. O.; Hellman, A.; Thomas, J. M.; Grönbeck, H., Efficient Hydrogenation over Single-Site Bimetallic Rusn Clusters. *Physical Chemistry Chemical Physics* **2013**, *15*, 9694-9700.

29 Stöhr, J.; Sette, F.; Johnson, A. L., Near-Edge X-Ray-Absorption Fine-Structure Studies of Chemisorbed Hydrocarbons: Bond Lengths with a Ruler. *Physical review letters* **1984**, *53*, 1684.

30 Proch, S.; Wirth, M.; White, H. S.; Anderson, S. L., Strong Effects of Cluster Size and Air Exposure on Oxygen Reduction and Carbon Oxidation Electrocatalysis by Size-Selected Pt_n (N ≤ 11) on Glassy Carbon Electrodes. *J. Am. Chem. Soc.* **2013**, *135*, 3073−3086.

31 von Weber, A.; Baxter, E. T.; Proch, S.; Kane, M. D.; Rosenfelder, M.; White, H. S.; Anderson, S. L., Size-Dependent Electronic Structure Controls Activity for Ethanol Electro-Oxidation at Pt_n/Indium Tin Oxide (N = 1 to 14). *Phys. Chem. Chem. Phys.* **2015**, *17*, 17601-17610.

32 Chusuei, C. C.; Lai, X.; Luo, K.; Goodman, D. W., Modeling Heterogeneous Catalysts: Metal Clusters on Planar Oxide Supports. *Top. Catal.* **2001**, *14*, 71-83.

33 Bagus, P. S., Chemical Information from Xps Binding Energy Shifts: A Unified View. *Abstracts of Papers, 225th ACS National Meeting, New Orleans, LA, United States, March 23-27, 2003* **2003**, COLL-446.

34 Dai, Y.; Gorey, T. J.; Anderson, S. L.; Lee, S.; Lee, S.; Seifert, S.; Winans, R. E., Inherent Size Effects on Xanes of Nanometer Metal Clusters: Size-Selected Platinum Clusters on Silica. *J. Phys. Chem. C* **2016**, *(submitted)*.

35 Kaden, W. E.; Büchner, C.; Lichtenstein, L.; Stuckenholz, S.; Ringleb, F.; Heyde, M.; Sterrer, M.; Freund, H.-J.; Giordano, L.; Pacchioni, G.; Nelin, C. J.; Bagus, P. S., Understanding Surface Core-Level Shifts Using the Auger Parameter; a Study of Pd Atoms Adsorbed on Sio2 Ultra-Thin Films. *Phys. Rev. B* **2014**, *89* 115436 1-8.

36 Roberts, F. S.; Anderson, S. L.; Reber, A. C.; Khanna, S. N., Initial and Final State Effects in the Ultraviolet and X-Ray Photoelectron Spectroscopy (Ups and Xps) of Size-Selected Pdn Clusters Supported on TiO_2(110). *J. Phys. Chem. C* **2015**, *119*, 6033-6046.

37 Rabalais, J. W., *Principles and Applications of Ion Scattering Spectrometry : Surface Chemical and Structural Analysis*; Wiley: New York, 2003, p 336.

38 Aizawa, M.; Lee, S.; Anderson, S. L., Deposition Dynamics and Chemical Properties of Size-Selected Ir Clusters on TiO_2. *Surf. Sci.* **2003**, *542*, 253-275.

39 Kane, M. D.; Roberts, F. S.; Anderson, S. L., Alumina Support and Pd_n Cluster Size Effects on Activity of Pd_n for Catalytic Oxidation of Co. *Faraday Discuss.* **2013**, *162*, 323 - 340.

40 Kane, M. D.; Roberts, F. S.; Anderson, S. L., Effects of Alumina Thickness on Co Oxidation Activity over Pd_{20}/Alumina/Re(0001): Correlated Effects of Alumina Electronic Properties and Pd_{20} Geometry on Activity. *J. Phys. Chem. C* **2015**, *119*, 1359–1375.

41 Kaden, W. E.; Kunkel, W. A.; Roberts, F. S.; Kane, M.; Anderson, S. L., Co Adsorption and Desorption on Size-Selected Pdn/Tio2(110) Model Catalysts: Size Dependence of Binding Sites and Energies, and Support-Mediated Adsorption. *J. Chem. Phys.* **2012**, *136*, 204705/1-204705/12.

42 Kaden, W. E.; Kunkel, W. A.; Anderson, S. L., Cluster Size Effects on Sintering, Co Adsorption, and Implantation in Ir/Sio_2. *J. Chem. Phys.* **2009**, *131*, 114701, 1-15.

43 Kane, M. D.; Roberts, F. S.; Anderson, S. L., Mass-Selected Supported Cluster Catalysts: Size Effects on Co Oxidation Activity, Electronic Structure, and Thermal Stability of Pd_n/Alumina (N ≤ 30) Model Catalysts. *Int. J. Mass Spectrom.* **2014**, *370*, 1-15.

44 Chen, P. J.; Goodman, D. W., Epitaxial Growth of Ultrathin Al_2o_3 Films on Ta(110). *Surf. Sci.* **1994**, *312*, L767-L773.

45 Street, S. C.; Goodman, D. W., Chemical and Spectroscopic Studies of Ultrathin Oxide Films. *Chem. Phys. Solid Surf.* **1997**, *8*, 375-406.

46 Lai, X.; Chusuei, C. C.; Luo, K.; Guo, Q.; Goodman, D. W., Imaging Ultrathin Al2o3 Films with Scanning Tunneling Microscopy. *Chem. Phys. Lett.* **2000**, *330*, 226-230.

47 Wu, Y.; Garfunkel, E.; Madey, T. E., Growth of Ultrathin Crystalline Al2o3 Films on Ru(0001) and Re(0001) Surfaces. *J. Vac. Sci. Technol., A* **1996**, *14*, 2554-2563.

48 Wu, Y.; Garfunkel, E.; Madey, T. E., Growth and Oxidation of Ultra-Thin Al Films on the Re(0001) Surface. *Surf. Sci.* **1996**, *365*, 337-352.

49 Chen, M. S.; Goodman, D. W., Ultrathin, Ordered Oxide Films on Metal Surfaces. *J. Phys.: Condens. Matter* **2008**, *20*, 264013 (11 pages).

50 Kane, M. D.; Roberts, F. S.; Anderson, S. L., Mass-Selected Supported Cluster Catalysts: Size Effects on Co Oxidation Activity, Electronic Structure, and Thermal Stability of Pd_n/Alumina (N ≤ 30) Model Catalysts. *Int. J. Mass Spectrom.* **2014**, *370*, 1-15.

51 Kresse, G.; Furthmüller, J., Efficiency of Ab-Initio Total Energy Calculations for Metals and Semiconductors Using a Plane-Wave Basis Set. *Computational Materials Science* **1996**, *6*, 15-50.

52 Kresse, G.; Furthmüller, J., Efficient Iterative Schemes for Ab Initio Total-Energy Calculations Using a Plane-Wave Basis Set. *Physical review B* **1996**, *54*, 11169.

53 Kresse, G.; Hafner, J., Ab Initio Molecular Dynamics for Liquid Metals. *Physical Review B* **1993**, *47*, 558.

54 Kresse, G.; Hafner, J., Ab Initio Molecular-Dynamics Simulation of the Liquid-Metal–Amorphous-Semiconductor Transition in Germanium. *Physical Review B* **1994**, *49*, 14251.

55 Kresse, G.; Joubert, D., From Ultrasoft Pseudopotentials to the Projector Augmented-Wave Method. *Physical Review B* **1999**, *59*, 1758.

56 Perdew, J. P.; Burke, K.; Ernzerhof, M., Generalized Gradient Approximation Made Simple. *Physical review letters* **1996**, *77*, 3865.

57 Bourdillon, A.; El-Mashri, S.; Forty, A., Application of Tem Extended Electron Energy Loss Fine Structure to the Study of Aluminium Oxide Films. *Philosophical Magazine A* **1984**, *49*, 341-352.

58 Levin, I.; Brandon, D., Metastable Alumina Polymorphs: Crystal Structures and Transition Sequences. *Journal of the American Ceramic Society* **1998**, *81*, 1995-2012.

59 Ahn, J.; Rabalais, J., Composition and Structure of the Al 2 O 3 {0001}-(1× 1) Surface. *Surface Science* **1997**, *388*, 121-131.

60 Wang, X.-G.; Chaka, A.; Scheffler, M., Effect of the Environment on A− Al 2 O 3 (0001) Surface Structures. *Physical Review Letters* **2000**, *84*, 3650.

61 Zhai, H.; Ha, M.-A.; Alexandrova, A. N., Affck: Adaptive Force-Field-Assisted Ab Initio Coalescence Kick Method for Global Minimum Search. *Journal of chemical theory and computation* **2015**, *11*, 2385-2393.

62 Averkiev, B., Geometry and Electronic Structure of Doped Clusters Via the Coalescence Kick Method. **2009**.

63 Tian, W. Q.; Ge, M.; Sahu, B.; Wang, D.; Yamada, T.; Mashiko, S., Geometrical and Electronic Structure of the Pt7 Cluster: A Density Functional Study. *The Journal of Physical Chemistry A* **2004**, *108*, 3806-3812.

64 Dadras, J.; Jimenez-Izal, E.; Alexandrova, A. N., Alloying Pt Sub-Nano-Clusters with Boron: Sintering Preventative and Coke Antagonist? *ACS Catalysis* **2015**, *5*, 5719-5727.

65 Ha, M.-A.; Dadras, J.; Alexandrova, A., Rutile-Deposited Pt–Pd Clusters: A Hypothesis Regarding the Stability at 50/50 Ratio. *ACS Catalysis* **2014**, *4*, 3570-3580.

CHAPTER 4

Boron Switch for Selectivity of Catalytic Dehydrogenation on Size-Selected Pt Clusters on Al_2O_3

4.1. INTRODUCTION

In the subnano-regime of cluster catalysis, size-selected surface-supported clusters often exhibit non-monotonic trends in reactivity and selectivity, inspiring the hunt for cluster sizes that are particularly active, selective, and resistant to deactivation.[1-4] Not only can they exhibit special catalytic properties due to size effects on electronic and geometric structure, but also most or all of the atoms in sub-nano clusters are available to bind reactants, making them a promising and rising class of catalysts. In addition, size-selected clusters provide a theoretically tractable approach to testing strategies for catalyst improvement. We recently showed that Pt_7 deposited on alumina both binds and dehydrogenates ethylene more efficiently than Pt_4 or Pt_8 on either a *per* cluster or a *per* Pt atom basis. This higher activity was shown to result from the diverse cluster morphologies accessible to Pt_7, particularly at higher temperatures and reagent coverages.[1] However, this finding is bittersweet, because these clusters and especially the most active Pt_7, easily deactivate via a combination of coke (i.e. carbon) deposition and sintering. Coke formation deactivates many catalysts in reactions such as Fischer-Tropsch synthesis[5], cracking of hydrocarbons[6], and alkene dehydrogenation[7]. Sintering, i.e. cluster migration, ripening, and agglomeration into larger nanoparticles, where fewer atoms are available on the surface, is another major route of activity loss.[8] Thus, improved cluster catalysts would sustain the activity and selectivity of the highly promising Pt_n, while resisting coking and sintering.

In this work, we test the strategy of nano-alloying to tune the selectivity for dehydrogenation by Pt_n / Al_2O_3, focusing on Pt_7, with the goal of minimizing deactivation by coking and sintering. Doping and alloying can be used to tune the properties of bulk Pt. Alloying Pt with Sn[9] and Zn[10,11] has been used for selectivity control and with Pd to reduce sintering[12,13]. Here, our inspiration is drawn from the boration (boron-doping) of extended surfaces of Co and Ni, used in Fischer-Tropsch synthesis and steam methane reforming, respectively.[14,15] Boration of these metal surfaces extended the lifetime of the catalyst by preventing coke adsorption. In general, boron interacting with metals can lead to a variety of interesting phenomena, such as

alloy ultra-hardening[16], emergence of topological and Kondo insulators[17], exotic magnetism[18], surface reconstructions[19], record coordination chemistry[20], and the selectivity of Pd catalysts in hydrogenation[21,22]. Recently, we began to theoretically probe boron as a dopant for small Pt clusters deposited on magnesia,[23] and found it to reduce affinities of these systems to carbon atoms. Building from this promising initial result, we now address the effect of boration on the selectivity of catalytic dehydrogenation and coking sensitivity of Pt_7 on alumina, using both *ab initio* and statistical mechanical theory, in conjunction with experiment. In what follows, we show that nano-alloying with boron dramatically changes the properties toward alkene binding and dehydrogenation.

4.2. RESULTS AND DISCUSSION

Size-selected $Pt_{4,7,8}$ on alumina have been prepared as discussed in detail previously,[1,24] and then borated by exposure to diborane (B_2H_6). Boration and its effects on binding and dehydrogenation of a model alkene, ethylene, were probed by temperature programmed desorption/reaction (TPD/R), low energy ion scattering (ISS), plane wave density-functional theory (PW-DFT) calculations, and molecular dynamics (MD) simulations. Initial studies suggested that Pt_7 is not only the most active, but also the most susceptible to the effect of boration. We therefore focused our experimental and theoretical work on Pt_7, and will explore size effects in future studies.

We find that diborane adsorbs dissociatively on the Pt_7 clusters, undergoing both B-H and B-B bond scission, and leaving atoms of boron in the clusters, as it has been reported to do also on the surfaces of Ni[25], Pd[26], Ru[27], Fe or steel[28], Al_2O_3[29], and Pt/Al_2O_3[30]. Pt^0 complexes are also well known for the successful formation of unique boronated complexes containing borenes, boranes, borylanes.[31,32] Notably, Söderlund, et. al. observed the formation of BH_3, B_3H_7, B_3H_9, B_5H_9, and B_6H_{10} in fixed bed reactor studies of diborane on Pt/Al_2O_3 and it is likely that this also occurs in our experiments.[30] ISS of as-deposited Pt_7/alumina (**Figure 4.1a**) shows peaks for O, Al, and Pt. B, itself, is undetectable due to a combination of low ISS sensitivity for

B, low B coverage, and high background at low E/E_0. Nonetheless, because adsorbates attenuate ISS signal from underlying atoms, the presence of diborane and fragments thereof, can be inferred by the effects on other signals.

Considering the Pt signal as reported previously,[1] efficient substrate-mediated adsorption of background CO (~5 x 10^{-11} mbar) leaves ~0.5 CO molecules adsorbed *per* cluster, on average, and by extrapolation we estimate that the as-deposited Pt signal is ~30% below the adsorbate-free limit (indicated by a star). Only a small recovery of Pt ISS signal is seen after 700 K heating to desorb adventitious CO, indicating that heating also causes structural changes that result in a smaller fraction of Pt in the surface layer.[1]

Initial exposure of a Pt_7/alumina sample to 1.5 L of B_2H_6 at 130 K results in ~80 % attenuation of the Pt ISS signal (**Figure 4.1a**), demonstrating that diborane binds efficiently on top of Pt_7.[1,24] Note that 1.5 L exposure may lead to adsorption of more than one diborane *per* cluster. Due to computational limits, only adsorption of a single diborane adsorbed to Pt_7 clusters was pursued (**Figure 4.1b**).

PW-DFT calculations were performed to probe adsorption of a single diborane on Pt_7 isomers. In these 0 K and *in vacuo* calculations, binding of diborane on the prismatic global minimum of Pt_7 results in B-H bond scission with some hydrogen leaving for Pt sites; on the more catalytically active[1] single layer isomer, the B-B bond also breaks with diborane spontaneously decomposing to form BH_y fragments. These results are consistent with the large Pt ISS attenuation observed. The Al and O ISS peaks in ISS underwent only a small attenuation upon diborane exposure at 130 K, indicating that only a small amount of diborane binds to alumina at 130 K, possibly at defects, and the Al and O peaks largely recover when the sample is heated to 300 K, indicating that most of this initial coverage desorbs at low temperatures.

In the sample heated to 300 K, the Pt signal recovered to ~50% of the as-deposited value, indicating some desorption of diborane or its fragments, but with a significant B_xH_y coverage remaining, attenuating ISS signal from underlying Pt. After heating to 700 K, the Pt

signal recovered to the as-deposited value, but was still ~30% below the expected adsorbate-free limit, and also below the signal observed after heating without diborane exposure.

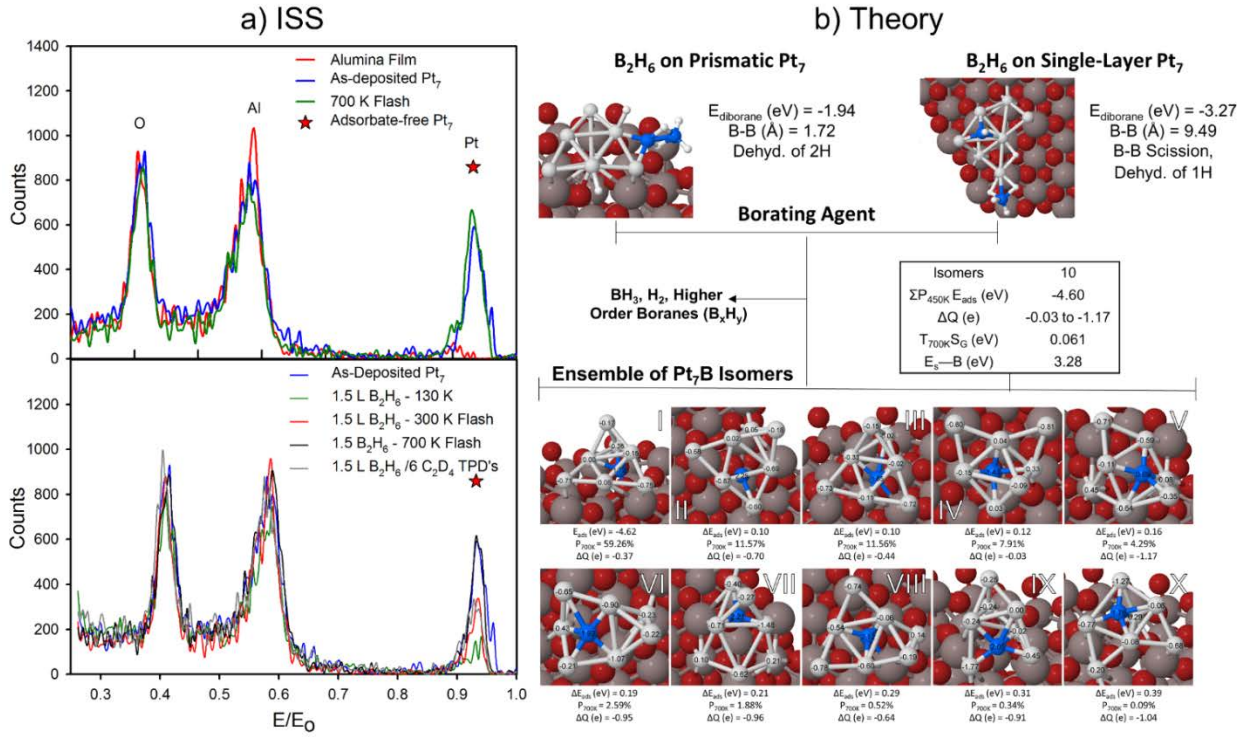

Figure 4.1 (a) Raw ISS spectra for Pt_7/alumina samples (TOP) measured immediately after depositing 0.1 ML of Pt_7 (blue) and after flashing Pt_7/alumina to 700 K (green). The spectrum for Pt-free alumina is shown for comparison. (BOTTOM) Raw ISS spectra for: as deposited (blue), after 1.5 L B_2H_6 exposure at 130 K (green),), after 1.5 L B_2H_6 at 130 K exposure followed by heating to 300 K (red) or 700 K (black), and after 700 K boration followed by 6 C_2D_4 TPD/R runs (gray). The extrapolated value for adsorbate free Pt_7/alumina is shown by stars. **(b)** Diborane adsorption results in borated Pt subnanoclusters (TOP). The lowest minima of adsorbed isomers of Pt_7B with adsorption energy (E_{ads}), adsorption energies of local minima relative to the global minimum (ΔE_{ads}), Boltzmann populations at 700 K, and charge transfer (ΔQ) (BOTTOM). Aluminum atoms are dark gray; oxygen, dark red; platinum, light gray; boron, blue; and hydrogen, white.

CO TPD (**Figure 4.2**) probed the number and energetics of exposed Pt sites. For CO on as-deposited Pt_7, the main desorption peak is between 300 and 600 K, with a small peak below 200 K. If as-deposited Pt_7 is first simply heated to 700 K in UHV, the total amount of CO desorbing from Pt sites is reduced by ~10%, but the temperature dependence is essentially unchanged. A similar effect is observed if the Pt_7/alumina is exposed to a saturation dose of D_2

then heated to 700 K (not shown), consistent with the ISS suggesting thermal restructuring causing a small reduction in the number of exposed Pt sites.

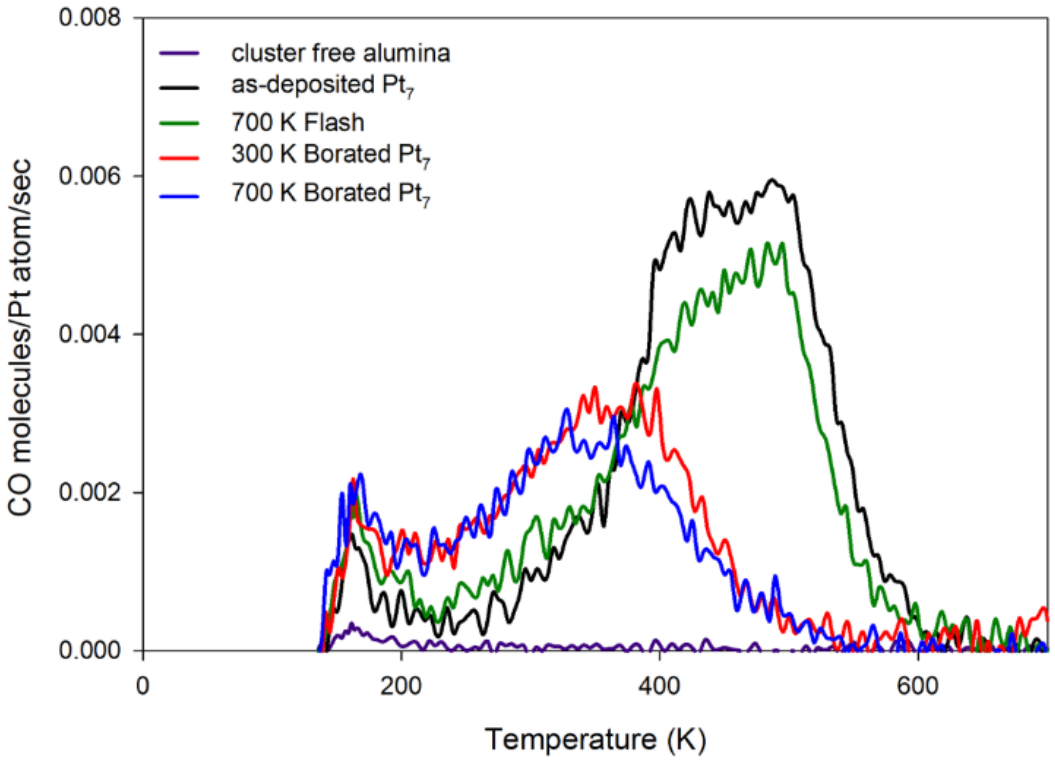

Figure 4.2. The figure compares CO TPD for a set of Pt_7/alumina samples that were first exposed to a particular manipulation and then probed by CO TPD (10 L ^{13}CO exposure at 150 K, heating at 3 K/sec to 700 K).

Sintering/agglomeration of the Pt_7 into larger clusters, with fewer exposed Pt sites, could potentially account for this small decrease in CO desorption, however, a previous study of CO TPD from Pt_n/alumina/Re(0001) ($2 \leq n \leq 18$)[24], found that this CO desorption feature *increased* significantly with increasing cluster size. Therefore, we conclude that the observed decrease in temperature CO desorption after heating cannot be explained by sintering/agglomeration alone. As discussed previously,[1] theory suggests that the ensemble of Pt_7/isomers favors more prismatic isomers that would also provide fewer CO binding sites.

In any case, it is clear that boronation has a much larger effect. For Pt_7 first exposed to 1.5 L of B_2H_6 and heated to 300 K, the CO desorption is attenuated by ~40%, and the main CO desorption peak shifts ~100 K, demonstrating that boration significantly weakens the Pt-CO binding. B_2H_6 exposure followed by 700 K heating has little additional effect on either the number or energetics of CO binding sites, despite the observation that 700 K heating results in recovery of the Pt ISS signal to the as-deposited value. The recovery of Pt ISS signal to the as-deposited value following the 700 K heating is further evidence that the observed changes in the CO binding are not a result of thermal sintering.

DFT calculations show that diborane adsorbs dissociatively atop the clusters as fragments of H, B_xH_y, or BH_y (**Figure 3.1b**), consistent with the low Pt ISS intensity observed after diborane exposure. However, the majority of Pt_7B/Al_2O_3 structures accessible at 700 K feature the boron acting as a B-O_{surf} anchor between the cluster and the support (R(B-O_{surf}) ~1.4 Å, Isomers I-IV, VII-VIII) with some structures displaying flatter, single-layer geometries with highly-coordinated Pt-B bonds (Isomers V-VI, IX-X, **Figure 3.1b**). All these structures expose a large fraction of Pt atoms in the surface layer, accounting for high Pt ISS intensity. Pt atoms bonded to B and reduced charge transfer from the support, presumably account for the weakened CO binding. The decomposition of diborane may undergo many pathways[33-35] and a future study will elucidate the complex interactions between the borating agent and size-selected clusters.

In our study of non-borated Pt_n/alumina,[1] it was shown that the experimental results were consistent with the theoretical finding of cluster size-dependent ensembles of thermally accessible structures. Predicted evolution of the ensembles with respect to both temperature and ethylene binding was essential to interpreting the ISS and ethylene adsorption results. Because of the increase in complexity of the borated system, such detailed experiment-theory comparison is not feasible, however, theory indicates, perhaps not surprisingly, that Pt_7B/alumina has an even more complex ensemble than Pt_7/alumina.

In Pt_7B, 10 distinct isomers contribute significantly to the ensemble at 700 K, with the global minimum constituting only 59% of the population. For comparison, the global minimum of Pt_7 on alumina comprised 66% of the ensemble and, for the less active Pt_8, 88%.[1] Thus, the structural diversity unique to Pt_7/alumina[1] leading to a manifold of binding sites is enhanced in the Pt_7B/alumina ensemble. Having access to diverse isomers introduces the possibility of at least one of them being dominant in catalysis, making the entire ensemble more active, although in more complicated reactions diversity can have an adverse effect on selectivity. At the same time, Pt_7B's diversity results in a substantial increase in the configurational entropy's contribution to the free energy of the system (**SI Tables S8.3.3-4**).[12] These observations are valid only if all thermodynamically-accessible isomers are also kinetically accessible.

The effects of boration on ethylene binding and dehydrogenation on Pt_7 were also probed by TPD/R. **Figure 4.3b** compares the temperature dependence for C_2D_4 and D_2 desorption from separate Pt_7/alumina samples, studied as-deposited and after heating to 300 or 700 K, with and without prior 130 K 1.5 L diborane exposure. For as-deposited Pt_7/alumina, unreacted ethylene desorbs in two components. The low temperature component is identical to that seen for Pt-free alumina and is attributed to ethylene bound to the alumina support. Desorption from Pt_7 sites occurs in a broad component from ~ 200 to 500 K. D_2 desorption (dehydrogenation) is not observed for alumina, but appears between ~ 300 and 650 K for as-deposited Pt_7/alumina. We previously showed that the onset temperature for D_2 desorption is determined by the activation energy for C_2D_4 dehydrogenation rather than for D_2 desorption.[1] Integrating the desorption signal allows us to estimate the number of C_2D_4 and D_2 molecules desorbing, which, after subtraction of C_2D_4 desorption from alumina, amount to ~2.1 C_2D_4 and ~1.5 D_2 molecules *per* Pt_7 cluster. Assuming that no hydrogen is left on the surface at 700 K,[1] the number of C_2D_4 molecules initially adsorbed is ~2.6 *per* Pt_7 cluster. For as-deposited Pt_7/alumina heated to 700 K prior to C_2D_4 TPD/R, the amount of C_2D_4 (~1.8/Pt_7) and D_2 (~1.3/Pt_7) is 10 - 15% lower, and shifted to lower temperatures. The reduction in desorption is

stronger if Pt_7/alumina is heated to only 300 K prior to C_2D_4 TPD/R, (~1.4 C_2D_4, ~1.0 D_2), presumably because 300 K causes some cluster restructuring, but does not desorb adventitious CO.

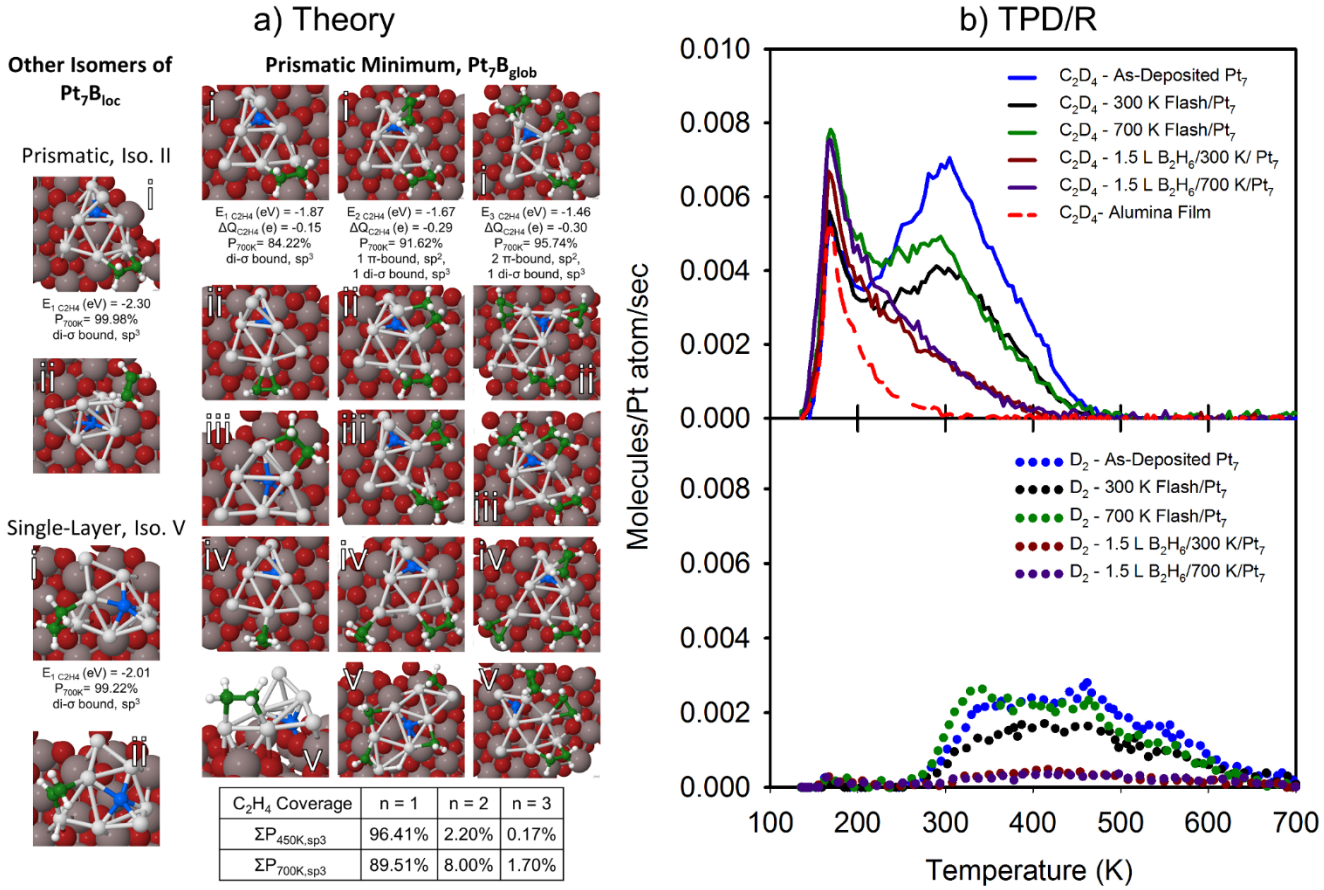

C_2H_4 Coverage	n = 1	n = 2	n = 3
$\Sigma P_{450K,sp3}$	96.41%	2.20%	0.17%
$\Sigma P_{700K,sp3}$	89.51%	8.00%	1.70%

Figure 4.3. (a) Deposition of ethylene on Isomers I, II, and V of Pt_7B from DFT. In π-bound ethylene, both C atoms adsorb to a single Pt site and remain sp^2-hybridized (bond angles of ~120° and a C-C bond-length of ~1.4 Å). Di-σ bound ethylene binds to two Pt sites and becomes sp^3-hybridized (bond angles of ~109° and a C-C bond of ~1.5 Å). With increasing temperature and coverage, less and less ethylene binds as di-σ. Additional minima not visualized here may be found in the SI along with other structural data such as charges and bonding discussion. Aluminum atoms are dark gray; oxygen, dark red; platinum, light gray; boron, blue; carbon, green; and hydrogen, white. **(b)** Intact C_2D_4 (solid) and D_2 (dots) desorbing from Pt_7/alumina samples after various treatments: As-deposited (blue), 300 K flash (black), 700 K flash (green), 1.5 L of B_2H_6 with 300 K flash (dark red), 1.5 L B_2H_6 with 700 K flash (purple). The (red) dashed line represents ethylene desorption from the cluster-free alumina.

Crampton et al. recently reported a study of ethylene hydrogenation to ethane over size-selected Pt_n deposited on MgO that provides an interesting point of comparison.[36] In their experiment, they coadsorbed hydrogen and ethylene before carrying out TPR, and measured desorption of ethane. In our experiments, there could potentially also be hydrogen present on

the surface due to dissociative adsorption of ethylene, however, we did not see any evidence for ethane production. This absence of ethane production may simply reflect the relatively low concentration of hydrogen, compared to a situation where hydrogen is dosed along with ethylene. However, we note that Crampton et al. did not observe hydrogenation for Pt_n smaller than Pt_{10}.

The effects of boration, i.e., of 1.5 L diborane exposure and heating, are more dramatic. For either 300 or 700 K heating, desorption of C_2D_4 is strongly attenuated and shifted to lower temperatures (**Figure 4.3b**). Note that we do observe a small amount of boron deposition on Pt-free alumina films, presumably at defects, however, this is found to have no effect on the amount or temperature of C_2D_4 desorption. After subtracting these contributions, the integrated C_2D_4 desorption is found to be only 0.75/Pt_7 (300 K) and 0.9/Pt_7 (700 K). Boration has no significant effect on the temperature onset for D_2 production, but the amount of D_2 is more than five times lower than for as-deposited Pt_7/alumina (0.27 and 0.25/Pt_7-B_2H_6 for 300 and 700 K heating, respectively). Assuming again that no hydrogen is left on the surface at 700 K, the total initial coverage of ethylene is ~0.83/Pt_7B and ~1.02/Pt_7B for samples heated to 300 and 700 K, respectively. It is somewhat surprising that there is not a larger difference between the ethylene chemistry on samples prepared by diborane exposure followed by heating to 300 K or 700 K. ISS shows that substantially more B_xH_y adsorbates remain on the surface of the Pt clusters after 300 K heating, yet they appear to have only a modest effect on the amount of ethylene binding and its propensity to dehydrogenate.

One question is whether any hydrogen is left on the Pt clusters after boronation, i.e., after diborane exposure and heating to 700 K. If so, this would complicate measurement of ethylene TPD/R because of possible H/D exchange. To test for this process in a somewhat simpler system, we exposed a borated sample to D_2, which adsorbs dissociatively on Pt_7/alumina, undergoing recombinative desorption between ~200 and 350 K. If there were

significant H concentration on the sample, significant HD (mass 3) desorption should occur. None was observed, indicating insignificant residual H concentration on the borated samples.

From the perspective of coke reduction, these effects of boration should increase the durability of the catalyst. In alkane dehydrogenation, the goal is to produce alkenes plus hydrogen, but to avoid further dehydrogenation to coke precursors like alkylidenes or alkynes.[6,9,37,38] It is clear that boration substantially reduces the ethylene adsorption energy to Pt_7, such that desorption occurs below the onset temperature for dehydrogenation (**Figure 4.3b**). This constitutes the main result of the present work. Boration tempers, but does not kill the catalytic activity of Pt clusters and thus provides a lever for adjusting the selectivity of the catalytic process and a way to eventually optimize it.

DFT provides insight into the mechanism for boron's effects on ethylene binding and decomposition. Pt_7 on alumina is negatively charged from 1.2 to 1.4 e^-, depending on cluster isomer, due to electron transfer from alumina. Upon boration, the amount of net electron transfer (ΔQ) to the cluster decreases, ranging from nearly neutral -0.3 to -1 e^-, depending on the isomer. Thus, the nucleophilicity of the Pt_7B/alumina ensemble is substantially reduced compared to pure Pt_7/alumina. There is charge separation between atoms: positive Pt coordinated to O_{surf}, negative Pt to Al_{surf}, and positive B to O_{surf}, i.e. Pt atoms within the clusters are charged non-uniformly. Negative charge is associated with cluster nucleophilicity and strong ethylene binding[1], thus a substantial reduction in ethylene adsorption energy would be predicted just based on the effects of boron on clusters' charge, consistent with the TPD/R results.

The propensity for coking is governed by how likely ethylene is to desorb from the catalyst rather than undergo dehydrogenation to form coke precursors (CH_y or C_n).[1,7,37-41] Therefore, we theoretically probed ethylene binding on the ensemble of Pt_7B/alumina structures at relevant temperatures and up to the maximum coverage observed experimentally (~3 ethylene/Pt_7, see **Figure 4.3a**). Ethylene binds to Pt in either π- or di-σ-bonded geometries, the latter being associated with further dehydrogenation.[1,7,37-41] We extracted the structural

information for all isomers considered, to construct ensemble percentages of di-σ-bound ethylene as a metric of ethylene activation at rising temperatures and coverages (**Figure 4.3a**, see SI for details). As noted above, in the experiment, borated Pt_7 binds roughly one ethylene molecule per cluster. DFT shows that ethylene preferentially binds to the more nucleophilic Pt sites on the cluster periphery and avoids the electropositive B (**SI Figures S8.3.4-8, Tables S8.3.5-7**). Moreover, with increasing coverage, ethylene reflects less cooperative adsorption on Pt_7B than observed on Pt_7: it destabilizes the system by ~0.2 eV/ethylene in Pt_7B, but stabilizes by ~0.3 eV/ethylene in Pt_7.[1]

The Pt_7B cluster ensemble also activates a decreasing fraction of ethylene as compared to Pt_7.[1] Pt_7 binds and activates for dehydrogenation more and more ethylene as the temperature and coverage increase. At 700 K with low coverage, only 15% of Pt_7 isomers contain di-σ ethylene; with high coverage, the percentage increases to >69%. On Pt_7B the effect is the opposite: as the temperature and coverage increase, less additional ethylene bind in the di-σ fashion. This occurs because the population becomes enriched in the species that do not activate ethylene such as the π-configuration. While the first ethylene may bind in the di-σ fashion, all subsequent ethylene molecules prefer the weaker, π-configuration associated with hydrogenation or the desorption observed in experiment. At higher coverage, configurations containing additional sp^3, di-σ bound ethylene drop from ~90% to 1.7 %. This is the key to the reduced activity of Pt_7B.

Additionally, this illustrates the importance of the ensemble description of cluster catalysts. Note that if we take just the lower limit of temperature and coverage (i.e. consider just global minima with low ethylene content), we would be tempted to conclude that boration promotes rather than suppresses dehydrogenation, based on the prevalence of di-σ-bound ethylene. This result emphasizes that size- and composition-specific properties of surface-deposited cluster catalysts are not just the properties of a single structure, but of the ensembles present under reaction conditions. A number of studies have noted the importance of dynamic

fluxionality in the presence of reagents, such as gas phase Au clusters with CO/H_2O[42] or H_2,[43] H_2S splitting by hetero-trimetallic anions[44], and supported Au on magnesia[45] or ceria[46] for CO oxidation. Our theoretical study provides a comprehensive perspective of ensembles, moving the discussion beyond the low-coverage and low-temperature limit into the realm of real catalysis as evidenced by our discussion and agreement with experiment.

Born-Oppenheimer MD simulations reveal further differences between Pt_7 and Pt_7B interacting with ethylene (**SI Figures S8.3.9-13**). In a previous publication, we predicted that in pure Pt_7 clusters, prismatic geometries would stabilize to single-layer geometries during ethylene adsorption.[1] We observe this in MD trajectories at 450, 700, and 1000 K (**SI Figure 8.3.9**). At 450 and 700 K, the prismatic geometry undergoes multiple transformations: it opens up from a prism to a distorted hexagon (circa MD step 150) and varies between other prismatic configurations and other single-layer configurations. At 1000 K, ethylene adsorbed to either the prismatic or single-layer Pt_7 converts to the di-σ configuration. On single-layer Pt_7, ethylene exhibits C-H bond activation, followed by H_2 formation (**SI Figure 8.3.10**). These MD trajectories demonstrate the high reactivity of single-layer structures, particularly, in pure Pt_7.

We considered Pt_7B isomers I, II, and V as representatives of different structural classes. At 450 and 700 K with one bound ethylene molecule, the prismatic isomers I and II undergo flattening into single-layer and extended, branched configurations around the $B\text{-}O_{surf}$ anchor, exhibiting high fluxionality. At 700 K, the strongly bound, di-σ ethylene either desorbs (on Isomer I) or inter-converts to π-bound (on Isomer II), i.e. reverts to a geometry where it should tend to hydrogenate or desorb. On the single-layer isomer V of Pt_7B, we observe activation of the C-C and C-H bonds. At 450 K, we see the activation of the C-H bonds proceeding to dissociation of 2H. At 700 K, minor re-structuring of the single-layer cluster isomer occurs, and the di-σ-bound ethylene converts to π-bound. Dehydrogenation appears to proceed through a transition of an H atom from C to a neighboring Pt atom. Born-Oppenheimer MD shows that a vast variety of structures of Pt_7B with bound ethylene are dynamically visited at temperatures of 450 K and 700

K (see **SI Figures S8.3.11-13**). Even though these MD trajectories give only a partial view on the kinetic accessibility of the isomers, the results of dynamics simulations support the high isomeric diversity and the ensemble description used throughout this study. Thus, MD of these representative Pt_7B isomers available for catalysis supports the reduced activity of borated Pt_7 as compared to pure Pt_7.

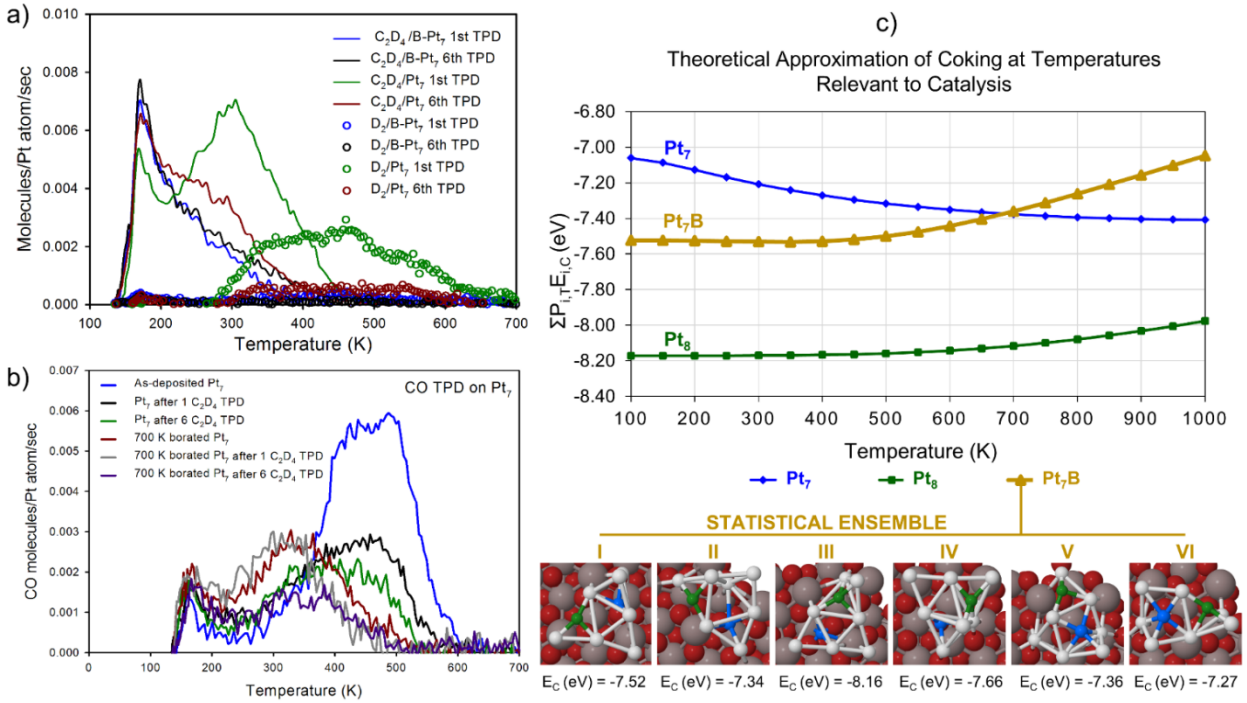

Figure 4.4. (a) Intact C_2D_4 (solid) and D_2 (dots) desorbing from Pt_7/alumina samples after various treatments: Pt_7 1st TPD/R run (green), Pt_7 6th C_2D_4 TPD/R run (dark red), borated Pt_7 1st TPD/R run (blue), borated Pt_7 6th TPD/R run (black). **(b)** CO TPD from Pt_7 with different treatments: Pt_7 as deposited (blue), Pt_7 after one C_2D_4 TPD/R run (black), Pt_7 after six C_2D_4 TPD/R runs (green), borated Pt_7 as prepared (dark red), borated Pt_7 after one C_2D_4 TPD/R run (gray), borated Pt_7 af-ter six C_2D_4 TPD/R runs (purple). The number of CO binding sites on pure Pt_7/alumina dramatically decreases after dehydrogenation whereas borated clusters show fewer CO binding sites and shift toward weaker CO binding. **(c)** First-order approximation of coking: Boltzmann-weighted C-sticking energies for an ensemble. The isomers included in the ensemble are visualized at the bottom. As temperature rises, borated Pt exhibits increasing resistance to carbon. Boltzmann-weights utilized as-deposited Pt_7B adsorption energies. Aluminum atoms are dark gray; oxygen, dark red; platinum, light gray; boron, blue; and carbon, green.

Evidence that boration stabilized the catalyst is provided by monitoring changes during 6 sequential TPD/R runs (**Figure 4.4a**). For Pt_7/alumina, the amounts of both

C_2D_4 and D_2 desorbing decrease substantially, and post-reaction XPS shows significant carbon deposition.[1] For borated Pt_7/alumina, there is essentially no change in C_2D_4 and D_2 desorption and no XPS-detectable carbon deposition. Indeed, boration lowers the C_2D_4 binding energy such that desorption, rather than dehydrogenation and coking is favored.

The CO TPD in **Figure 4.4b** reveals additional details. For pure Pt_7, the number of CO binding sites is reduced dramatically after 1 C_2D_4 TPD/R run, and continues to drop during 6 C_2D_4 TPD/R runs, exhibiting binding site loss from some combination of coke deposition and cluster sintering/restructuring. Borated clusters also show a gradual decrease in the number of CO sites from sequential C_2D_4 TPD/R runs. Since no C deposits are detected with XPS, we conclude that the effect is likely attributable to cluster sintering, as supported by the smaller calculated binding energies of Pt_7B to the support (**SI Tables S8.3.3-4**) and greater fluxionality of shapes seen in MD, as compared to Pt_7.

Finally, we consider coking in terms of the affinity of the clusters to C atoms. As a first-order approximation, we analyzed the Boltzmann-weighted ensemble-averages of the C-binding energies (E_C) of the isomers that constitute >96% of the population at 450 and 700 K, for Pt_7, Pt_7B, and Pt_8 (**Figure 4.4c**), the latter included because it tends to have prismatic isomers like Pt_7B. Carbon affinity is both temperature- and isomer-dependent, but the temperature dependence for Pt_7 and Pt_7B is opposite. For Pt_7, the ensemble-average E_C increases with temperature, i.e. the population evolves to include more isomers with high carbon affinity. In contrast, for Pt_7B, higher-energy planar configurations (Isomers V and VI) in which B is exposed, rather than anchored to alumina (Isomers I-IV) exhibit weaker E_C. As a result, the evolving ensemble for Pt_7B has decreasing carbon affinity and therefore increasing coke-resistance as temperature rises. For Pt_8, E_C also decreases with temperature, but remains much higher than for Pt_7B. Pt_7B's resistance to carbon can again be traced to its reduced negative charge and nucleophilicity.

4.3. CONCLUSION

We show that nano-alloying of small, alumina-supported Pt clusters with boron has a substantial effect on the selectivity of catalytic dehydrogenation of ethylene. Boration reduces the ethylene binding energy and thus the tendency toward undesired dehydrogenation to coke precursors. Coking is one of the major mechanisms for cluster catalyst deactivation and therefore the proposed strategy of its mitigation might be broadly valuable. The effect is linked to cluster morphologies in the statistical ensemble accessible at experimental conditions of temperature and ethylene coverage. As both temperature and coverage increase, borated clusters activate less ethylene for dehydrogenation and bind less carbon more weakly, as an ensemble, while the opposite is true for pure Pt clusters. Fundamentally, this work illustrates how size- and composition-specific properties of cluster catalysts are necessarily ensemble-averages and cannot be described by individual structures, even if they are the global minima.

4.4. METHODOLOGY

4.4.1. Experimental Section

In The experimental protocol has been detailed elsewhere.[1] Briefly, experiments were performed using an instrument that allows *in situ* sample preparation by cluster deposition and characterization by a variety of methods. Pt_7/alumina samples were prepared in ultra-high vacuum (~1.5×10^{-10} Torr) by growing an alumina thin film (~3 nm) on a Ta(110) single crystal, and soft landing (1 eV/atom) mass-selected Pt_7 clusters onto the support. The alumina thin films were grown using procedures adapted from the work of the Goodman[47-49] and Madey[50,51] groups. A detailed study by Chen and Goodman[47] concluded that alumina thin (~1.5 Å) films grown on a Ta(110) single crystal have slightly distorted hexagonal symmetry that can be related to either the (0001) face of α-Al_2O_3 or the (111) face of γ-Al_2O_3. Because the films were inert to a variety of gas molecules under vacuum, the films were proposed to be preferentially oxygen terminated. In previous publications,[52,53] we demonstrated that the adsorbate binding,

reactivity, and electronic properties of Pd clusters deposited on these alumina thin films were independent of film thickness in the 3 – 10 nm range. In the present study we used 3-6 nm thick films. Cluster coverage was controlled by monitoring the cluster neutralization current. All samples contained Pt_7 coverage corresponding to 1.5×10^{14} atoms/cm^2 (~0.1 Pt monolayer). Deposition took ~ 5 to 15 minutes.

TPD/R measurements were made with a differentially pumped mass-spectrometer that views the sample through a ~2.5 mm diameter orifice in a skimmer cone, which is surrounded by directional dose tubes allowing gas exposures to the sample. For the ethylene TPD/R measurement the sample was exposed to 5 L of C_2D_4 at sample temperature of 150 K. The sample was then cooled to 135 K and ramped to 700 K at 3 K/sec, while monitoring masses of interest desorbing from the surface. For CO TPD, samples were exposed to 10 L of $^{13}C^{16}O$ at a sample temperature of 150 K, cooled to 135 K, and ramped to 700 K at 3 K/sec, while monitoring desorption of ^{13}CO and other masses of interest. Boration was done by exposing samples to 1.5 L of B_2H_6 at a sample temperature of 130 K, and then ramping the sample temperature up to either 300 or 700 K at 3 K/sec. Note that all experiments were carried out on separately prepared samples to avoid thermal or adsorbate-induced changes to the samples.

Low energy He^+ ion scattering spectroscopy (1 keV He^+, 45° angle of incidence, normal detection) was used to observe the effects of cluster size, sample heating, boration, and ethylene TPD/R on the fraction of Pt atoms exposed in the surface layer. ISS peaks result from He^+ scattering from single atoms in the surface layer, identifying the masses of those atoms. Because ISS is a destructive technique all measurements were made on separately prepared samples or at the end of a series of experimental sequences.

4.4.2. Computational

As discussed previously,[1] PW-DFT calculations were performed using the Vienna Ab initio Simulation Package (VASP)[54-57] utilizing projector augmented wave potentials[58,59] and the PBE[60] functional. A dense Monkhorst–Pack 8 × 8 × 3 k-point grid was implemented for bulk

calculations of the α-Al_2O_3 unit cell with large kinetic energy cutoffs of 520.0 eV. The optimized lattice constants of *a* = 4.807 Å and *c* = 13.126 Å exhibited a slight increase of <0.1 Å as compared to experiment, typical of GGA functionals.[61,62] The unit cell was grown to a (3 × 3) surface with the bottom half of the surface kept fixed and a vacuum gap of 15 Å. A 1 × 1 × 1 k-point grid centered at Γ-point, stringent convergence criteria of 10^{-5} (10^{-6}) eV for geometric (electronic) relaxations, and kinetic energy cutoffs of 400.0 eV were employed in all calculations. The Adaptive Force Field Coalescence Kick (AFFCK)[63], an adaptive global minimum and local minima search based on the Coalescence Kick (CK)[64], was used to find gas phase Pt_7B. A *per manum* search of adsorbed structures consisted of deposition of the lowest 5-6 gas phase structures (**SI Figure 8.3.1**) under PBE levels of theory with a thorough sampling of cluster faces to possible binding sites. It must be noted that with larger gas phase clusters, the order of the lowest minima may be DFT method dependent.[63] All relevant equations such as the adsorption of reagents, sintering penalty, Gibbs or configurational entropy, amongst others may be found in the SI. MD calculations were also performed in VASP requiring electronic iterations to reach a convergence criterion of 10^{-8} eV per 1 fs time-step. MD trajectories of >1.5 ps were analyzed in order to compare adsorption behavior of ethylene on pure Pt versus borated Pt. The Nose-Hoover Thermostat was used to equilibrate the system, approximating conditions to that of the NVT ensemble.

4.5. REFERENCES

1 Baxter, E. T.; Ha, M.; Cass, A. C.; Alexandrova, A. N.; Anderson, S. L. *ACS Cat.* **2017***, 7*, 3322-3335.

2 Kaden, W. E.; Wu, T.; Kunkel, W. A.; Anderson, S. L. *Science.* **2009***, 326*, 826-829.

3 Vajda, S.; Pellin, M. J.; Greeley, J. P.; Marshall, C. L.; Curtiss, L. A.; Ballentine, G. A.; Elam, J. W.; Catillon-Mucherie, S.; Redfern, P. C.; Mehmood, F. *Nat. Mat.* **2009***, 8*, 213-216.

4 Lee, S.; Molina, L. M.; López, M. J.; Alonso, J. A.; Hammer, B.; Lee, B.; Seifert, S.; Winans, R. E.; Elam, J. W.; Pellin, M. J. *Angew. Chem.* **2009***, 121*, 1495-1499.

5 Schulz, H. *App. Cat. A: Gen.* **1999***, 186*, 3-12.

6 Rahimi, N.; Karimzadeh, R. *App. Cat. A: Gen.* **2011***, 398*, 1-17.

7 Shaikhutdinov, S. K.; Frank, M.; Bäumer, M.; Jackson, S. D.; Oldman, R. J.; Hemminger, J. C.; Freund, H. *Cat. Lett.* **2002***, 80*, 115-122.

8 Hansen, T. W.; DeLaRiva, A. T.; Challa, S. R.; Datye, A. K. *Acc. Chem. Res.* **2013***, 46*, 1720-1730.

9 Galvita, V.; Siddiqi, G.; Sun, P.; Bell, A. T. *J. Cat.* **2010***, 271*, 209-219.

10 Dadras, J.; Shen, L.; Alexandrova, A. *J. Phys. Chem. C.* **2015***, 119*, 6047-6055.

11 Shen, L.; Dadras, J.; Alexandrova, A. N. *Phys. Chem. Chem. Phys.* **2014***, 16*, 26436-26442.

12 Ha, M.; Dadras, J.; Alexandrova, A. *ACS Cat.* **2014***, 4*, 3570-3580.

13 Johns, T. R.; Gaudet, J. R.; Peterson, E. J.; Miller, J. T.; Stach, E. A.; Kim, C. H.; Balogh, M. P.; Datye, A. K. *ChemCatChem* **2013***, 5*, 2636-2645.

14 Tan, K. F.; Chang, J.; Borgna, A.; Saeys, M. *J. Cat.* **2011***, 280*, 50-59.

15 Xu, J.; Chen, L.; Tan, K. F.; Borgna, A.; Saeys, M. *J. Cat.* **2009***, 261*, 158-165.

16 Levine, J. B.; Tolbert, S. H.; Kaner, R. B. *Adv. Funct. Mat.* **2009***, 19*, 3519-3533.

17 Cooley, J.; Aronson, M.; Fisk, Z.; Canfield, P. *Phys. Rev. Lett.* **1995***, 74*, 1629.

18 Küpers, M.; Lutz-Kappelman, L.; Zhang, Y.; Miller, G. J.; Fokwa, B. P. *Inorg. Chem.* **2016***, 55*, 5640-5648.

19 Nandula, A.; Trinh, Q. T.; Saeys, M.; Alexandrova, A. N. *Angew. Chem., Int. Ed.* **2015***, 54*, 5312-5316.

20 Popov, I. A.; Jian, T.; Lopez, G. V.; Boldyrev, A. I.; Wang, L. S. *Nat. Commun.* **2015***, 6*, 8654.

21 Chan, C. W. A.; Mahadi, A. H.; Li, M. M.; Corbos, E. C.; Tang, C.; Jones, G.; Kuo, W. C. H.; Cookson, J.; Brown, C. M.; Bishop, P. T. *Nat. Commun.* **2014***, 5*.

22 Krawczyk, M.; Sobczak, J.; Palczewska, W. *Cat. Lett.* **1993***, 17*, 21-28.

23 Dadras, J.; Jimenez-Izal, E.; Alexandrova, A. N. *ACS Cat.* **2015***, 5*, 5719-5727.

24 Roberts, F. S.; Kane, M. D.; Baxter, E. T.; Anderson, S. L. *Phys. Chem. Chem. Phys.* **2014***, 16*, 26443-26457.

25 Desrosiers, R. M.; Greve, D. W.; Gellman, A. J. *J. Vac. Sci. Tech. A: Vac. Surf. Films.* **1997***, 15*, 2181-2189.

26 Krawczyk, M. *Appl. Surf. Sci.* **1998***, 135*, 209-217.

27 Rodriguez, J. A.; Truong, C. M.; Corneille, J.; Goodman, D. W. *J. Phys. Chem.* **1992***, 96*, 334-341.

28 Casadesus, P.; Frantz, C.; Gantois, M. *Metallurg. Mater. Trans. A.* **1979***, 10*, 1739-1743.

29 Weiss, H.; Knight, J.; Shapiro, I. *J. Am. Chem. Soc.* **1959***, 81*, 1826-1827.

30 Söderlund, M.; Mäki-Arvela, P.; Eränen, K.; Salmi, T.; Rahkola, R.; Murzin, D. Y. *Cat. Lett.* **2005***, 105*, 191-202.

31 Arnold, N.; Braunschweig, H.; Dewhurst, R. D.; Ewing, W. C. *J. Am. Chem. Soc.* **2016***, 138*, 76-79.

32 Cui, Q.; Musaev, D. G.; Morokuma, K. *Organometallics.* **1998***, 17*, 742-751.

33 McKee, M. L. *J. Phys. Chem.* **1990***, 94,* 435-440.

34 Curtiss, L. A.; Pople, J. A. *J. Chem. Phys.* **1989***, 90*, 2522-2523.

35 Ganguli, P.; McGee Jr, H. *J. Chem. Phys.* **1969***, 50*, 4658-4660.

36 Crampton, A. S.; Rötzer, M. D.; Ridge, C. J.; Schweinberger, F. F.; Heiz, U.; Yoon, B.; Landman, U. *Nat. Commun.* **2016***, 7*.

37 Neurock, M.; van Santen, R. A. *J. Phys. Chem. B.* **2000***, 104*, 11127-11145.

38 Chen, Y.; Vlachos, D. G. *J. Phys. Chem. C.* **2010***, 114*, 4973-4982.

39 Anderson, A. B.; Choe, S. *J. Phys. Chem.* **1989***, 93*, 6145-6149.

40 Windham, R. G.; Koel, B. E. *J. Phys. Chem.* **1990***, 94*, 1489-1496.

41 Windham, R.; Koel, B. E.; Paffett, M. *Langmuir.* **1988***, 4*, 1113-1118.

42 Xing, X.; Li, X.; Yoon, B.; Landman, U.; Parks, J. H *Int. J. Mass Spect.* **2015***, 377*, 393-402.

43 Gao, M.; Lyalin, A.; Takagi, M.; Maeda, S.; Taketsugu, T. *J. Phys. Chem. C.* **2015***, 119*, 11120-11130.

44 Adhikari, D.; Raghavachari, K. *J. Phys. Chem. A.* **2016***, 120*, 466-472.

45 Häkkinen, H.; Abbet, S.; Sanchez, A.; Heiz, U.; Landman, U. *Angew. Chem., Int. Ed.* **2003***, 42*, 1297-1300.

46 Ghosh, P.; Farnesi Camellone, M.; Fabris, S. *J. Phys. Chem. Lett.* **2013***, 4*, 2256-2263.

47 Chen, P.; Goodman, D. *Surf. Sci.* **1994***, 312*, L767-L773.

48 Street, S.; Goodman, D.; King, D.; Woodruff, D. *Chem. Phys. Solid Surf.* **1997***, 8*, 375-406.

49 Lai, X.; Chusuei, C. C.; Luo, K.; Guo, Q.; Goodman, D. *Chem. Phys. Lett.* **2000***, 330*, 226-230.

50 Wu, Y.; Garfunkel, E.; Madey, T. E. *Surf. Sci.* **1996***, 365*, 337-352.

51 Wu, Y.; Garfunkel, E.; Madey, T. E. *J. Vac. Sci. Tech. A: Vac. Surf. Films.* **1996***, 14*, 2554-2563.

52 Kane, M. D.; Roberts, F. S.; Anderson, S. L. *Faraday Discuss.* **2013***, 162*, 323-340.

53 Kane, M. D.; Roberts, F. S.; Anderson, S. L. *J. Phys. Chem. C.* **2015***, 119*, 1359-1375.

54 Kresse, G.; Hafner, J. *Phys. Rev. B.* **1993***, 47*, 558.

55 Kresse, G.; Hafner, J. *Phys. Rev. B.* **1994***, 49*, 14251.

56 Kresse, G.; Furthmüller, J. *Comput. Mater. Sci.* **1996***, 6*, 15-50.

57 Kresse, G.; Furthmüller, J. *Phys. Rev. B.* **1996***, 54*, 11169.

58 Blöchl, P. E. *Phys. Rev. B.* **1994***, 50*, 17953.

59 Kresse, G.; Joubert, D. *Phys. Rev. B.* **1999***, 59*, 1758.

60 Perdew, J. P.; Burke, K.; Ernzerhof, M. *Phys. Rev. Lett.* **1996***, 77*, 3865.

61 Bourdillon, A.; El-Mashri, S.; Forty, A. *Philos. Mag. A.* **1984***, 49*, 341-352.

62 Levin, I.; Brandon, D. *J. Am. Ceram. Soc.* **1998***, 81*, 1995-2012.

63 Zhai, H.; Ha, M.; Alexandrova, A. N. *J. Chem. Theory Comput.* **2015***, 11*, 2385-2393.

64 Averkiev, B. PhD Thesis, Utah State University, Logan, UT 84322, USA, **2009**.

CHAPTER 5

Diborane Interactions with Pt_7/alumina: Preparation of Size-Controlled Boronated Pt Model Catalysts with Improved Coking Resistance

5.1. INTRODUCTION

Carbon deposition (i.e. “coking”) leads to deactivation of catalysts in important reactions such as Fisher-Tropsch synthesis,[1] hydrocarbon cracking,[2] and alkene dehydrogenation.[3] It has been demonstrated that boration of extended surfaces of Co[4] and Ni[5] can extend the lifetime of catalysts without compromising their activity toward Fischer-Tropsch synthesis and steam reforming, respectively. In both processes coking is the mechanism of deactivation. We recently showed that boration also reduces coking on size-selected Pt clusters deposited on alumina during dehydrogenation of alkenes.[6] This type of catalytic system is novel and so-far largely under-investigated, including several aspects of their preparation, experimental characterization, theoretical analysis, and structural, dynamical, and chemical properties.

Model catalysts with atomically size-selected clusters on well characterized supports provide a useful platform for studying catalysis mechanisms, allowing independent control of the size and density of catalytic sites, and facilitating detailed theoretical studies. Bimetallic catalysts provide important opportunities to tune catalytic activity, selectivity, and stability. However, extending the size-selected model catalyst approach to bimetallic clusters is challenging. One approach is to use alloy or dual target cluster sources that directly produce bimetallic clusters in the gas phase, which can then be mass selected and deposited to create bimetallic model catalysts.[7-10] This approach is quite general, in principle, however, for several reasons it becomes increasingly difficult as the cluster size increases. The cluster source intensity is “diluted” over an increasing number of possible M_xN_y combinations, and the intensity is further decreased by the need for high mass-selector resolution to separate closely-spaced masses. Intensity is important, because clusters quickly become contaminated due to substrate-mediated adsorption,[11-13] even in ultra-high vacuum (UHV). In many cases, natural isotope distributions exacerbate these problems such that clean selection of both size and composition may be impossible except for very small clusters. For example, Pt has *major* isotopes with atomic masses 194, 195, 196, and 198, and boron has isotopes with atomic masses 10 and 11.

Thus, even for clusters containing only three Pt atoms, the width of the Pt isotopologue distribution is greater than the boron mass, resulting in mass overlaps between Pt_3B_n and $Pt_3B_{n\pm1}$.

One motivation for this paper is to report a complementary approach to producing size-selected bimetallic cluster catalysts, in which mass-selected cluster deposition is used to create a size-selected model catalyst (here, Pt_n/alumina), which is then used to seed deposition of a second element to create a bimetallic model catalyst (here, Pt_nB_m/alumina). The challenge is to find conditions where boron deposits only on the Pt clusters, and then to characterize the nature of the resulting doped clusters.

5.2. METHODOLOGY

As outlined below, alumina-supported size-selected $Pt_{4,7,8}$ model catalysts were prepared, and then exposed to diborane and heated to drive decomposition and H_2 desorption. The goal is to selectively borate the Pt clusters, thus it is important to understand how diborane interacts with both Pt_n clusters and the alumina support. These interactions were probed by temperature-programmed desorption and reaction (TPD/R), low energy He^+ ion scattering (ISS), and X-ray photoelectron spectroscopy (XPS) experiments on both Pt-free alumina and Pt_n/alumina samples, by plane wave density functional theory (PW-DFT) calculations of adsorption geometries and energetics, and molecular dynamic (MD) simulations of borane surface chemistry. We previously showed that the chemical consequences of boration are similar for different Pt cluster sizes.[6] Here we focus on the boration mechanism, using Pt_7/alumina as the example system.

5.2.1. Computational

As discussed previously in detail,[14] PW-DFT calculations with projector augmented wave potentials[15-16] and the PBE[17] functional were implemented in the Vienna Ab initio Simulation Package (VASP).[18-21] The bulk-optimized unit cell with lattice constants of a = 4.807 Å and c = 13.126 Å was grown to a (3 × 3) surface, a slight expansion as compared to experiment.[22-23] A

vacuum gap of 15 Å was added to the slab. The bottom half of the surface was kept fixed. For all calculations, convergence criteria of 10^{-5} (10^{-6}) eV for geometric (electronic) relaxations, expansion of the plane waves' kinetic energy to 400.0 eV, and a k-point grid of 1 × 1 × 1 centered at the Γ-point were instituted. We previously discussed the global optimization of Pt_7 on the model α-alumina surface,[14] finding a number of low-lying isomers for Pt_7/alumina. As shown below, the global minimum has Pt_7 in a prismatic (i.e., 3D) structure with Pt_7-alumina adsorption energy of -5.09 eV, however, there are isomers only 0.05 eV higher in energy in which all Pt atoms are in a single layer bound to the alumina surface.

A *per manum* search for diborane adsorption geometries associated with both the prismatic and single layer Pt_7/alumina structures was made, starting with the molecule positioned at bridging, hollow, and atomic (atop) sites, oriented both parallel and normal to the surface plane, and rotated in various orientations. The starting geometries focused on adsorption of diborane to the Pt clusters, rather than to the α-Al_2O_3 surface. The adsorption energy of diborane was calculated via the relation:

$$E_{B2H6} = E[Surf + Pt_7\text{-}B_2H_6] - E[B_2H_6]_{gas} - E[Surf + Pt_{7,glob}].$$

Ab-initio MD calculations, starting at the lowest minimum of diborane adsorbed on both the prismatic and single-layer Pt_7/alumina structures, were also performed. Equilibration of the system utilized the Nose-Hoover thermostat and an electronic convergence criterion of 10^{-8} eV per 1 fs time-step was implemented. The global optimization of Pt_4B_4 adsorbed on alumina was performed using the Basin Hopping method adapted for surface deposited clusters.[24] The local minima search for gas phase Pt_4B_4 also utilized Basin Hopping. The adsorption energy of Pt_4B_4 was taken as $E_{ads} = E[Surf + Pt_4B_4] - E[Pt_4B_4]_{gas,glob} - E[Surf]$.

5.2.2. Experimental

The experiments were conducted with an instrument consisting of a mass-selected metal cluster ion deposition beamline[25] that terminates in an ultrahigh vacuum (~1.5×10^{-10} Torr) analysis chamber that allows *in situ* sample preparation and characterization, as discussed

previously, along with several of the experimental protocols used here.[12, 26-27] The Pt_n/alumina model catalysts were prepared on a 7×7 mm Ta(110) single crystal mounted using Ta heating wires to a liquid nitrogen reservoir at the end of a manipulator. The sample temperature was controlled between 110 and >2100 K by the combination of resistive and electron-bombardment heating and liquid nitrogen cooling. Temperature was measured by a C-type thermocouple spot welded to the back of the Ta single crystal.

Procedures for alumina film growth were adapted from the Goodman[28-30] and Madey[31-32] groups. At the beginning of each experiment, the Ta single crystal was annealed above 2100 K for 5 minutes or until no surface contaminants were detected by XPS and ISS. For alumina film growth, the Ta(110) substrate was transferred to a separately pumped UHV antechamber, heated to 970 K in 5×10^{-6} Torr of O_2, while exposed to Al evaporating from a crucible mounted normal to the Ta(110) surface. In previous studies, we demonstrated that the reactivity, adsorbate binding, and electronic properties of Pd clusters deposited on alumina were independent of film thickness in the 3-10 nm range. For these studies the typical growth rate was ~0.2 nm/min and 3-6 nm thick films were used.

Before beginning cluster deposition, the alumina/Ta(110) support was flashed to ~800 K to desorb adventitious adsorbates. To minimize the time the clusters were exposed to background gases, Pt cluster deposition was done as the sample cooled after the flash, beginning when the sample reached ~300 K. The clusters were deposited onto the alumina support through a 2 mm diameter mask, and cluster coverage was controlled by monitoring the neutralization current of soft landed (~1 eV/atom) clusters on the support. Unless stated otherwise, all samples were prepared with Pt_7 coverage of 2.14×10^{13} clusters/cm^2, amounting to 1.5×10^{14} Pt atoms/cm^2, equivalent to ~10% of a close-packed Pt monolayer.

TPD/R measurements were made using a differentially pumped mass spectrometer that views the main UHV chamber through the ~2.5 mm diameter aperture in a skimmer cone. The cone was surrounded by four directional dose tubes that pointed at the sample position, and gas

doses for both TPD/R and diborane exposure were done using the tubes to minimize gas exposures to the vacuum system. To calibrate the exposures, we compared sub-saturation CO TPD signals for CO delivered through the dose tubes and through a gas inlet remote from the sample position. During both gas dosing and the subsequent TPD/R heat ramp, the chamber pressure was monitored by a nude ion gauge, and ion signals of interest were measured by the differentially pumped mass spectrometer. Diborane TPD/R was done by exposing samples to B_2H_6 at 130 K sample temperature, followed by heating to 700 K. For ethylene TPD/R, the sample was exposed to 5 L of C_2D_4 at a sample temperature of 150 K (to minimize multilayer adsorption), cooled to 130 K, and then heated to 700 K while monitoring signals for $C_2D_4^+$, D_2^+, and various background gases.

Boron was introduced into the UHV system in the form of a diborane/argon gas mixture that we characterized mass spectrometrically to have actual composition of 4.8% diborane, 85% argon, and 10.2% H_2, the latter assumed to result from diborane decomposition during storage.[33] Diborane exposures were calculated based on the measured diborane mole fraction. In most experiments, boration was done by exposing the samples to 1.5 L of diborane at a sample temperature of 130 K, followed by heating to 700 K, which was found to be sufficient to drive desorption to completion. Note that 1.5 L diborane exposure corresponds to ~5.8 x 10^{14} diborane molecules impinging *per* cm^2, i.e., smaller than the total number of surface atoms, but almost four times larger than the number of Pt atoms. A few experiments were performed using a 0.5 L diborane exposure, where the number of impinging diborane molecules (1.9 x $10^{14}/cm^2$) was only ~25% greater than the number of Pt atoms present. The dose variation had little effect on the sample properties, suggesting that 1.5 L should be more than sufficient to saturate the Pt cluster binding sites.

Because the gas mixture contained hydrogen, and diborane decomposition also produces hydrogen, we studied TPD following pure D_2 exposure, in separate experiments. H_2

desorption during diborane TPD/R could not be monitored because the mass 2 background in the mass spectrometer was too high.

XPS (Al Kα) was used to examine both alumina and Pt_7/alumina samples after B_2H_6 exposure, both while holding the sample at the 130 K dose temperature, and after heating the sample to 700 K. Since both boron and Pt are present only in the surface layer, and we know the Pt coverage quite precisely, the boron coverage was estimated from the ratio of B 1s and Pt 4d XPS integrated intensities. The Pt 4d XPS signal was used because of overlap between Pt 4f and Al 2p. Both Pt and B are present at low coverage, and because the B 1s photoemission cross section is ~40 times smaller than that for Pt 4d,[34] the boron XPS signal is quite weak. To improve the signal/noise, the boron XPS measurements were done using samples with double the normal Pt_n coverage (i.e., 0.2 ML). Higher cluster coverage undoubtedly resulted in some increase in cluster agglomeration during deposition and heating, however, because the effects of boration do not appear to be very dependent on cluster size,[6] a modest degree of agglomeration is unlikely to have a significant effect on the B/Pt ratio. To insure that the diborane exposure was sufficient to saturate the larger number of Pt_7 present, we also doubled the diborane dose to 3.0 L.

For ISS, a beam of 1 keV He^+ was loosely focused onto the surface at 45° angle of incidence and the energy distribution of He^+ scattered along the surface normal was measured. Peaks in ISS result from scattering of He^+ from single atoms in the sample, predominantly in the surface layer.[35] Multiple scattering and scattering from sub-surface layers contributes primarily to a weak background. In these experiments, ISS was used to monitor the intensities associated with Pt, Al, and O atoms in the top sample layer. H is undetectable by ISS, and the boron ISS signal also proved to be undetectable, due to the combination of low He^+ scattering cross section ($\sigma_{scatt} \propto Z_{target}$), low boron coverage, and rising background in that energy range from multiple scattering. Because ISS is a destructive technique, the ISS experiments were done either on separately prepared samples or at the end of other experimental sequences.

5.3. RESULTS

5.3.1. Temperature Programmed Desorption/Reaction Following Adsorption of B_2H_6 and D_2

TPD/R experiments were used to identify species desorbing from alumina and Pt_7/alumina surfaces, and the associated temperature dependences (i.e. energetics). Because the literature shows that diborane can polymerize on surfaces,[36] we monitored masses relevant to known boranes of various sizes. **Figure S8.4.1** in the supporting information shows the raw TPD signals for ion masses 11, 26, 48, and 59, which are low background masses corresponding to $B_1H_x^+$,$B_2H_x^+$, $B_4H_x^+$, and $B_5H_x^+$ (the ^{11}B:^{10}B isotope ratio is ~80:20). **Figure 5.1** shows the data corrected, as described below, for the estimated contributions from fragmentation of higher boranes during election impact ionization (EI). Data are shown for desorption from both alumina and Pt_7/alumina samples, each exposed to 1.5 L of B_2H_6 at 130 K, then heated at 3 K/sec. Note that desorption starts at ~120 K, i.e. slightly below the dose temperature. This reflects the fact that diborane pumps out of the system slowly, so that there was a small additional exposure as the sample cooled to the TPD/R start temperature.

The assignment of the ion signals to desorbing species is complicated by the fact that boranes fragment extensively in EI.[37] We corrected the TPD signals for fragmentation of diborane, tetraborane (B_4H_{10}) and pentaborane (B_5H_9), which all have tabulated standard EI mass spectra, but did not attempt to correct for possible contributions from higher boranes (i.e., B_nH_m, $n > 5$). The dominant EI fragment ions for boranes tend to preserve the number of boron atoms ($B_nH_m \rightarrow B_nH_{m-x}^+$), however, there is some signal for essentially all possible $B_xH_y^+$ ($x \leq n$, $y \leq m$) fragments.[37] For example, mass 59 is the strongest peak in the EI mass spectrum of pentaborane (MW = 63.13), and mass 48 is the strongest peak for tetraborane (MW = 53.32), however, pentaborane EI also produces mass 48 with ~18% of the mass 59 intensity. Mass 26 is the most intense peak in the EI mass spectrum of diborane (MW=27.67), but 26 is also produced at the few percent level by EI of tetra- and pentaborane.

In **Figure 5.1**, no correction was made to the mass 59 intensity for possible contributions from EI of B_nH_m ($n \geq 6$), but the mass 48 signal was corrected for cracking of pentaborane, the mass 26 signal was corrected for cracking of pentaborane and tetraborane, and the mass 11 signal was corrected for contributions from penta-, tetra-, and diborane, using NIST standard mass spectra.[37] As can be seen by comparing **Figures 5.1** and **S8.4.1**, the corrections are generally quite small. The only qualitatively obvious change is that a peak in the raw signal for mass 48 in the 150 – 170 K range is shown to result almost entirely from EI cracking of pentaborane.

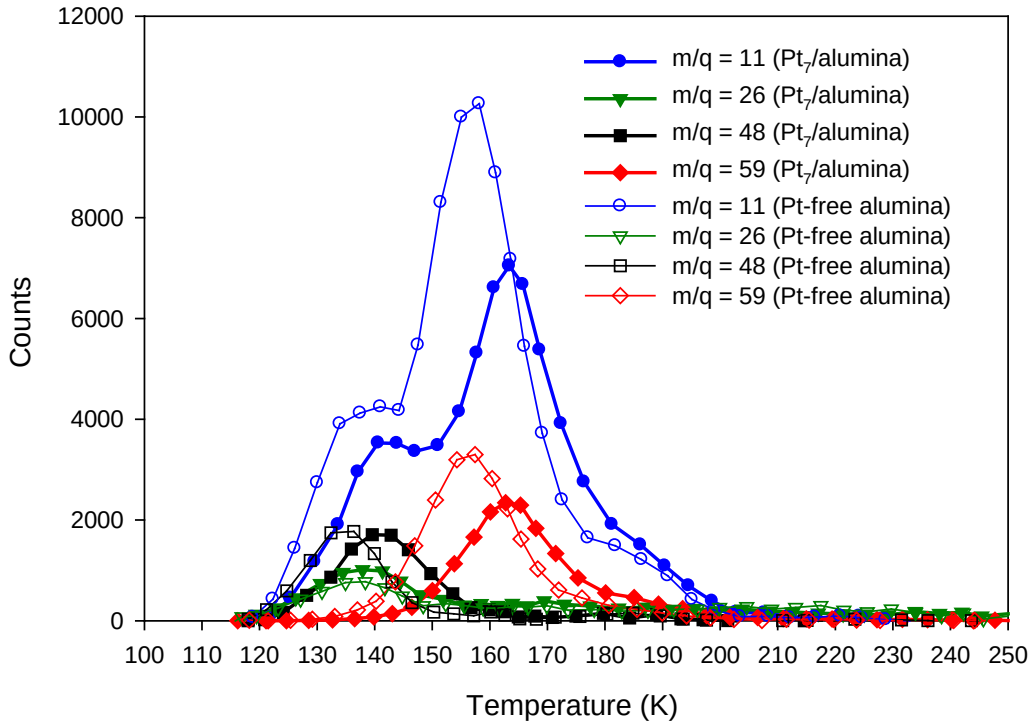

Figure 5.1. TPD spectra for select ion signals, corrected for EI cracking of borane species. Alumina and Pt_7/alumina samples were exposed to 1.5 L of diborane at 130 K, then heated at 3 K/sec while monitoring desorption mass spectrometrically.

One surprise is that the mass 11 signal ($^{11}B^+$ and $^{10}BH^+$) is quite high, even after subtraction of the expected contributions from EI fragmentation of di-, tetra-, and pentaborane.

We considered the possibility that the high mass 11 intensity might be an artifact of high mass spectrometer sensitivity to light masses, but this explanation is ruled out by the excellent agreement of our mass spectrum for diborane with the NIST standard diborane spectrum.[37] For example, when we leak diborane into our UHV system, we measure a mass 11 : 26 intensity ratio of ~0.3 : 1, in good agreement with the 0.28 : 1 ratio reported in the NIST database. It is also unlikely that the high mass 11 signal could result from EI fragmentation of higher boranes (B_nH_m, $n \geq 6$), because these, if present in high enough yield to account for such high mass 11 signal, would also result in much higher mass 59 signal than is observed. For example, hexaborane (B_6H_{10}) fragments in EI to produce both masses 11 and 59, however, the mass 59 intensity is ~1.5 times that of mass 11.[37]

Therefore, we conclude that the high mass 11 signal must largely result from desorption of some BH_x species, such as borane (BH_3). Diborane is a hydrogen-bridge-bonded dimer, with gas-phase dissociation enthalpy to 2 BH_3 of only 1.78 eV (i.e. 0.89 eV/BH_3),[38] and both BH_3 and BH_2 are detected mass spectrometrically in gas-phase pyrolysis of diborane at 300 °C.[39] We observe mass 11 desorption signal at low temperatures, raising the question of how BH_2 or BH_3 production is energetically feasible. For reactions of diborane on a surface, the energy required to generate gas-phase BH_x may be supplied by recombination reactions (e.g. producing tetra- and pentaborane) or by formation of strong B-surface bonds.

We also looked for possible desorption of diborane surface reaction products during the 130 K dose, by monitoring masses 11, 26, 48, and 59 during diborane dosing. Signals for masses 11 and 26 were observed in a 0.27:1 ratio, as expected for gas phase diborane, indicating that the diborane sticking probability at 130 K is less than unity, and that little or no borane (BH_3) desorbs during the dose. Sub-unit sticking probability is unsurprising, given that 130 K is only 10 K below the peak of the diborane desorption during TPD/R. Small signals were also observed for masses 48 and 59 during the dose, but these were only 1.2 % and 0.4 % of the mass 26 (diborane) signal for the alumina sample and just 0.2 % and 0.1 % of the diborane

signal for Pt_7/alumina. Clearly, if borane, tetraborane, or pentaborane form on the surface during the diborane dose, they mostly remain adsorbed until the sample is heated.

We estimated desorption energies for the different species by fitting the TPD/R temperature dependence to a second order kinetic model, i.e., assuming that the rate-limiting step is recombination of adsorbed B_xH_y fragments to generate the various boranes observed. The desorption energy distributions are shown in **Figures S8.4.2** and **S8.4.3**, and the desorption energies all fall in the 0.4 to 0.5 eV range.

Diborane surface chemistry will be discussed in more detail after the rest of the experimental and theoretical results are presented. The most important points to keep in mind are:

1. Because all boranes fragment in EI to produce at least some mass 11, the absence of mass 11 signal above ~200 K implies that desorption of boron-containing species is complete by 200 K.

2. The mass 11 signal is far too large to be explained by EI fragmentation of B_nH_m ($n \geq 2$), implying that there is considerable desorption of BH_x.

3. The fact that masses 11, 48, and 59 are observed with higher intensities than mass 26 implies that most of the desorbing boron fraction is in the form of reaction products, rather than diborane.

4. Desorption from alumina and Pt_7/alumina are qualitatively similar, as might be expected, considering that 90% of the Pt_7/alumina surface is alumina.

5. The total amount of B_nH_m desorption is ~13% lower when Pt_7 is present at 10% coverage, and the desorption peaks are shifted 5 to 10 K to higher temperatures.

Species such as B_4H_{10} and B_5H_9 have the H:B ratios that are smaller than that for diborane (3:1). In addition, the XPS results discussed next show that a significant amount of boron remains on the surface after B_nH_m desorption has gone to completion. It is clear, therefore, that hydrogen must also be desorbing during diborane TPD/R. Observation of the

diborane → H_2 desorption channel is not possible, both because the mass 2 background is high, and because the diborane reactant gas mixture has substantial H_2 concentration. To provide some insight into the binding/desorption behavior of hydrogen on Pt_7/alumina, we measured D_2 desorption from a separate Pt_7/alumina sample dosed with 5 L of D_2 at 130 K, and the result is shown in **Figure S8.4.5**. A small amount of D_2 desorption is observed in the temperature range below ~200 K, where borane desorption occurs, but ~90% of hydrogen desorption occurs at higher temperatures, between 200 and 400 K.

5.3.2. X-Ray Photoelectron Spectroscopy

TPD/R probes the B_nH_m species that desorb upon heating, but from the perspective of selectively borating the Pt clusters, it is more important to understand the fate of the boron that remains on the surface. XPS was used to probe the fraction of B on the samples before and after heating. **Figure 5.2** compares B 1s spectra for both alumina and Pt_7/alumina samples, after exposure to 3 L of B_2H_6 at 130 K and after subsequent heating to 700 K. As noted above, the low B 1s photoemission cross section results in poor signal, and the XPS experiments were done using a sample with Pt_7 deposited at twice the normal coverage (~3 x 10^{14} Pt atoms/cm^2).

The B 1s XP spectrum of diborane adsorbed at 130 K on Pt_7/alumina is noisy (bottom right frame) but clearly indicates the presence of two components, fit by peaks at 189.7 and 193.9 eV, suggesting the presence of at least two boron chemical environments. The 130 K spectrum for Pt-free alumina (bottom left) has similar intensity peaking near 193 eV, but the low binding energy intensity is weaker than in the Pt_7/alumina sample. A similar two-component fit was used for this spectrum, resulting in peaks centered at 189.7 and 193.1 eV. After heating to 700 K, only a single broad B 1s feature remains for both alumina and Pt_7/alumina, peaking at 190.5 eV binding energy.

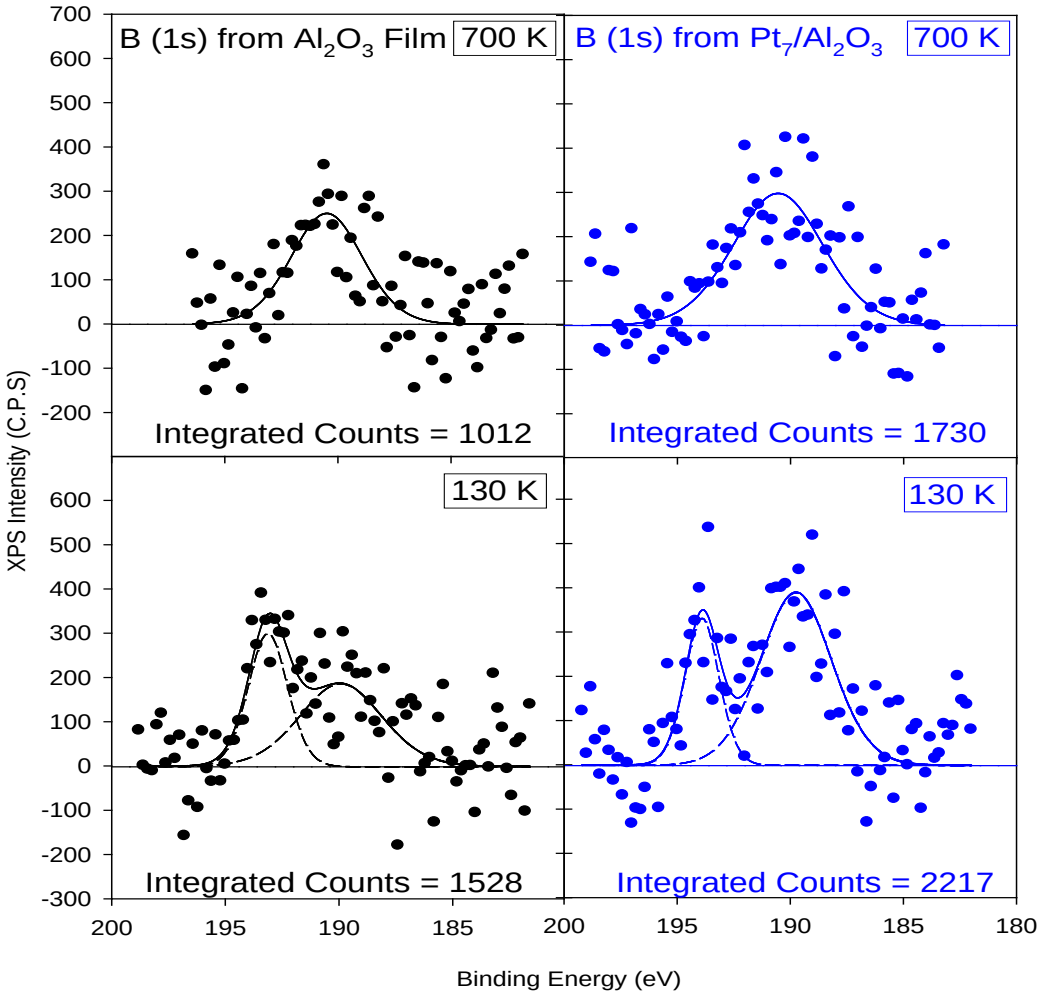

Figure 5.2. XPS spectra obtained for both Pt-free alumina (black) and Pt_7/alumina (blue) samples following exposure to 3 L of B_2H_6 at 130 K and after heating to 700 K.

The integrated intensities, indicated in each frame of the figure, provide additional insight into diborane interactions with alumina and Pt_7. Note that the integrated B 1s intensity at 130 K, i.e., the total amount of boron adsorbed, is ~45% higher when Pt_7 is present. Heating to 700 K to desorb all volatile boron species, leads to loss of ~34% of the initial B 1s signal for alumina, but only ~22% of the (initially larger) B 1s signal for Pt_7/alumina. Thus, after heating, the amount of boron remaining on the sample is ~71% higher when Pt_7 is present, even though the Pt_7 coverage was only ~20%. This result can be compared to the TPD/R results, which showed ~13% less desorption of boron-containing species when Pt_7 was present (at 10% coverage). Taken together, both TPD/R and XPS show that substantially more boron adsorbs when Pt_7 is

present, but that less desorbs, i.e., the presence of a low coverage of Pt_7 leads to substantially more boron deposition on the samples.

5.3.3. Temperature-dependent Ion Scattering Spectroscopy

The final experimental probe of diborane-surface interactions was temperature-dependent He^+ ion scattering (TD-ISS). TD-ISS involves cooling the sample, exposing it to an adsorbate of interest, then monitoring changes in ISS intensities as the sample is heated. A typical raw ISS scan (**Figure S8.4.4**) shows distinct peaks for single scattering from Pt, O, and Al atoms in the surface layer,[35] along with a featureless background due to multiple and subsurface scattering. As discussed previously,[12, 14] Pt_7 deposits in an ensemble of prismatic and single layer structures, with most of the Pt in the surface layer, and thus detectable by ISS. Adsorbates attenuate ISS signals from the underlying surface through a combination of shadowing, blocking, and reduced ion survival probability.[35, 40] For our scattering geometry, attenuation primarily affects signal from atoms directly under, or surrounding, the adsorbate. Thus, adsorbates binding directly on top of the Pt clusters attenuate Pt signal, with little or no effect on Al or O signals. Conversely, adsorption on the alumina film, or at sites around the periphery of the clusters, tends to attenuate Al and O signals, with little or no effect on the Pt signal. As heating drives desorption, the attenuated ISS signals should tend to recover toward the adsorbate-free values. To the extent that diborane exposure and heating leads to cluster agglomeration, forming larger multilayer Pt particles, this would reduce the fraction of Pt in the surface layer, and thus the Pt ISS signal.

As shown in **Figure S8.4.4**, there is no obvious ISS signal for boron ($E/E_0 \approx 0.26$) in the spectrum taken immediately after diborane exposure at 110 K, nor is B ISS signal observed after heating the sample, despite the evidence that boron must be present on these samples (**Figures 5.1** and **5.2**). Lack of boron signal could be taken as evidence that boron is not in the surface layer, however, boron may simply have been undetectable due to a combination of low coverage, small He^+-B scattering cross section ($\propto$ target atomic number[35]), and high multiple-

scattering background at low E/E_0.

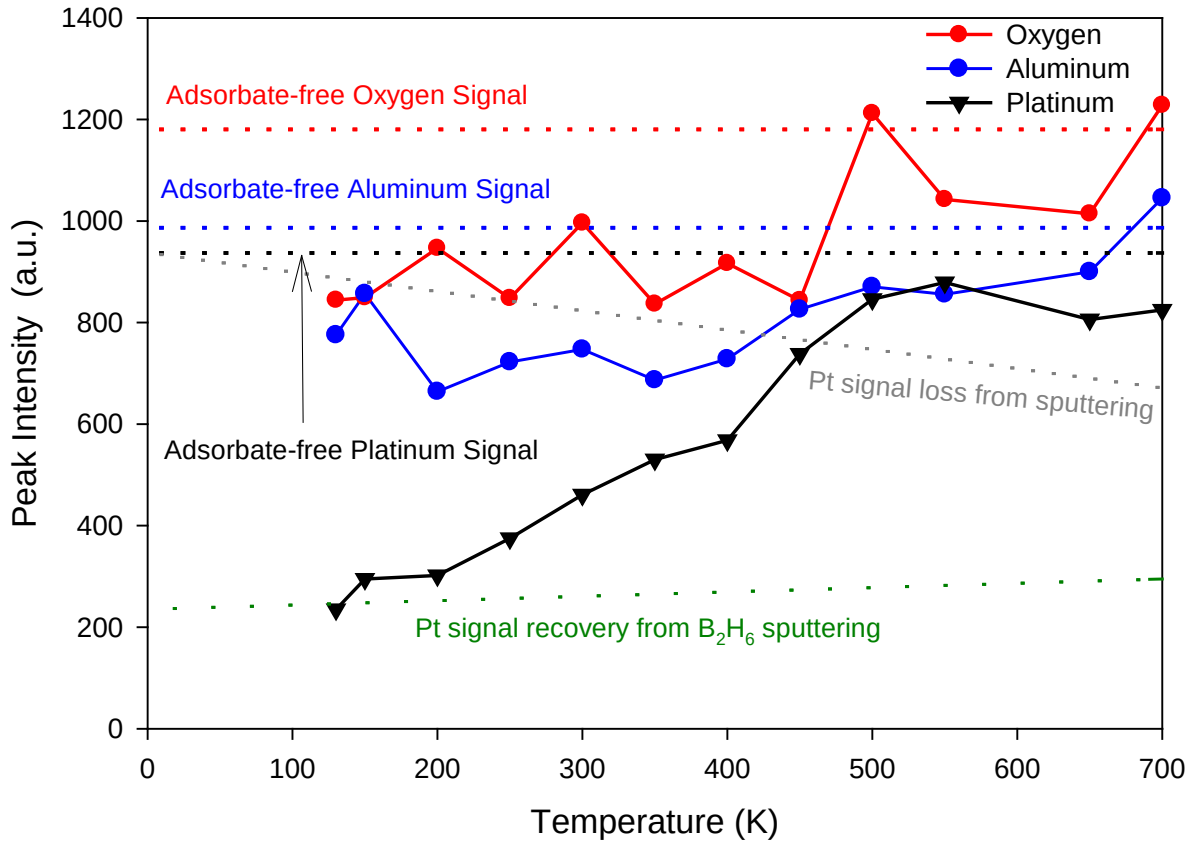

Figure 5.3. TD-ISS of Pt_7/alumina exposed to 1.5 K of diborane at 130 K. The intensities for adsorbate-free Pt_7/alumina, measured separately, are indicated as horizontal dashed lines. The effects of He^+ sputtering on Pt signal in adsorbate-free and diborane-dosed Pt_7/alumina held at 110 K are shown as dashed lines labeled "Pt signal loss from sputtering" and "Pt signal recovery from B_2H_6 sputtering", respectively.

Figure 5.3 compares the Pt, O, and Al ISS signals as a function of temperature, for a Pt_7/alumina sample that was exposed to 1.5 L of B_2H_6 at 110 K, probed by ISS, and then heated to 700 K in 50 K steps, with an ISS measurement made at each temperature. All spectra were collected with low (0.1 μA) He^+ flux impinging at 45° and detected along the surface normal, with 30 second scan time used to minimize sample damage. The horizontal dashed lines show the Pt, O, and Al intensities measured for adsorbate-free Pt_7/alumina in a separate experiment.

Compared to these adsorbate-free values, the signals measured after the B_2H_6 dose are attenuated by ~80% for Pt and ~20% for O and Al, indicating that B_2H_6 binds preferentially in sites that attenuate Pt ISS signal. ISS, thus, is consistent with the XPS and TPD/R results indicating that diborane binds preferentially in association with Pt_7, and provides the additional insight that some or all of this Pt-associated diborane binds on top of the clusters, where it attenuates scattering from underlying Pt. The ~20% attenuation of Al and O signals indicates that some diborane binds in sites that shadow or block scattering from alumina, which could include both sites around the periphery of the clusters, and on the alumina film remote from the clusters.

Interpretation of changes in signal as the sample is heated requires knowledge of the effects of He^+ bombardment occurring during the repeated ISS scans used in TD-ISS. To probe the rate of Pt loss by sputtering, an experiment was made on a separate adsorbate-free Pt_7/alumina sample, held at constant temperature, while taking a series of ISS spectra. The rate of Pt ISS signal decrease is indicated in the Figure by the dashed line labeled “Pt signal loss from sputtering”. Conversely, for a diborane-covered Pt_7/alumina sample held at 110 K, the Pt signal slowly increased during successive ISS scans, due to sputtering of adsorbates initially bound on top of the clusters, as indicated by the line labeled “Pt signal recovery from B_2H_6 sputtering”. The Al and O ISS signals were not observed to change significantly in either control experiment, presumably because the diborane coverage on alumina is low, and sputtering of Al or O from the top layer simply exposes more Al and O in the 2nd layer.

As shown in **Figure 5.3**, the Pt ISS signal starts to recover significantly faster than would be expected from B_2H_6 sputtering at ~200 K, gradually recovering to ~95% of the adsorbate-free value by ~550 K, then is constant at higher temperatures. The Al and O signals remain attenuated up to ~450 K but then recover to their adsorbate-free values by 700 K.

5.3.4. DFT Results for Adsorption of Diborane on Pt_7 Clusters

PW-DFT calculations were performed to identify low energy adsorption geometries for diborane on Pt_7/alumina, as summarized in **Figure 5.4**. We previously reported on the energetics and geometries of numerous isomers of Pt_7 and Pt_8 bound to alumina.[14] Here, we focus on adsorption of diborane on the two lowest energy minima of Pt_7/alumina, which are shown in the small figures next to the titles of each section of **Figure 5.4**. The most stable Pt_7/alumina structure is prismatic (E_{ads} = -5.09 eV, relative to alumina + gas phase Pt_7), but there is a single-layer isomer that is only slightly higher in energy (E_{ads} = -5.04 eV). Seven different isomers of diborane adsorbed on both prismatic and single layer Pt_7/alumina are shown, all of which would contribute to the population at 700 K and below, according to Boltzmann statistics. In these 0 K, *in vacuo* calculations, the most stable configurations of diborane on the prismatic Pt_7 cluster preserve the B-B bond and are adsorbed atop or peripherally to the cluster. On single-layer Pt_7, however, the most stable structures involve B-B bond scission.

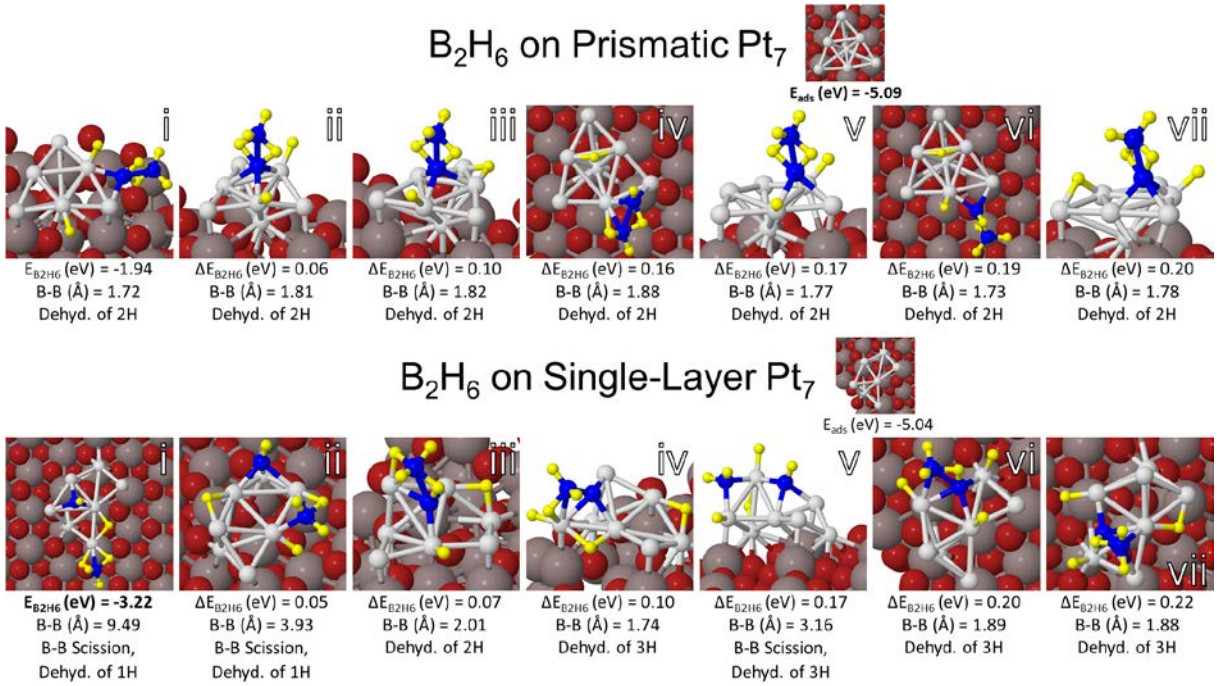

Figure 5.4. The seven lowest minima of diborane (B_2H_6) adsorbed on the two lowest minima of Pt_7, which also represent two different structural classes of Pt clusters, i.e., "prismatic" and "single-layer". The most stable adsorbate-free Pt_7/alumina isomer is prismatic, but with diborane adsorbed the single layer isomer becomes more stable by over 1 eV. Boron atoms are depicted in blue, platinum in light gray, hydrogen in yellow, aluminum in dark gray, oxygen in red.

There are several factors to bear in mind in comparing theory to experiment. Due to computational limits, our DFT calculations were restricted to adsorption of only a single diborane and focused on the strongest diborane binding sites, i.e., diborane binding on the clusters. The experimental diborane coverages were higher and populated binding sites on both Pt_7 and the alumina film. As a result, the calculations cannot address complex chemistry such as higher borane formation and desorption. In addition, while the minima found by DFT clearly illustrate a variety of binding arrangements, we cannot guarantee that they represent all possible low energy binding geometries. Indeed, the fluxionality of these clusters is important in their catalysis but also resists facile theoretical description.[6, 14, 41-44] The complexity of the problem will certainly increase at elevated temperatures or for increasing coverage of B_2H_6.

For prismatic Pt_7/alumina, the most stable isomer in absence of adsorbates, diborane adsorbs atop or at peripheral sites on the cluster. The B-B bond is preserved with only one or two H atoms transferred from diborane to Pt sites. The B-B bond lengths range from 1.72 to 1.88 Å, compared to 1.76 Å calculated for gas-phase diborane (**Figure S8.4.6**), in excellent agreement with the experimental value (1.7645 Å).[45] Relative to prismatic Pt_7/alumina + gas phase B_2H_6, the most stable binding geometry for diborane on prismatic Pt_7 has E_{ads} = -1.94 eV, and the other structures shown are all within 0.2 eV (ΔE_{ads}). The atomic charges for the various isomers of diborane adsorbed on prismatic Pt_7/alumina are shown in **Figure S8.4.7**.

Diborane binds more strongly to the single layer Pt_7/alumina isomer, with E_{ads} = -3.22 eV for the most stable structure. Note that three of the seven isomers shown involve B-B bond scission and other isomers feature a B-B bond elongated by 7-14% compared to gas-phase B_2H_6. All isomers involve transfer of up to three H atoms from B to Pt sites. The atomic charges for the various isomers of diborane adsorbed on single layer Pt_7/alumina are shown in **Figure S8.4.8**.

The substantially higher E_{ads} for diborane on the single layer Pt_7 isomer implies that with one diborane adsorbed, single layer Pt_7/alumina becomes the global minimum by ~1.2 eV. The

barrier height for diborane-induced isomerization from the prismatic local minimum to the single layer global minimum is unknown, but comparison with ethylene adsorption is suggestive. DFT also found that ethylene adsorbed more strongly on single layer Pt_7/alumina (E_{ads} = -1.97 eV), compared to prismatic Pt_7/alumina (E_{ads} = -1.29 eV), and in that case, adsorption of three ethylene molecules was sufficient to eliminate the prismatic-to-single-layer isomerization barrier for Pt_7.[14] The difference in adsorption energy for diborane on the two Pt_7 isomers is almost twice as large as the difference for ethylene, suggesting that isomerization is not unlikely at the diborane exposures used in the experiments.

5.3.5. Molecular Dynamics Simulations of Diborane/Pt_7/Alumina Thermal Chemistry

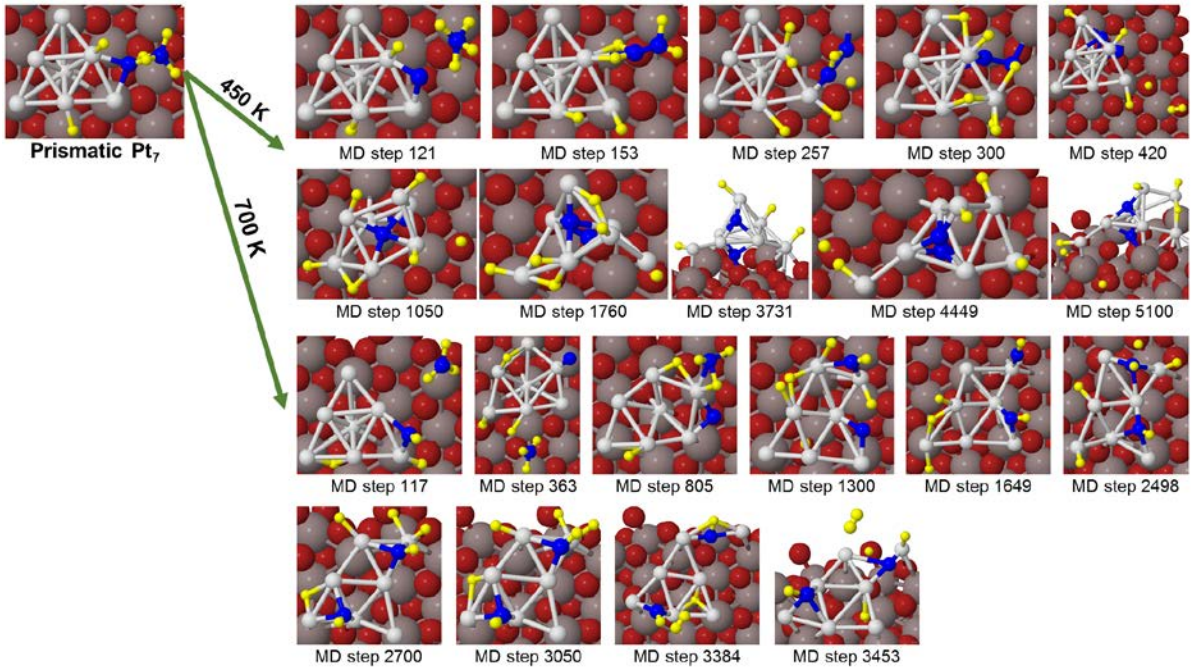

Figure 5.5. MD trajectories of diborane decomposition on prismatic Pt_7 reveal that diborane may either split apart to form a B-O_{surf} anchor or maximize Pt-B bonds by adsorbing onto a Pt cluster facet. The prismatic structure can also distort significantly or form a flattened, single-layer geometry. At 450 K, beyond 3.0 ps, the cluster changed very little with only the hydrogens translating from one atom to the next or H_2 diffusing through the vacuum gap. Each MD time step corresponded to 1 fs.

To probe adsorbate effects and chemistry at the elevated temperatures used in the experiments, we used Born-Oppenheimer MD simulations to examine the fate of diborane adsorbed on Pt_7 at 450 and 700 K. Both of these temperatures are well above the range where

B_nH_m desorption is observed (**Figure 5.1**) and in the range where H_2 desorption occurs on Pt clusters (**Figure S8.4.5**). This is also the range of interest for ethylene dehydrogenation, which peaks near 450 K for Pt_7/alumina and goes to completion below 700 K.[14] The prismatic and single-layer minima of Pt_7 represent different initial geometries for diborane to adsorb and react on. Selected highlights from MD trajectories on each structure at both temperatures are given in **Figures 5.5** and **5.6**, respectively (each MD time step corresponds to 1 fs).

Starting with the lowest energy minimum for diborane on prismatic Pt_7, MD shows that at these elevated temperatures diborane undergoes B-B scission to form BH_2, BH_3, or BH_4 fragments, which may then re-adsorb onto Pt sites (**Figure 5.5**). Interestingly, in the 450 K trajectory, diborane dehydrogenated completely with one of the boron atoms moving to a position underneath the Pt_7 cluster, forming Pt-B-O_{surf} bonds and anchoring the cluster to the alumina surface. In contrast, in the 700 K trajectory, the Pt cluster flattened to a triangular, single-layer structure with BH fragments maximizing the number of Pt-B bonds. Throughout the MD trajectories, at both temperatures, hydrogen atoms are mobile, translating to adsorb onto the Pt cluster, to Al, O atoms on alumina, or forming H_2 (shown desorbing from the surface). Moreover, both the 450 and 700 K MD trajectories favored B-B bond scission early on, within the first 120 fs of the simulation.

Starting with lowest energy isomer of diborane on single-layer Pt_7, at either 450 or 700 K, the Pt cluster retains much of its structure with B or BH_y fragments making small translations (**Figure 5.6**). Similar to the prismatic Pt cluster, at 450 K, diborane's boron atoms either sit on top of the cluster to maximize Pt-B bonds or move below the cluster to form Pt-B-O_{surf} anchor bonds. At 700 K, BH fragments sit on the Pt cluster facets, forming 3-4 Pt-B bonds.

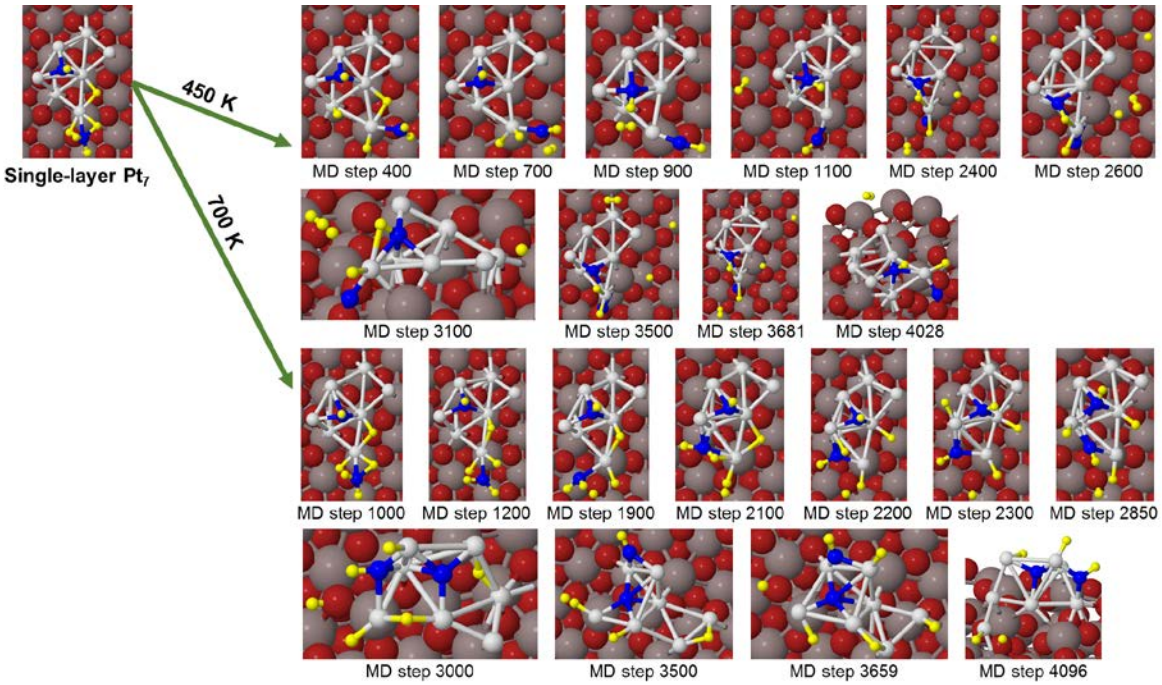

Figure 5.6. MD trajectories of the decomposition of diborane on single-layer Pt_7 reveal similar bonding trends to prismatic Pt_7. The stability of the single-layer structure observed in ground state calculations is retained during MD trajectories at these elevated temperatures of 450 and 700 K. At 450 K, MD steps >3100 resemble MD step 2600. Angled side views of the system at MD steps 3100 and 4028 were taken in order to highlight the B-O_{surf} anchor. Each MD time step corresponded to 1 fs.

Due to computational time limitations, we were only able to run a few trajectories, following the dynamics for ~5 ps. Of course, the MD picture is incomplete, and only accesses a small portion of configurational space accessible to our systems. Nonetheless, these MD results give insight into possible decomposition mechanisms of diborane on alumina-supported Pt clusters. One obvious point is that Pt, B, and H atoms are all mobile at these temperatures, consistent with the DFT finding of numerous structures within a few tenths of an eV of the global minimum. By the end of the trajectories, the Pt_7 clusters remained intact, but most of the initial B-H bonds had broken, with H atoms binding instead to Pt or to O atoms of the support, and some H atoms recombined to form H_2 seen desorbing from the surface, even on the relatively short time scale of the trajectory. Boron atoms prefer to bind either under the cluster, forming Pt-B-O_{surf} linkages, or to facets of the Pt clusters, forming multiple Pt-B bonds. Boron atoms bound to Pt facets may block preferred carbon adsorption sites or weaken carbon adsorption, which

may account for the observed resistance to coking of boronated Pt clusters.[4-6] However, B bound between the cluster and the support also affect the affinity to C by altering the electronic structure of the system, particularly, the charge transfer from the support to the cluster, as was shown previously.[6]

At the higher diborane coverages of the experiments, additional processes, presumably, would occur, such as coupling of BH fragments to form higher boranes that might desorb (**Figure 5.1**) and more extensive recombinative desorption of H_2. Over longer time scales, particularly at 700 K, additional hydrogen desorption would almost certainly occur, leaving behind Pt_7B_x clusters. The simulations suggest that the Pt_7B_x clusters would have a range of Pt morphologies (prismatic and single-layer) and boron binding sites (Pt facets, Pt-B-O_{surf}), and the cluster structures are likely fluxional at high temperatures.

5.3.6. Pt_4B_4/Alumina

As a computationally tractable model for Pt_nB_m clusters with higher boron mole fraction, as probably form in the experiments, we chose to study Pt_4B_4 clusters. The global optimization search for gas-phase and adsorbed Pt_4B_4 was performed utilizing the Basin Hopping method,[24] and the set of low energy isomers is shown in **Figures 5.7** and **S8.4.9** for Pt_4B_4/alumina and gas-phase Pt_4B_4, respectively. Both gas-phase and adsorbed Pt_4B_4 structures tend to be (quasi-)planar. Huynh, et. al. ascribed the drive towards planarity with increasing boron concentration to the covalent nature of boron-boron bonds and boron-metal bonding in mixed metal-boron clusters in B_nAl_{6-n} and LiB_nAl_{6-n} systems, and proposed that this effect may be general to other metal-boron systems.[4-6, 46] Noticeably, their study found the transition from predominantly 3D to 2D structures occurs when the Al:B ratio is 1:1. The Pt-B clusters seem to follow a similar pattern, with the single-layer geometry dominating in gas-phase Pt_4B_4 (isomers i-iii, see SI) as compared to Pt_7B (isomer v).[6]

For alumina-supported Pt_4B_4, the Pt_4 moiety is also near-planar, however, the B atoms tend to be bent toward the alumina support to allow formation of short B-O_{surf} bonds anchoring

the Pt_4 moiety to the alumina. The B-B bonds in surface-bound clusters are ~1.7 Å, and Pt-B bonds are ~2 Å. The results also show that, even for high boron concentrations, the energetically favorable structures have all the Pt atoms in the surface layer, with most or all of the B atoms underneath the clusters. This has important implications for interpretation of the TD-ISS results, and also means that all the Pt atoms are exposed and available to act as catalytic sites.

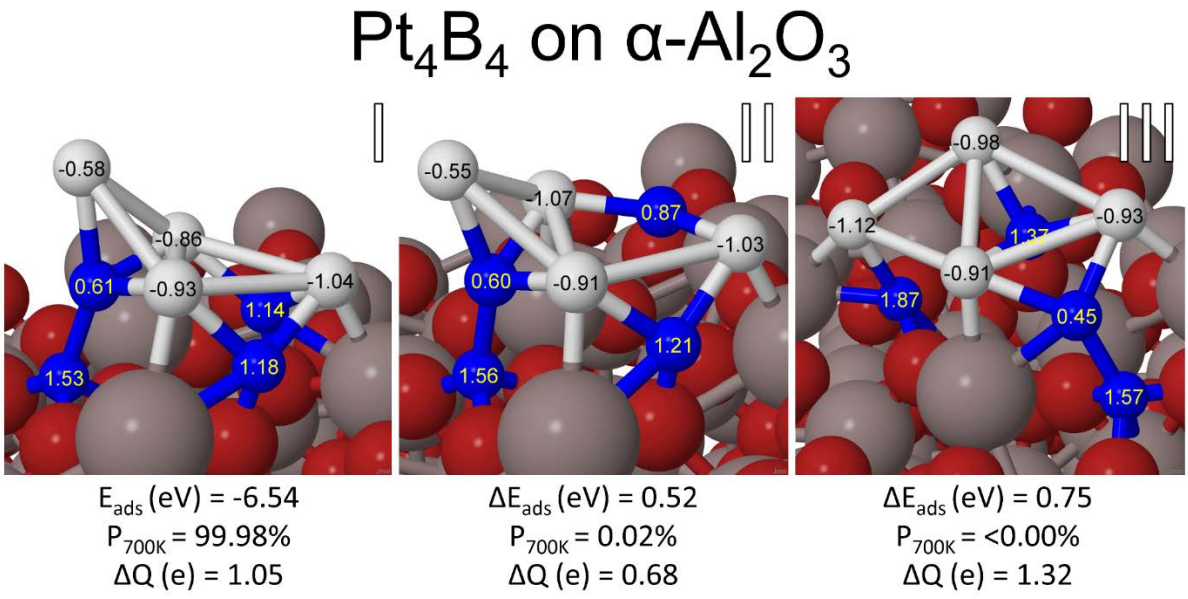

Figure 5.7. The three lowest minima of Pt_4B_4 adsorbed on alumina with their associated adsorption energies (E_{ads}), Boltzmann populations at 700 K (P_{700K}), and Bader charges on individual atoms. Boron atoms are depicted in blue, platinum in light gray, aluminum in dark gray, oxygen in red. Isomer II is very similar to Isomer I but with a B-O_{surf} anchor broken.

In previous publications, we predicted that addition of electropositive boron would temper the highly active and electronegative Pt clusters by reducing the charge of the cluster.[6, 47] High electron density favors ethylene adsorption in sp^3-hybridized geometries, a precursor to dehydrogenation. On the other hand, sp^2-hybridization tends to favor hydrogenation or desorption.[1, 3, 48-50] In pure Pt_7 and Pt_8 clusters on alumina, Pt atoms were found to have charges ranging from +0.78 e, when bound primarily to O_{surf}, to -0.73 e, when bound primarily to Al_{surf}, with net cluster charge being ca. -1 e.[14] For Pt_7B on alumina, the net charge on the clusters

dropped to ca. -0.35 e, with strong variations from one isomer to another.[6] With increasing boron content, Pt_4B_4 clusters on alumina become positively charged, between +0.68 and +1.32 e. In addition, the charge separation between Pt and B atoms increases with increasing boron concentration: Pt remains negative, ranging from -0.5 to -1.1 e, and B atoms are positively charged, between +0.4 e, when forming a mix of Pt-B or B-B bonds within the cluster, and +1.87 e, when forming a $B\text{-}O_{surf}$ anchor. Increasing the B:Pt ratio also increases the stability of supported Pt-B clusters with Pt_4B_4 adsorbing more strongly by ~1.9 eV as compared to Pt_7B (E_{ads} = -4.62 eV[6]). This may be attributed to the cluster maximizing $B\text{-}O_{surf}$ interactions and optimizing the electrostatic attraction between the electronegative Pt atoms and electropositive B atoms with a 1:1 ratio of Pt:B.[51] .

5.4. DISCUSSION

5.4.1. Decomposition of Diborane on Pt_7/alumina

From our previous study of ethylene dehydrogenation on borated Pt clusters, we know that boration of Pt_7/alumina substantially reduces the ethylene desorption temperature, resulting in a significant decrease in the fraction of ethylene that undergoes unwanted dehydrogenation.[6] The obvious questions are how much boron is deposited on the Pt_7/alumina surface by the boration process used, and in what kinds of binding sites is it found.

Figure 5.1 shows that quite complex chemistry occurs when diborane is adsorbed on both alumina and Pt_7/alumina surfaces. The chemistry is qualitatively similar for the two surfaces, reflecting the fact that the Pt_7 coverage is only 10%. Similarities include the low intensity for diborane desorption (mass 26), and higher intensities for desorption of both BH_x (mass 11) and higher boranes such as tetraborane (mass 48) and pentaborane (mass 59). The fact that desorption is dominated by B_1 or B_n ($n \geq 4$) species indicates that adsorbed diborane dissociates at low temperatures, undergoing complex recombination chemistry.

The DFT results support this conclusion, showing that, even at 0 K, diborane spontaneously loses H atoms on both prismatic and single layer Pt_7, and that on the single layer

isomer, B-B bond scission also occurs. Given that the single layer isomer becomes the global minimum upon diborane adsorption, extensive diborane decomposition is expected. That expectation is supported by the MD trajectory results, in which B-B bond scission and Pt_7 isomerization is observed on the picosecond time scale at moderate temperatures. Experimentally (**Figure S8.4.5**) and computationally (**Figure 5.6**), hydrogen recombinative desorption is observed at moderate temperatures, suggesting that the final state of the borated Pt_7/alumina samples consists primarily of Pt and B atoms, binding in some fashion to the alumina support.

The XPS results in **Figure 5.2** show that a significant fraction of the boron initially adsorbed as diborane is left behind after thermal desorption is complete. The amount of boron on the surface can be estimated from XPS peak intensities. For this analysis we take advantage of the fact both Pt and B are deposited on the sample surface at low coverage, and that we know the amount of Pt deposited quite precisely (1.5×10^{14} Pt atoms/cm^2). Attenuation by inelastic scattering can be neglected for photoelectrons emitted by atoms in the surface layer, thus for the Pt_7/alumina sample, the B/Pt coverage ratio can be calculated from the ratio of integrated B 1s and Pt 4d intensities. The only information needed for this calculation is the ratio of B 1s and Pt 4d photoemission cross sections, for which we used theoretical cross sections reported by Yeh *et al.*[34] ($\sigma_{B1s} = 6.6 \times 10^{-3}$ Mb, $\sigma_{Pt4d} = 2.64 \times 10^{-1}$ Mb), which we checked against empirical atomic sensitivity factors[52] taking the electron attenuation length into account.[53] (For our 54.7° x-ray source-analyzer angle, photoemission asymmetry can be neglected).[54] For the Pt-free alumina sample, we determined the boron coverage by comparison to the Pt_7/alumina sample studied under identical conditions. Because of the extremely weak B 1s signal (**Figure 5.2**), the resulting boron coverages are estimated to have uncertainties of ±40%.

For the Pt-free alumina film, this analysis gives a boron coverage immediately after 130 K diborane exposure of ~9.8 B atoms/nm^2 corresponding to ~5 B_2H_6/nm^2. From its structure, we can estimate that an intact diborane molecule lying flat on a surface would occupy roughly 0.06

nm^2, thus the boron coverage is equivalent to roughly 30% of a close-packed monolayer. That can be compared to the ~20% attenuation of Al and O ISS signals observed after 130 K diborane exposure in the ISS experiment (**Figure 5.3**). After heating the alumina sample to 700 K, the B 1s signal decreased by ~34% to ~6.5 B/nm^2, compared to ~15 O atoms, and 10 Al atoms *per* nm^2 of the alumina film.

For the sample containing 0.2 ML-equivalent of Pt_7 clusters, the amount of B_2H_6 adsorbed at 130 K increased to ~14.2 B/nm^2 or ~7 B_2H_6/nm^2. If we assume the diborane coverage on the alumina portion of the 0.2 ML Pt_7/alumina sample is just 0.8 of the coverage observed on Pt-free alumina, we can estimate that ~4 of the B_2H_6 molecules are on alumina sites, and ~3 are associated with Pt sites. This 0.2 ML-equivalent sample had 0.43 Pt_7 clusters deposited *per* nm^2, leading to the conclusion that ~7 diborane molecules are associated with each Pt_7 cluster. The large attenuation of Pt ISS signal upon diborane exposure (**Figure 5.3**) shows that a significant fraction of the Pt-associated diborane is bound in sites on top of the clusters, but we cannot rule out some diborane in sites around the cluster periphery. We note that for a single B_2H_6, DFT found that diborane fragments occupy both “on top” and peripheral sites (**Figure 5.3**). Heating the sample to 700 K resulted in final B coverage of ~11 B/nm^2. On Pt-free alumina, the final B coverage was 6.5 B/nm^2, thus from the 80:20 alumina:Pt area ratio, we can estimate that of the 11 B/nm^2, ~5.2 are bound to alumina sites, and the remaining ~5.8 B are bound to Pt sites, or 13.5 B atoms/Pt_7. Prior to heating, there were 7 diborane molecules = 14 B atoms in Pt-associated sites. This observation suggests that diborane initially adsorbed in Pt-associated sites decomposes during heating, leaving nearly all of its boron atoms on the surface. The implication is that essentially all the boranes desorbing from Pt_7/alumina (**Figure 5.1**) can be attributed to diborane initially adsorbed on alumina sites. If that conclusion is correct, we would expect ~10% less borane desorption from 0.1 ML Pt_7/alumina, compared to Pt-free alumina, which is reasonably consistent with the observation of ~13% less desorption.

The B 1s binding energies also provide insight into the nature of the binding. Diborane adsorbed at 130 K on Pt_7/alumina gives rise to a high binding energy peak at 193.9 and a broader low binding energy feature that peaks around 189.7 eV. For diborane on alumina, there is a peak at 193.1 eV with similar intensity to that for Pt_7/alumina but the signal at low binding energies is much weaker than for the Pt_7/alumina. The higher binding energy features are in the energy range (193 – 193.7 eV) typically reported for fully oxidized boron (B^{3+}) in compounds such as boron oxide or boric acid.[55] Elemental boron (B^0) is reported to have binding energies around 188 eV,[55] thus the broad 189.7 eV features are suggestive of boron in some partially oxidized form, which obviously is more prevalent when Pt_7 is present. DFT was used to calculate the charges for a single diborane on both prismatic and single layer isomers of Pt_7/alumina, as shown in **Figures S8.4.7** and **S8.4.8**, respectively. It can be seen that roughly half the boron atoms in the various isomers tend to be fully oxidized (B^{3+}), and half are in intermediate oxidation states ($B^{1.5+}$ to $B^{1.6+}$). These results appear to be in good agreement with the observed binding energies. It should be noted, however, that for the higher diborane coverages in the experiments, higher boranes form on the surface. B 1s binding energies for such species are not known, but we note that an orthocarborane ($B_{10}C_2H_{12}$) film deposited on copper is reported to have B 1s binding energy of 189.3 eV,[56] also in reasonable agreement with the lower binding energy feature. For reference, in previous studies of low temperature diborane adsorption/decomposition on Mo(100) and Ni(100) two B 1s peaks were observed at 189.2 eV and 187.6 eV, but in those experiments the boranes were binding directly to metals, rather than oxides.

After heating to 700 K, both alumina and Pt_7/alumina samples show a single broad B 1s peak at ~190.5 eV, suggesting boron is present in a distribution of intermediate oxidation states. This conclusion is broadly consistent with the distribution of boron oxidation states ($B^{0.5+}$ - $B^{1.9+}$) found for B atoms in Pt-B-O_{surf} bridge bonds, as shown for Pt_4B_4 in **Figure 5.7**.

In summary, XPS indicates that at 130 K, diborane adsorbs preferentially in association with Pt clusters, compared to the alumina support, and that little, if any, of this Pt-associated boron desorbs during heating to 700 K. As a result, the boration process investigated leaves Pt clusters with much larger boron coverages than the alumina support. The final B:Pt ratio for the clusters is estimated to be quite high, but we note that the absolute coverages are uncertain by ~ ±40%, due to the very weak B 1s signal. Note also that both the cluster coverage and diborane exposure used in these XPS experiments was twice those for all the other experiments. It is not clear how these changes might have affected the amount of boron deposited *per* cluster, however, we did study how the diborane exposure used in boration affected subsequent ethylene TPD/R. Boration with 0.5 L diborane exposure was found to be almost as effective at suppressing dehydrogenation as boration with 1.5 L exposure, i.e., at least the *chemical effects* of boration appear to saturate at exposures below those used in all the experiments described in this report.

XPS also shows that the boration process leads to some boron deposition on the alumina film support, thus it is important to know how the catalytic properties of the samples are affected by the boron atoms on (or in) the support. To address this question, **Figure 5.8** compares the ethylene adsorption, desorption and dehydrogenation behavior of three samples:

1. As-deposited Pt_7/alumina with no boron exposure ("Pt_7/alumina").

2. Pt_7/alumina borated after cluster deposition, i.e. both Pt_7 and alumina with boron ("B/Pt_7/alumina").

3. Pt_7 deposited on a pre-borated alumina support, i.e., only the alumina was borated ("Pt_7/B/alumina").

Boration was done using our standard method (1.5 L B_2H_6 exposure at 130 K, followed by heating to 700 K), and ethylene TPD/R was carried out under conditions identical to those used in our previous studies[6, 14] (5 L C_2D_4 exposure at 150 K, heating at 3 K/sec to 700 K). Ethylene desorbs from Pt_7/alumina in two components. The low temperature feature was shown

to result from ethylene desorbing from defect sites in the alumina film, and the broad feature peaking near 300 K results from ethylene adsorbed at Pt_7 sites.[14] A substantial amount of D_2 desorption is observed above 300 K for Pt_7/alumina, but none is observed for the alumina film alone. Boration of both the clusters and the support (B/Pt_7/alumina) leads to a substantial decrease in the desorption temperature distribution for ethylene, and near-total attenuation of D_2 desorption. In contrast, borating only the alumina support (Pt_7/B/alumina) has little effect on the Pt_7 chemistry. The low temperature ethylene desorption feature attributed to desorption from the alumina support is less intense and sharper for this sample, suggesting that boration of the alumina support weakens the ethylene-alumina binding, possibly due to boron occupying alumina defect sites. Pre-boration has little effect, however, on the amount or temperature dependence of ethylene desorbing from Pt sites, or on the D_2 production, suggesting that the presence of a small amount of boron in the support has little effect on supported Pt clusters. Clearly, the large effects of boron on chemistry of supported Pt clusters are due to boration of the Pt clusters, rather than the support.

XPS probes boron on the surface, thus providing an indirect method to estimate the fraction that desorbs during heating. TPD/R (**Figure 5.1**) provides a complementary probe of the desorbing fraction, provided that we can convert the measured $B_xH_y^+$ ion signals to fluxes of various neutrals desorbing from the surface. It is impractical to directly calibrate the mass spectrometer for detection of species such as BH_3, tetraborane, or pentaborane (toxic, pyrophoric, not commercially available), but we can do an approximate analysis. We previously calibrated the ion intensity – neutral desorption relationship for C_2D_4,[14] which should have EI cross section similar to that for B_2H_6, and also has similar EI cracking behavior. For desorbing BH_x, B_4H_{10}, and B_5H_9, we note that the EI cross section should scale roughly with number of B atoms, i.e., the total ionization signal should increase roughly linearly with borane size. The extent of EI cracking also increases with borane size,[37] however, such that the fraction of the ion signal appearing at the detected mass values decreases with siz[6]e. As a result of these two

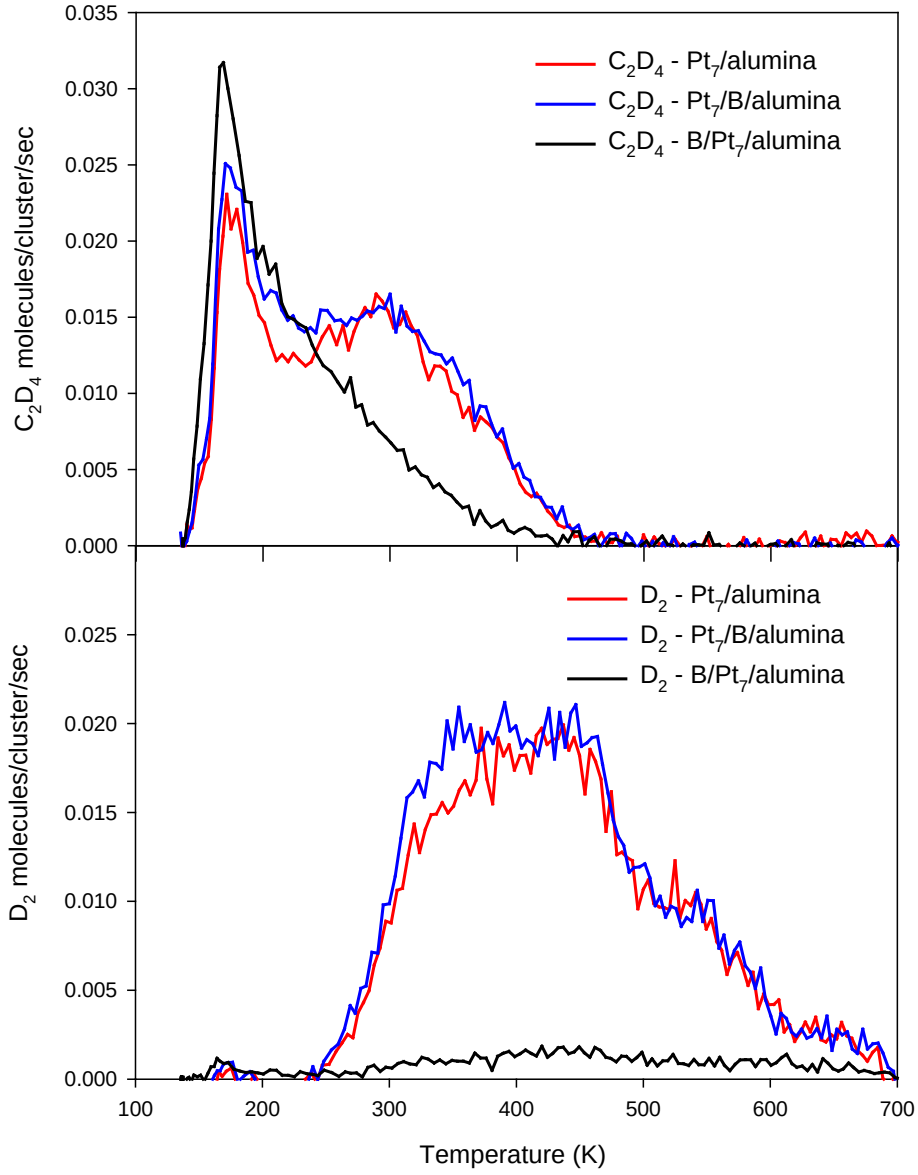

Figure 5.8. Thermal desorption spectra of unreacted ethylene and deuterium product obtained from three samples: (Red) As-deposited Pt_7/alumina with no boron exposure, (blue) Pt_7 deposited on pre-borated alumina, and (black) Pt_7/alumina borated after Pt_7 deposition. Each sample was exposed to 5 L C_2D_4 at 150K. Boration was done using our standard method (1.5 L B_2H_6 at 130 K, heating to 700 K). Separate samples were used for each experiment.

factors, we expect that the detection sensitivity for the various borane products should be similar, and that they should be similar to that for ethylene. Using this crude approximation, we can estimate that of the ~5 B_2H_6 molecules found by XPS to be adsorbed at 130 K, the equivalent of ~0.9 B_2H_6/nm^2 (~20%) desorbs in the form of various boranes, which is in reasonable agreement with the ~30% desorption estimated from XPS. For Pt_7/alumina, ~7 B_2H_6

$_6$/nm^2 adsorb at 130 K, but only the equivalent of ~0.80 B_2H_6/nm^2 (~11%) desorb, compared to ~21% boron desorption estimated by XPS. Considering the crude approximations required for this analysis, and low XPS signal, the TPD and XPS results are in reasonable agreement regarding the amount of boron lost during heating.

Figures S8.4.2 and **S8.4.3** give the desorption energy distributions for the various borane products observed, all of which are below 0.5 eV. The DFT adsorption energies for diborane on Pt_7/alumina are all much higher – ranging up to ~3 eV on the single layer isomer. This discrepancy is easily explained. The DFT calculations were done to find the structure and energetics for a single diborane molecule in the strongest binding sites, which are on the Pt clusters. The experiments were done at much higher diborane coverages and include diborane bound to Pt sites and to the alumina film. As shown by XPS, boron bound to the Pt clusters does not desorb during heating, thus the TPD/R experiments are only sensitive to boranes desorbing by recombination of B_xH_y and H adsorbed on the alumina support, where the binding energies are clearly much lower than for Pt-associated sites.

XPS shows the amount of boron associated with Pt, but provides no insight into the nature of the boron-Pt binding. TPD/R gives the temperature ranges in which boranes (**Figure 5.1**) and hydrogen (**Figure S8.4.5**) desorb, but provides no insight into the sites they desorb from. Analysis of the TD-ISS results (**Figure 5.3**) in light of the XPS and TPD data provides some of this structural information. The large attenuation of Pt ISS signal, and much smaller attenuations of Al and O signals, are consistent with the XPS results. Both show that diborane adsorbs more efficiently in association with the Pt clusters than on alumina sites, and ISS shows that a significant fraction adsorbs on top of the clusters where it attenuates Pt signal. **Figure 5.1** shows that desorption of B_nH_m species is complete by ~200 K, thus it is surprising that there is no significant recovery of Pt, O, or Al ISS signals as the sample is heated to 200 K. Recovery of the Pt ISS signal occurs in two stages at higher temperatures. Between 200 and 400 K, the Pt signal increases to about half the expected value for adsorbate-free Pt_7. This is the temperature

range in which hydrogen desorbs from Pt_7 (**Figure S8.4.5**), suggesting that desorption of hydrogen exposed some Pt atoms but that ~half the Pt atoms remained blocked by adsorbed boron. This conclusion is consistent with the XPS results indicating that little of the boron associated with Pt sites desorbs, i.e., the borane desorption observed in TPD/R originates almost entirely from the alumina film.

Between 400 and 550 K, the Pt signal recovers to almost the adsorbate-free limit. Since nothing desorbs in this temperature range, the recovery of Pt ISS signal must reflect a structural change in the Pt clusters, and the DFT results suggest the explanation. Both the MD simulations (**Figures 5.5** and **5.6**) and the structures found for adsorbed Pt_4B_4 indicate that the most stable binding sites for boron atoms in Pt_nB_m clusters are in Pt-B-O_{surf} bridging sites, where the B atoms are under the Pt cluster, anchoring it to the surface. As a result, the Pt atoms are in surface layer and detectable by ISS.

The fact that the Pt ISS signal recovers to 95% of the value for adsorbate-free Pt_7 also suggests that sintering or agglomeration of the clusters during the boration process is limited, because either process would tend to form larger, 3D clusters in which a smaller fraction of Pt is in the ISS accessible surface layer. Indeed, the final Pt ISS signal is well above what would be expected from He^+ sputtering of Pt during the series of ISS scans. This, too, is consistent with the XPS results, which indicate high diborane coverage on the Pt clusters, which would tend to shield the underlying Pt from most of the sputtering that occurs for adsorbate-free clusters.

5.5. CONCLUSION

We have shown that diborane exposure followed by heating, preferentially deposits boron atoms on supported Pt clusters, with a much smaller boron coverage on the alumina support. The boron on the alumina support is shown to have essentially no effect on ethylene binding or dehydrogenation on the supported Pt clusters. Therefore, the weakening of the ethylene binding and suppression of dehydrogenation when Pt_n/alumina is borated can be attributed to boron atoms associated with the Pt clusters. This boron is found by DFT, in

agreement with TD-ISS, to move to sites beneath the Pt clusters, forming Pt-B-O_{surf} bonds that anchor the clusters to the support.

5.6. REFERENCES

1 Schulz, H. Short History and Present Trends of Fischer–Tropsch Synthesis. *Appl. Catal., A* **1999**, *186*, 3-12.

2 Rahimi, N.; Karimzadeh, R. Catalytic Cracking of Hydrocarbons over Modified Zsm-5 Zeolites to Produce Light Olefins: A Review. *Appl. Catal., A* **2011**, *398*, 1-17.

3 Shaikhutdinov, S. K.; Frank, M.; Bäumer, M.; Jackson, S. D.; Oldman, R. J.; Hemminger, J. C.; Freund, H.-J. Effect of Carbon Deposits on Reactivity of Supported Pd Model Catalysts. *Catal. Lett.* **2002**, *80*, 115-122.

4 Tan, K. F.; Chang, J.; Borgna, A.; Saeys, M. Effect of Boron Promotion on the Stability of Cobalt Fischer–Tropsch Catalysts. *J. Catal.* **2011**, *280*, 50-59.

5 Xu, J.; Chen, L.; Tan, K. F.; Borgna, A.; Saeys, M. Effect of Boron on the Stability of Ni Catalysts During Steam Methane Reforming. *J. Catal.* **2009**, *261*, 158-165.

6 Ha, M.-A.; Baxter, E. T.; Cass, A. C.; Anderson, S. L.; Alexandrova, A. N. Boron Switch for Selectivity of Catalytic Dehydrogenation on Size-Selected Pt Clusters on Al2o3. *J. Am. Chem. Soc.* **2017**, *139*, 11568-11575.

7 Rousset, J.; Cadrot, A.; Cadete Santos Aires, F.; Renouprez, A.; Mélinon, P.; Perez, A.; Pellarin, M.; Vialle, J.; Broyer, M. Study of Bimetallic Pd–Pt Clusters in Both Free and Supported Phases. *J. Chem. Phys.* **1995**, *102*, 8574-8585.

8 Yang, B.; Khadra, G.; Tuaillon-Combes, J.; Tyo, E. C.; Pellin, M. J.; Reinhart, B.; Seifert, S.; Chen, X.; Dupuis, V.; Vajda, S. Temperature-Dependent Evolution of the Oxidation States of Cobalt and Platinum in Co1–Xptx Clusters under H2 and Co + H2 Atmospheres. *J. Phys. Chem. C* **2016**, *120*, 21496-21504.

9 Bardotti, L.; Tournus, F.; Albin, C.; Boisron, O.; Dupuis, V. Self-Organisation of Size-Selected Coxpt1-X Clusters on Graphite. *Phys. Chem. Chem. Phys.* **2014**, *16*, 26653-26657.

10 Moskovkin, P.; Pisov, S.; Hou, M.; Raufast, C.; Tournus, F.; Favre, L.; Dupuis, V. Model Predictions and Experimental Characterization of Co-Pt Alloy Clusters. *Eur. Phys. J. D* **2007**, *43*, 27-32.

11 Kaden, W. E.; Kunkel, W. A.; Anderson, S. L. Cluster Size Effects on Sintering, Co Adsorption, and Implantation in Ir/Sio_2. *J. Chem. Phys.* **2009**, *131*, 114701, 1-15.

12 Roberts, F. S.; Kane, M. D.; Baxter, E. T.; Anderson, S. L. Oxygen Activation and Co Oxidation over Size-Selected Ptn/Alumina/Re(0001) Model Catalysts: Correlations with Valence Electronic Structure, Physical Structure, and Binding Sites. *Phys. Chem. Chem. Phys.* **2014**, *16*, 26443 – 26457.

13 Aizawa, M.; Lee, S.; Anderson, S. L. Deposition Dynamics and Chemical Properties of Size-Selected Ir Clusters on Tio2. *Surf. Sci.* **2003**, *542*, 253-275.

14 Baxter, E. T.; Ha, M.-A.; Cass, A. C.; Alexandrova, A. N.; Anderson, S. L. Ethylene Dehydrogenation on Pt4,7,8 Clusters on Al2o3: Strong Cluster Size Dependence Linked to Preferred Catalyst Morphologies. *ACS Catal.* **2017**, *7*, 3322-3335.

15 Blöchl, P. E. Projector Augmented-Wave Method. *Phys. Rev. B* **1994**, *50*, 17953.

16 Kresse, G.; Joubert, D. From Ultrasoft Pseudopotentials to the Projector Augmented-Wave Method. *Phys. Rev. B* **1999**, *59*, 1758.

17 Perdew, J. P.; Burke, K.; Ernzerhof, M. Generalized Gradient Approximation Made Simple. *Phys. Rev. lett.* **1996**, *77*, 3865.

18 Kresse, G.; Furthmüller, J. Efficient Iterative Schemes for Ab Initio Total-Energy Calculations Using a Plane-Wave Basis Set. *Phys. Rev. B* **1996**, *54*, 11169-86.

19 Kresse, G.; Furthmüller, J. Efficiency of Ab-Initio Total Energy Calculations for Metals and Semiconductors Using a Plane-Wave Basis Set. *Comput. Mater. Sci.* **1996**, *6*, 15-50.

20 Kresse, G.; Hafner, J. Ab Initio Molecular Dynamics for Liquid Metals. *Phys. Rev. B* **1993**, *47*, 558.

21 Kresse, G.; Hafner, J. Ab Initio Molecular-Dynamics Simulation of the Liquid-Metal–Amorphous-Semiconductor Transition in Germanium. *Phys. Rev. B* **1994**, *49*, 14251.

22 Bourdillon, A.; El-Mashri, S.; Forty, A. Application of Tem Extended Electron Energy Loss Fine Structure to the Study of Aluminium Oxide Films. *Philos. Mag. A* **1984**, *49*, 341-352.

23 Levin, I.; Brandon, D. Metastable Alumina Polymorphs: Crystal Structures and Transition Sequences. *J. Am. Ceram. Soc.* **1998**, *81*, 1995-2012.

24 Wales, D. J.; Doye, J. P. Global Optimization by Basin-Hopping and the Lowest Energy Structures of Lennard-Jones Clusters Containing up to 110 Atoms. *J. Phys. Chem. A* **1997**, *101*, 5111-5116.

25 Boyd, K. J.; Lapicki, A.; Aizawa, M.; Anderson, S. L. A Phase-Space-Compressing, Mass-Selecting Beamline for Hyperthermal, Focused Ion Beam Deposition. *Rev. Sci. Instrum.* **1998**, *69*, 4106-4115.

26 Kane, M. D.; Roberts, F. S.; Anderson, S. L. Mass-Selected Supported Cluster Catalysts: Size Effects on Co Oxidation Activity, Electronic Structure, and Thermal Stability of Pd_n/Alumina (N ≤ 30) Model Catalysts. *Int. J. Mass Spectrom.* **2014**, *370*, 1-15.

27 Kane, M. D.; Roberts, F. S.; Anderson, S. L. Effects of Alumina Thickness on Co Oxidation Activity over Pd_{20}/Alumina/Re(0001): Correlated Effects of Alumina Electronic Properties and Pd_{20} Geometry on Activity. *J. Phys. Chem. C* **2015**, *119*, 1359–1375.

28 Chen, P. J.; Goodman, D. W. Epitaxial Growth of Ultrathin Al_2o_3 Films on Ta(110). *Surf. Sci.* **1994**, *312*, L767-L773.

29 Street, S. C.; Goodman, D. W. Chemical and Spectroscopic Studies of Ultrathin Oxide Films. *Chem. Phys. Solid Surf.* **1997**, *8*, 375-406.

30 Lai, X.; Chusuei, C. C.; Luo, K.; Guo, Q.; Goodman, D. W. Imaging Ultrathin Al2o3 Films with Scanning Tunneling Microscopy. *Chem. Phys. Lett.* **2000**, *330*, 226-230.

31 Wu, Y.; Garfunkel, E.; Madey, T. E. Growth and Oxidation of Ultra-Thin Al Films on the Re(0001) Surface. *Surf. Sci.* **1996**, *365*, 337-352.

32 Wu, Y.; Garfunkel, E.; Madey, T. E. Growth of Ultrathin Crystalline Al2o3 Films on Ru(0001) and Re(0001) Surfaces. *J. Vac. Sci. Technol., A* **1996**, *14*, 2554-2563.

33 Yu, J.; Boatz, J. A.; Anderson, S. L. Borane-Aluminum Surface Interactions: Enhanced Fracturing and Generation of Boron-Aluminum Core-Shell Nanoparticles. *J. Phys. Chem. C* **2017**, *121*, 14176-14190.

34 Yeh, J. J.; Lindau, I. Atomic Subshell Photoionization Cross Sections and Asymmetry Parameters: 1< Z < 103. *At. Data and Nucl. Data Tables* **1985**, *32*, 1-155.

35 Rabalais, J. W. *Principles and Applications of Ion Scattering Spectrometry : Surface Chemical and Structural Analysis*; Wiley: New York, 2003; pp 336.

36 Bandiera, J.; Naccache, C.; Mathieu, M. V. Products Formed by the Hydrolysis of Diborane in Contact with Γ-Alumina. *C. R. Acad. Sci., Paris, Ser. C* **1969**, *268*, 901-4.

37 Stein, S. E., director Ir and Mass Spectra. In *Nist Chemistry Webbook, Nist Standard Reference Database Number 69*, Mallard, W. G.; Linstrom, P. J., Eds. NIST Mass Spec Data Center, National Institute of Standards and Technology: Gaithersburg MD 20899 (http://webbook.nist.gov). 2000.

38 Chase, M. W., Jr. ; Davies, C. A.; Downey, J. R., Jr.; Frurip, D. J.; McDonald, R. A. Janaf Thermochemical Tables, Third Edition. *J. Phys. Chem. Ref. Data* **1985**, *14*

39 Fehlner, T. P.; Koski, W. S. Direct Detection of the Borane Molecule and the Boryl Radical by Mass Spectrometry. *J. Am. Chem. Soc.* **1964**, *86*, 2733-2734.

40 Kaden, W. E.; Kunkel, W. A.; Roberts, F. S.; Kane, M.; Anderson, S. L. Co Adsorption and Desorption on Size-Selected Pdn/Tio2(110) Model Catalysts: Size Dependence of Binding Sites and Energies, and Support-Mediated Adsorption. *J. Chem. Phys.* **2012**, *136*, 204705/1-204705/12.

41 Zhai, H.; Alexandrova, A. N. Fluxionality of Catalytic Clusters: When It Matters and How to Address It. *ACS Catal.* **2017**, *7*, 1905-1911.

42 Gao, M.; Lyalin, A.; Takagi, M.; Maeda, S.; Taketsugu, T. Reactivity of Gold Clusters in the Regime of Structural Fluxionality. *J. Phys. Chem. C* **2015**, *119*, 11120-11130.

43 Hakkinen, H.; Abbet, S.; Sanchez, A.; Heiz, U.; Landman, U. Structural, Electronic, and Impurity-Doping Effects in Nanoscale Chemistry: Supported Gold Nanoclusters. *Angew. Chem., Int. Ed.* **2003**, *42*, 1297-1300.

44 Xing, X.; Li, X.; Yoon, B.; Landman, U.; Parks, J. H. Dynamic Fluxionality and Enhanced Co Adsorption in the Presence of Coadsorbed H 2 O on Free Gold Cluster Cations. *Int. J. Mass Spectrom.* **2015**, *377*, 393-402.

45 Sams, R. L.; Blake, T. A.; Sharpe, S. W.; Flaud, J. M.; Lafferty, W. J. High-Resolution Infrared Study of the N14, N17, and N18bands Of11b2h6and10b11bh6. *J. Mol. Spectrosc.* **1998**, *191*, 331-342.

46 Huynh, M. T.; Alexandrova, A. N. Persistent Covalency and Planarity in the B N Al6–N 2–and Lib N Al6–N–(N= 0–6) Cluster Ions. *J. Phys. Chem. Lett.* **2011**, *2*, 2046-2051.

47 Dadras, J.; Jimenez-Izal, E.; Alexandrova, A. N. Alloying Pt Sub-Nano-Clusters with Boron: Sintering Preventative and Coke Antagonist? *ACS Catal.* **2015**, 5719-5727.

48 Perry, D. A.; Hemminger, J. C. Σ-Bond Metathesis on a Surface: Dehydrogenation of Cyclohexane on Hydrogen-Saturated Pt (111). *J. Am. Chem. Soc.* **2000**, *122*, 8079-8080.

49 Carlsson, A.; Madix, R. The Dynamics of Ethylene Adsorption on Pt (111) into Di-Σ and Π-Bonded States. *J. Chem. Phys.* **2001**, *115*, 8074-8082.

50 Stöhr, J.; Sette, F.; Johnson, A. L. Near-Edge X-Ray-Absorption Fine-Structure Studies of Chemisorbed Hydrocarbons: Bond Lengths with a Ruler. *Phys. Rev. Lett.* **1984**, *53*, 1684.

51 Ha, M.-A.; Dadras, J.; Alexandrova, A. Rutile-Deposited Pt–Pd Clusters: A Hypothesis Regarding the Stability at 50/50 Ratio. *ACS Catal.* **2014**, *4*, 3570-3580.

52 Moulder, J. F.; Stickle, W. F.; Sobol, P. E.; Bomben, K. D.; J. Chastain & R. C. King, J., eds. *Handbook of X-Ray Photoelectron Spectroscopy*; Physical Electronics: Eden Prarie, MN, 1995.

53 Powell, C. J.; Jablonski, A. *Nist Electron Effective-Attenuation-Length Database* 1.0; NIST: Gaithersburg, 2001.

54 Briggs, D.; Seah, M. P. *Practical Surface Analysis, Volume 1 : Auger and X-Ray Photoelectron Spectroscopy,* , 2nd ed.; John Wiley & sons: Chichester, 1992; Vol. 1; pp 1-657.

55 Wagner, C. D.; Naumkin, A. V.; Kraut-Vass, A.; Allison, J. W.; Powell, C. J.; Jr., J. R. R. Nist X-Ray Photoelectron Spectroscopy Database. *NIST Standard Reference Database 20, Version 3.2 (Web Version)* **2000**.

56 Pasquale, F. L.; Kelber, J. A. Site-Specific Electron-Induced Cross-Linking of Ortho-Carborane to Form Semiconducting Boron Carbide. *Appl. Surf. Sci.* **2012**, *258*, 2639-2642.

CHAPTER 6

Photocatalysis with Defective Anatase

6.1. INTRODUCTION

Photocatalytic CO_2 reduction in the presence of water may participate in reactions as diverse as hydrogen evolution,[1] methane production[2,3], and the formation of bicarbonate/carbonic acid species[4,5] Notably, these reactions may be tuned and improved at the catalytic interface with the addition of titania. Anpo, et. al. suggested that the presence of defects in titania such as oxygen vacancies provide active sites for CO_2 and H_2O reduction, the key reaction intermediates for methanol production.[6] In collaboration with experiment, PW-DFT calculations were performed investigating mechanisms of CO_2 reduction and H_2O splitting on defective anatase, a metastable phase of TiO_2. The introduction of titania on photocathodes composed of InP/Cu and heterojunctions of GaAs resulted in improved photocatalytic performance.

TiO_2-passivated InP with Cu nanopillars were fabricated for CO_2 reduction at an applied overpotential of -0.6 V vs normal hydrogen electrode (NHE).[7] In addition to providing a stable photocatalytic surface, the TiO_2-passivation layer provides substantial enhancement in the photoconversion efficiency through the introduction of O vacancies associated with the non-stoichiometric growth of TiO_2 by atomic layer deposition. The TiO_2 film increases the Faraday efficiency of methanol production by 5.7x to 4.79% under an applied potential of -0.6 V vs. NHE, which is 1.3V below the standard redox potential of $E^o(CO_2/CO_2^-)$ = -1.9 eV (see **Figure 6.1**). An additional investigation on GaAs/TiO_2 heterojunctions with a thin surface TiO_2 layer found they are conductive with applications to water splitting for hydrogen evolution.[8] The photocatalytic performance of these heterostructures shows a very strong dependence on the thickness of the TiO_2 over the range of 0 - 15nm. Thinner films (1 - 10nm) are amorphous and show enhanced catalytic performance with respect to bare GaAs (see **Figure 6.2**). Our theoretical work focuses on anatase, a metastable phase of TiO_2 known for its reactivity, in order to study the advantageous effects of this material on the reagents of interest. DFT calculations show that

water molecules and CO_2 molecules may bind stably or reactively to vacancy sites on defective anatase, which can further improve the photocatalytic charge transfer process in these systems.

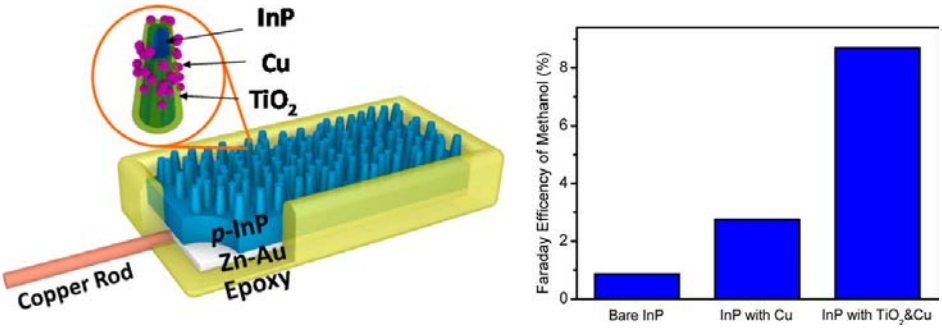

Figure 6.1. (LEFT) The schematic of the photocathode displays the complex catalytic interface participating in methanol production. (RIGHT) The addition of titania resulted in the most significance increase of the Faraday efficiency of methanol production from the bare InP photocathode.

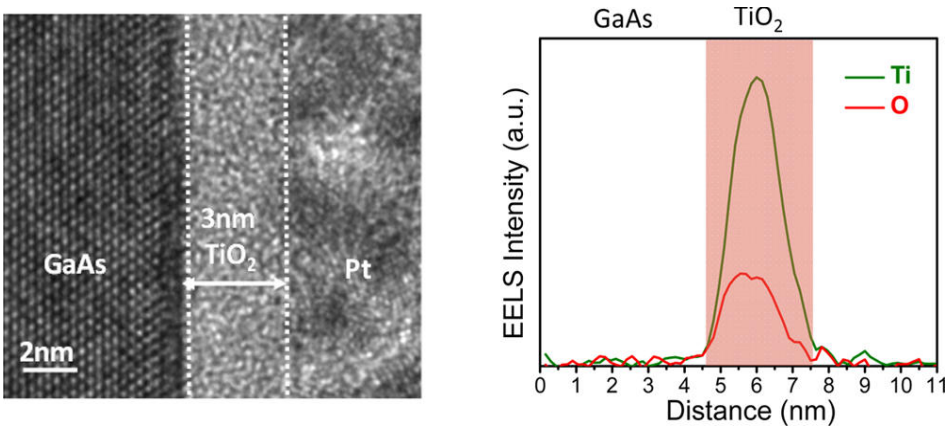

Figure 6.2. (LEFT) High resolution transmission electron microscopy image of TiO_2 film deposited after 75 cycles. (RIGHT) Electron energy-loss spectroscopy show the spatial profile of Ti L edge (green line) and O K edge map (red line) after 75 cycles of TiO_2 deposition on the GaAs sample.

.

6.2. METHODOLOGY

As in previous publications[7,8], plane-wave density functional theory (PW-DFT) calculations utilizing ultrasoft pseudopotentials containing scalar relativistic corrections were performed with the Quantum Espresso package.[9-12] These spin-unrestricted calculations employed the Perdew-Burke-Ernzerhof[13] (PBE) functional with Grimme's method for dispersion corrections[14] (+D) and a Hubbard *U* parameter of 3.6 eV (+*U*). The wave functions (charge

density) were expanded to 435.2 (4.352) eV. The small (101) anatase surface of 16 TiO_2 units was utilized for single-adsorbate calculations of H_2O and CO_2. In order to accommodate coadsorption of the two reagents, H_2O and CO_2, the 16 TiO_2 surface was grown to a large (2 × 2 × 1) slab with a vacuum gap >12 Å (see SI). The Monkhorst-Pack k-point grid of (1 × 1 × 1) centered at Γ proved sufficient for both the small and the large slab.

Adsorption energies were calculated by subtracting energies of the two components (reagent and surface) from the energy of the adsorbed system:

$$E_{ads}=E[surf+molecule]-E[surf]-E[molecule]$$

where the surface was stoichiometric anatase or defective anatase with a surface oxygen vacancy and the reagent molecule (CO_2, CO_2^{-}, or H_2O)

Coadsorption energies were calculated by subtracting surface and reagent energies from the total energy of the adsorbed system:

$$E_{coads}\ (eV) = E[surf + H_2O + CO_2] – E[surf] – E[H_2O] – E[CO_2]$$

where E[surf] was the energy of the anatase surface with a surface oxygen vacancy, $E[H_2O]/E[CO_2]$ are the $[H_2O]/[CO_2]$'s gas phase energy alone, and $E[surf + H_2O + CO_2]$ refers to the coadsorbed system. The formation energy of oxygen vacancy remained reasonable at E_{vac} = -3.93 eV.[15] The formation energy of the oxygen vacancy was calculated from the equation

$$E_{vac} = E_{tot}\ (def) – E_{tot}\ (no\ def) + ½\ \mu\ (O_2)$$

where E_{tot} (def) represents the total energy of the defective surface, E_{tot} (no def) the total energy of the stoichiometric surface, and μ (O_2) the total energy of gas phase O_2.

6.3. RESULTS AND DISCUSSION

A manual search was performed to determine the global minimum of adsorbed H_2O, CO_2, and CO_2^{-} to the anatase support reproducing the same geometries found in Tilocca et al.'s study on water on anatase and Sorescu, et. al's study on CO_2.[5,16] These energies differ from those of Tilocca et al. and Sorescu, et. al due to possible interactions across our smaller supercell, the additional consideration of dispersion forces, and our differing *U* parameter.

Adsorption energies generally increased in magnitude from deposition onto a stoichiometric to deposition onto a defective surface, suggesting that the presence of a surface oxygen vacancy stabilizes reaction intermediates considerably.

Table 6.1. Adsorption energies of reaction intermediates H_2O, CO_2, and CO_2^- on Anatase (101)

Adsorbed Molecule	$E_{ads,stoich}$ (eV)	$E_{ads,def}$ (eV)
H_2O	-1.26	-1.50
CO_2	-0.48	-0.94
CO_2^-	4.39	2.57

In our study of CO_2 reduction, we investigated alternative roles of the anatase support such as stabilization of the CO_2^- intermediate. However, the adsorption of CO_2^- to stoichiometric and defective anatase resulted in repulsive, unstable systems, requiring thermodynamically unfavorable energies of 4.39 eV and 2.57 eV, respectively, to form. Chemical bonding analysis was obtained using the Bader charge localization scheme[17] (figures of this may be found in the SI of the publication). In **Figure 6.3c**, the linear, neutral CO_2 molecule becomes bent upon adsorption to the defective anatase support, its C effectively filling the bridging oxygen vacancy. In our calculations, CO_2 gains an electron (-0.897e) spontaneously from the TiO_2 support. This calculation indicates that O vacancies primarily provide active sites for CO_2 absorption and reduction, and no overpotential is required to form the CO_2^- intermediate. In fact, 4 of the 8 minima found by Sorescu, et. al. formed the CO_2^- intermediate.[5]

In our study of H_2O splitting, the water molecule attempts to both fill the oxygen vacancy with its oxygen (colored green) and retain a hydrogen-bond to the neighboring surface oxygen on the oxide support. The hydrogen-bond might be considered an “activated” bond with a length of 1.71 Å as compared to 1.89 Å on the stoichiometric support (in the SI) indicating that the system is approaching the proton transfer to the O atom of the support. In a molecular dynamics study, Tilocca et al. estimated the activation barrier from adsorption of H_2O to dissociation of the H_2O to two hydroxyls to be ~0.1 eV.[16]

Moreover, Fujimori, et al. maintained that hydroxylation of their MgO support provided the pathway for two mechanisms of hydrogen evolution: the direct redox process and the water-gas shift reaction in the presence of CO.[1] This indicates that Ti^{3+}-O sites are more energetically favorable for H_2O adsorption, which results in higher H_2 evolution efficiencies, consistent with previous reports in the literature.[18] This calculation combined with our previous finding of spontaneous CO_2 reduction on defective anatase (a charge transfer of 0.897 *e* from the support to CO_2) indicates that the O vacancies provide catalytically active sites for CO_2 and H_2O adsorption, and no overpotential is required to form the CO_2^- intermediate.

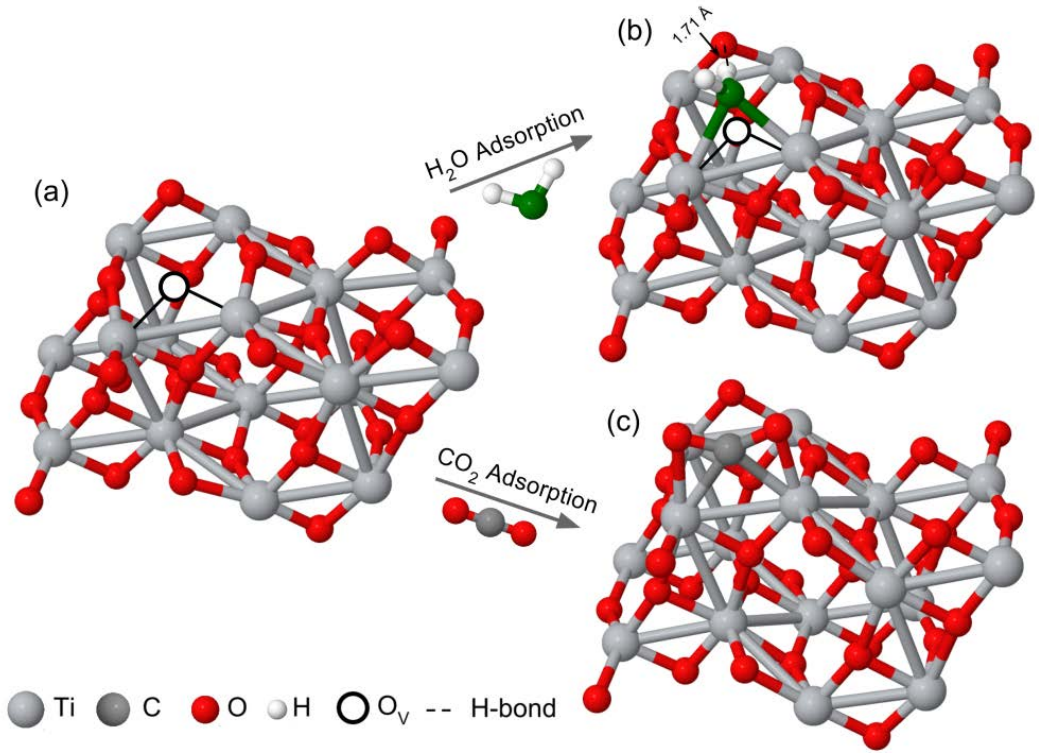

Figure 6.3. (a) Defective anatase with a surface oxygen vacancy. Global minimum structures of **(b)** H_2O adsorbed onto defective anatase and **(c)** CO_2 adsorbed onto defective anatase.[8]

This published work[7,8] was extended to consider co-adsorption of CO_2 and H_2O on defective anatase. Co-adsorption was predicted to lower activation barriers for the water gas shift reaction or redox process for hydrogen evolution. Sorescu, et. al. observed the formation of

carbonate- and bicarbonate-like products in their DFT study of co-adsorption of CO_2 and H_2O on rutile phase of TiO_2.[19] The high reactivity of reduced anatase is well-known and in this vein, our DFT calculations focused on the co-adsorption of water and carbon dioxide on anatase with an oxygen vacancy. Co-adsorption may lower activation barriers for the water gas shift reaction or redox process for hydrogen evolution.

With this larger surface, adsorbed H_2O's energy was raised from to -1.23 eV as compared to previous results of -1.48 to -1.50 eV.[8,20] This suggests that the defective anatase surface may favor higher coverages of H_2O as was modeled in these smaller systems. The preferred adsorbed geometry of H_2O occupying the oxygen vacancy was reproduced with a slightly longer O_{surf}-H hydrogen bond of 1.79 Å (see SI). Due to the strength of H_2O adsorption on defective anatase, the H_2O would block CO_2 from adsorbing at the oxygen vacancy site or even replace pre-adsorbed CO_2, similar to what has been observed experimentally on the rutile surface.[4] Starting geometries for coadsorption of CO_2 consisted of straight and bent CO_2 deposited on neighboring surface O, Ti, and H sites with the perimeter of this search outlined in the **SI, Figure S8.5.5**. Many minima were found, exhibiting greater stabilization (E_{coads} > -1.6 eV) than in the co-adsorption study by Sorescu, et. al. on reduced rutile (E_{coads} < -0.6 eV). Not all minima were included in this study, with a cut-off of ΔE_{coads} <0.34 eV limiting the number of configurations discussed and illustrated here.

In the presence of CO_2, water spontaneously dissociates to form 2 surface hydroxyls ($O_{surf}H$) as illustrated in **Figure 6.4**. These hydroxyls may then participate in either the direct redox process or the water-gas-shift reaction for hydrogen evolution.[1] The estimated barrier from Tilocca, et. al.'s molecular dynamics study of water dissociation to hydroxyls is ~0.1 eV.[16] Therefore, CO_2 appears to make this barrier negligible by promoting water dissociation. Other local minima produce other organic species such as $-(CO_2H)^{+1}$ in Config. II and formic acid (CO_2H_2) in Config. III. Indeed, Config. II may also be interpreted as an intermediate species (monodentate formate) to form the weakly, hydrogen-bonded formic acid in Config. III. Indeed,

Miller, et. al. noted in their theoretical study that monolayers of monodentate formate in the presence of hydroxyls spontaneously formed formic acid.[21] Stable coadsorption also occurs, visualized in Config. IV, VI-VIII (**Figure 6.5**). These configurations suggest that CO_2 may be relatively mobile on the surface and must overcome some activation barrier in order to react with water. Evaluation of these barriers is beyond the scope of this current study but future work will elucidate this. CO_2 may also desorb from the surface, but this is relatively unfavorable with the relative coadsorption energy of +0.31 eV as compared to Config. I (**Figure 6.5**).

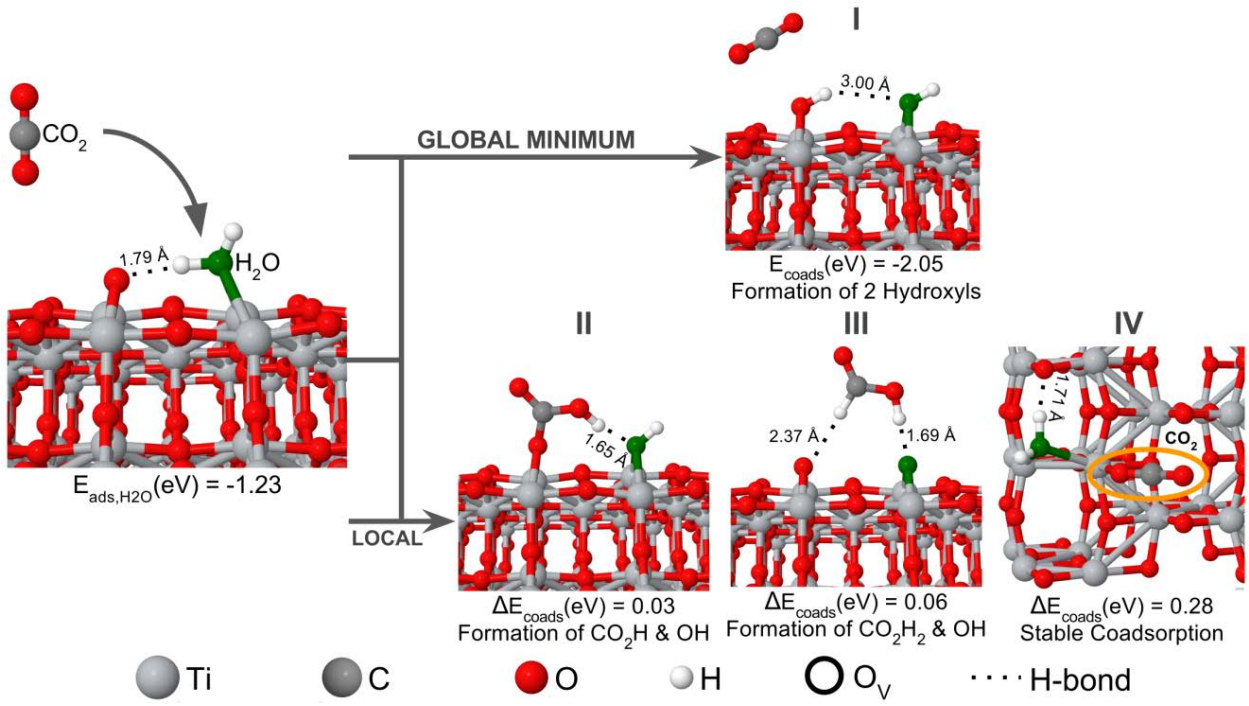

Figure 6.4. The four lowest minima found from DFT calculations of co-adsorption of CO_2 and H_2O. The presence of CO_2 can promote the dissociation of water to form two hydroxyls (Config. I) or the formation of other species (Config. II and III).

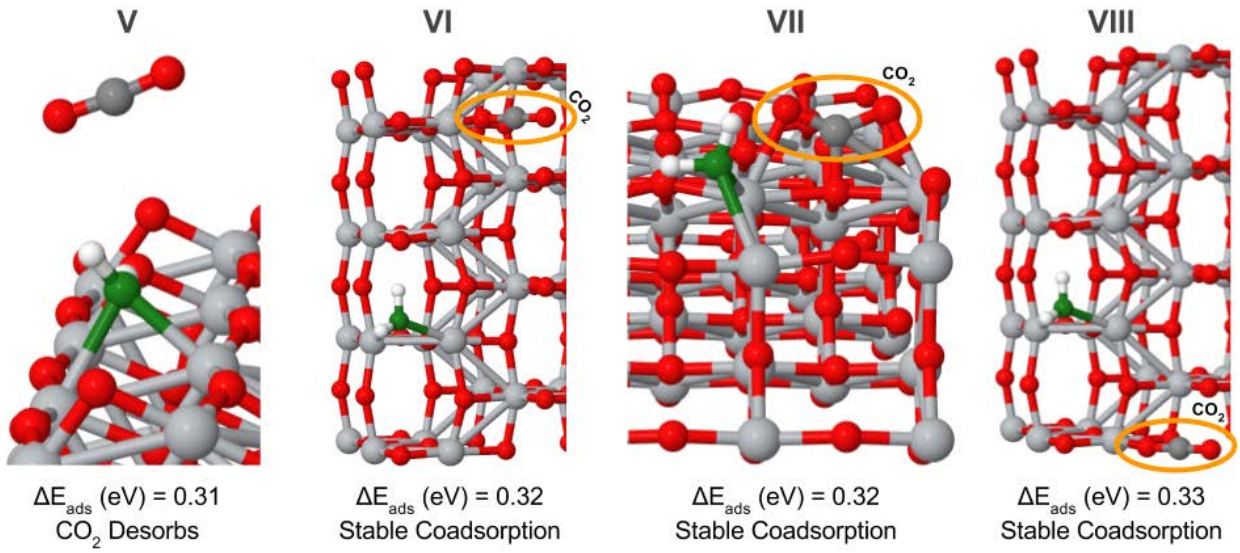

Figure 6.5. Other co-adsorption configurations that have a relative energy of <0.35 eV from the global minimum.

6.4. CONCLUSION

PW-DFT calculations of singly-adsorbed and co-adsorbed CO_2 and H_2O on anatase establish both the importance of oxygen vacancies and clarify the role of co-adsorbed reagent species. Oxygen vacancies introduce highly active sites and the co-adsorbed reagent species reduce or even eliminate activation barriers to water splitting to form hydroxyls or formation of organic species. In particular, these calculations support and verify experimental evidence of improved catalytic performance through the incorporation of defective titania in their systems.

In addition to providing a stable photocatalytic surface on InP-Cu nanopillars, the TiO_2-passivation provides substantial enhancement in the photoconversion efficiency through the introduction of O vacancies associated with the non-stoichiometric growth of TiO_2 by atomic layer deposition. The role of these oxygen vacancies as catalytically active sites in the photocatalytic reduction of CO_2 is established by PW-DFT calculations, which indicate that CO_2 binds stably to these oxygen vacancies and gains an electron (-0.897e) spontaneously from the TiO_2 support**.** Therefore, no externally applied overpotential is required to form the CO_2^-

intermediate, which can subsequently react with H_2O to form methanol. In GaAs photocathodes, the performance for both water splitting and CO_2 reduction of these heterostructures show a very strong dependence on the thickness of the TiO_2 over the range of 0 – 15 nm. Thinner TiO_2 films are amorphous and show enhanced catalytic performance with respect to bare GaAs, whereas thicker TiO_2 films (15nm) are single crystal and have poor charge transfer due to the insulating nature of crystalline TiO_2. The enhanced stability and activity of oxygen vacancy sites observed here in DFT calculations of defective anatase may be amplified in thin, armophous films of TiO_2.

6.5. REFERENCES

1 Fujimori, Y.; Kaden, W. E.; Brown, M. A.; Roldan Cuenya, B.; Sterrer, M.; Freund, H. Hydrogen Evolution from Metal–Surface Hydroxyl Interaction. *The Journal of Physical Chemistry C* **2014***, 118*, 17717-17723.

2 Varghese, O. K.; Paulose, M.; LaTempa, T. J.; Grimes, C. A. High-rate solar photocatalytic conversion of CO2 and water vapor to hydrocarbon fuels. *Nano letters* **2009***, 9*, 731-737.

3 Liu, L.; Zhao, H.; Andino, J. M.; Li, Y. Photocatalytic CO2 reduction with H2O on TiO2 nanocrystals: Comparison of anatase, rutile, and brookite polymorphs and exploration of surface chemistry. *Acs Catalysis* **2012***, 2*, 1817-1828.

4 Henderson, M. A. Evidence for bicarbonate formation on vacuum annealed TiO 2 (110) resulting from a precursor-mediated interaction between CO 2 and H 2 O. *Surf. Sci.* **1998***, 400*, 203-219.

5 Sorescu, D. C.; Al-Saidi, W. A.; Jordan, K. D. CO2 adsorption on TiO2 (101) anatase: A dispersion-corrected density functional theory study. *J. Chem. Phys.* **2011***, 135*, 124701.

6 Anpo, M.; Yamashita, H.; Ichihashi, Y.; Ehara, S. Photocatalytic reduction of CO2 with H2O on various titanium oxide catalysts. *J Electroanal Chem* **1995***, 396*, 21-26.

7 Qiu, J.; Zeng, G.; Ha, M.; Ge, M.; Lin, Y.; Hettick, M.; Hou, B.; Alexandrova, A. N.; Javey, A.; Cronin, S. B. Artificial photosynthesis on TiO2-passivated InP nanopillars. *Nano letters* **2015***, 15*, 6177-6181.

8 Qiu, J.; Zeng, G.; Ha, M.; Hou, B.; Mecklenburg, M.; Shi, H.; Alexandrova, A. N.; Cronin, S. B. Microscopic Study of Atomic Layer Deposition of TiO2 on GaAs and Its Photocatalytic Application. *Chemistry of Materials* **2015***, 27*, 7977-7981.

9 Giannozzi, P.; Baroni, S.; Bonini, N.; Calandra, M.; Car, R.; Cavazzoni, C.; Ceresoli, D.; Chiarotti, G. L.; Cococcioni, M.; Dabo, I. QUANTUM ESPRESSO: a modular and open-source software project for quantum simulations of materials. *Journal of Physics: Condensed Matter* **2009***, 21*, 395502.

10 Kohn, W.; Sham, L. J. Self-consistent equations including exchange and correlation effects. *Physical Review* **1965***, 140*, A1133.

11 Lee, C.; Yang, W.; Parr, R. G. Development of the Colle-Salvetti correlation-energy formula into a functional of the electron density. *Physical review B* **1988***, 37*, 785.

12 Burke, K.; Werschnik, J.; Gross, E. Time-dependent density functional theory: Past, present, and future. *J. Chem. Phys.* **2005***, 123*, 062206.

13 Perdew, J. P.; Burke, K.; Ernzerhof, M. Generalized gradient approximation made simple. *Phys. Rev. Lett.* **1996***, 77*, 3865.

14 Grimme, S.; Antony, J.; Ehrlich, S.; Krieg, H. A consistent and accurate ab initio parametrization of density functional dispersion correction (DFT-D) for the 94 elements H-Pu. *J. Chem. Phys.* **2010***, 132*, 154104.

15 Ha, M.; Alexandrova, A. N. Oxygen Vacancies of Anatase(101): Extreme Sensitivity to the Density Functional Theory Method. *J. Chem. Theory Comput.* **2016***, 12*, 2889-2895.

16 Tilocca, A.; Selloni, A. Reaction pathway and free energy barrier for defect-induced water dissociation on the (101) surface of TiO2-anatase. *J. Chem. Phys.* **2003***, 119*, 7445-7450.

17 Henkelman, G.; Arnaldsson, A.; Jónsson, H. A fast and robust algorithm for Bader decomposition of charge density. *Computational Materials Science* **2006***, 36*, 354-360.

18 Lu, G.; Linsebigler, A.; Yates Jr, J. T. Ti3 defect sites on TiO2 (110): production and chemical detection of active sites. *J. Phys. Chem.* **1994***, 98*, 11733-11738.

19 Sorescu, D. C.; Lee, J.; Al-Saidi, W. A.; Jordan, K. D. Coadsorption properties of CO2 and H2O on TiO2 rutile (110): A dispersion-corrected DFT study. *J. Chem. Phys.* **2012***, 137*, 074704.

20 Tilocca, A.; Selloni, A. Structure and reactivity of water layers on defect-free and defective anatase TiO2 (101) surfaces. *The Journal of Physical Chemistry B* **2004***, 108*, 4743-4751.

21 Miller, K. L.; Musgrave, C. B.; Falconer, J. L.; Medlin, J. W. Effects of water and formic acid adsorption on the electronic structure of anatase TiO2 (101). *The Journal of Physical Chemistry C* **2011***, 115*, 2738-2749.

CHAPTER 7

Exceptional Oxygen Reduction Reaction Activity and Durability of Platinum-Nickel Nanowires Through Synthesis and Post-Treatment Optimization

7.1. INTRODUCTION

Platinum remains the premier catalyst in a variety of applications, including the hydrogen oxidation reaction (HOR at the anode) and the oxygen reduction reaction (ORR at the cathode) of proton exchange membrane fuel cells (PEMFCs). Due to its high cost, alternative Pt-based catalysts have been developed to reduce the amount of Pt required in the device. ORR presents the highest barrier to commercialization of automotive fuel cells, occurring at a rate of six orders of magnitude slower than HOR and requiring a Pt-loading of >0.1 mg cm^{-2}.[1] In their 2014 Annual Merit Review, the US Department of Energy (DOE) highlighted Pt-loading to be the key focus area for research and development, citing that 49% of PEFMC cost belongs to the catalyst layer alone.[2] Extended surface catalysts (nanowires) minimize Pt-loadings by being composed of a metal core (such as Ni or Co) and utilizing galvanic displacement to deposit Pt at the surface.[3,4]

We have previously used galvanic displacement to deposit thin layers of Pt onto extended nanostructures, and demonstrated a dramatic increase in the Pt surface areas of extended surface electrocatalysts (> 90 m^2 g_{Pt}^{-1}).[3-7] At that time, our extended surface catalysts of Pt—Ni nanowires (NW) exceeded the 2017-2020 target, 0.44 A mg_{Pt}^{-1}, in rotating disk electrode half-cells, with as-synthesized materials producing >0.90 A mg_{Pt}^{-1} at 0.90 V. These materials, however, suffered from moderate specific activity and were prone to performance loss and Ni dissolution. Post-synthesis processing parameters, including thermal treatment (annealing) under reducing and oxidizing conditions, and acid leaching to selectively remove Ni, have been optimized to significantly improve the site-specific activity without appreciably impacting surface area. The resulting materials also minimized durability performance losses, including activity and Ni dissolution. The results of these studies represent the first example of extended surface materials with both exceptionally high specific activity (>6000 mA mg_{Pt}^{-1}) and exceptionally high surface area (> 90 m^2 g_{Pt}^{-1}).

Plane-wave density function theory (PW-DFT) calculations were performed to understand the role of heterogeneity (e.g., facets or differential alloying) on the stability of the

Pt-Ni interface. The modeling of these catalyst supports presents a non-trivial computational effort in order to capture the range of interactions, those between the sub-layer of Pt-Ni alloy to Pt. This study answered fundamental questions regarding the sub-alloy's effect by: 1) isolating the sub-alloy's stabilization effects on surface Pt and 2) examining the effects of Pt-skin thickness in order to identify optimized coverage of Pt to alloy. Namely, experiment and theory converged upon the same lattice constant (circa ~ 3.7 Å) and facet distribution {100} of the layered interface. Moreover, we found that the stability of the Pt-Ni surface was dependent on Pt-skin thickness: a Pt-skin of 3 layers was more stable than a Pt-skin of 1 layer on a sub-alloy of Pt-Ni.

7.2. METHODOLOGY

PW-DFT calculations were performed in the Vienna Ab-Initio Simulation Package (VASP).[8-11] Projector augmented waves basis sets with the Perdew-Burke-Ernzerhof functional were implemented since they are known to reproduce well physico-chemical properties.[12-14] Stringent convergence criteria of 10^{-6} ev (10^{-5}) on electronic (geometric) relaxations were placed on calculations with a large kinetic energy cut-off of 520 eV applied to the basis set. The Methfessel-Paxtom smearing for electronic occupations was implemented. Pt—Ni alloys, Ni_3Pt and Pt_3Ni, were first relaxed in the bulk under a Monkhorst-Pack grid of 13 x 13 x 13 centered at Γ and then appropriately sliced to expose (100), (110), and (111) facets. These surfaces, grown from the primitive surface cell to a (2 x 2) supercell, were evaluated alone and with a Pt-skin of 1 and 3 layers. Surface calculations occurred under a *k*-point sampling of 4 x 4 x 1 except for the (111) surface composed of Pt-skin of three layers on an alloy, which utilized a grid of 2 x 2 x1. Reference atomic energies were calculated at the Γ point in a box of volume >1000 $Å^3$ with the symmetry of the cell broken to replicate appropriate spin states. Cohesive energies (E_{coh}) were determined with the equation

$$E_{coh}\left({}^{eV}/_{atom}\right) = \frac{E_{tot,surf} - n_{Pt}E_{Pt} - n_{Ni}E_{Ni}}{n_{Pt} + n_{Ni}}$$

where $E_{tot,surf}$ is the total energy in VASP of the surface, E_{Ni} (E_{Pt}) are reference atomic energies, and n_{Ni} (n_{Pt}) are the number n of the Ni (Pt). Our cohesive energies follow the convention of negative energies indicating attraction between atoms for stabilization.

DFT calculations were performed in order to understand relative stabilities of a Pt-skin on Pt—Ni alloys, both on Ni_3Pt and Pt_3Ni, and on the relevant facets of (100), (110), and (111) of these alloys (see **Figure** and **SI** for more details). Appropriate lattice constants were chosen to consider conditions the alloy's compressed lattice constant, a lattice constant mid-way between the alloy and Pt, and pure Pt. For a Pt-skin on Ni_3Pt, lattice constants of 3.62, 3.77, and 3.92 Å were explored; on Pt_3Ni, 3.82, 3.87, and 3.92 Å. These lattice-constants represent a sampling of the range of surface phenomena that would be present on the nanowires. Moreover, the stability of the Pt-skin on these alloys were further explored by modelling a Pt-skin composed of a single layer and composed of three layers on Pt—Ni alloys. This provides a first order approximation of the stability of Pt-skin growth on the faceted alloy. On the (100) and (110) surfaces of Ni_3Pt, the alloy alternates between a layer of Ni and a layer of Pt and Ni atoms. The Pt-skin was evaluated on both in order to consider the Ni-enrichment, sub-layer effect on Pt—Ni.[15]

7.3. RESULTS AND DISCUSSION

Experimentally, the lattice constant of both alloys and pure Pt may vary within 10^{-2} Å. From experimental observations of the Pt—Ni alloys, the Ni_3Pt and Pt_3Ni alloys of the $L1_2$ structure were noted more frequently than that of Pt—Ni of the $L1_0$ structure.[16-19] Typically, the alloys' lattice parameters range from 3.81–3.84 Å for Pt_3Ni and 3.66 Å for Ni_3Pt.1-2 It has been noted that alloys often reflect a lattice parameter of circa $0.25f_{Ni} + 0.75f_{Pt}$ or $0.75f_{Ni} + 0.25f_{Pt}$, where f is the lattice parameter of the bulk, pure fcc metal. Therefore, an "ideal" lattice parameter was assumed for the alloy of 3.62 and 3.82 Å for Ni_3Pt and Pt_3Ni, respectively. In mixtures of Ni:Pt with less determinate ratios, nanoparticles may also feature lattice parameters of 3.75-3.79 Å.[18] In order to represent the sampling of surface phenomena present at the

surface of these nanowires, we approximated surface morphology by accounting for both the (100), (110), and (111) facets under varying lattice constants appropriate to an alloy, pure Pt (3.92 Å), and a mid-way point typical of Pt:Ni mixtures (**Table 7.1**). This would account for conditions of compression and expansion that alloy surfaces with a Pt-skin might stabilize to.

Table 7.1. Lattice Parameters of Interest in Order to Approximate Surface Morphology at the Interface of the Pt—Ni Nanowires

	Ni_3Pt	Mid-way between Ni_3Pt and Pt	Pt_3Ni	Mid-way between Pt_3Ni	Pt
Lattice Constant (Å)	3.62	3.77	3.82	3.87	3.92

Cohesive Energies (E_{coh}) and Relative Cohesive Energies (ΔE_{coh}) with respect to the sub-surface alloy are presented in **Table 7.2** (Pt-skins on Ni_3Pt) and **SI Table S8.6.1** (Pt-skins on Pt_3Ni). Modelling of a varying thickness of the Pt-skin on various facets of the Pt—Ni alloy indicate certain trends regarding Pt-skin thickness (an approximation of the Pt-skin growth on an alloy), faceting, and even influences from a mixed or Ni sublayer. - ΔE_{coh} indicates stabilization with respect to the ideal lattice of the alloy and + ΔE_{coh} indicates destabilization with respect to the ideal lattice of the alloy. Most conspicuously, the Pt-skin on (100) Ni3Pt remains unusually stable with a cohesive energy comparable to that of a Pt-skin on (111). This trend also occurred with a Pt-skin on the facets of Pt_3Ni. The effect was less pronounced, but very much present.

Generally, as the Pt-skin thickened, the surface became more stable. At the ideal lattice constant of the alloy, a thicker Pt-skin on Ni_3Pt resulted in greater stabilization than the alloy with cohesive energies lowering by ~ 0.2 to 0.4 eV/atom; on Pt_3Ni, by ~ 0.1 to 0.3 eV/atom. Moreover, the (110) and (100) facets often favored compression over that of the (111). On both the sub-surfaces of Ni_3Pt and Pt_3Ni, expansion of the lattice beyond that typical of the alloy resulted in energy penalties of +0.01 to +0.19 ΔE_{coh} (ev/atom) with the (110) facet often incurring the higher penalty. These energetic observations would most likely influence surface morphology and catalytic activity and will be analyzed with oxidation reduction reaction

intermediates in a future publication. It is most likely that the factors discussed regarding thickness of the Pt-skin and exposed facets would contribute in an ensemble effect for the high durability and activity observed from the Pt—Ni nanowires.

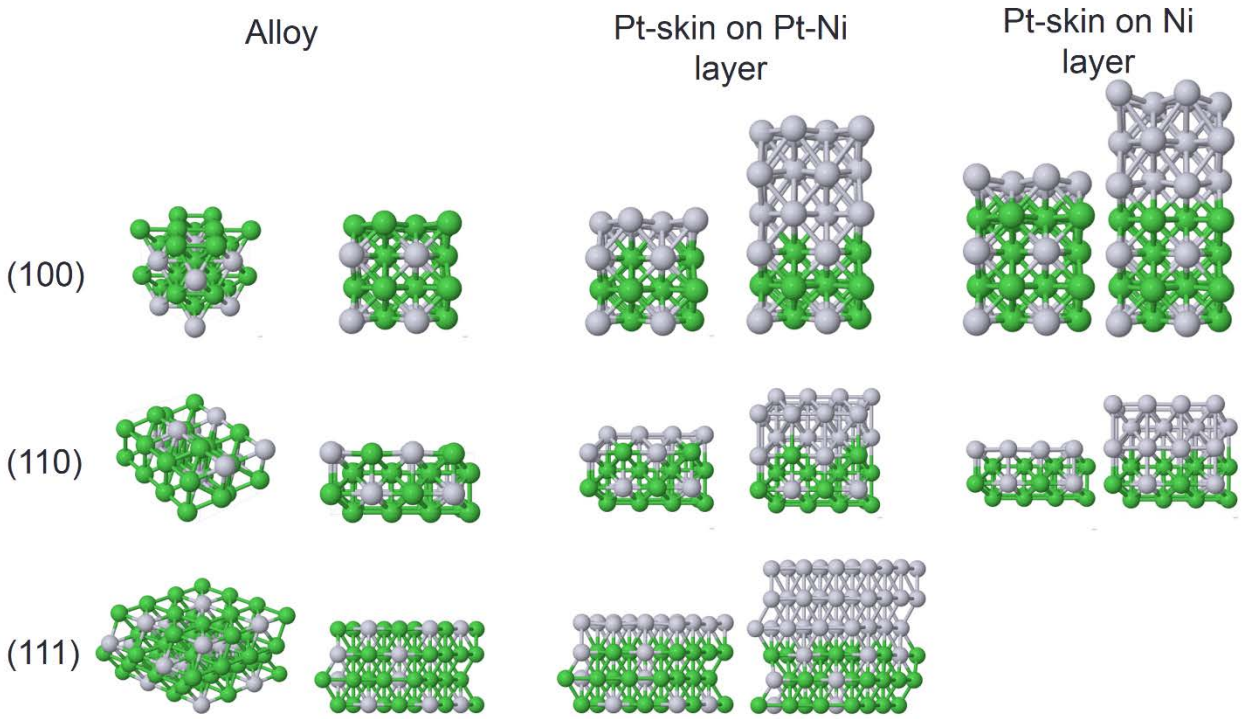

Figure 7.1. The (2 x 2) supercells utilized in this study on surface stability with varying facet and Pt-skin thickness. It is indicated in the figure when a Pt-skin sat on a sub-layer of a Ni or mixed Pt—Ni layer of the Ni3Pt alloy.

Table 7.2. Cohesive Energies (E_{coh}) and Relative Cohesive Energies (ΔE_{coh}) of a Pt-skin with Varying Thickness and Sub-layer Alloy on Ni_3Pt

Systems (Ni:Pt)	**3.62 Å**	**3.77 Å**	**3.92 Å**
(100)	E_{coh}(ev/atom)	ΔE_{coh}(ev/atom)	ΔE_{coh}(ev/atom)
Pt—Ni alloy (3:1)	-4.68	0.06	0.15
1 Pt-skin on Pt—Ni (1:1)	-4.85	0.01	0.10
3 Pt-skin on Pt—Ni (1:2)	-4.97	-0.06	-0.02
1 Pt-skin on Ni (3:2)	-4.89	0.02	0.10
3 Pt-skin on Ni (3:4)	-4.98	-0.04	0.00
(110)			
Pt—Ni alloy (3:1)	-4.48	0.08	0.22
1 Pt-skin on Pt—Ni (3:2)	-4.69	0.03	0.13
3 Pt-skin on Pt—Ni (3:4)	-4.88	-0.01	0.05
1 Pt-skin on Ni (5:3)	-4.56	0.06	0.19
3 Pt-skin on Ni (5:7)	-4.82	0.00	0.05
(111)			
Pt—Ni alloy (3:1)	-4.80	0.06	0.18
1 Pt-skin on Pt—Ni (9:7)	-4.91	-0.02	0.08
3 Pt-skin on Pt—Ni (3:5)	-4.98	-0.05	-0.02

Note: ΔE_{coh} is with respect to E_{coh} under a lattice constant 3.62 Å.

Experimentally, our specific activities of the Pt—Ni nanowires were more than 10 times larger than those of Pt/HSC. Pt—Ni nanowire catalysts offer potential advantages in site-specific activity, by the extended surface avoiding low coordinate surface sites and/ or reduced particle size effects.[20,21] The increase in specific activity observed with the hydrogen annealing temperature can be rationalized as an increased alloying effect, with Ni-induced Pt lattice compression weakening Pt—O chemisorption.[22,23] The improved mixing of the Pt and Ni phases with the annealing temperature was confirmed with XANES and EXAFS. Pt lattice compression was probed directly by X-ray diffraction (XRD), where examination of the Pt(111) reflection revealed a gradual shift from a characteristically Pt lattice into a shoulder on the Ni(111) reflection at 500 °C (**Figure 4a**). Through Rietveld refinement of the XRD patterns, the average Pt lattice constant compressed from 3.911 Å in the as-synthesized material to 3.551 Å after annealing to 500 °C. Differences in the exposed Pt facets may have influenced activity but likely did not provide a significant benefit for the Pt—Ni nanowires. Studies on the redox of adsorbed germanium and tellurium confirmed a wide distribution of surface Pt facets; a majority

(50−65%), however, were in the {100} set, previously found to be less active for Pt—Ni alloys (Ni_3Pt, **Figure 4**).[15,24-26] The distribution of Pt facets was generally consistent for all Pt—Ni nanowires examined and did not significantly change with the annealing temperature. In contrast, Pt/HSC contained more Pt{111} (46.3%) than {100} (26.1%) in comparable tests.

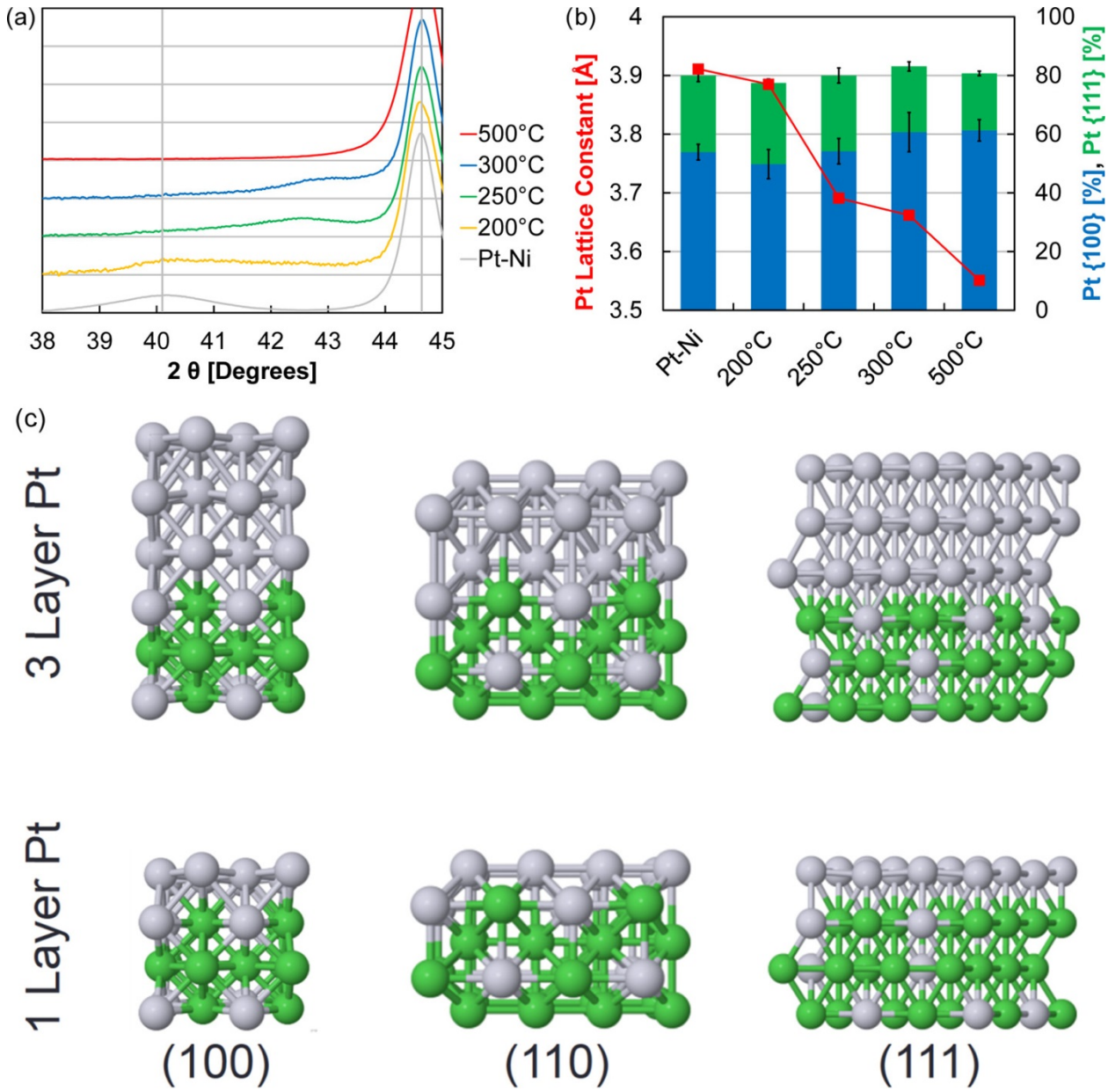

Figure 7.2. (a) XRD patterns of Pt—Ni nanowires (7.3 ± 0.3 wt % Pt), as-synthesized and annealed in hydrogen. **(b)** Pt lattice constants (by Rietveld refinement of XRD patterns) and Pt facet data, as determined by germanium and tellurium underpotential deposition. **(c)** Surface models of Pt skins on the Ni_3Pt alloy. The alloying effect of Ni_3Pt was more pronounced than that of Pt_3Ni as the Ni-enriched alloy particularly stabilizes both (100) ~ (111) over (110) with a compressed lattice constant ca. 3.7 Å (at the experimental high performer).

The observed Pt facet distribution may not have improved the ORR activity. Understanding why the Pt—Ni nanowires contained a high proportion of Pt {100}, however, was of significant interest, and DFT calculations were performed to examine the relative stabilities of the Pt facets and lattices found in the Pt—Ni nanowires. DFT calculations were completed on a Pt skin on the Pt—Ni alloys ($N_{i3}Pt$ and Pt_3Ni), on the relevant facets of (100), (110), and (111, **Figures 7.1** and **7.2**, **Table 7.2** and **SI Figure S8.6.1** and **Table S8.6.1**). Calculations were completed on $N_{i3}Pt$ and Pt_3Ni substructures, on a single and three Pt over-layers, to give a range of Pt lattices and bracket the range found in the XRD patterns. Calculations confirmed that (111) is the most stable surface for the alloys, with >99% of exposed facets being (111, Boltzmann distribution). The presence of a Pt skin, however, resulted in a reordering of facet stabilities. Specifically, the (100) facet of $N_{i3}Pt$ with a Pt skin of three layers was stabilized with cohesive energies comparable to those of the (111) facet. A lattice constant of 3.62 Å resulted in cohesive energies of E_{coh} (100) = −4.98 and E_{coh} (111) = −5.01 eV/atom; likewise, a lattice of 3.77 Å resulted in E_{coh} (100) = −5.03 and E_{coh} (111) = −5.06 eV/atom. The alloying effect of $N_{i3}Pt$ was more pronounced than that of Pt_3Ni as the Ni-enriched alloy particularly stabilizes both (100) ~ (111) over (110) with a compressed lattice constant ca. 3.77 Å.

This effect may become more pronounced as the Pt skin grows thicker and may have far-reaching effects on the electrocatalytic activity exhibited by the high-performer. Stabilization of the Pt skin on $N_{i3}Pt$ varied depending on both skin thickness and the size of the lattice—a single Pt layer was more stabilized on a sublayer of Ni, whereas a thicker Pt layer was more stabilized on a sublayer of mixed Pt—Ni. Although (111) is the most stable surface of face-centered cubic metals in vacuum, the competitive stability of a Pt skin on (100) $N_{i3}Pt$ appears to explain how the Pt—Ni nanowires can contain a high amount of Pt(100) on the surface with a compressed lattice. The DFT calculations addressed the synthesized catalyst by focusing on the extended surface and the $N_{i3}Pt$ substructure to induce Pt lattice compression. A three-layer Pt skin on (100) $N_{i3}Pt$ was representative of the high-performing nanowires (hydrogen-annealed,

250 °C), as the lattices approximately matched, and the (100) facet was dominant electrochemically.

7.4. CONCLUSION

This work represented a concerted effort to match theoretical research in heterogeneous catalysis to the complex rigors present in manufacturing and real-world devices through high-performance computing. Our theoretical consideration of the complex interface has been validated by experiment. Namely, we have predicted physicochemical properties related to stability by considering the distribution of surfaces available for catalysis. The sub-alloy layer of Ni_3Pt resulted in the stability of Pt-facets' (100) ~ (111) > (110) with increasing Pt skin thickness at a compressed lattice constant of ~ 3.7 Å (supported in part by XRD patterns and facet characterization through Ge, Te adatom deposition).

7.5. REFERENCES

1 Debe, M. K. Electrocatalyst approaches and challenges for automotive fuel cells. *Nature* **2012***, 486*, 43-51.

2 Papageorgopoulos, D. In *In Fuel Cells Program - Plenary Presentation;* 2014 U.S. Department of Energy (DOE) Hydrogen and Fuel Cells Program and Vehicle Technologies Office Annual Merit Review and Peer Evaluation Meeting; Department of Energy, Hydrogen and Fuel Cells Program: Washington, D.C., 2014; .

3 Alia, S. M.; Larsen, B. A.; Pylypenko, S.; Cullen, D. A.; Diercks, D. R.; Neyerlin, K. C.; Kocha, S. S.; Pivovar, B. S. Platinum-Coated Nickel Nanowires as Oxygen-Reducing Electrocatalysts. *ACS Catalysis* **2014***, 4*, 1114-1119.

4 Alia, S. M.; Pylypenko, S.; Neyerlin, K. C.; Cullen, D. A.; Kocha, S. S.; Pivovar, B. S. Platinum-Coated Cobalt Nanowires as Oxygen Reduction Reaction Electrocatalysts. *ACS Catalysis* **2014***, 4*, 2680-2686.

5 Alia, S.; Yan, Y.; Pivovar, B. Galvanic displacement as a route to highly active and durable extended surface electrocatalysts. *Catalysis Science & Technology* **2014**, *4*, 3589-3600.

6 Alia, S. M.; Jensen, K.; Contreras, C.; Garzon, F.; Pivovar, B.; Yan, Y. Platinum coated copper nanowires and platinum nanotubes as oxygen reduction electrocatalysts. *Acs Catalysis* **2013**, *3*, 358-362.

7 Alia, S. M.; Jensen, K. O.; Pivovar, B. S.; Yan, Y. Platinum-coated palladium nanotubes as oxygen reduction reaction electrocatalysts. *Acs Catalysis* **2012**, *2*, 858-863.

8 Kresse, G.; Hafner, J. Ab initio molecular dynamics for liquid metals. *Physical Review B* **1993**, *47*, 558.

9 Kresse, G.; Hafner, J. Ab initio molecular-dynamics simulation of the liquid-metal–amorphous-semiconductor transition in germanium. *Physical Review B* **1994**, *49*, 14251.

10 Kresse, G.; Furthmüller, J. Efficiency of ab-initio total energy calculations for metals and semiconductors using a plane-wave basis set. *Computational Materials Science* **1996**, *6*, 15-50.

11 Kresse, G.; Furthmüller, J. Efficient iterative schemes for ab initio total-energy calculations using a plane-wave basis set. *Physical Review B* **1996**, *54*, 11169.

12 Kresse, G.; Joubert, D. From ultrasoft pseudopotentials to the projector augmented-wave method. *Physical Review B* **1999**, *59*, 1758.

13 Blöchl, P. E. Projector augmented-wave method. *Physical Review B* **1994**, *50*, 17953.

14 Perdew, J. P.; Burke, K.; Ernzerhof, M. Generalized gradient approximation made simple. *Phys. Rev. Lett.* **1996**, *77*, 3865.

15 Stamenkovic, V. R.; Fowler, B.; Mun, B. S.; Wang, G.; Ross, P. N.; Lucas, C. A.; Markovic, N. M. Improved oxygen reduction activity on Pt3Ni(111) via increased surface site availability. *Science* **2007**, *315*, 493-497.

16 Mukerjee, S.; Srinivasan, S.; Soriaga, M. P.; McBreen, J. Role of structural and electronic properties of Pt and Pt alloys on electrocatalysis of oxygen reduction An in situ XANES and EXAFS investigation. *J. Electrochem. Soc.* **1995***, 142*, 1409-1422.

17 Fowler, B.; Lucas, C. A.; Omer, A.; Wang, G.; Stamenković, V. R.; Marković, N. M. Segregation and stability at Pt 3 Ni (111) surfaces and Pt 75 Ni 25 nanoparticles. *Electrochim. Acta* **2008***, 53*, 6076-6080.

18 Godínez-Salomón, F.; Hallen-López, M.; Solorza-Feria, O. Enhanced electroactivity for the oxygen reduction on Ni@ Pt core-shell nanocatalysts. *Int J Hydrogen Energy* **2012***, 37*, 14902-14910.

19 Wadayama, T.; Todoroki, N.; Yamada, Y.; Sugawara, T.; Miyamoto, K.; Iijama, Y. Oxygen reduction reaction activities of Ni/Pt (111) model catalysts fabricated by molecular beam epitaxy. *Electrochemistry Communications* **2010***, 12*, 1112-1115.

20 Gasteiger, H. A.; Kocha, S. S.; Sompalli, B.; Wagner, F. T. Activity benchmarks and requirements for Pt, Pt-alloy, and non-Pt oxygen reduction catalysts for PEMFCs. *Applied Catalysis B: Environmental* **2005***, 56*, 9-35.

21 Bregoli, L. The influence of platinum crystallite size on the electrochemical reduction of oxygen in phosphoric acid. *Electrochim. Acta* **1978***, 23*, 489-492.

22 Sha, Y.; Yu, T. H.; Merinov, B. V.; Shirvanian, P.; Goddard III, W. A. Mechanism for Oxygen Reduction Reaction on Pt3Ni Alloy Fuel Cell Cathode. *The Journal of Physical Chemistry C* **2012***, 116*, 21334-21342.

23 Stamenkovic, V.; Mun, B. S.; Mayrhofer, K. J.; Ross, P. N.; Markovic, N. M.; Rossmeisl, J.; Greeley, J.; Nørskov, J. K. Changing the activity of electrocatalysts for oxygen reduction by tuning the surface electronic structure. *Angewandte Chemie* **2006***, 118*, 2963-2967.

24 Marković, N.; Adžić, R.; Cahan, B.; Yeager, E. Structural effects in electrocatalysis: oxygen reduction on platinum low index single-crystal surfaces in perchloric acid solutions. *J Electroanal Chem* **1994***, 377*, 249-259.

25 Solla-Gullón, J.; Rodríguez, P.; Herrero, E.; Aldaz, A.; Feliu, J. M. Surface characterization of platinum electrodes. *Physical Chemistry Chemical Physics* **2008***, 10*, 1359-1373.

26 Gómez, R.; Llorca, M.; Feliu, J.; Aldaz, A. The behaviour of germanium adatoms irreversibly adsorbed on platinum single crystals. *J Electroanal Chem* **1992***, 340*, 349-355.

8. APPENDIX

8.1. SUPPORTING INFORMATION FOR CHAPTER 2

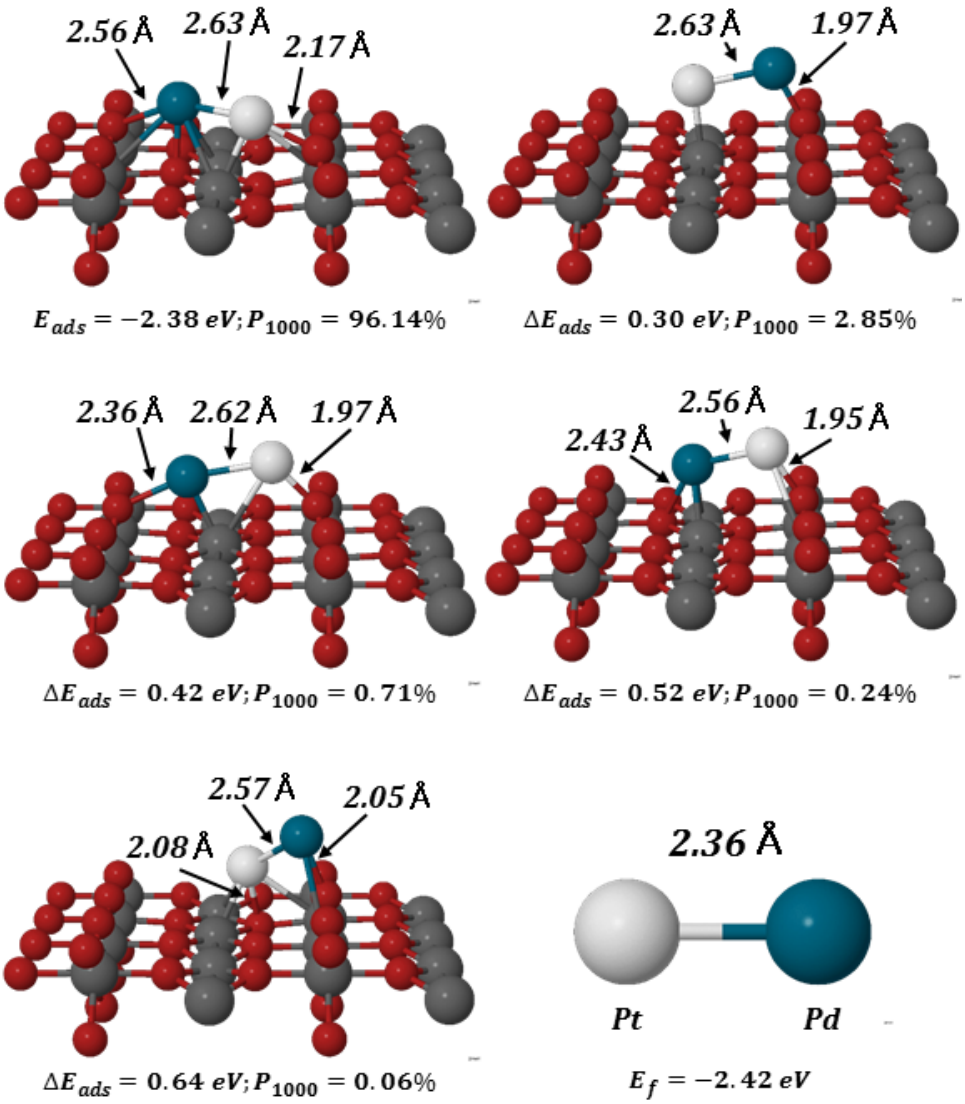

Figure S8.1.1. Structures of the gas phase and surface-deposited dimers: both the global and low-energy local minima are shown, with their relative energies and Boltzmann populations at 1,000 K. The absolute adsorption energy is displayed for the global minimum, all adsorption energies following the global minimum are relative adsorption energies.

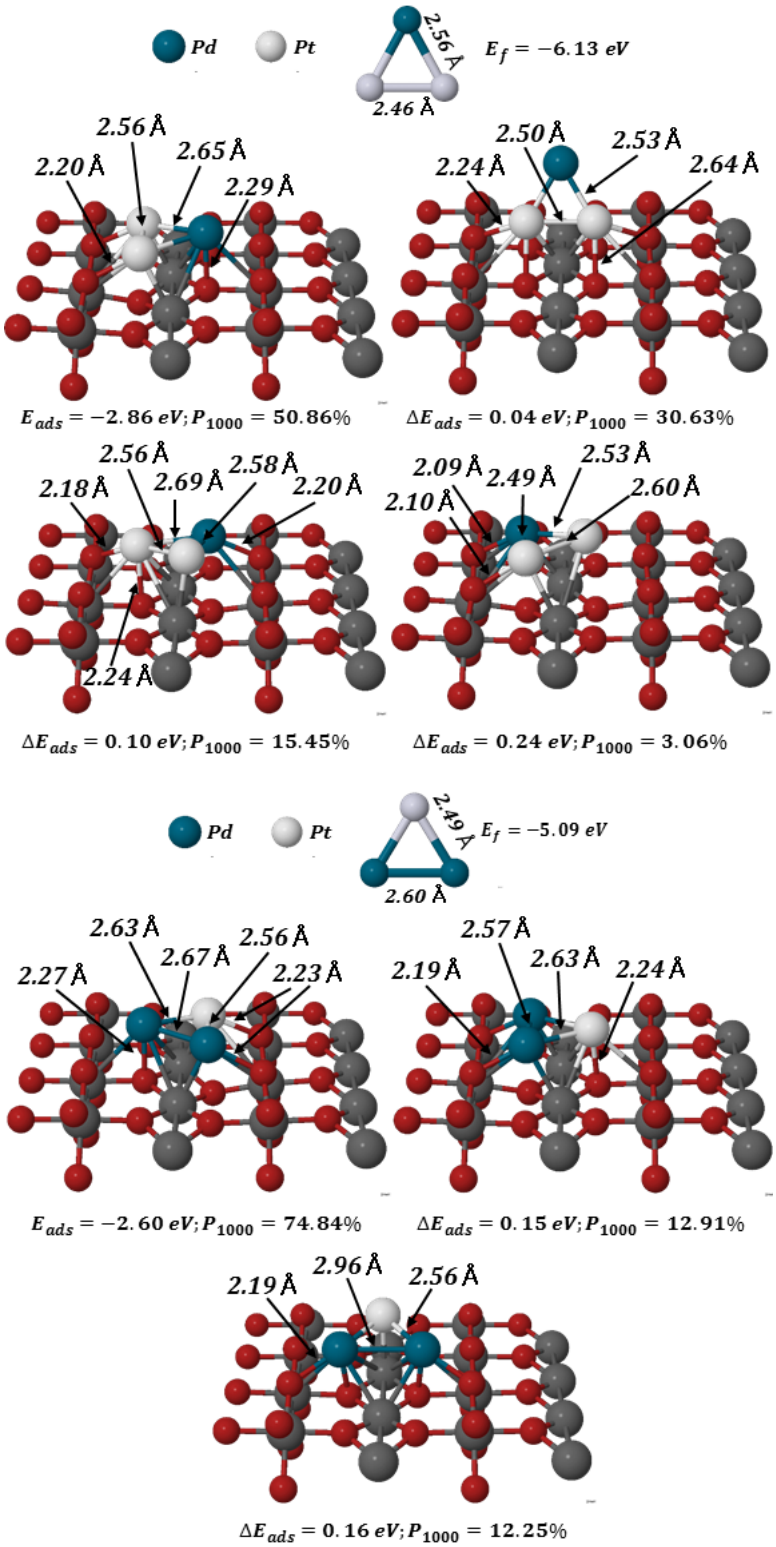

Figure S8.1.2. Structures of the gas phase and surface-deposited Pt_2Pd (left) and Pd_2Pt (right) trimers: both the global and low-energy local minima are shown, with their relative energies and Boltzmann populations at 1,000 K.

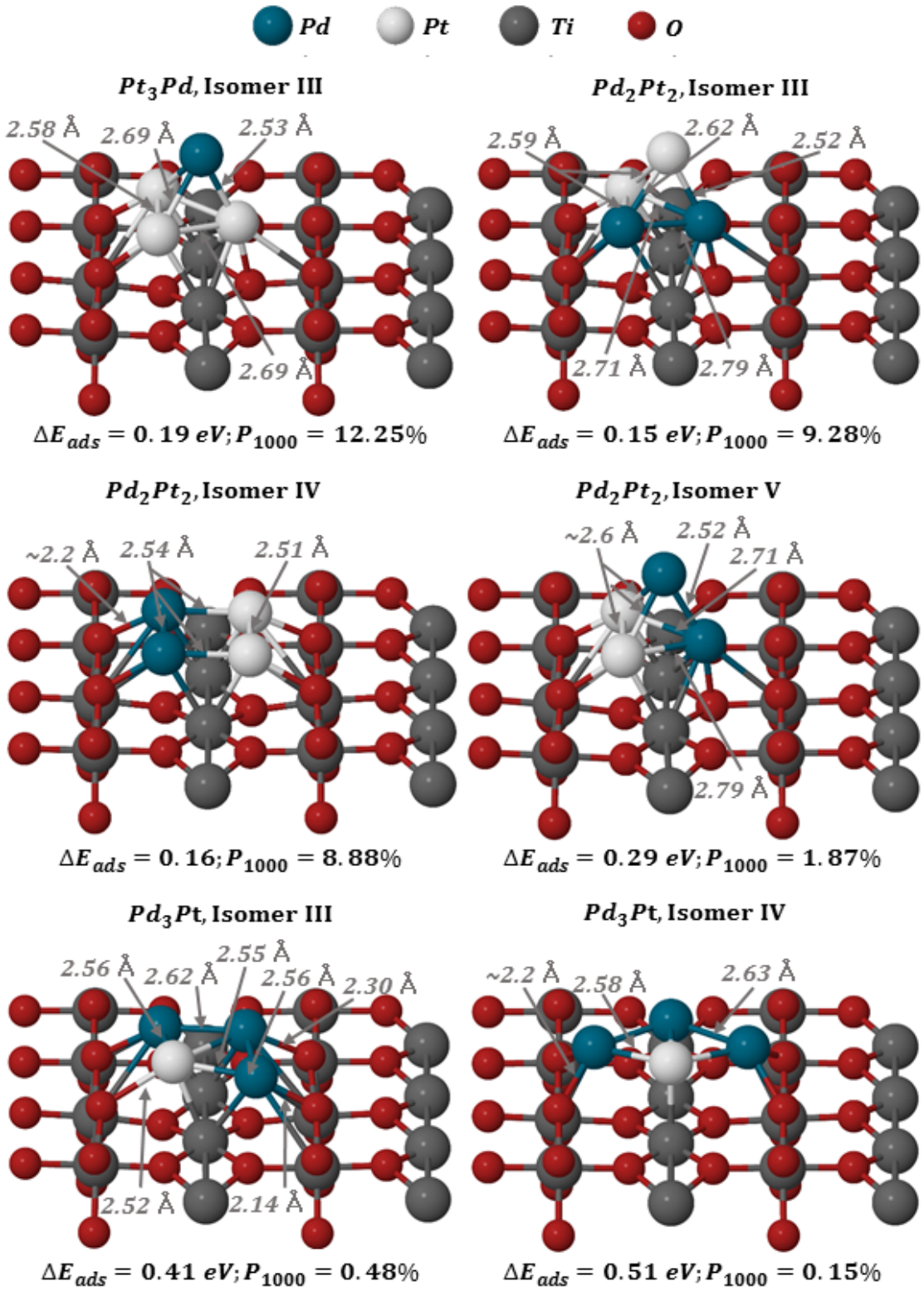

Figure S8.1.3. Less probable structures of the surface-deposited tetramers, with their relative energies and Boltzmann populations at 1,000 K. Pd_3Pt Isomers III and IV are structures, which minimize coordination to surface oxygen due to their distortion into a rhombus or a diamond.

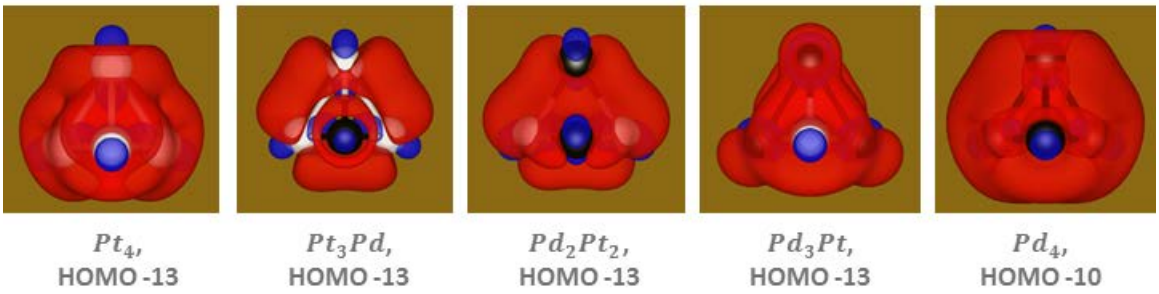

Figure S8.1.4. σ-aromaticity of gas-phase global minima clusters; for clarity, Pt is white and Pd is black.

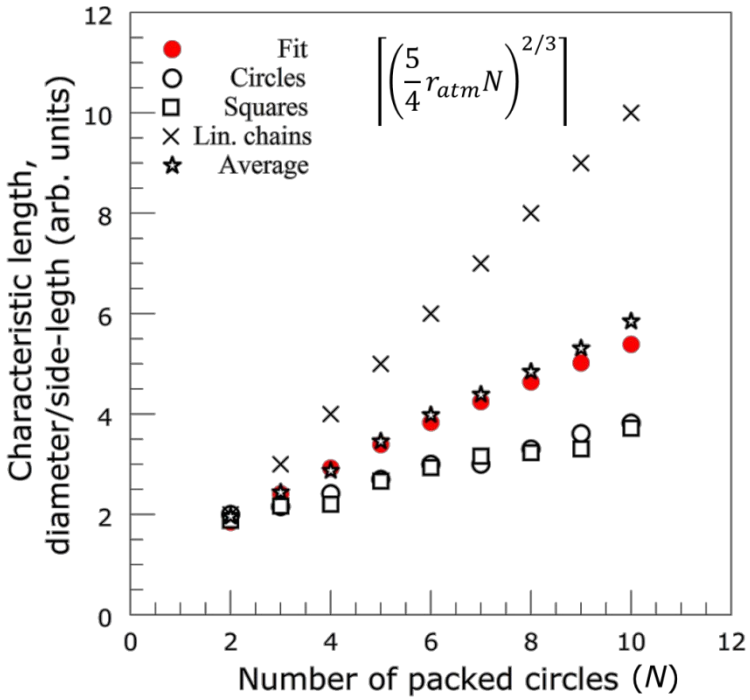

Figure S8.1.5. Analytical fit to the average size of a particle formed by optimally packing unit-circles into circles, squares, and linear chains. Used to ensure that a monomer properly dissociates from a filamentary-like *N*-mer; relevant due to the finer grid-spacing in the new sintering model.

Table S8.1.1. Calculated relative energies of the gas phase Pt_4 tetramers. Comparison of TPSS(h)/aug-cc-pVTZ and PW-DFT results.

Method	Isomer I (eV), Tetrahedral	Isomer II (eV), Planar
TPSS/aug-cc-pVTZ-PP	-10.75, C_{3v}, 3 [1]	-10.45, D_{2h}, 3 [2]
TPSSh/aug-cc-pVTZ-PP	-9.86, T_d, 3 [3]	-9.57, D_{4h}, 1 [4]

[1] The T_d structure is slightly higher in energy (~1 kcal/mol) and has two imaginary frequencies.
[2] The quintet is slightly lower in energy (~1 kcal/mol), but is a transition state; both D_{2h} structures are favored over D_{4h} ones.
[3] The quintet differs by ~2 kcal/mol, but contains two imaginary frequencies.
[4] The quintet differs by ~4 kcal/mol; both the singlet and quintet are transition states.

Table S8.1.2. Calculated relative energies of the gas phase Pd_1Pt_3 tetramers. Comparison of TPSS(h)/aug-cc-pVTZ and PW-DFT results.

Method	Isomer I (eV), Tetrahedral	Isomer II (eV), Planar
TPSS/aug-cc-pVTZ-PP	-9.75, C_{3v}, 3	-9.48, C_{2v}, 5 [1]
TPSSh/aug-cc-pVTZ-PP	-9.26, C_1, 3	-8.55, C_{2v}, 1 [2]

[1] The triplet is degenerate, differing by < 1 kcal/mol; both are local minima with no imaginary frequencies.
[2] The triplet is degenerate, differing only by half a kcal/mol; the singlet is a transition state, while the triplet is a local minimum.

Table S8.1.3. Calculated relative energies of the gas phase Pd_2Pt_2 tetramers. Comparison of TPSS(h)/aug-cc-pVTZ and PW-DFT results.

Method	Isomer I (eV), Tetrahedral	Isomer II (eV), PdPdPtPt (planar)	Isomer III (eV), PdPtPdPt (planar)
TPSS/aug-cc-pVTZ-PP	-8.75, C_{2v}, 3	-8.48, C_{2v}, 3 [1]	-8.39, D_{2h}, 3 [1, 2]
TPSSh/aug-cc-pVTZ-PP	-8.52, C_{2v}, 3	-7.59, C_{2v}, 3 [1]	-7.50, D_{2h}, 1 [1]

[1] Transition-state.
[2] The singlet is degenerate, slightly higher in energy by ~ 1 kcal/mol.

Table S8.1.4. Calculated relative energies of the gas phase Pd_3Pt tetramers. Comparison of TPSS(h)/aug-cc-pVTZ and PW-DFT results.

Method	Isomer I (eV), Tetrahedral	Isomer II (eV), Planar
TPSS/aug-cc-pVTZ-PP	-8.40, C_{3v}, 3	-7.40, C_{2v}, 1 [1]
TPSSh/aug-cc-pVTZ-PP	-7.67, C_{3v}, 3	-6.55, C_{2v}, 1 [1]

[1] Transition-state.

Table S8.1.5. Calculated relative energies of the gas phase Pd_4 tetramers. Comparison of TPSS(h)/aug-cc-pVTZ and PW-DFT results.

Method	Isomer I (eV), Tetrahedral	Isomer II (eV), Planar
TPSS/aug-cc-pVTZ-PP	-7.32, C_1, 3 [1]	-6.36, D_{4h}, 1 [2]
TPSSh/aug-cc-pVTZ-PP	-6.56, C_1, 3 [3]	-5.49, D_{4h}, 1 [2]

[1] The T_d structure is slightly higher in energy (< 1 kcal/mol) and has two imaginary frequencies.
[2] Transition-state.
[3] The T_d and C_{3v} structures are slightly higher in energy (< 1 kcal/mol) and have two imaginary frequencies

Table S8.1.6. NBO Population Analysis of Charges at higher levels of theory compared to Quantum Espresso of Planar Structures of Mixed Gas Phase Clusters[1]

	TPSSh/NBO				QE/Bader
Config.	Spin	Atom	Natural Charge[2]	Valence Charge	Valence Charge
Pt_3Pd	1	Pd	0.20990	0.21	0.21
		Pt	-0.03374	-0.04	0.02
		Pt	-0.08808	-0.08	-0.11
		Pt	-0.08808	-0.08	-0.11
Pd_2Pt_2	3	Pd	0.10776	0.11	0.12
(PdPdPtPt)		Pt	-0.10776	-0.10	0.00
		Pd	0.10776	0.11	0.02
		Pt	-0.10776	-0.10	-0.15
Pd_2Pt_2	1	Pt	-0.18063	-0.18	-0.13
(PdPtPdPt)		Pt	-0.18063	-0.18	-0.13
		Pd	0.18063	0.19	0.13
		Pd	0.18063	0.19	0.13
Pd_3Pt	1	Pt	-0.25211	-0.26	-0.12
		Pd	0.06741	0.06	-0.07
		Pd	0.09235	0.09	0.09
		Pd	0.09235	0.09	0.09

[1] Pure Pd and Pt planar structures demonstrated charges of 0.00 in the singlet and triplet state. Only in the quintet state did the atoms attain a charge, Pt_4 alternated a natural charge of -/+ 0.13621 e/Pt and Pd_4 alternated -/+ 0.18843 e/Pd for a summation of 0.00 natural charge. [2] The natural charge in Gaussian 09 considers shifts in electronic population between the core, valence, and Rydberg states.

Table S8.1.7. NBO Population Analysis of Charges at higher levels of theory compared to Quantum Espresso of Tetrahedral Structures of Mixed Gas Phase Clusters[1]

	TPSSh/NBO				QE/Bader
Config.	Spin	Atom	Natural Charge[2]	Valence Charge	Valence Charge
Pt_3Pd	3	Pd	0.17514	0.19	0.15
		Pt	-0.10488	-0.11	-0.10
		Pt	-0.03510	-0.05	-0.05
		Pt	-0.03510	-0.05	0.00
Pd_2Pt_2	3	Pt	-0.12715	-0.13	-0.16
		Pt	-0.12715	-0.13	-0.05
		Pd	0.12715	0.13	0.11
		Pd	0.12715	0.13	0.10
Pd_3Pt	3	Pt	-0.19381	-0.19	-0.17
		Pd	0.06459	0.07	0.09
		Pd	0.06461	0.07	0.05
		Pd	0.06461	0.07	0.02

[1] Pure Pd and Pt tetrahedral structures demonstrated charges of 0.00. [2] The natural charge in Gaussian 09 considers shifts in electronic population between the core, valence, and Rydberg states.

8.2. SUPPORTING INFORMATION FOR CHAPTER 3

Experimental

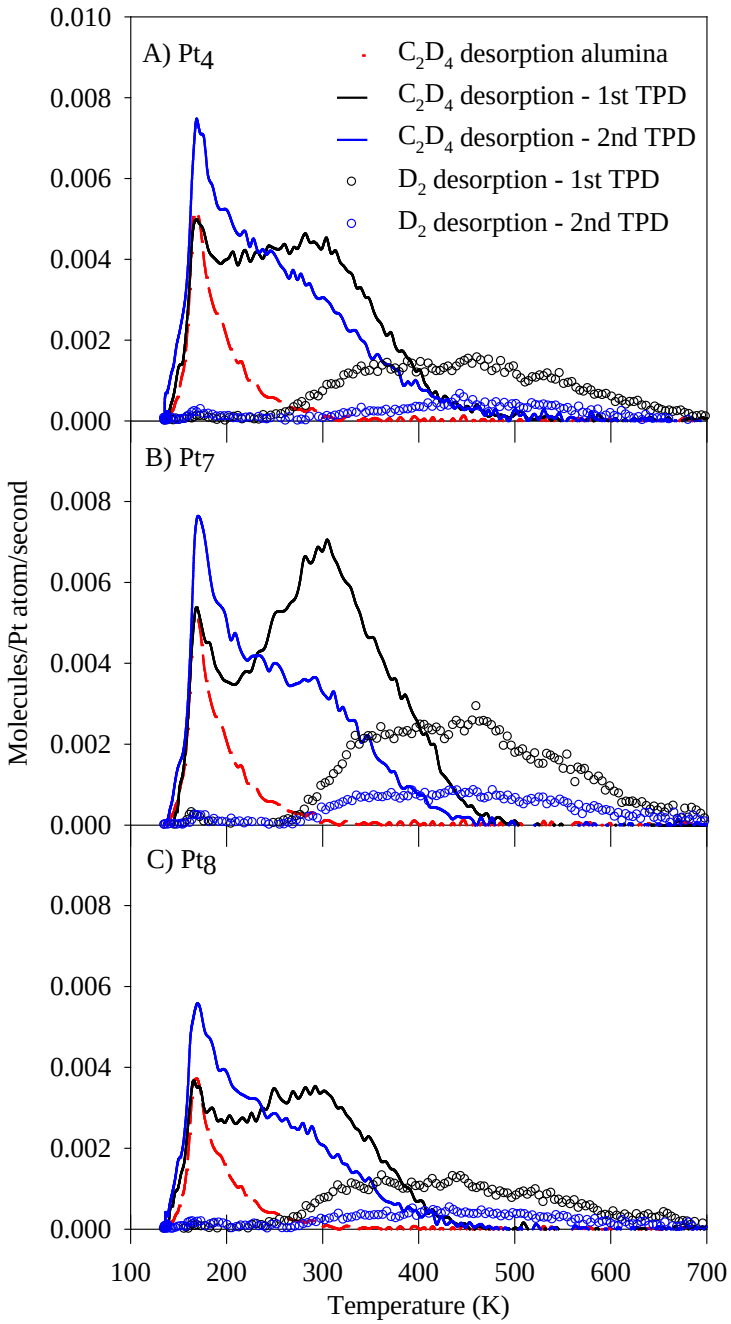

Figure S8.2.1. Intact C_2D_4 (solid) and D_2 (circles) desorbing from Pt_n/alumina/Ta(110) (n=4,7,8) sample during two consecutive TPD measurements. Intact C_2D_4 (red dashed line) desorbing from a cluster free alumina/Ta(110) sample. All samples were exposed to 5 L of C_2D_4 at 150 K before starting the TPD measurement. The D_2 signal has not be corrected for the amount of D_2 produced from the fragmentation of C_2D_4 caused by electron impact ionization.

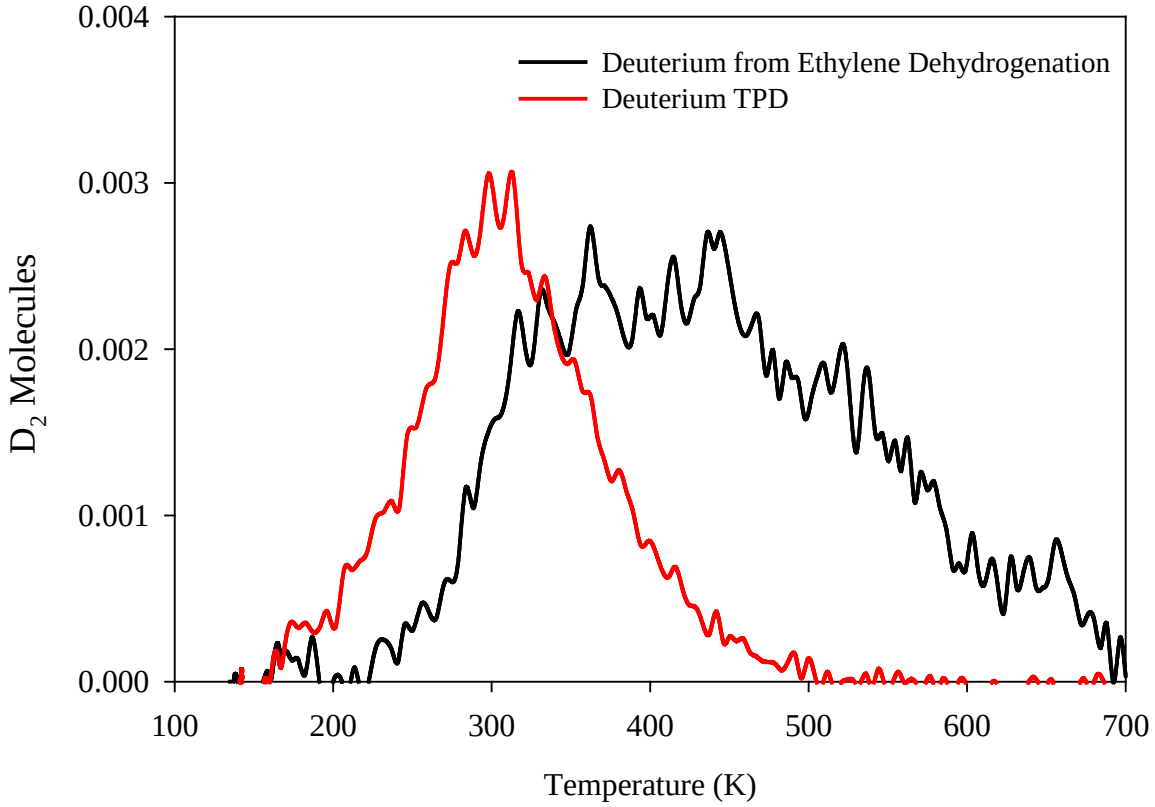

Figure S8.2.2. D_2 desorbing from Pt_8/alumina/Ta(110) after exposing the sample to 5 L of D_2 at 150 K (red). D_2 produced by C_2D_4 dehydrogenation during a C_2D_4 TPD/R measurement (black).

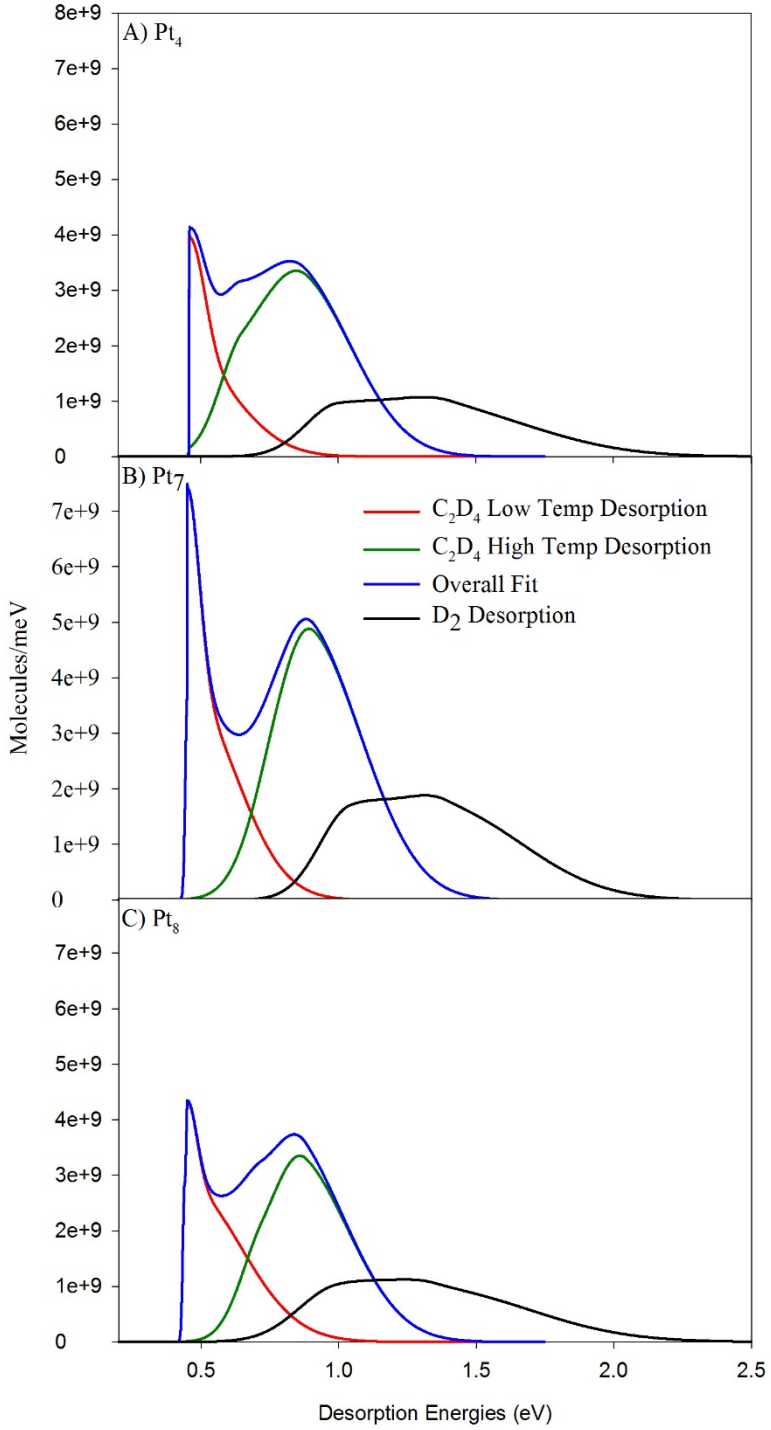

Figure S8.2.3. Energy of desorption fits for C_2D_4 and D_2 desorbing during the first C_2D_4 TPD/R experiments for Pt_4, Pt_7, and Pt_8

TPD fitting method and results:

A distribution of population in sites with different energies for desorption/dehydrogenation, θ(E), is assumed, and then the TPD/R spectra are fit using the first order rate equation:

$$I(t)\ \alpha\ \frac{-d\theta}{dt} = (\theta(E) \cdot\ \nu)\ e^{\frac{-E}{kT(t)}},$$

where I(t) is the desorption as a function of time, ν is a prefactor and T(t) is the temperature as a function of time. θ(E) is adjusted until the simulated I(t) matches the experiment. Because size-selected cluster samples are time consuming to prepare, and irreversibly changed by a single TPD/TPR run, it is simply not practical to extract ν from a series of coverage-dependent experiments on every cluster size. Therefore, the simulations were tested for ν ranging from 10^{13} to 10^{15} s^{-1}, covering a range often found in TPD.[3] The simulated desorption/dehydrogenation energies shift by only ~7% *per* order-of-magnitude variation in ν, and in Figure S3 we present the θ(E) distributions obtained for ν = 10^{14} s^{-1}.

XPS results

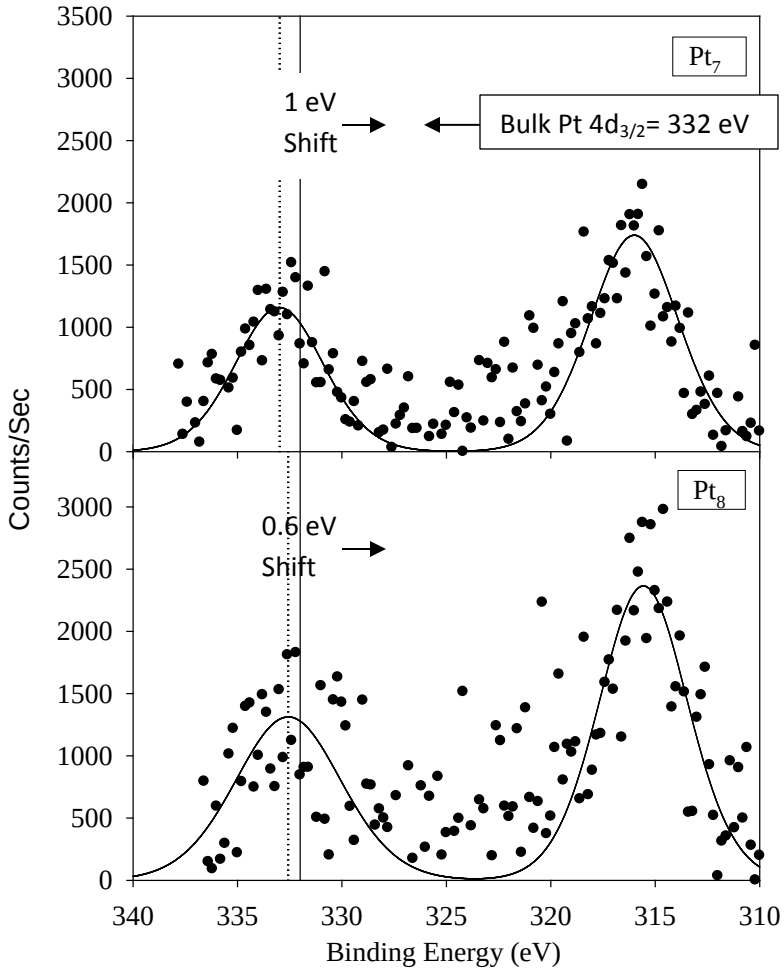

Figure S8.2.4. Pt 4d XPS for Pt_7 and Pt_8, as-deposited on alumina/Ta(110)

ISS extrapolation method

Figure S8.2.5 shows the normalized Pt ISS intensity as a function of He^+ exposure in a sequence of low He^+ flux (0.1 μA) ISS measurements. The increase in Pt signal during the initial measurements is evidence of a small coverage of adventitious adsorbates (CO and H_2O as determined by separate TPD measurements) that had adsorbed onto the clusters during the ~ 15 min cluster deposition time. The initial increase in Pt signal is a result of the adsorbates being sputtered off the cluster to expose the underlying Pt to He^+ scattering. The Pt signal eventually reaches a maximum and begins to decrease due to Pt sputtering. To determine the as-deposited value the Pt intensity is extrapolated back to the limit of zero He^+ exposure and zero adsorbate coverage as shown by the fit in Figure **S8.2.5**.

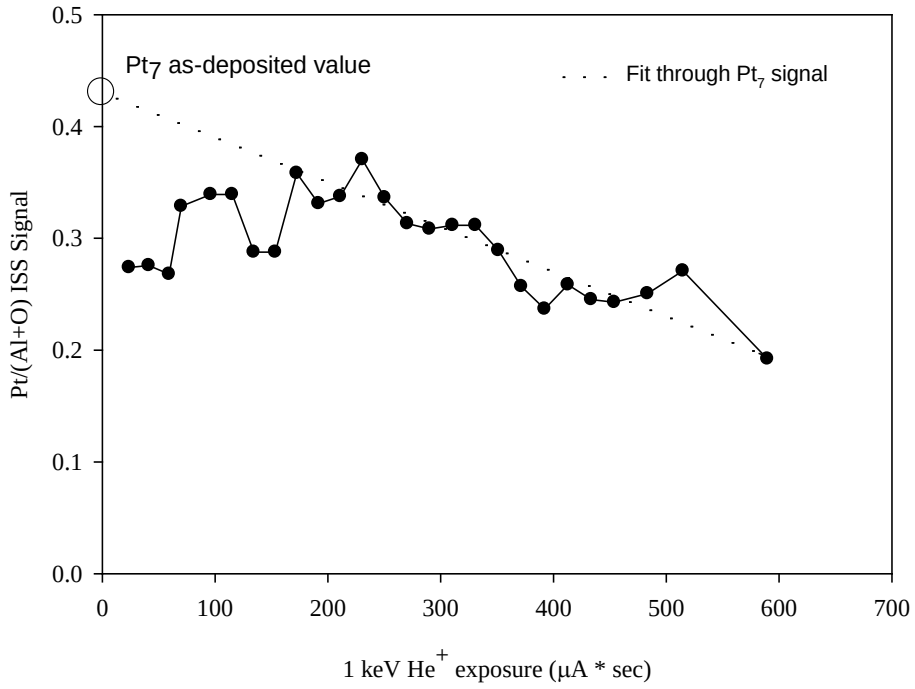

Figure S8.2.5. Normalized Pt intensity for Pt_7 as a function of He^+ exposure during a sequence of low He^+ flux (0.1 μA) ISS scans. The as-deposited value of the Pt intensity can be determined by extrapolating back to the limit of zero exposure and adsorbate coverage as shown by the fit

Pt_4 CO TD-ISS

Figure S8.2.6 shows the results from a $^{13}C^{16}O$ TPD and a TD-ISS experiment performed in our group by F. Sloan Roberts and Matthew Kane on the Pt_4/alumina/Re(0001) system. The $^{13}C^{16}O$ TPD (blue) measurement was collected by exposing a freshly prepared Pt_4/alumina/Re(0001) sample with 10 L of $^{13}C^{16}O$ at a 180 K. The sample was allowed to cool to 140 K before heating the sample at a rate of 3 K/sec while detecting the amount of $^{13}C^{16}O$ desorbing from the surface.

The TD-ISS measurements were collected by exposing a separately prepared Pt_4/alumina/Re(0001) sample to 10 L of $^{13}C^{16}O$ at 180 K and colleting an ISS spectrum with a single low He^+ flux (0.1μA) scan. The succeeding points in the TD-ISS curve were collected by heating the sample in 50 K increments and measuring the ISS spectrum at the indicated temperatures. The loss of Pt signal due to sputtering, the recovery of Pt signal due to removal of $^{13}C^{16}O$, and the as-deposited Pt signal are represented by sloping dashed lines and were determined on separately prepared samples using the same procedure that was used for **Figure 3.2**.

From the TPD results, heating the sample to 350 K desorbs ~35 % of the total $^{13}C^{16}O$ coverage but results in an insignificant recovery in the Pt ISS signal. As the sample is heated from 350 to 650 K there is a sharp recovery of the Pt ISS signal as the remaining $^{13}C^{16}O$ coverage desorbs. These results suggest that the weakly bound $^{13}C^{16}O$ that is desorbed at temperatures < 350 K is bound in sites that are inefficient at blocking or shadowing the He^+ from scattering off the Pt, such as around the periphery of the cluster. On the other hand, the $^{13}C^{16}O$ desorbed at temperatures above 350 K leads to a strong recovery of the Pt ISS signal suggesting it desorbs from sites that efficiently attenuate the signal, such as on top sites.

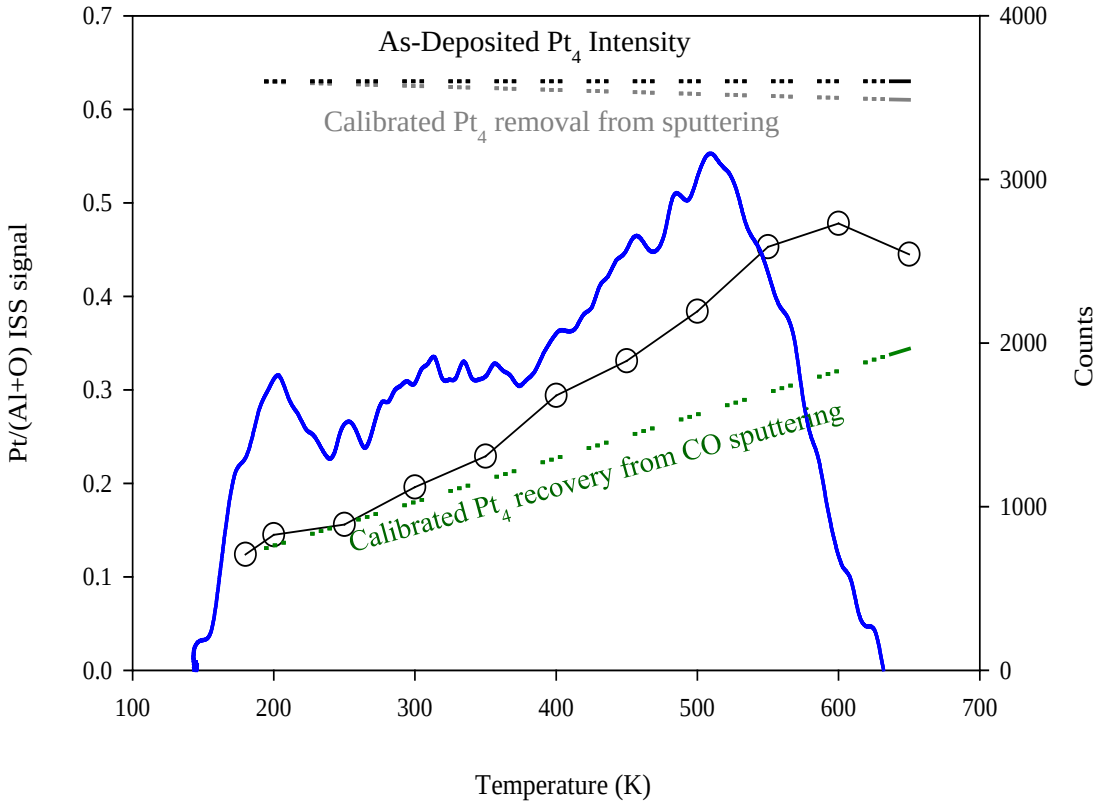

Figure S8.2.6. Pt/(Al+O) ISS signal as function of temperature (circles) after exposing the sample with 10 L of $^{13}C^{16}O$ at 180 K. CO desorbing from a separately prepared Pt_4/alumina/Re(0001) sample exposed to 10 L of $^{13}C^{16}O$ at 180 K during the first TPD measurement(blue). Both samples contained a 0.1 ML of deposited Pt_4 clusters.

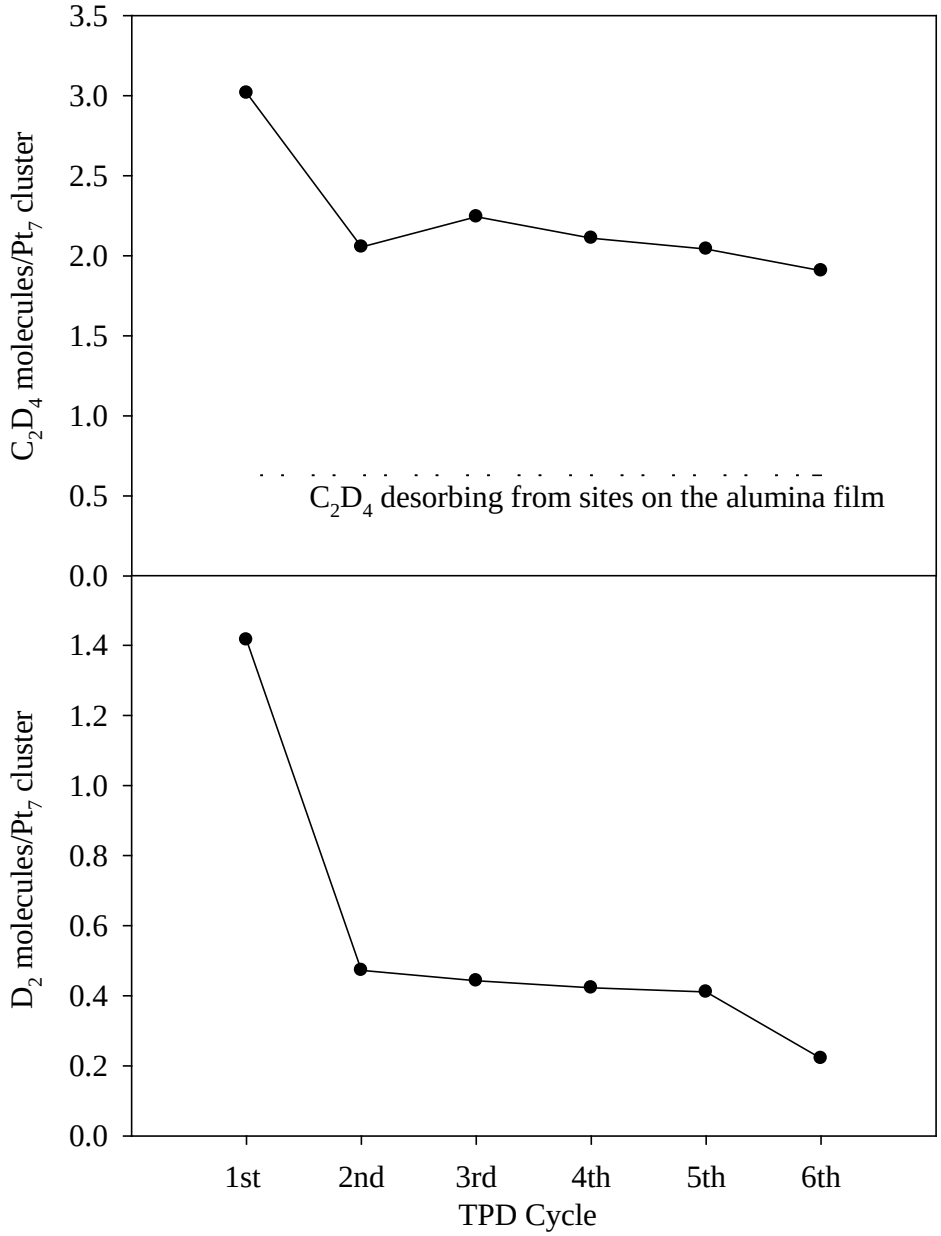

Figure S8.2.7. Integrated amounts of C_2D_4(top) and D_2(bottom) desorbing, *per* deposited Pt_7 cluster, during a sequence of 6 TPD/R runs under the conditions used in Fig. 2. The dashed horizontal line gives an estimate for the C_2D_4 desorbing from alumina sites, taken from the integrated desorption measured for cluster-free alumina.

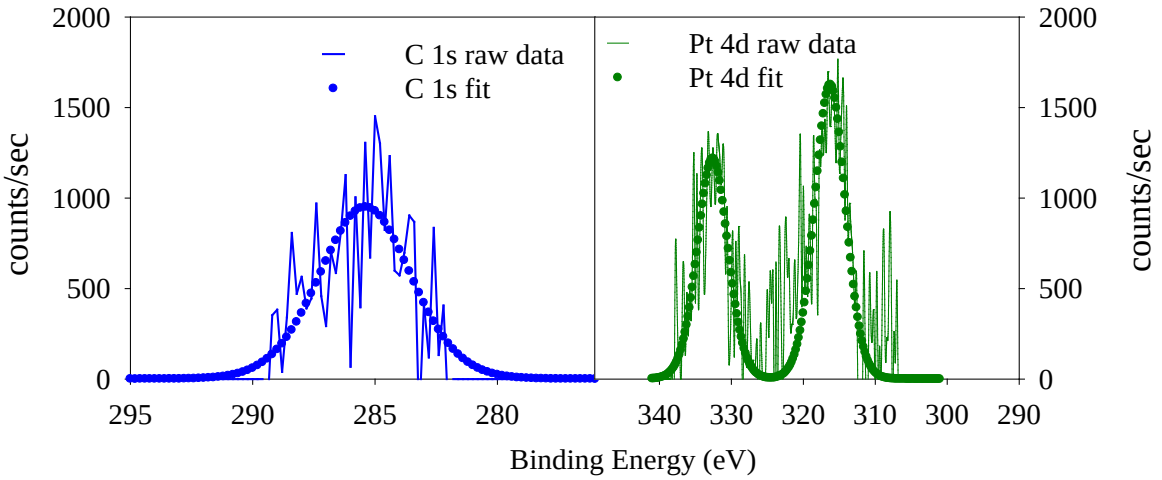

Figure S8.2.8. C 1s and Pt 4d peaks measured by XPS after 6 consecutive TPD cycles on a Pt_7/alumina sample. The presence of carbon suggest that dehydrogenation of ethylene leads to the deposition of carbon onto the model catalyst

Theoretical Methods

The relevant equations regarding formation (E_{form}), adsorption (E_{ads}), and sintering energies (E_s) are described in the following. E_{form} is VASP's DFT energy of the gas phase cluster with the component, atomic energies already subtracted. The atomic energies arise from the calculated energies of the elements from which the pseudopotential was generated.

$$E_{ads}[Pt_n] = E[Surf+Pt_n]-E[Surf]-Egas,min[Pt_n]$$

where E [Surf + Pt_n] is the total DFT energy of the supported cluster system, E[Surf] is the total energy of the bare support, and $E_{gas,min}$[Pt_n] is the global minimum of the gas-phase cluster.

An analogous equation to E_{ads} for reagent species (*reag*) such as ethylene and C (a single carbon atom is used as a first-order approximation to coking) is detailed below:

$$E_{reag} = E[Surf+Pt_n+reag]-E[Surf+Pt_n]-E_{reag}$$

where $E[Surf+Pt_n+reag]$ is the total DFT energy of the supported cluster system with the reagent species and E_{reag} is the total energy of the gas-phase cluster. In coverage calculations of ethylene, E_{reag} will encompass the $n \times E_{ethyl}$, where E_{ethyl} is the energy of ethylene in the gas-phase.

Statistical analysis is performed through use of the Boltzmann probability for *i*-th configuration (P_i) by taking the Boltzmann distribution of each minimum (e^{-E_i/k_BT}) divided by the sum of the distributions of all relevant low energy minima:

$$P_i = \frac{e^{-E_i/k_BT}}{\sum e^{-E_i/k_BT}}$$

where E_i is the *i*-th configuration energy of a gas phase cluster (i.e. E_{form} as defined above), adsorbed cluster $(E[Surf+Pt_mB_n])$ or adsorbed cluster with a reagent $(E[Surf+Pt_n+reag])$, k_B is the Boltzmann constant, and T is the temperature.

The entropic contribution of relevant minima may also be found by considering the fundamental thermodynamic relation of the Helmholtz free energy ($F = U - TS$). Specifically, the

Gibbs' entropy equation (S_G) allows us to analyze the effect of discrete states with their respective Boltzmann probabilities on the ensemble of particular cluster types:

$$S_G = -k_B \sum_i P_i \, ln(P_i)$$

where the P_I are the Boltzmann weights and k_B is the Boltzmann constant. In this way, we may analyze the entropic contribution at a catalytically relevant temperature (TS_G).

In the gas phase, the septamer and octamer contain many isomers whose energies are within 0.2-0.3 eV of the most stable geometry (**Figure S8.2.9**).[1] The gas phase isomers present a mixture of 2D and 3D geometries. Adsorbed structures were formed from the deposition of the lowest 5-6 gas phase structures, with a thorough sampling of cluster faces to possible binding sites. The complexity of the corrugated alumina surface leads to a combination of Pt-Al and Pt-O coordination so that single-layer gas phase isomers crinkle in order to maximize wetting of the surface (observed in Pt_7, Isomer II, Main text **Figure 3.1**). As the surface is Al-terminated, Pt coordinating to electropositive Al gains a negative charge. Likewise, Pt-O coordination yields positively charged Pt so that a single cluster features a range of electronic depletion or augmentation from one atom to the next. These atomic charges (Δq) are visualized in the main text's **Figure 3.1**. The charge separation between atoms yields an electrostatic potential that further stabilizes clusters and attenuates their site reactivity.

There is an apparent switch in dimensionality between Pt_7 to Pt_8, where Pt_7 on average features more open geometries that wet the corrugated support. The adsorbed Pt_7 clusters feature a prismatic geometry (ΣP_{700K} = 66.67%, Isomers I and IV) and a single-layer geometry (ΣP_{700K} = 33.33%, Isomers II, III, and V). This mix of structures offers a complex and rich set of binding sites for adsorbates. In contrast, all of the isomers of Pt_8 are prismatic. In prismatic structures, some of the Pt atoms are buried inside the cluster, becoming unavailable as binding sites. These results are in agreement with the experimental findings that suggest that Pt_7 provides more binding sites for ethylene as compared to Pt_8. Additionally, there is a greater uniformity in the nature of the exposed binding sites, as can be judged by their partial charges.

The septamer optimizes the cluster-support interactions with a relatively high charge transfer ($\Delta Q > -1.20$ e) in the global minimum, and, unsurprisingly, features the most favorable adsorption. The added negative charge does not distribute uniformly over the cluster; instead, there is a polarization of Pt atoms in Pt_7. Pt_8 preserves the charge transfer behavior of Pt_7, but adsorption to the support is weaker: of the global minimum of Pt_8, $Pt_{8,glob}$, it is 0.2 eV weaker than that of $Pt_{7,glob}$. The Pt atoms within $Pt_{8,glob}$ are charged more uniformly (details in Table S4).

Table S8.2.1. Formation energies of Global Minima of Pt_7, Pt_8

	Pt_7	**Pt_8**
E_{form} (eV)	-27.05	-31.97
E_{form}/atom (eV)	-3.86	-4.00

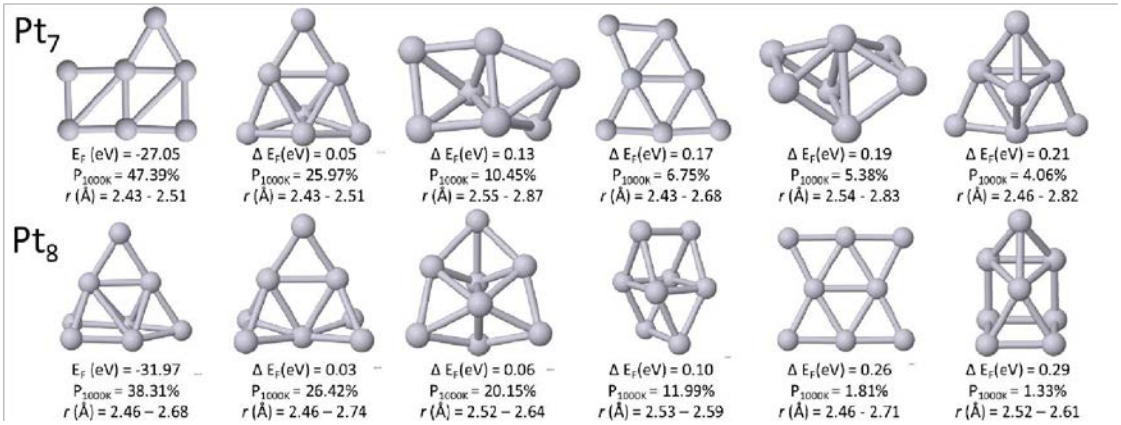

Figure S8.2.9. Gas phase isomers of Pt_7, Pt_8 at catalytically relevant temperature of 1000K

Table S8.2.2. Gas phase isomers

Cluster	**Isomer**	**ΔE_{form} (eV)**	**$P_{450\ K}$**	**$P_{1000\ K}$**
Pt_7	I	0.00	75.60%	47.39%
	II	0.05	19.85%	25.97%
	III	0.13	2.63%	10.45%
	IV	0.17	0.99%	6.75%
	V	0.19	0.60%	5.38%
	VI	0.21	0.32%	4.06%
Pt_8	I	0.00	56.98%	38.31%
	II	0.03	24.95%	26.42%
	III	0.06	13.66%	20.15%
	IV	0.10	4.31%	11.99%
	V	0.26	0.06%	1.81%
	VI	0.29	0.03%	1.33%

Table S8.2.3. Gas phase isomers under def2/TZVPP basis with pure and hybrid functionals calculated in TURBOMOLE V6.6

Cluster	Isomer	Δ E_{form} (eV), Multiplicity	Δ E_{form} (eV), Multiplicity	Δ E_{form} (eV), Multiplicity	Δ E_{form} (eV), Multiplicity	Δ E_{form} (eV), Multiplicity
		VASP	TM/PBE	TM/PBE0	TM/TPSS	TM/TPSSh
Pt_7	I	0.00	0.00, 5	0.86, 5	0.34, 5	0.65, 5
	II	0.05	0.15, 5*	0.36, 5, I	0.18, 5	0.32, 5, I
	III	0.13	0.01, 5	0.00, 5	0.00, 5	0.00, 5
	IV	0.17	0.20, 5, I	0.72, 5	0.40, 3*	0.71, 3
	V	0.19	0.05, 5	0.31, 5, I	0.10, 5	0.15, 5
	VI	0.21	0.20, 5*	0.40, 5, I	0.26, 5*	0.16, 5

* geometries had difficulty converging, I = geometries with an imaginary frequency

Table S8.2.4. Adsorbed isomers of Pt_7, Pt_8 with Boltzmann Populations (P) at Experimentally Relevant Temperatures of 450 and 1000 K and Charge Transfer (ΔQ) from the Support

Cluster	Isomer	Δ E_{ads} (eV)	$P_{450\ K}$	$P_{700\ K}$	ΔQ (e)
Pt_7	I	0.00	75.27%	65.89%	-1.22
	II	0.04	24.49%	32.02%	-1.44
	III	0.24	0.16%	1.26%	-1.33
	IV	0.27	0.07%	0.77%	-1.25
	V	0.43	<0.01%	0.05%	-1.23
	$\Sigma P_T E_{ads}$ (eV)		-5.08	-5.07	
	TS_G (eV)		0.010	0.019	
Pt_8	I	0.00	97.65%	87.73%	-1.24
	II	0.17	1.14%	5.03%	-1.07
	III	0.19	0.74%	3.82%	-0.94
	IV	0.21	0.41%	2.61%	-1.08
	V	0.30	0.04%	0.57%	-1.22
	VI	0.39	<0.01%	0.14%	-1.08
	VII	0.41	<0.01%	0.10%	-0.80
	$\Sigma P_T E_{ads}$ (eV)		-4.89	-4.87	
	TS_G (eV)		0.002	0.009	

Table S8.2.5. Local Minima of Adsorbed Ethylene on Pt_7 (Isomer I and II)

Ads.	Config.	$\Delta E_{ethylene}$ (eV)	$P_{450\ K}$	$P_{700\ K}$	$\Delta Q_{ethylene}$ (e)	Hybrid.	C-C Bond Lengths (Å)	Bond Angles (°)
Pt_7, Isomer I	**i**	0.00	86.93%	72.48%	0.00	sp2	1.41	115.4–120.5
	ii	0.10	7.35%	14.81%	-0.07	sp3	1.49	100.6–114.9
	iii	0.11	5.72%	12.59%	0.00	sp2	1.40	116.0–120.5
	iv	0.38	<0.01%	0.13%	-0.16	sp3	1.49	99.7–115.4
	v	0.79	<0.01%	<0.01%	-0.10	sp3	1.50	97.5–114.9
	vi	0.87	<0.01%	<0.01%	-0.02	sp3	1.51	100.6–113.9
Pt_7, Isomer II	**i**	0.00	99.64%	96.30%	0.01	sp2	1.42	115.0–120.5
	ii	0.24	0.22%	1.90%	-0.01	sp2	1.41	114.6–121.0
	iii	0.26	0.12%	1.26%	-0.05	sp3	1.49	97.5–115.9
	iv	0.34	0.02%	0.36%	-0.03	sp2	1.42	114.8–120.4
	v	0.39	<0.01%	0.15%	-0.03	sp2	1.42	115.3-120.4
	vi	0.49	<0.01%	0.03%	-0.05	sp3	1.50	100.4–115.5

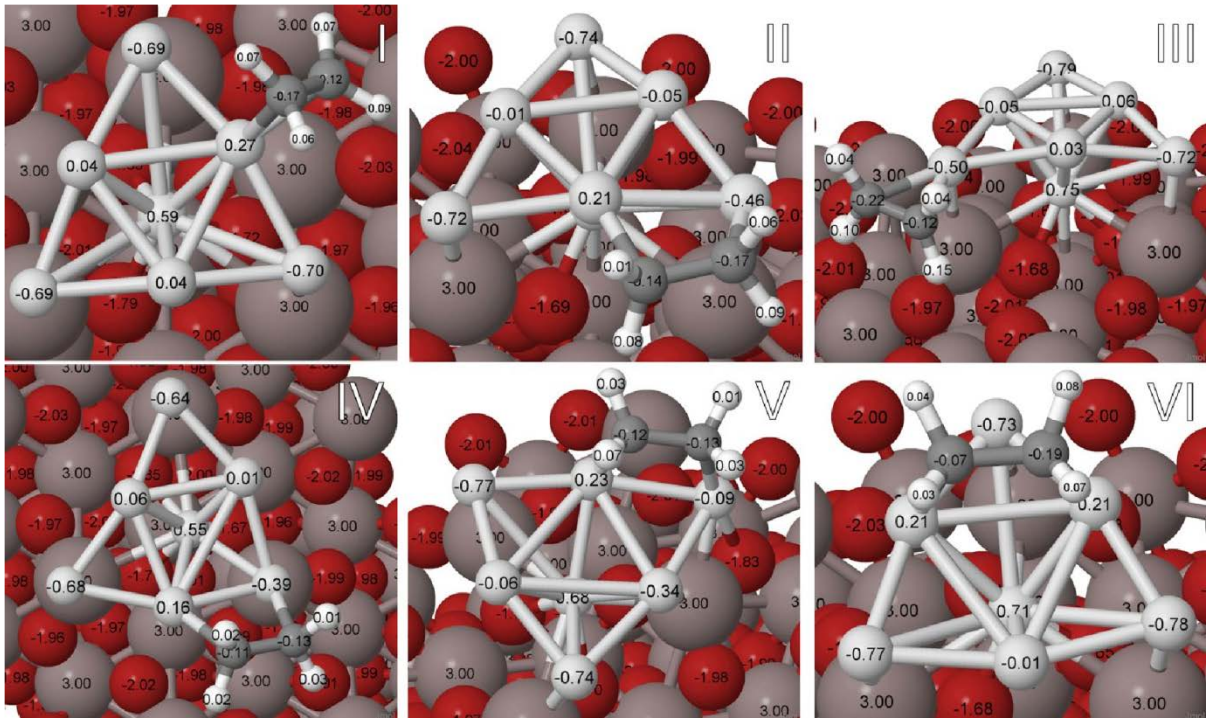

Figure S8.2.10. The lowest minima of ethylene adsorbed on $Pt_{7,\ glob}$, with calculated Bader charges.

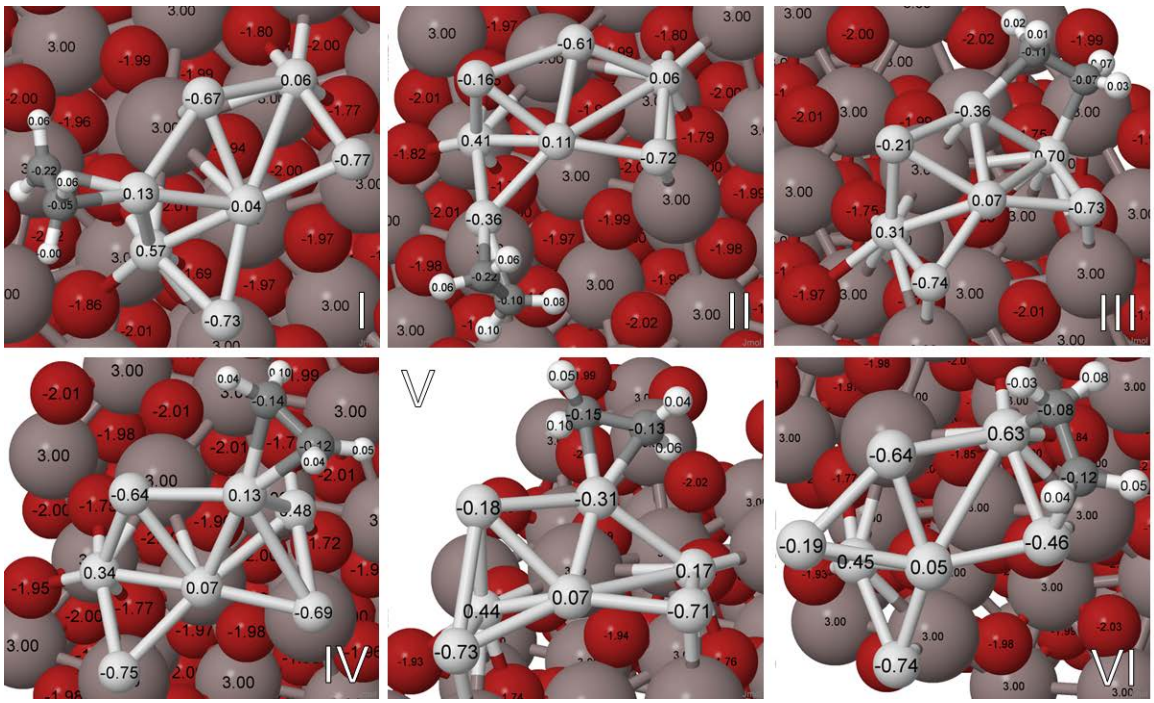

Figure S8.2.11. The lowest minima of ethylene adsorbed on the second lowest minimum of adsorbed Pt_7, with calculated Bader charges.

Table S8.2.6. Local Minima Configurations of a Coverage of 2 Ethylene on $Pt_{7,\ glob}$

Configurations	$P_{450\ K}$	$P_{700\ K}$	ΔE	$\Delta Q_{ethylene}$ (e)	Hybrid.
I	82.13%	67.60%	0.00	-0.02	sp2
II	15.45%	23.10%	0.06	-0.11	sp2, sp3
III	2.06%	6.32%	0.14	-0.08	sp2, sp3
IV	0.18%	1.32%	0.24	0.01	sp2
V	0.11%	0.96%	0.26	-0.02	sp2
VI	0.07%	0.70%	0.28	-0.02	V rot 90°, sp2

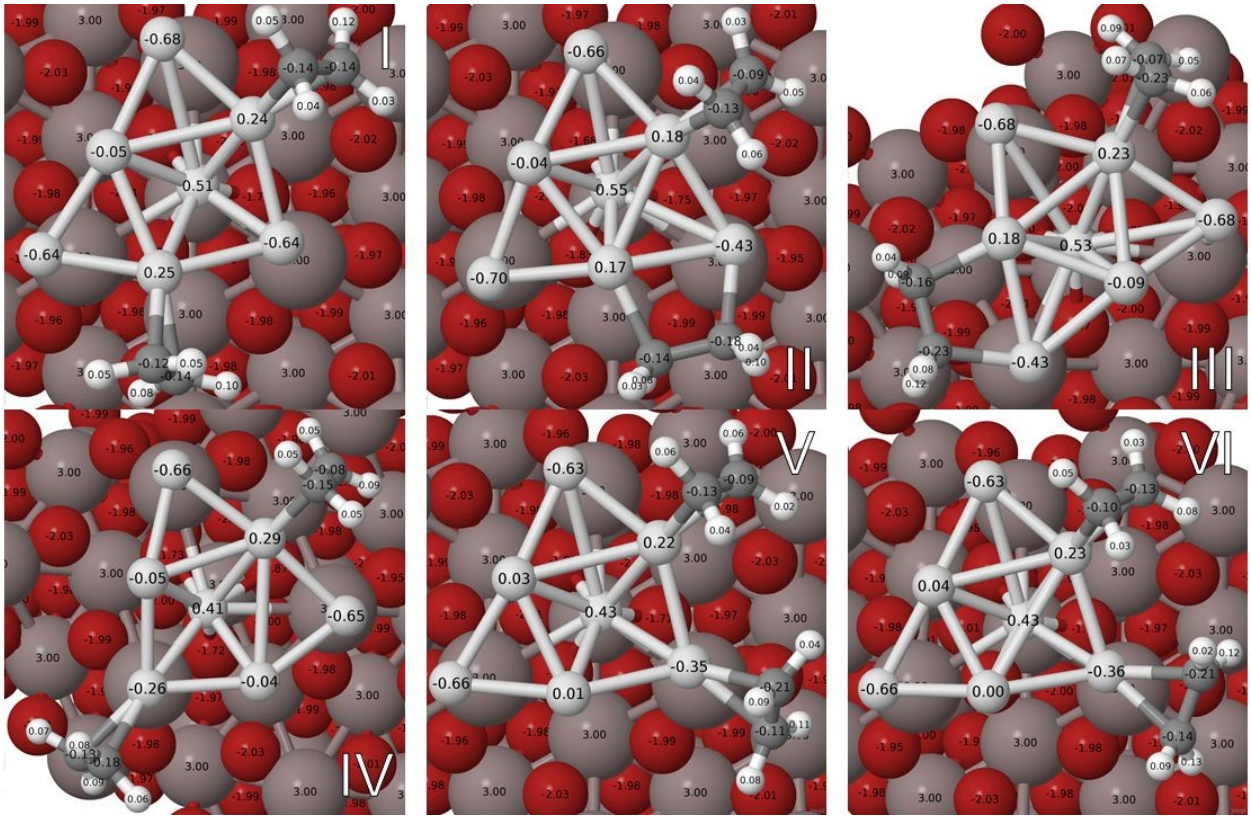

Figure S8.2.12. The lowest minima of 2 ethylene adsorbed on the Pt_7, Isomer I (the global minimum).

Table S8.2.7. Local Minima Configurations of a Coverage of 3 Ethylene on $Pt_{7,\ glob}$

Configurations	$P_{450\ K}$	$P_{700\ K}$	ΔE	$\Delta Q_{ethylene}$ (e)	Hybrid.
I	84.26%	69.22%	0.00	-0.30	2sp2, sp3
II	11.47%	19.21%	0.08	-0.08	3 sp2
III	4.02%	9.78%	0.12	-0.07	3 sp2
IV	0.24%	1.60%	0.23	0.07	3 sp2
V	>0.00%	0.12%	0.38	-0.04	3 sp2
VI	>0.00%	0.07%	0.41	-0.08	3 sp2

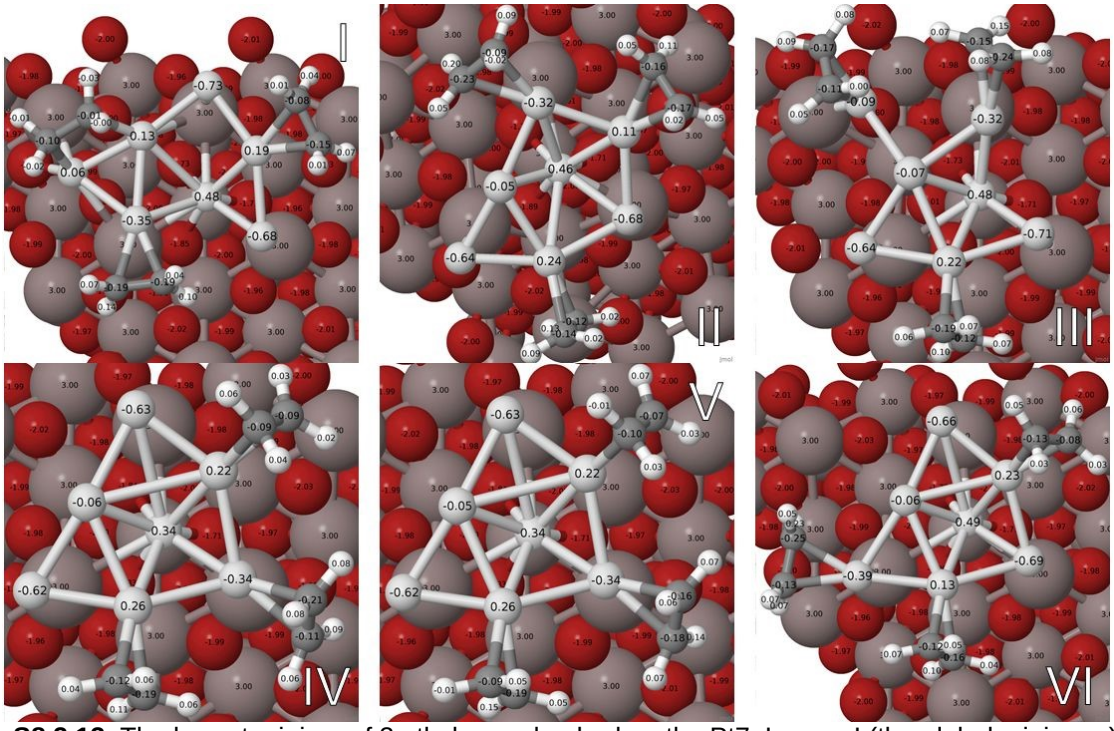

Figure S8.2.13. The lowest minima of 3 ethylene adsorbed on the Pt7, Isomer I (the global minimum).

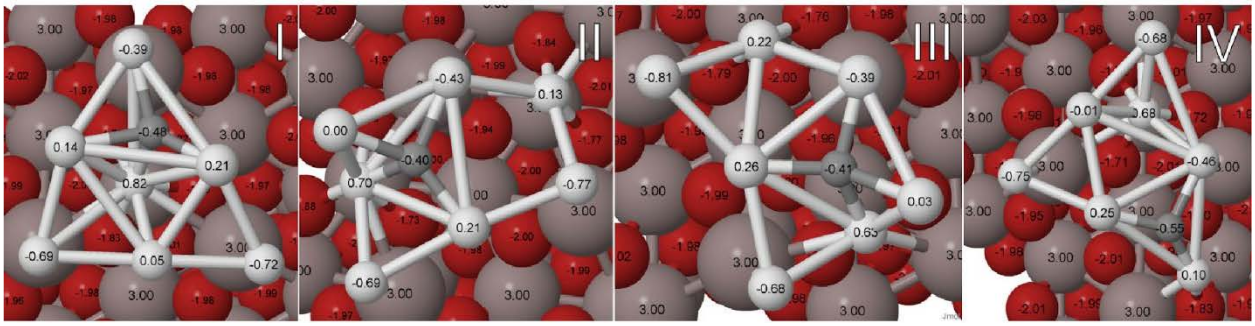

Figure S8.2.14. The C-sticking configurations of the lowest four isomers of Pt_7, with calculated Bader charges.

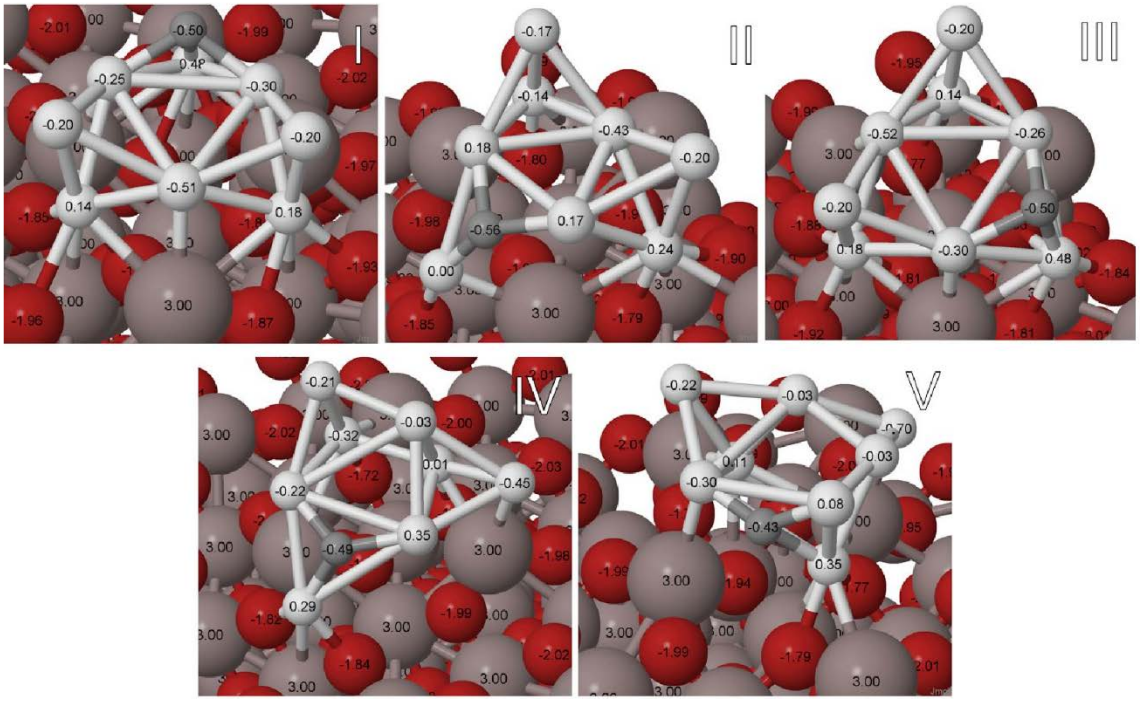

Figure S8.2.15. The C-sticking configurations of the lowest five isomers of Pt_8, with calculated Bader charges.

8.3. SUPPORTING INFORMATION FOR CHAPTER 4

Experimental

Further discussion of **Figure 4.2** in the main text: A small amount of CO is seen desorbing from the alumina film at low temperatures, presumably from defect sites in the alumina film. However, strong bimodal desorption of CO from the as-deposited Pt_7/alumina is seen, which we attribute to CO desorbing from sites related to the Pt cluster. Heating the sample to 700 K results in a small attenuation in high temperature desorption component and a small increase in the low temperature desorption component. Exposing the sample to 1.5 L of B_2H_6 and heating it to 300 K prior to the CO TPD resulted in the amount of CO desorbing at temperatures above ~350 K to decrease by 70%, presumably from a combination of cluster restructuring and site blocking from residual boron species left on the cluster. Heating the sample to 700 K following the 1.5 B_2H_6 exposure resulted in a small loss of CO desorption in the 300-400 K range.

Further discussion of **Figure 4.3** in the main text: Simply heating Pt_7/alumina to 300 K results in a ~38% decrease in the amount of C_2D_4 desorbing from Pt sites above 200 K (1.3 C_2D_4/Pt_7), and also a ~28% reduction in the amount D_2 production (1.0 D_2/Pt_7). Heating to 700 K has no further effect on C_2D_4 desorption above ~300 K, but results in a significant increase in desorption at lower temperatures, such that the total C_2D_4 desorption ($1.9/Pt_7$) is only ~10% below that for as-deposited Pt_7/alumina. D_2 production ($1.3/Pt_7$) recovers nearly to the as-deposited value, but shifts to slight lower temperatures. These effects are attributed to a combination of thermal changes to the cluster morphology, and desorption at temperatures above 300 K, of the small amount of adventitious CO present on the as-deposited Pt_7,[3] consistent with the ISS results in **Figure 4.1**.

Theoretical

The relevant equations regarding formation (E_{form}), adsorption (E_{ads}), and sintering energies (E_s) are described in the following. E_{form} is VASP's DFT energy of the gas phase cluster with the component, atomic energies already subtracted. The atomic energies arise from the calculated energies of the elements from which the pseudopotential was generated.

$$E_{ads}[\mathrm{Pt_7B}] = E[\mathrm{Surf} + \mathrm{Pt_7B}] - E[\mathrm{Surf}] - E_{gas,min}[\mathrm{Pt_7B}]$$

where E [Surf +$\mathrm{Pt_7B}$] is the total DFT energy of the supported cluster system, E[Surf] is the total energy of the bare support, and $E_{gas,min}$[$\mathrm{Pt}_m\mathrm{B}_n$] is the global minimum of the gas-phase cluster. Table III lists the adsorption energies of the global minima of adsorbed clusters as well as the sintering energy penalty, i.e. the energy cost of an atom of a given element to break away from an octomer, forming a septamer and a monomer on the support:

$$E_s[Pt_7B - B] = E[Surf + Pt_7] + E[Surf + B_1] - E[Surf + Pt_7B] - E[Surf]$$

$$E_s[Pt_8 - Pt] = E[Surf + Pt_8] + E[Surf + Pt_1] - E[Surf + Pt_7] - E[Surf]$$

In **Table S8.3.3**, the sintering energy penalty refers to the monomer energy $E[\mathrm{Surf} + \mathrm{Pt/B_1}]$ in the most favorable position on the support from potential energy surface (PES) calculations. Our PES utilized a fine 10 × 10 grid on a sample unit of our (3 × 3) surface.

An analogous equation to E_{ads} for reagent species (*reag*) such as diborane, ethylene, and C (a single carbon atom is used as a first-order approximation to coking) is detailed below:

$$E_{reag} = E[\mathrm{Surf} + \mathrm{Pt_7B} + reag] - E[\mathrm{Surf} + \mathrm{Pt_7B}] - E_{reag}$$

where $E[\mathrm{Surf} + \mathrm{Pt}_m\mathrm{B}_n + reag]$ is the total DFT energy of the supported cluster system with the reagent species and E_{reag} is the total energy of the gas-phase cluster. In coverage calculations of ethylene, ethylene adsorption reflected our method of sequential adsorption:

$$E_{2\ ethylene} = E_{2\ ethylene+glob,Pt7Bads} - E_{1\ ethylene+glob,Pt7Bads} - E_{1\ ethylene,gas}$$

$$E_{3\ ethylene} = E_{3\ ethylene+glob,Pt7Bads} - E_{2\ ethylene+glob,Pt7Bads} - E_{1\ ethylene,gas}.$$

Further statistical analysis is performed through use of the Boltzmann probability for *i*-th configuration (P_i) by taking the Boltzmann distribution of each minimum (e^{-E_i/k_BT}) divided by the sum of the distributions of all relevant low energy minima:

$$P_i = \frac{e^{-E_i/k_BT}}{\Sigma\, e^{-E_i/k_BT}}.$$

where E_i is the *i*-th configuration energy of a gas phase cluster cluster (i.e. E_{form} as defined above), adsorbed cluster ($E[\mathrm{Surf} + \mathrm{Pt}_m\mathrm{B}_n]$) or adsorbed cluster with a reagent ($E[\mathrm{Surf} + \mathrm{Pt}_m\mathrm{B}_n + reag]$), k_B is the Boltzmann constant, and T is the temperature.

The entropic contribution of relevant minima may also be found by considering the fundamental thermodynamic relation of the Helmholtz free energy ($F = U - TS$). Specifically, the Gibbs' entropy equation (S_G) allows us to analyze the effect of discrete states with their respective Boltzmann probabilities on the ensemble of particular cluster types:

$$S_G = -k_B \sum_i P_i \ln(P_i)$$

where the P_I are the Boltzmann weights and k_B is the Boltzmann constant. In this way, we may analyze the entropic contribution at a catalytically relevant temperature (TS_G).

Intra-cluster bonding was evaluated through a summation of the electrostatic potential present in a cluster:

$$V_C = k_e \sum_{i,j} \frac{q_i q_j}{r_{i,j}}$$

where q_i and q_j represent two different atoms, $r_{i,j}$ is the distance between them, and k_e is Coulomb's constant $\frac{1}{4\pi\varepsilon_0}$.

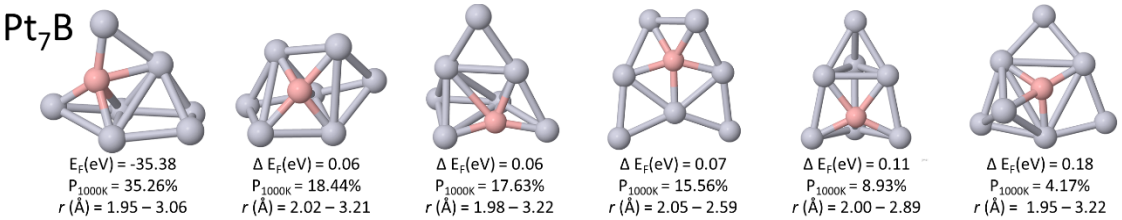

Fig. S8.3.1. Gas phase isomers of Pt_7B at catalytically relevant temperature of 1000K

Table S8.3.1. Formation energies of Global Minima of Pt_7, Pt_8, and Pt_7B

	Pt_7	**Pt_8**	**Pt_7B**
E_{form} (eV)	-27.05	-31.97	-35.38
E_{form}/atom (eV)	-3.86	-4.00	-5.05

Table S8.3.2. Gas phase isomers

Cluster	**Isomer**	**Δ E_{form} (eV)**	**P_{450K}**	**P_{1000K}**
Pt_7B	I	0.00	59.90%	35.26%
	II	0.06	14.19%	18.44%
	III	0.06	12.84%	17.63%
	IV	0.07	9.72%	15.56%
	V	0.12	2.83%	8.93%
	VI	0.18	0.52%	4.17%

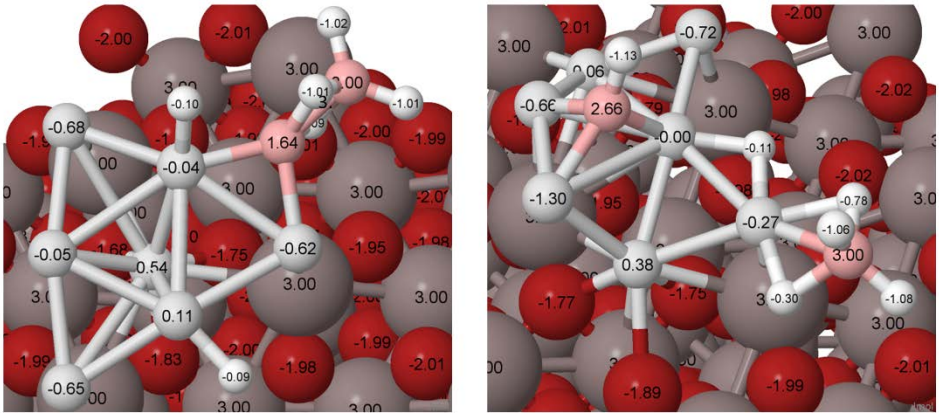

Fig. S8.3.2. Global Minima of Adsorbed Diborane on Pt_7, Isomer I (Prismatic) and II (Single-Layer)

In order to consider boration of the Pt-clusters, the adsorption of diborane on all bridging, atomic, and hollow sites of the two lowest minima of adsorbed Pt_7 (Isomer I, prismatic with E_{ads}

= -5.09 eV and Isomer II, single-layer with E_{ads} = -5.05 eV) were calculated.[3] Diborane was placed on these sites in two different orientations: orthogonal to the cluster-alumina surface or parallel. Initial positions with the diborane rotated every 45° with respect to the symmetry of the cluster were also calculated in order to take into account more configurations. We highlight here in **SI Figure S8.3.2** the lowest minimum of diborane adsorbed on the prismatic and single-layer Pt_7 clusters, respectively. In these ground-state calculations, hydrogen spontaneously leaves the diborane to adsorb on Pt atoms. These minima also demonstrate a marked difference in the decomposition route of diborane on prismatic isomer as compared to the single-layer isomer, with diborane breaking into fragmented BH and BH_4 on the single-layer isomer. In past experimental studies, diborane has successfully been used to borate Ni[4], Pd[5], and Ru[6]. Thermal desorption spectroscopy experiments of B_2H_6 in conjunction with other analytical techniques suggest that diborane adsorbs dissociatively on Pd(111)[5] at 300 K and on Ni(100)[4]. On Ru(0001)[6], diborane exhibits exposure dependence, at < 0.8 L the diborane completely decomposes and at > 2 L two desorption features for B_2H_6 (m/z=27) are seen. Moreover, as observed on Ni(100)[2] at coverages of ~2.5 L, B_2H_6 multilayers may also react to form higher order boranes such as B_4H_{10}. This suggests that single-layer Pt_7 clusters may also act as highly reactive “surfaces” to the diborane molecule. We also hope to theoretically and experimentally probe the mechanism of boration on Pt in greater detail in a future study.

The geometric diversity present in Pt_7 is enhanced even further in Pt_7B with 10 isomers. This results in a substantial increase in the configurational entropy’s contribution to the free energy of the system (**SI Tables S8.3.3-4**). In a previous study, 1:1 ratios of Pt:Pd were preferentially stabilized and sintering-resistant over other ratios of Pt:Pd due to intra-cluster bonding and the configurational entropy arising from the presence of many isomers.[7] Due to the limitation of our cluster sizes, the sintering modality is limited to extrapolation from Pt and B potential energy surfaces. Pt’s PES yields typical behavior of ~2 eV sintering penalty, observed in other systems, but B’s PES resists facile characterization. The B monomer adsorbs nearly as

strongly as the B-doped Pt clusters and distorts the surface by abstracting surface O-Al from their initial positions, raising them by 0.2-2.4 Å (**SI Figure S8.3.3**). Unlike other dopants such as the weakly-bound Zn[8], which can evaporate from oxides such as TiO_2 and MgO, or the mobile Pd/Pt[7] monomers, B will resist sintering by Ostwald ripening (**SI Table S8.3.3**). Thus, borated Pt may exhibit considerable stability compared to other dopants due to the stability of the B-O_{surf} anchor, the entropic influence of many isomers lowering the free energy of the system, and the intra-cluster attraction present in the clusters.

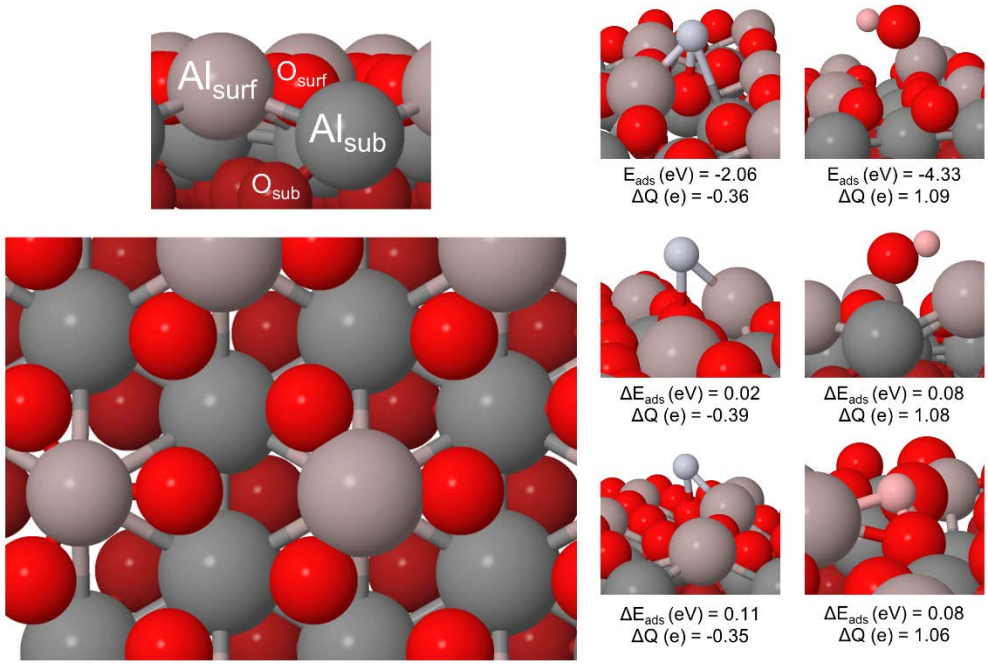

Fig. S8.3.3. The highest affinity configurations from Pt (light gray) and B (light pink) potential energy surface calculations.

Table S8.3.3. Characteristics of Borated Platinum vs Pure Platinum Clusters

	Pt_7	Pt_8	Pt_7B
Isomers	5	7	10
$\Sigma P_{450K} E_{ads}$ (eV)	-5.08	-4.89	-4.60
ΔQ (e)	-1.22 to -1.44	-0.94 to -1.24	-0.03 to -1.17
$T_{450K}S_G$ (eV)	0.010	0.002	0.013
$T_{700K}S_G$ (eV)	0.019	0.014	0.036
E_s—Pt		2.17	
E_s—B			3.28

Table S8.3.4. Adsorbed isomers of Pt_7, Pt_8, Pt_7B with Boltzmann Populations (P) at Experimentally Relevant Temperatures of 450 and 1000 K and Charge Transfer (ΔQ) from the Support

Cluster	Isomer	Δ E_{form} (eV)	P_{450K}	P_{700K}	ΔQ (e)	V_C (eV)
Pt_7	I	0.00	75.27%	65.89%	-1.22	-3.63
	II	0.04	24.49%	32.02%	-1.44	-1.32
	III	0.24	0.16%	1.26%	-1.33	-1.35
	IV	0.27	0.07%	0.77%	-1.25	-3.29
	V	0.43	<0.01%	0.05%	-1.23	-2.79
	$\Sigma P E_{ads}$ (eV)		-5.08	-5.07		
	TS_G (eV)		0.010	0.019		
Pt_8	I	0.00	97.65%	87.73%	-1.24	0.99
	II	0.17	1.14%	5.03%	-1.07	0.22
	III	0.19	0.74%	3.82%	-0.94	-1.37
	IV	0.21	0.41%	2.61%	-1.08	0.66
	V	0.30	0.04%	0.57%	-1.22	0.59
	VI	0.39	<0.01%	0.14%	-1.08	0.72
	VII	0.41	<0.01%	0.10%	-0.80	-0.47
	$\Sigma P E_{ads}$ (eV)		-4.89	-4.87		
	TS_G (eV)		0.002	0.014		
Pt_7B	I	0.00	81.22%	59.26%	-0.37	-11.85
	II	0.10	6.40%	11.57%	-0.70	-25.41
	III	0.10	6.39%	11.56%	-0.44	-10.95
	IV	0.12	3.54%	7.91%	-0.03	-6.83
	V	0.16	1.37%	4.29%	-1.17	-4.49
	VI	0.19	0.62%	2.59%	-0.95	-22.08
	VII	0.21	0.38%	1.88%	-0.96	-30.11
	VIII	0.29	0.05%	0.52%	-0.64	-18.84
	IX	0.31	0.03%	0.34%	-0.91	-30.32
	X	0.39	<0.01%	0.09%	-1.04	-21.92
	$\Sigma P E_{ads}$ (eV)		-4.66	-4.78		
	TS_G (eV)		0.013	0.036		

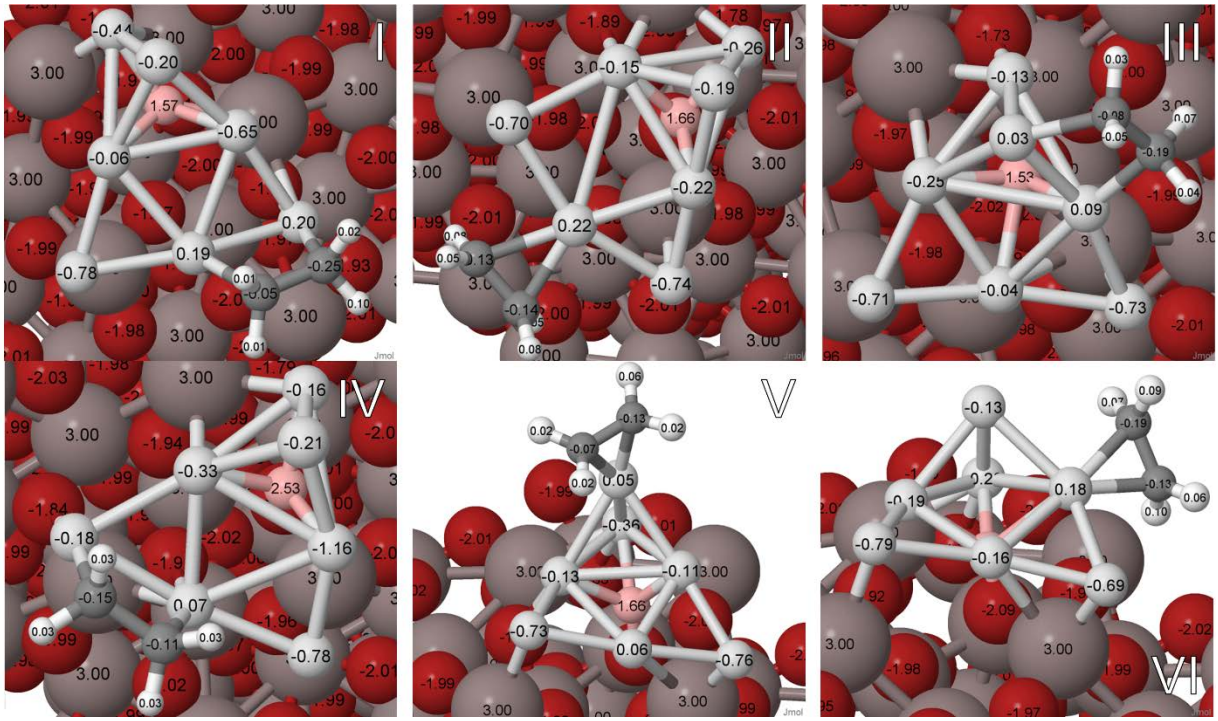

Fig. S8.3.4. The lowest minima of ethylene adsorbed on Pt_7B_{glob}.

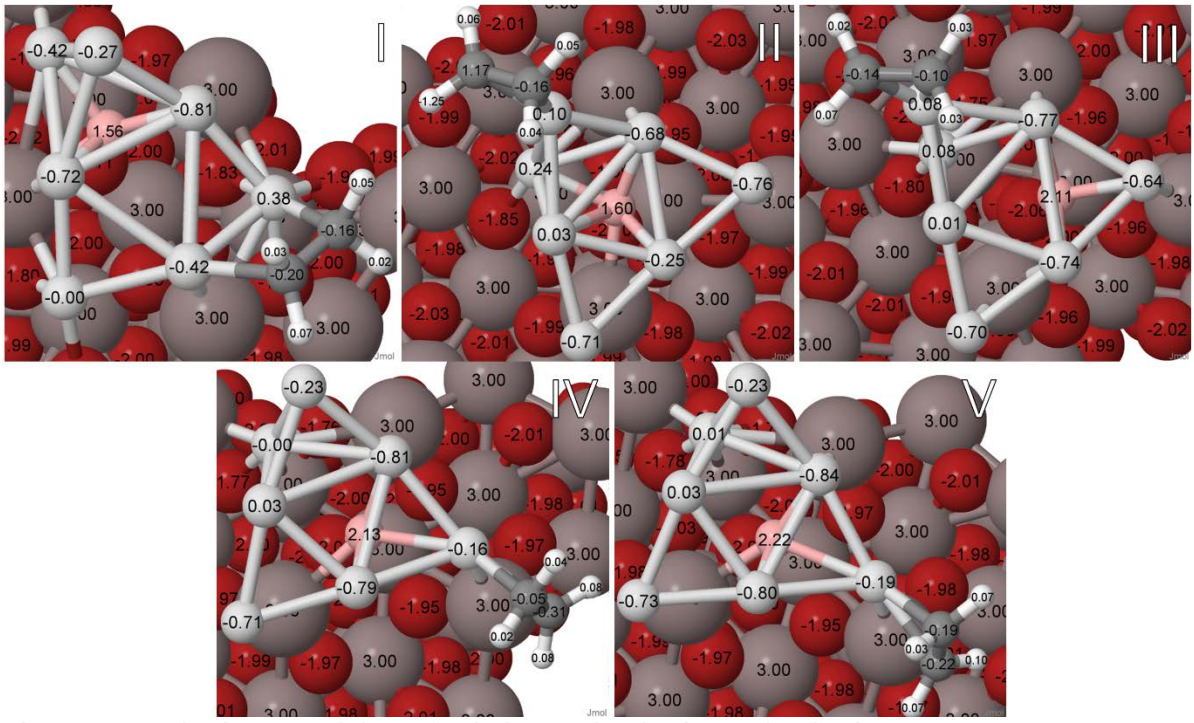

Fig. S8.3.5. The lowest minima of ethylene adsorbed on adsorbed Pt_7B, Isomer II.

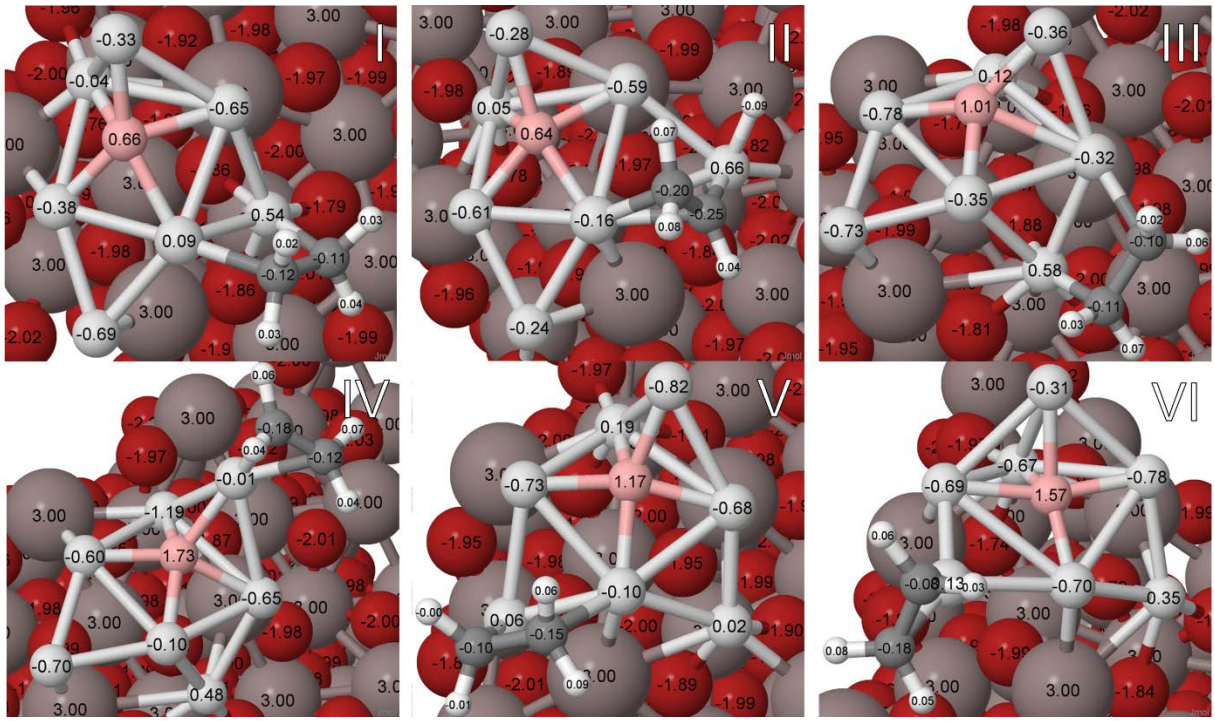

Fig. S8.3.6. The lowest minima of ethylene adsorbed on adsorbed Pt_7B, Isomer V.

Table S8.3.5. Local Minima of 1 Adsorbed Ethylene on Pt_7B (Isomer I, II, and V)

Ads.	Isomer	$\Delta E_{ethylene}$ (eV)	P_{450K}	P_{700K}	$\Delta Q_{ethylene}$ (e)	B-C Bond Distances (Å)	Hybrid.	C-C Bond Lengths (Å)	Bond Angles (°)
Pt_7B, Isomer I	**i**	0.00	95.21%	84.22%	-0.15	5.01-5.15	sp3	1.50	102.8–115.8
	ii	0.13	3.59%	10.22%	-0.01	5.28	sp2	1.42	114.8–120.3
	iii	0.17	1.18%	5.02%	-0.16	3.87-4.34	sp3	1.50	102.6–115.3
	iv	0.35	0.01%	0.27%	-0.14	4.39-4.88	sp3	1.52	102.1–114.3
	v	0.37	0.01%	0.19%	-0.09	5.16-5.41	sp2	1.41	115.3–120.8
	vi	0.42	<0.00%	0.08%	0.01	3.95-4.18	sp2	1.41	115.1–121.6
Pt_7B, Isomer II	**i**	0.00	100.00%	99.98%	-0.19	5.02-5.09	sp3	1.50	104.1–114.5
	ii	0.52	<0.00%	0.02%	-0.10	5.58-12.95	sp2	1.42	114.5–121.1
	iii	0.64	<0.00%	<0.00%	-0.08	5.69-6.22	sp2	1.42	114.8–120.8
	iv	0.81	<0.00%	<0.00%	-0.14	4.25-4.42	sp2	1.42	114.1–120.2
	v	0.82	<0.00%	0.01%	-0.13	4.62	sp2	1.42	114.1–120.2
Pt_7B, Isomer V	**i**	0.00	99.96%	99.22%	-0.11	3.97-4.52	sp3	1.50	102.4–115.0
	ii	0.30	0.04%	0.66%	-0.34	3.73-3.89	sp2	1.41	111.3–121.3
	iii	0.42	<0.00%	0.10%	-0.06	4.35-4.71	sp3	1.49	97.7–114.8
	iv	0.55	<0.00%	0.01%	-0.08	3.84-3.93	sp2	1.41	115.2–121.1
	v	0.60	<0.00%	<0.00%	-0.11	3.74-4.44	sp3	1.49	98.6–115.3
	vi	0.65	<0.00%	<0.00%	-0.03	4.84-9.74	sp2	1.43	114.6–120.7

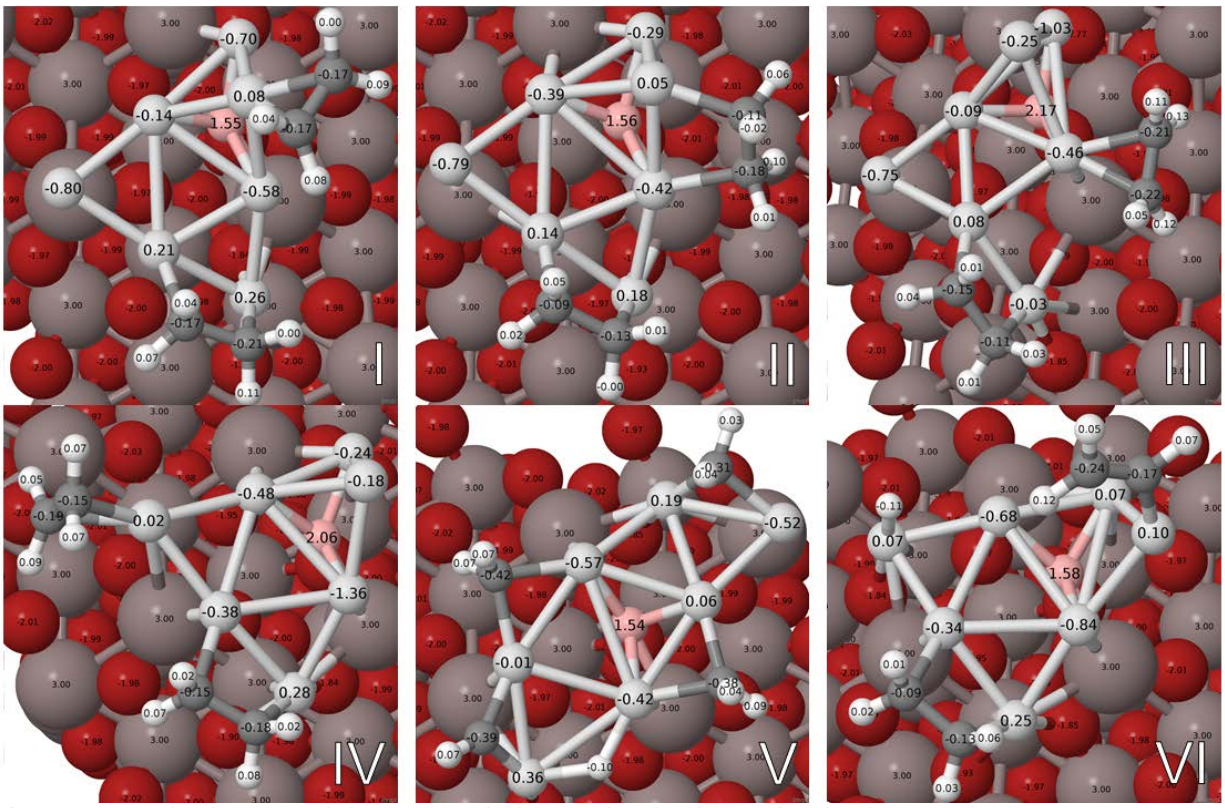

Fig. S8.3.7. The lowest minima of 2 ethylene adsorbed on adsorbed Pt_7B, Isomer I.

Table S8.3.6. Coverage of 2 Ethylene on Pt_7B_{glob}

Isomer	Δ $E_{ethylene}$ (eV)	P_{450K}	P_{700K}	$\Delta Q_{ethylene}$ (e)	Hybrid.	B-C Bond Distances (Å)
i	0.00	97.78%	91.62%	-0.29	sp2, sp3	4.79-5.29
ii	0.15	2.20%	8.00%	-0.30	sp3	3.57-5.14
iii	0.35	0.01%	0.27%	-0.19	sp2, sp3	3.60-6.00
iv	0.41	<0.01%	0.11%	-0.18	sp2, sp3	5.15-6.41
v	0.66	<0.01%	<0.01%	-1.17	C-C, C-H Scission	3.10-4.63
vi	0.69	<0.01%	<0.01%	-0.37	C-H Scission	4.51-5.06

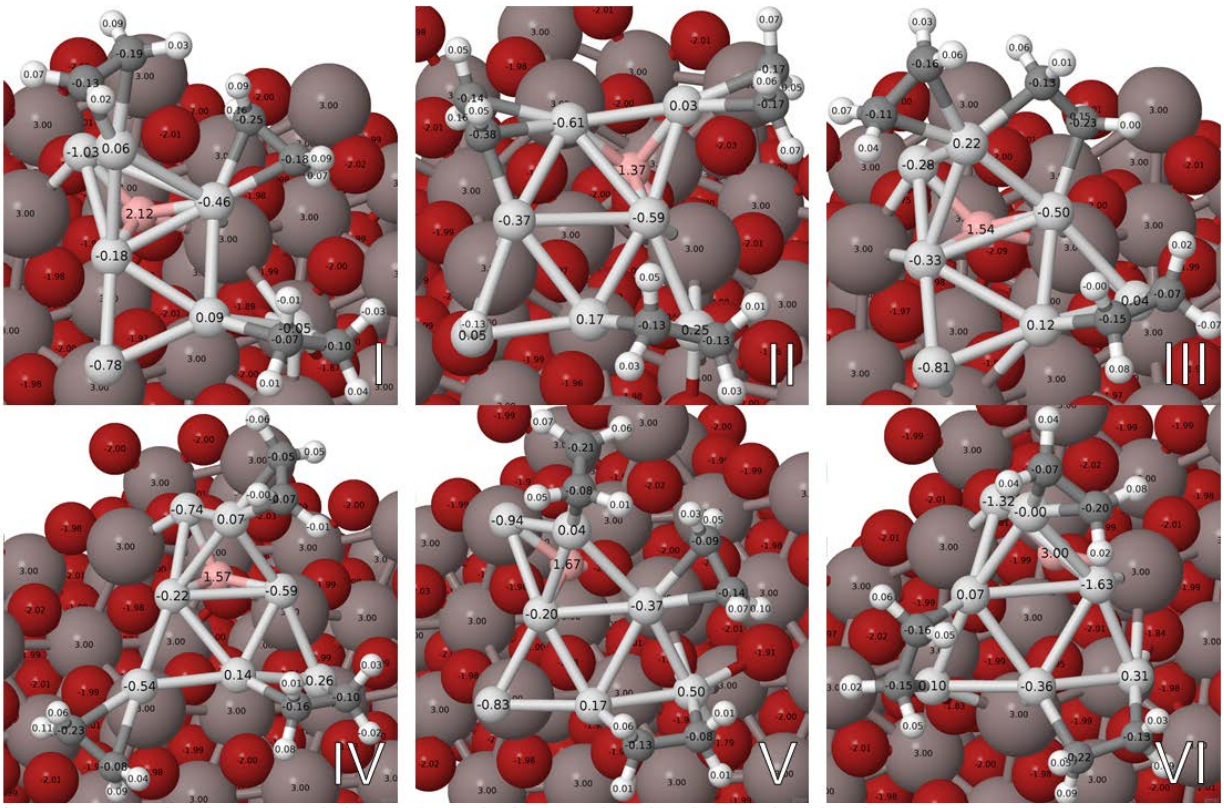

Fig. S8.3.8. The lowest minima of 3 ethylene adsorbed on adsorbed Pt_7B, Isomer I.

Table S8.3.7. Coverage of 3 Ethylene on Pt_7B_{glob}

Isomer	Δ $E_{ethylene}$ (eV)	P_{450K}	P_{700K}	$\Delta Q_{ethylene}$ (e)	Hybrid.	B-C Bond Distances (Å)
i	0.00	99.58%	95.74%	-0.30	sp3, 2sp2	3.48-5.94
ii	0.24	0.21%	1.84%	-0.62	sp3, 2sp2, C-H Scission	3.93-5.43
iii	0.25	0.17%	1.59%	-0.37	2sp3, sp2	3.46-5.12
iv	0.33	0.02%	0.39%	-0.31	sp3, 2sp2	4.80-6.42
v	0.34	0.02%	0.34%	-0.17	sp3, 2sp2	4.31-6.06
vi	0.41	<0.01%	0.10%	-0.31	2sp3, sp2	4.71-5.57

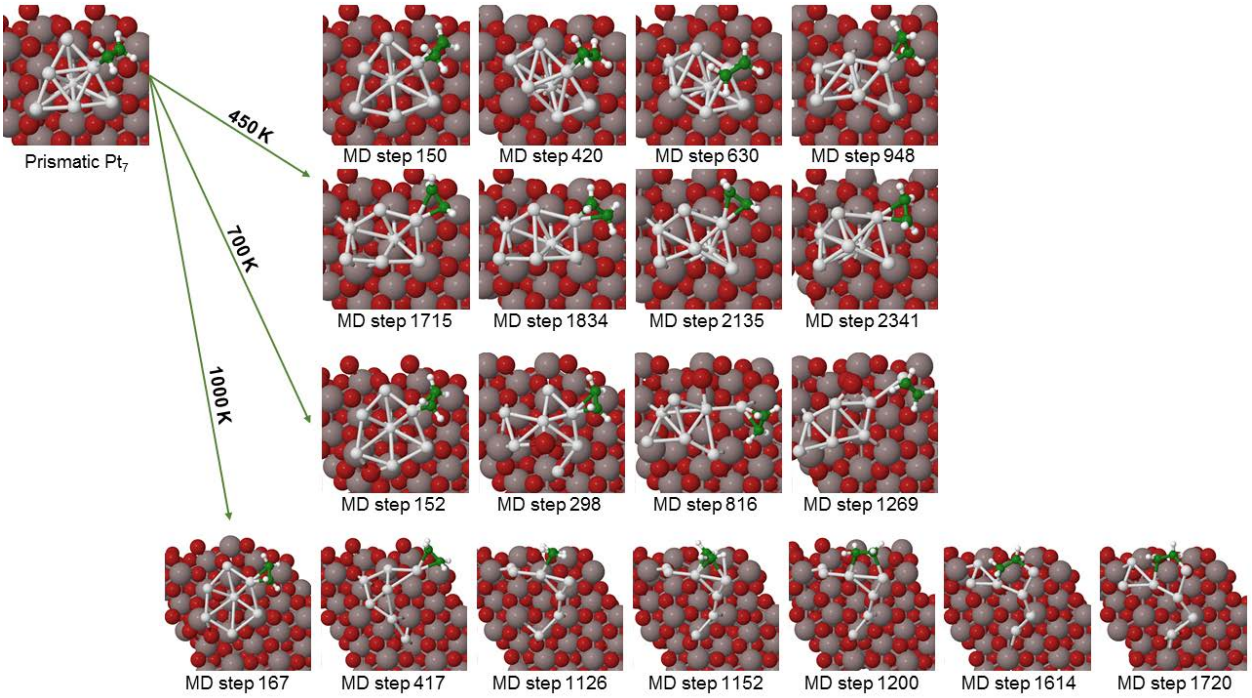

Fig. S8.3.9. Highlights from the MD trajectories of ethylene adsorbed on prismatic Pt_7 at catalytically relevant temperatures.

In order to analyze the effects of both temperature and reagent adsorption on structural reformation, Molecular Dynamics calculations were performed at higher temperatures relevant to catalysis. Notably, at 450 K after 2000 MD steps, the prismatic geometry has transformed to a configuration very similar to the single-layer. At higher temperatures such as 1000 K, the cluster may also fragment into extended, branched configurations that may be a precursor to the mobile monomers that contribute to sintering by Ostwald ripening. Moreover, the sp^2 adsorbed ethylene may interconvert to sp^3 adsorption. In MD trajectories of ethylene adsorbed on the single-layer Pt_7, at 450 and 700 K, the stability of this configuration leads to only twisting and rotation of ethylene at circa 2000 MD steps with little to no change in the Pt cluster's geometry.

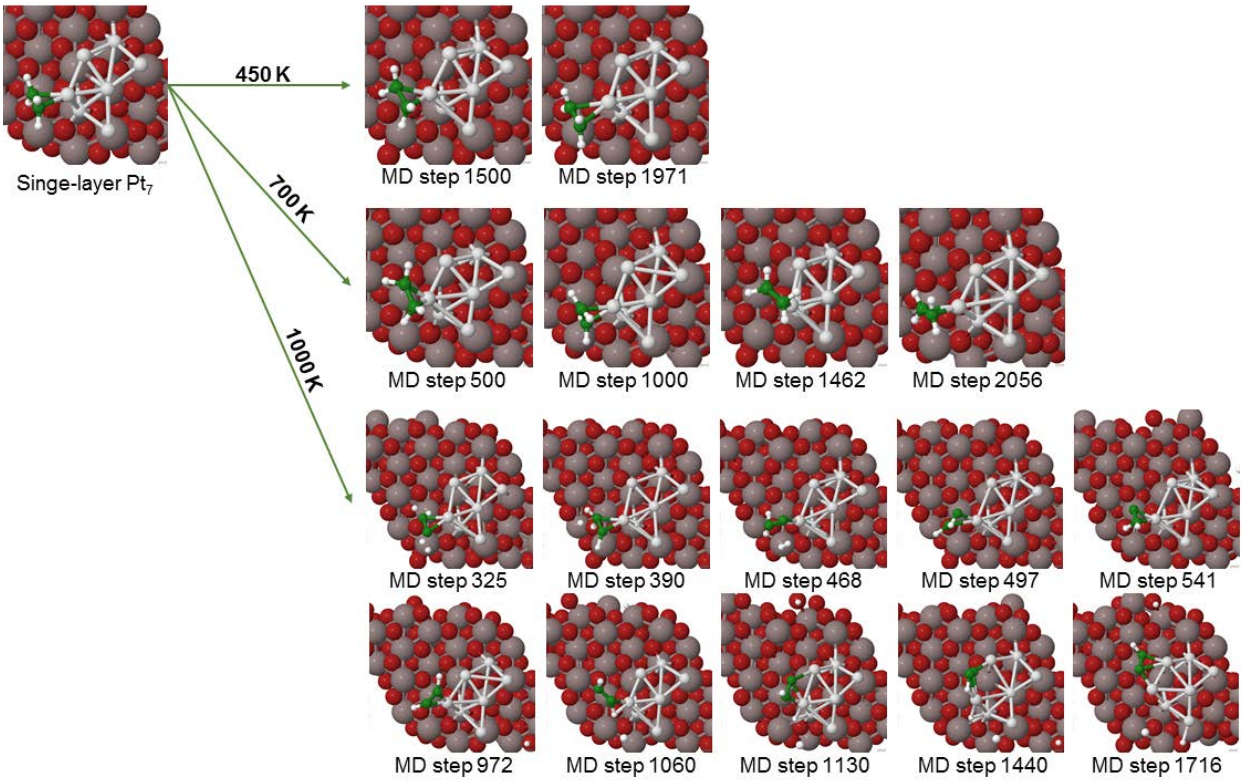

Fig. S8.3.10. Highlights from the MD trajectories of ethylene adsorbed on single-layer Pt_7 at catalytically relevant temperatures.

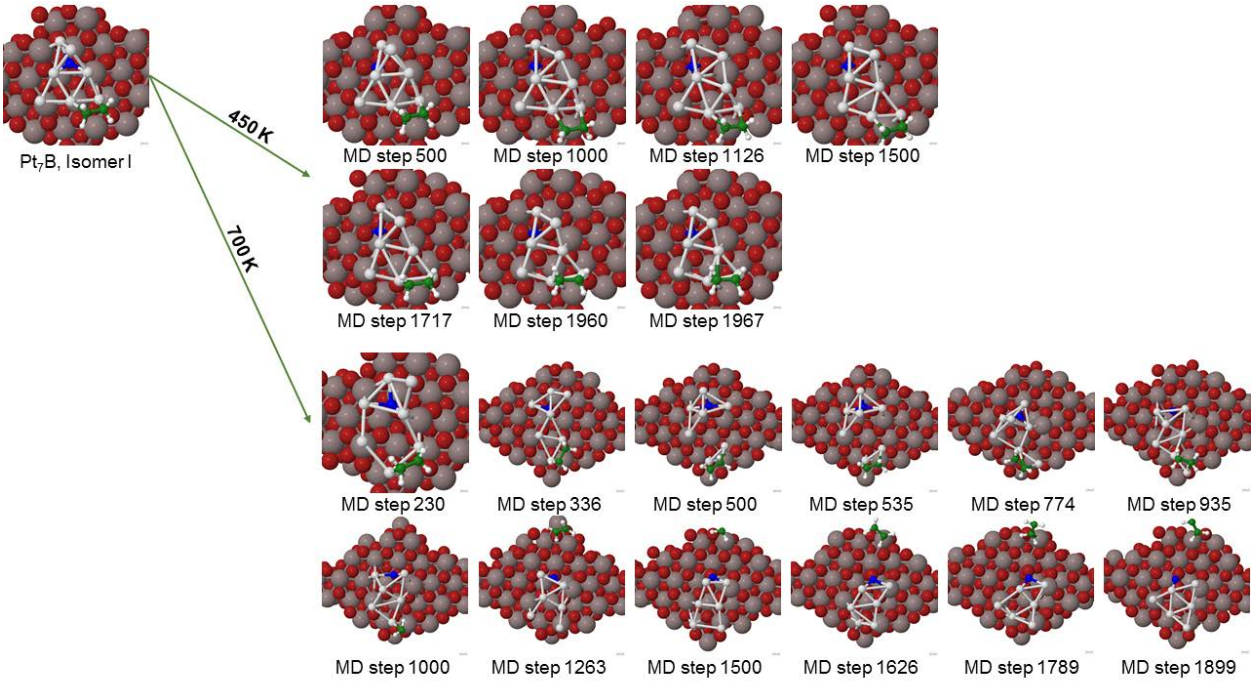

Fig. S8.3.11. Highlights from the MD trajectories of ethylene adsorbed on Pt_7B, Isomer I at catalytically relevant temperatures.

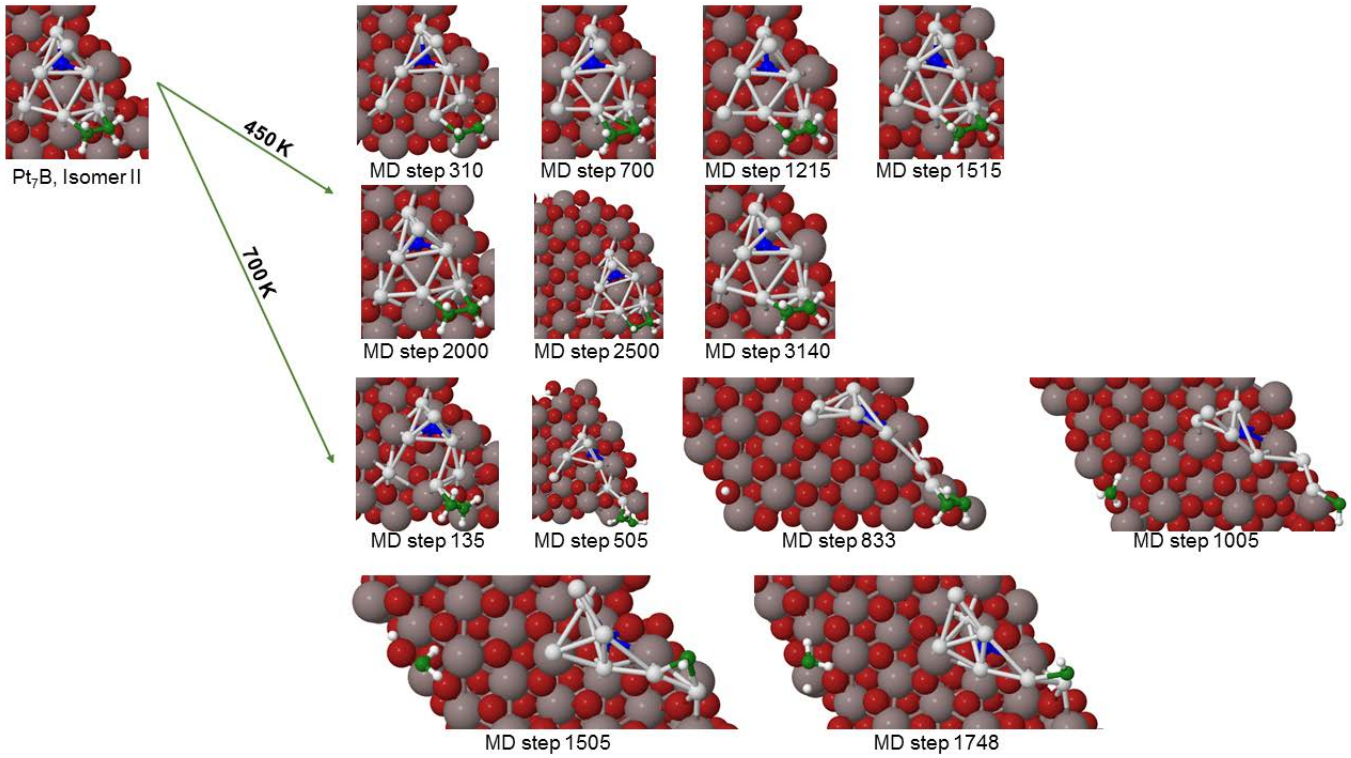

Fig. S8.3.12. Highlights from the MD trajectories of ethylene adsorbed on Pt_7B, Isomer II at catalytically relevant temperatures.

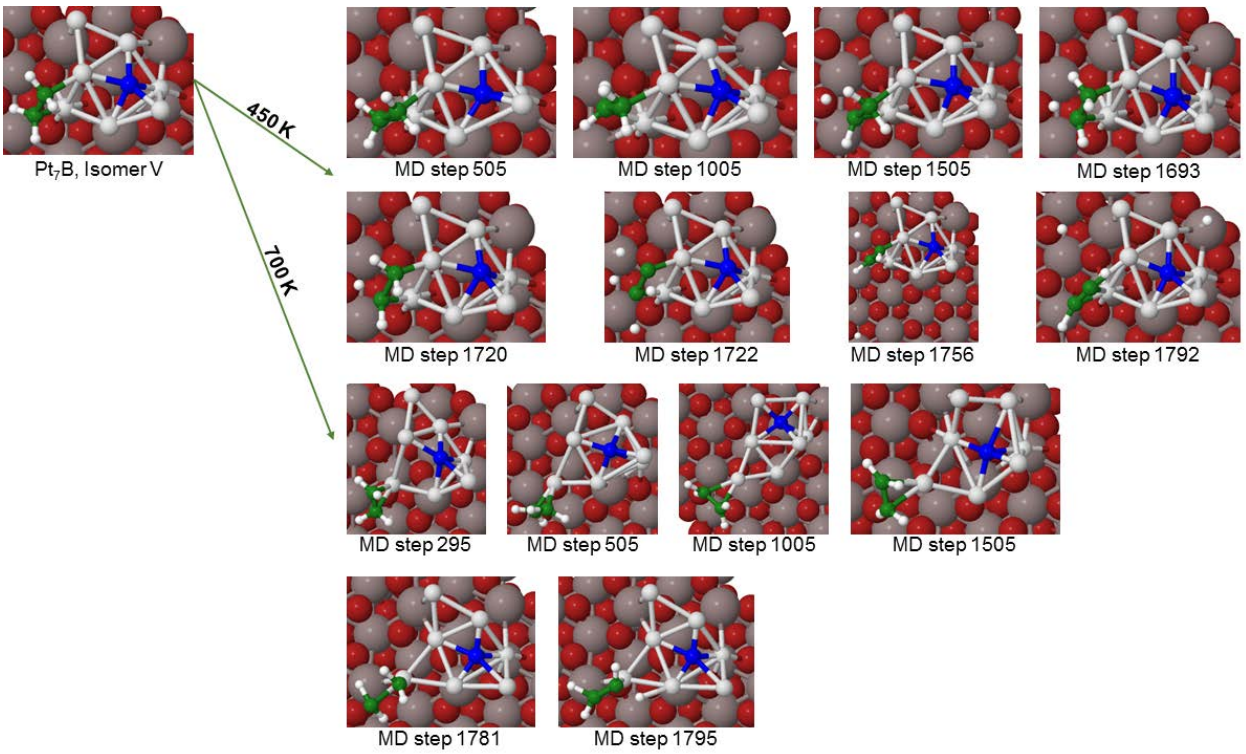

Fig. S8.3.13. Highlights from the MD trajectories of ethylene adsorbed on Pt_7B, Isomer V at catalytically relevant temperatures.

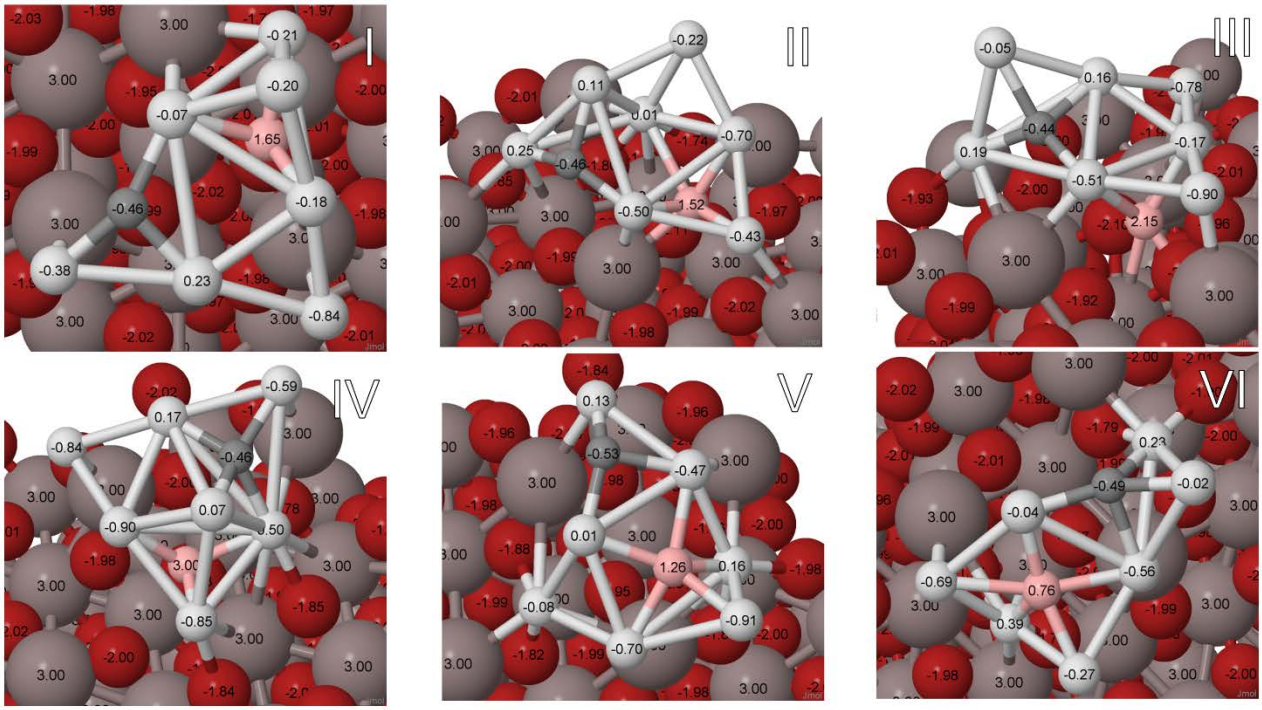

Fig. S8.3.14. The C-sticking configurations of the lowest six isomers of Pt_7B.

8.4. SUPPORTING INFORMATION FOR CHAPTER 5

Experimental

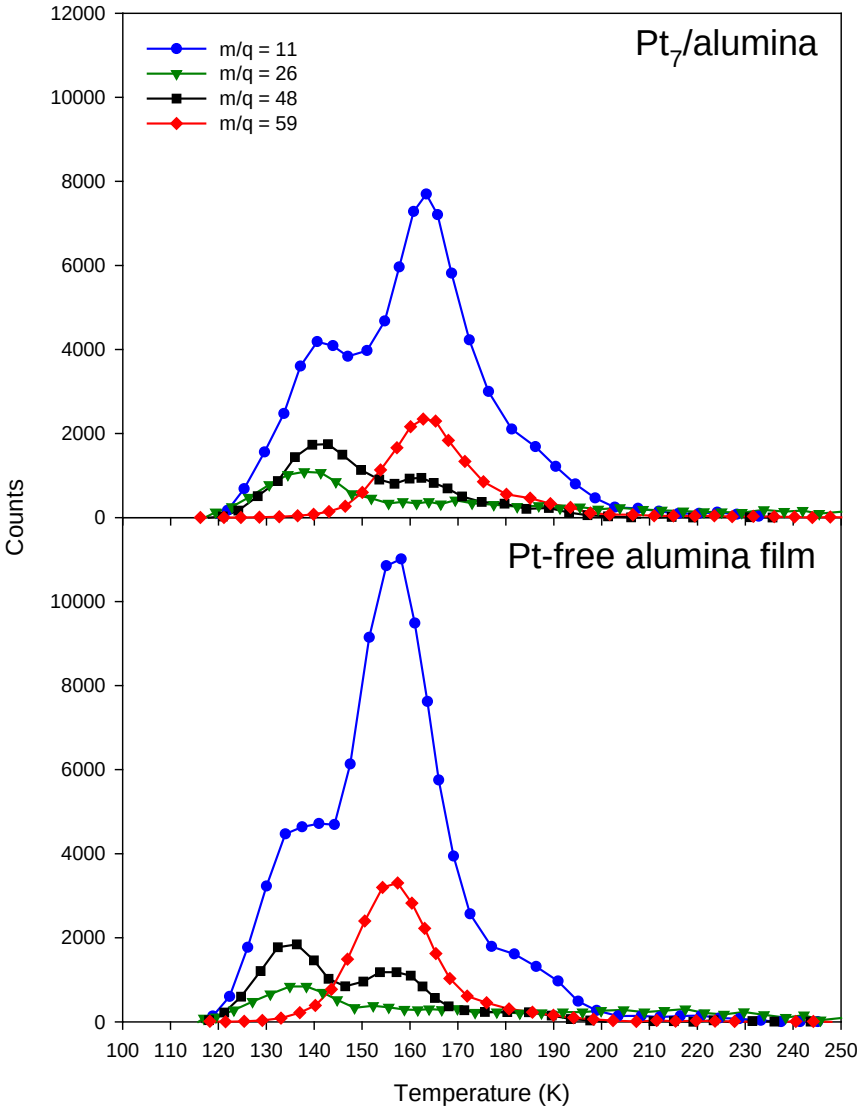

Fig. S8.4.1 Raw TPD spectra for select ion masses produced by electron impact ionization of species desorbing from Pt_7/alumina, and from a sample of the alumina/Ta(110) support, following exposure to 1.5 L of diborane at 130 K, followed by heating at 3 K/second

TPD fitting method and results:

In order to determine the distribution of desorption energies for the various borane products observed, TPD/R spectra were fit to the second order rate equation:

$$I(t)\ \alpha\ \frac{-d\theta}{dt} = (\theta^2(E)\cdot\ \nu)\ e^{\frac{-E}{kT(t)}},$$

where I(t) is the desorption as a function of time, v is a prefactor and T(t) is the temperature as a function of time. A distribution of population in sites with different energies for desorption, θ(E), is assumed and ran through the simulation, the calculated *I*(*t*) is compared to the experimental desorption vs. time, and then θ(E) is adjusted until the simulated I(t) matches the experiment. Because size-selected cluster samples are time consuming to prepare, and irreversibly changed by a single TPD/TPR run, it is simply not practical to extract v from a series of coverage-dependent experiments on every cluster size. Therefore, the simulations were tested for v ranging from 10^{13} to 10^{15} s^{-1}, covering a range often found in TPD. The simulated desorption/dehydrogenation energies shift by only ~7% *per* order-of-magnitude variation in v, and in **SI Figure S8.4.2-3** we present the θ(E) distributions obtained for v = 10^{14} s.

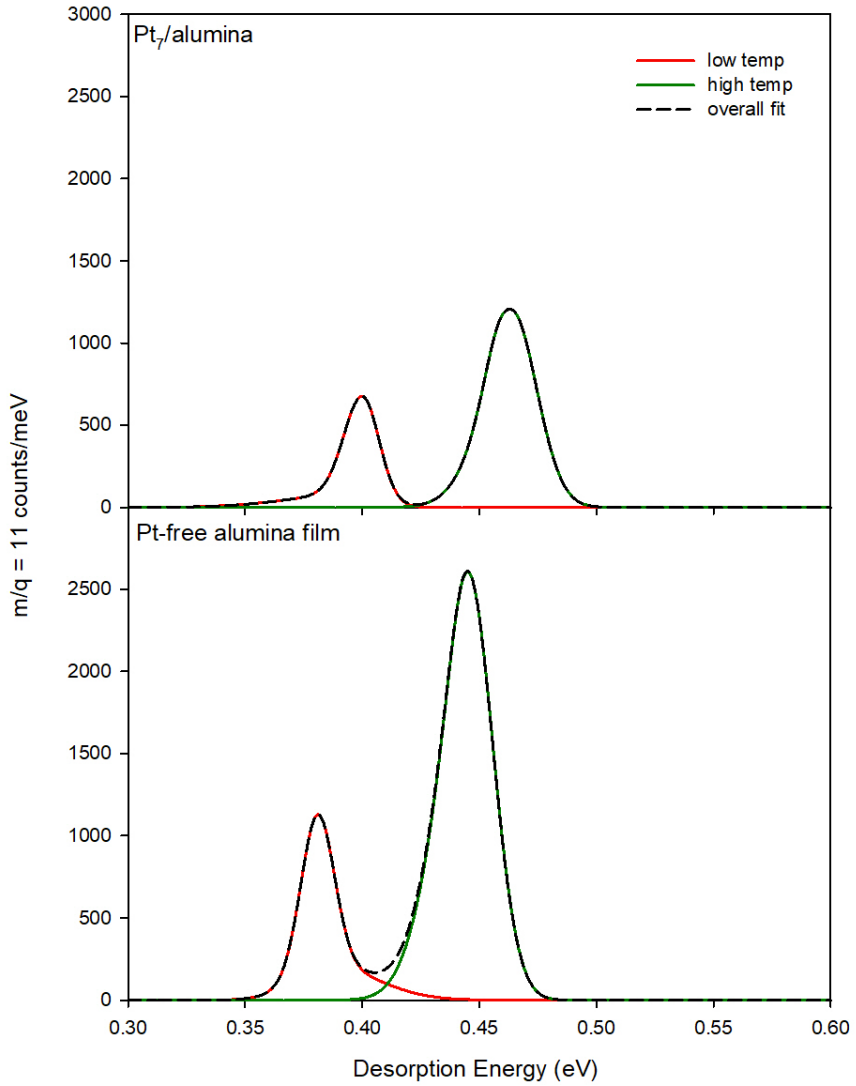

Fig. S8.4.2. Desorption energy distributions obtained by fitting the m/q = 11 desorption temperature dependences for B_2H_6 TPD/R experiments on Pt-free alumina and Pt_7/alumina.

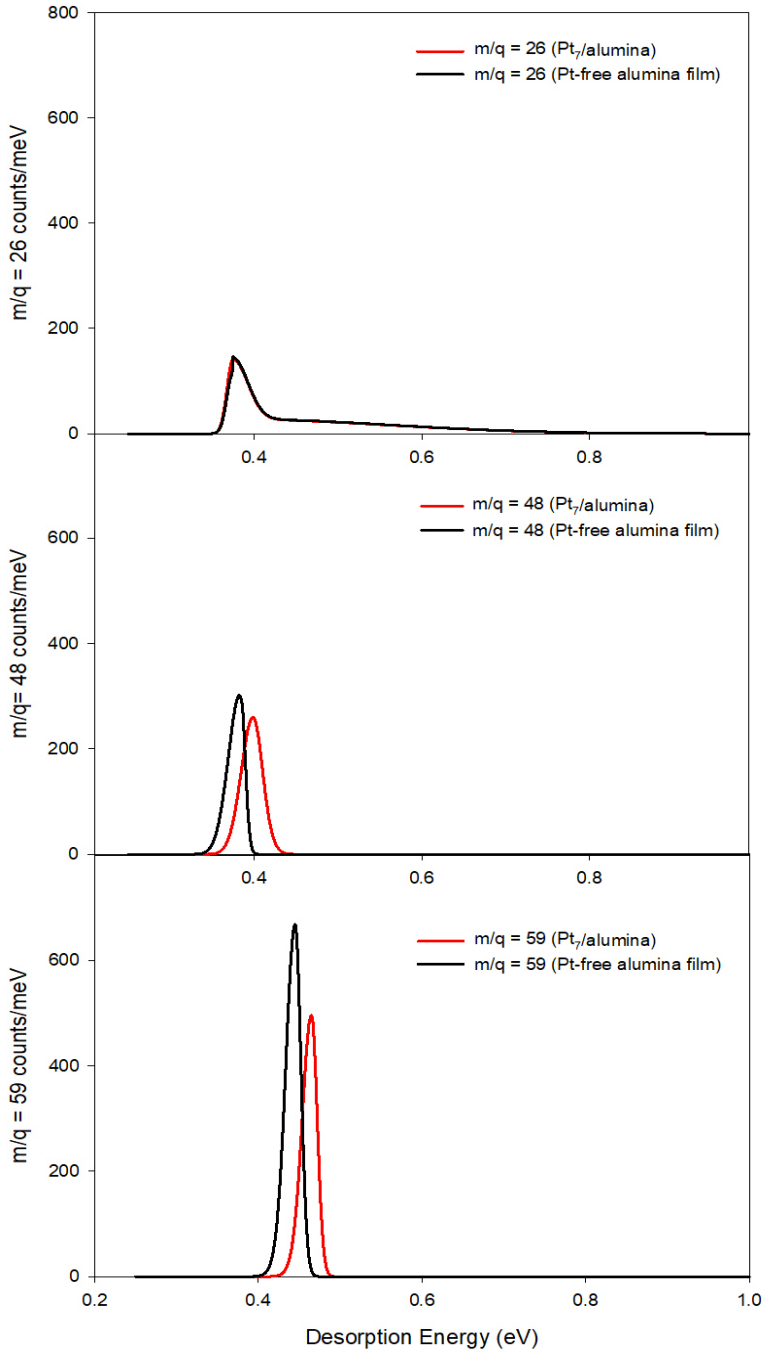

Fig. S8.4.3. Desorption energy distributions obtained by fitting the m/q = 26, 48, 59 desorption temperature dependences for B_2H_6 TPD/R experiments on Pt-free alumina and Pt_7/alumina

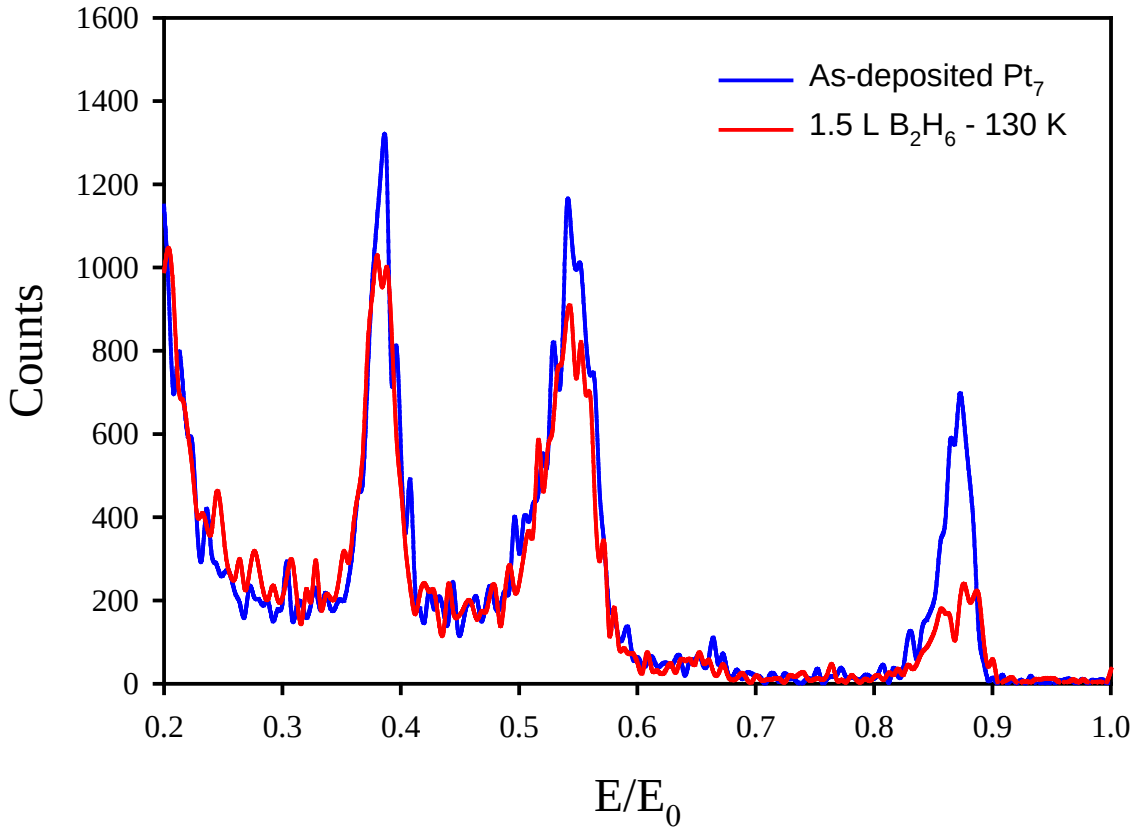

Fig. S8.4.4. Raw ISS for Pt_7/alumina samples. A spectrum measured immediately after depositing 0.1 ML of Pt_7 is shown in blue. A spectrum taken immediately after exposing a Pt_7/alumina sample to 1.5 L B_2H_6 at 130 K is shown in red. Note the large attenuation of Pt ISS signal ($E/E_0 \approx 0.93$), and smaller attenuations of the Al and O signals ($E/E_0 \approx 0.6$ and 0.41). Note also that no significant growth of signal is seen in the region expected for boron ($E/E_0 \approx 0.26$) after diborane exposure.

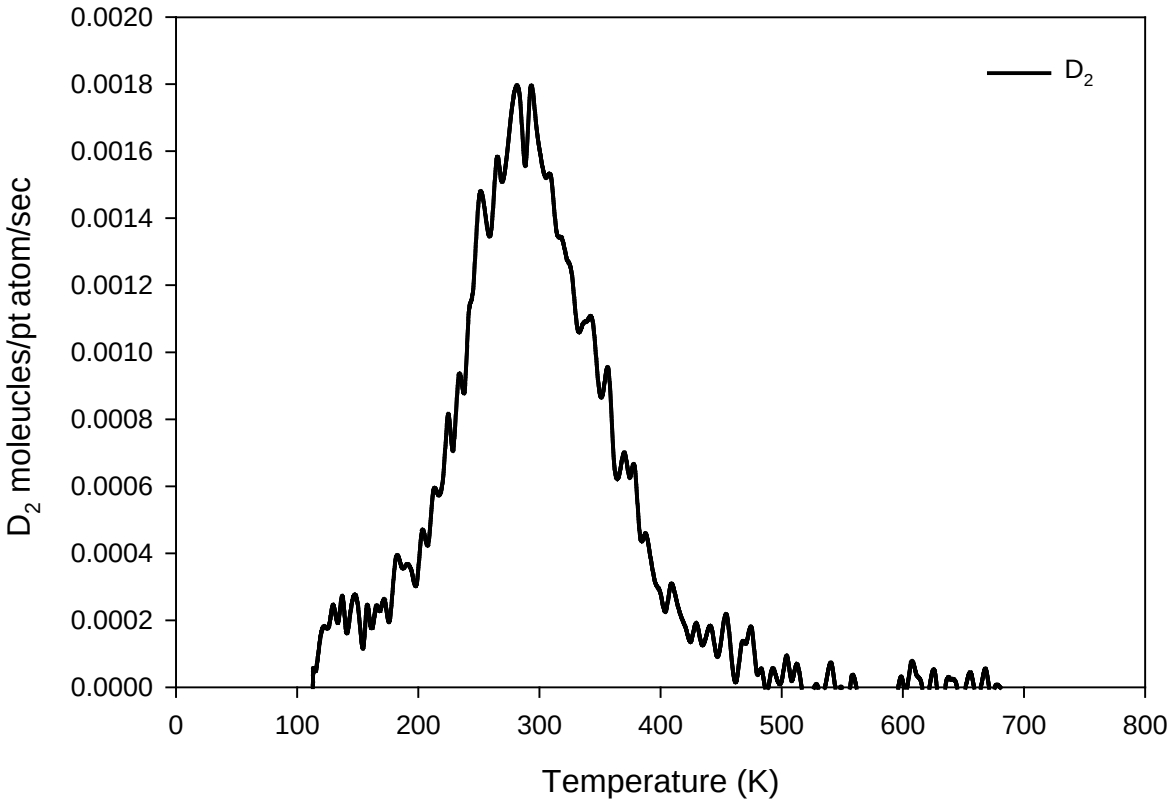

Fig. S8.4.5. TPD of D_2 from Pt_7/alumina, dosed with 5 L of D_2 at 130 K, then heated at 3 K/sec.

Computational

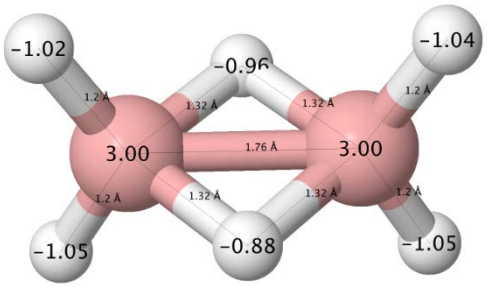

Fig. S8.4.6. Gas phase diborane with an E_{form} of -33.90 eV

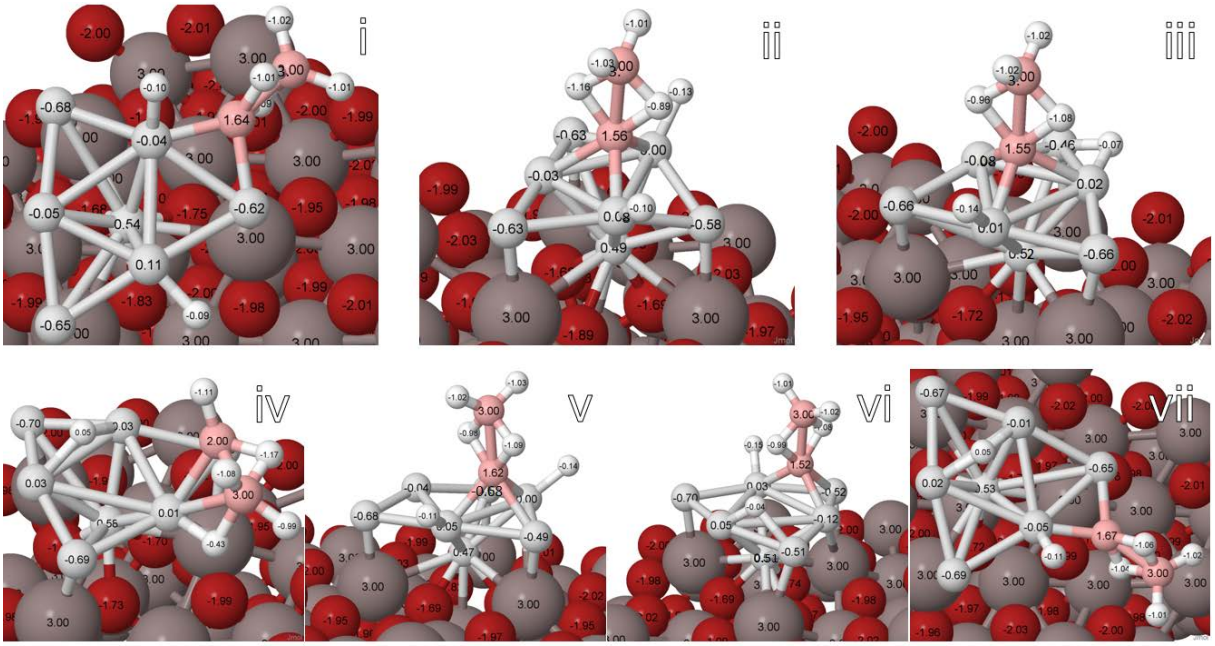

Fig. S8.4.7. Local Minima of Adsorbed Diborane on Pt_7, Isomer I (Prismatic)

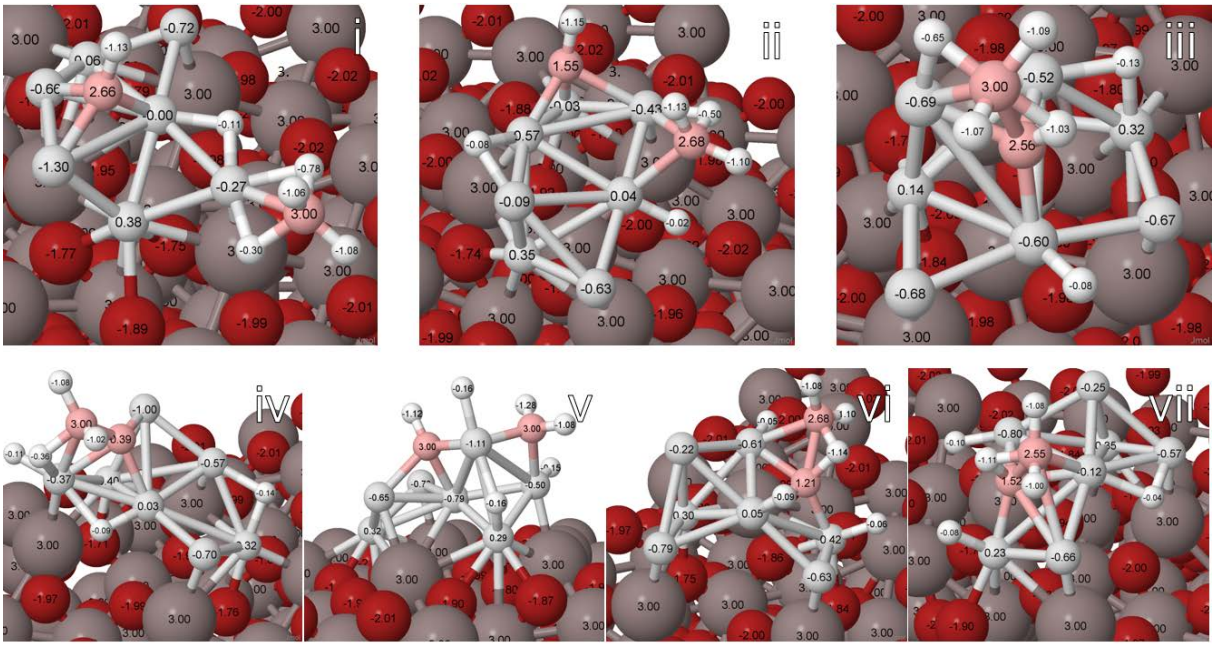

Fig. S8.4.8. Local Minima of Adsorbed Diborane on Pt_7, II (Single-Layer)

Multiplicity color: singlet. **Element color:** B, Pt.
All energies are relative to **the putative global minimum: -1.541025 [1] (#1.0.0), singlet**.

Range: 0.00 ~ 0.40 eV (8 structures)

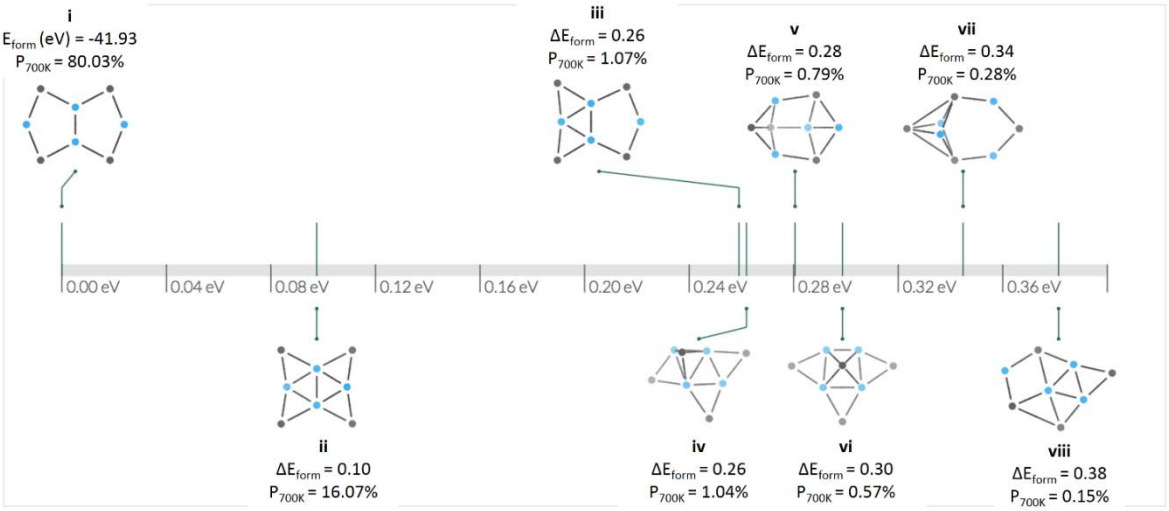

Fig. S8.4.9. Local Minima of Gas Phase Pt_4B_4

8.5. SUPPORTING INFORMATION FOR CHAPTER 6

Differences in adsorption energies and Bader charges between our calculations and Sorescu, et al.'s study may be accounted for by our different methods (their dispersion method was developed by Tkatchenko and Scheffler), cell sizes (doubled in the *x* and *y*-axes), and *U* (their *U = 3.5 eV*, our *U* = 3.6 eV).[9] We attributed our higher energies to interaction across the periodic cells.

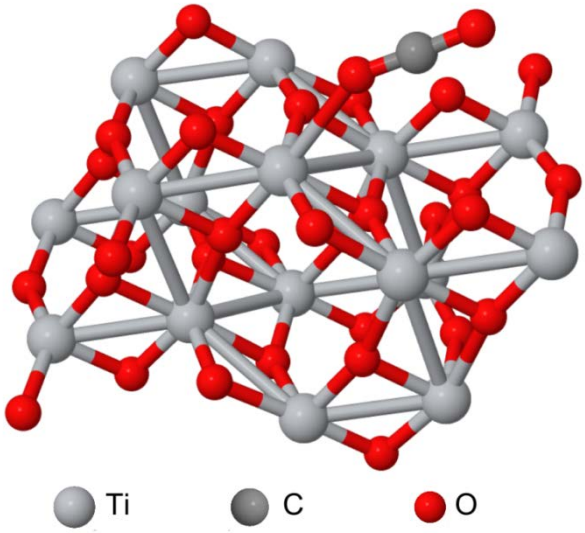

Fig. S8.5.1. PW-DFT result of neutral CO_2 adsorbed to the stoichiometric anatase 101 surface with a binding energy of -0.48 eV.

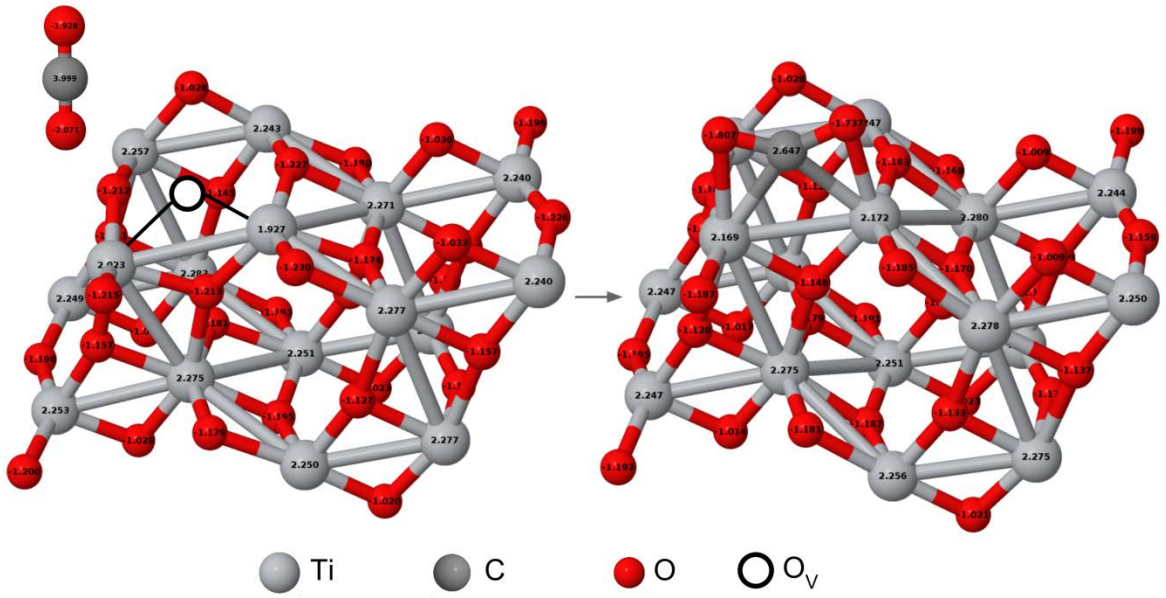

Fig. S8.5.2. PW-DFT calculated charge distribution for anatase TiO_2 with O vacancies before and after CO_2 adsorption and relaxation. Charges are in units of e.

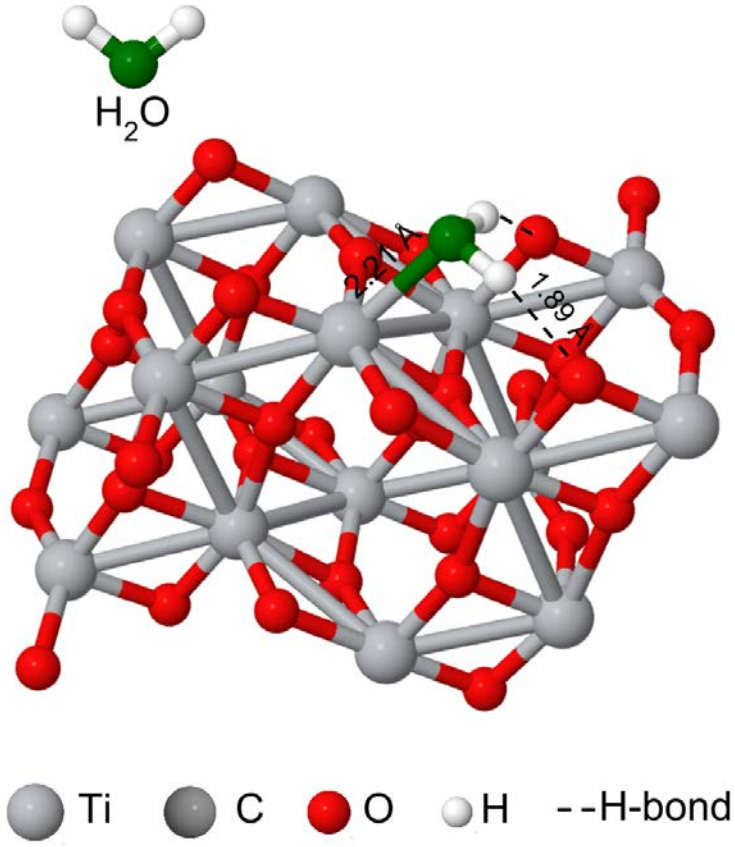

Fig. S8.5.3. H_2O adsorption on stoichiometric anatase with an adsorption energy of -1.26 eV.

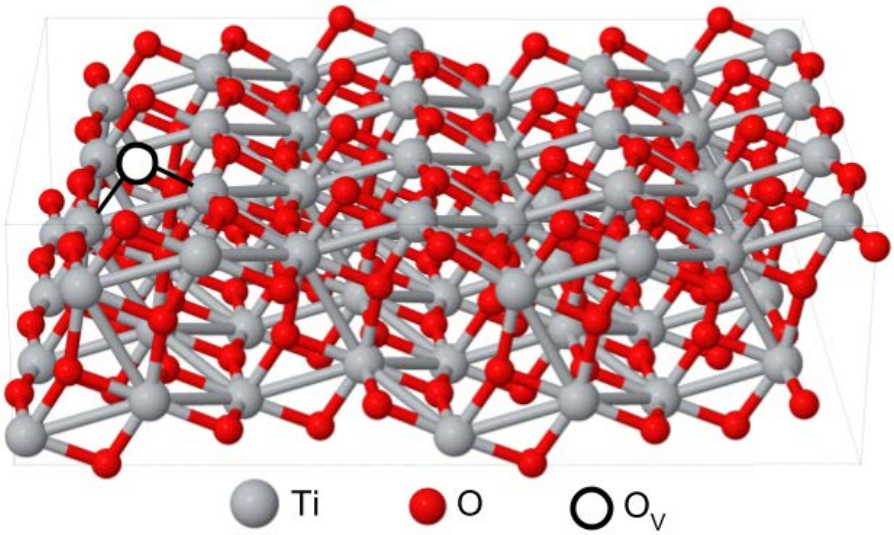

Fig. S8.5.4. The anastase surface with an oxygen vacancy utilized for co-adsorption calculations. This was grown from the original 16 TiO_2 unit cell utilized and discussed in previous publications.[10,11] As noted in a previous publication[12], the 2 delocalized electrons present due to the oxygen vacancy on the two surface Ti atoms closed to the oxygen vacancy.

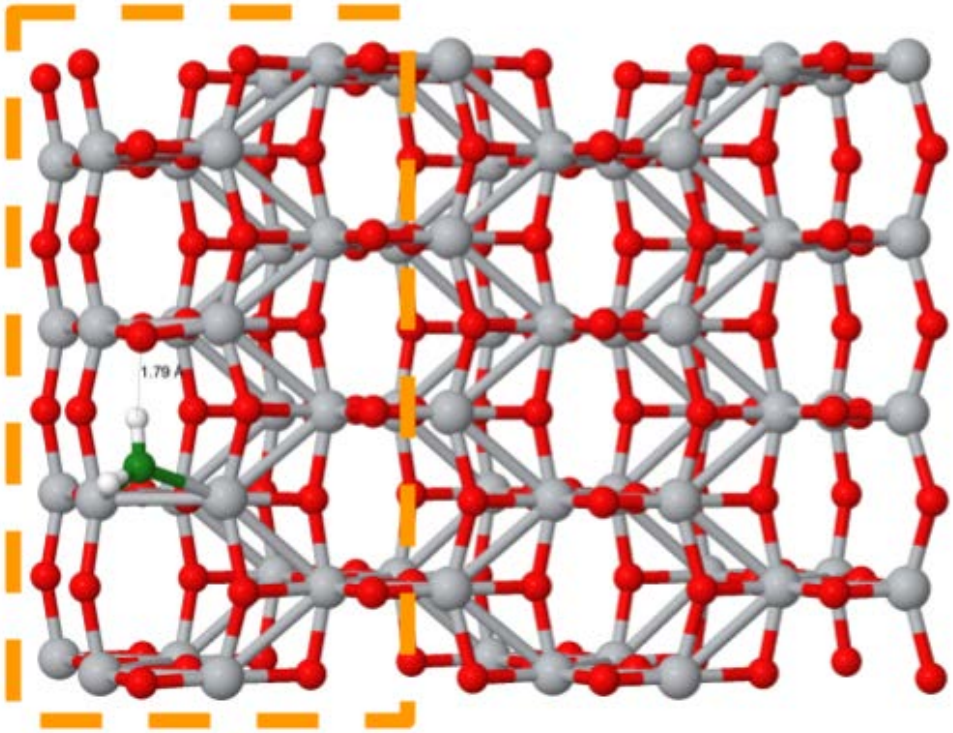

Fig. S8.5.5. The starting geometry for co-adsorption calculations of H_2O filling the oxygen vacancy with an adsorption energy of $E_{ads,H2O}$ (eV) = -1.27. This is slightly different from previous publications due to the surface size and subsequent coverage difference.[9-11] The yellow bound box indicates the area where CO_2 was deposited for co-adsorption calculations.

8.6. SUPPORTING INFORMATION FOR CHAPTER 7

Slabs were grown from the primitive surface cell to a (2 x 2) supercell (see **Figure 7.1** and **S8.6.1** for visualization of surfaces). All energies presented here are a result of spin unrestricted calculations. The Gaussian smearing for electronic occupation was implemented over the typical Methfessel-Paxton due to the increased speed of convergence under the stringent constraints placed for geometric and electronic relaxation. On most of the surfaces presented in this paper, cohesive energies changed by ~10^{-3} ev/atom when using Gaussian smearing over that of Methfessel-Paxton and total magnetization by ~10^{-1} μB. In most cases, the Gaussian smearing of electronic occupations under exacting parameters such as a smearing width of 0.01 eV, expansion of the basis set, and a 10^{-6} (10^{-5}) eV convergence limit on electronic (geometric) relaxations, reproduces accurate results. For all surfaces, the bottom 2 to 3 layers were held fixed with respect to the bulk. The alloy sub-layer in contact with a Pt-skin was always allowed to translate across all three dimensions. Moreover, the alloy sub-layer varied on Ni_3Pt between a Ni-layer and a mixed Pt- Ni layer. The (100), (110), and (111) surfaces were modelled, respectively, as cubic, orthorhombic, and hexagonal cells. The hexagonal cells for the (111) slabs required a Monkhorst-Pack centered at Γ.

Table S8.6.1. Cohesive Energies (E_{coh}) and Relative Cohesive Energies (ΔE_{coh}) of a Pt-skin with Varying Thickness and Sub-layer Alloy on Ni_3Pt

Systems	**3.82 Å**	**3.87 Å**	**3.92 Å**
(100)	E_{coh}(ev/atom)	ΔE_{coh}(ev/atom)	ΔE_{coh}(ev/atom)
1 Pt-skin on Pt-Ni (same as 100 facet) (1:3)	-4.97	0.01	0.03
3 Pt-skin on Pt-Ni (1:5)	-5.12	0.00	0.01
(110)			
Pt-Ni alloy (1:3)	-4.79	0.02	0.05
1 Pt-skin on Pt-Ni (1:4)	-4.93	0.01	0.03
3 Pt-skin on Pt-Ni	-5.09	0.00	0.01
(111)			
Pt-Ni alloy (1:3)	-5.10	0.01	0.03
1 Pt-skin on Pt-Ni	-5.14	0.00	0.02
3 Pt-skin on Pt-Ni	-5.22	-0.01	0.00

Note: ΔE_{coh} is with respect to E_{coh} under a lattice constant 3.82 Å.

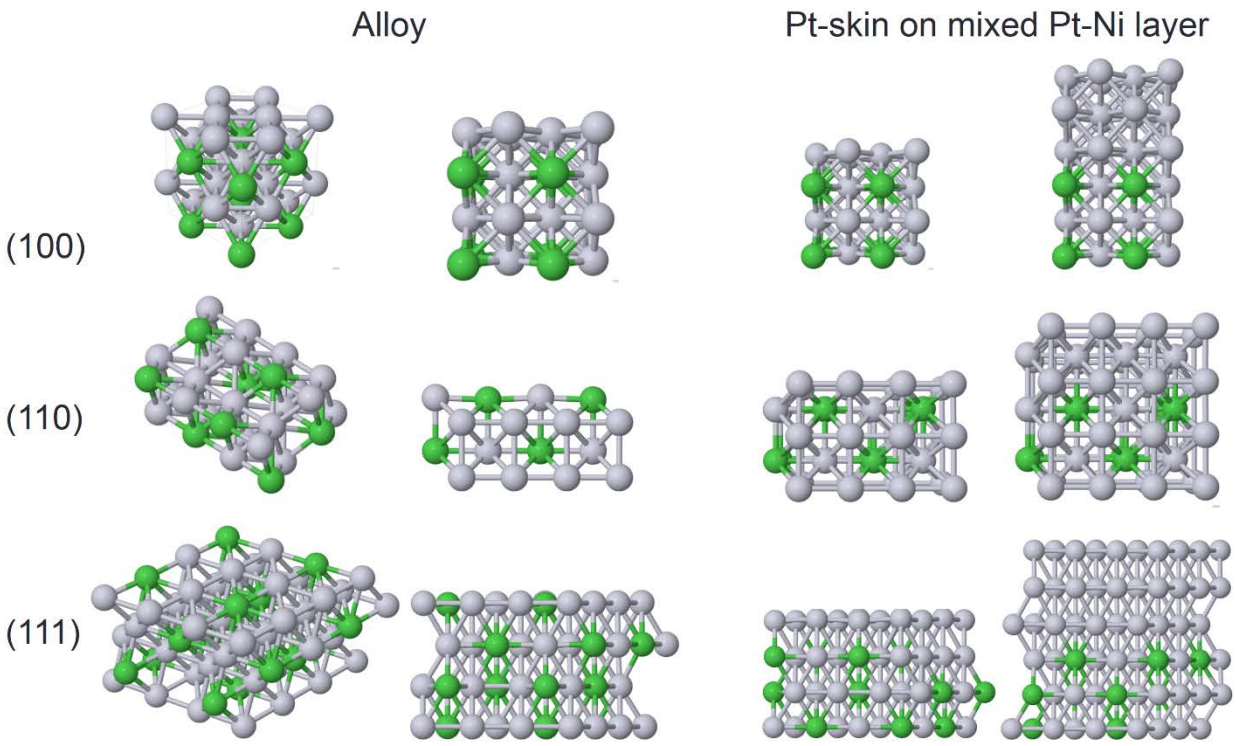

Fig. S8.6.1. The (2 x 2) supercells utilized in this study on surface stability with varying facet and Pt-skin thickness of the Pt_3Ni alloy.

REFERENCES

1 Zhai, H.; Ha, M.; Alexandrova, A. N. AFFCK: Adaptive Force-Field-Assisted ab Initio Coalescence Kick Method for Global Minimum Search. *Journal of Chemical Theory and Computation* **2015***, 11*, 2385-2393.

2 Tian, W. Q.; Ge, M.; Sahu, B.; Wang, D.; Yamada, T.; Mashiko, S. Geometrical and electronic structure of the Pt7 cluster: A density functional study. *The Journal of Physical Chemistry A* **2004***, 108*, 3806-3812.

3 Baxter, E. T.; Ha, M.; Cass, A. C.; Alexandrova, A. N.; Anderson, S. L. *ACS Cat.* **2017***, 7*, 3322-3335.

4 Desrosiers, R. M.; Greve, D. W.; Gellman, A. J. *J. Vac. Sci. Tech. A: Vac. Surf. Films.* **1997***, 15*, 2181-2189.

5 Krawczyk, M. *Appl. Surf. Sci.* **1998***, 135*, 209-217.

6 Rodriguez, J. A.; Truong, C. M.; Corneille, J.; Goodman, D. W. *J. Phys. Chem.* **1992***, 96*, 334-341.

7 Ha, M.; Dadras, J.; Alexandrova, A. *ACS Cat.* **2014***, 4*, 3570-3580.

8 Dadras, J.; Shen, L.; Alexandrova, A. *J. Phys. Chem. C.* **2015***, 119*, 6047-6055.

9 Sorescu, D. C.; Al-Saidi, W. A.; Jordan, K. D. CO2 adsorption on TiO2 (101) anatase: A dispersion-corrected density functional theory study. *J. Chem. Phys.* **2011***, 135*, 124701.

10 Qiu, J.; Zeng, G.; Ha, M.; Ge, M.; Lin, Y.; Hettick, M.; Hou, B.; Alexandrova, A. N.; Javey, A.; Cronin, S. B. Artificial photosynthesis on TiO2-passivated InP nanopillars. *Nano letters* **2015***, 15*, 6177-6181.

11 Qiu, J.; Zeng, G.; Ha, M.; Hou, B.; Mecklenburg, M.; Shi, H.; Alexandrova, A. N.; Cronin, S. B. Microscopic Study of Atomic Layer Deposition of TiO2 on GaAs and Its Photocatalytic Application. *Chemistry of Materials* **2015***, 27*, 7977-7981.

12 Ha, M.; Alexandrova, A. N. Oxygen Vacancies of Anatase(101): Extreme Sensitivity to the Density Functional Theory Method. *J. Chem. Theory Comput.* **2016***, 12*, 2889-2895.